CRANFIELD UNIVERSITY

JUAN R. REVELES

Development of a Total Lagrangian SPH Code for the Simulation of Solids Under Dynamic Loading.

SCHOOL OF ENGINEERING

PhD THESIS

CRANFIELD UNIVERSITY

SCHOOL OF ENGINEERING

PhD THESIS

2006-2007 Academic Year

JUAN R. REVELES

Development of a Total Lagrangian SPH Code for the Simulation of Solids Under Dynamic Loading.

Supervisor: Prof. Rade Vignjevic

Abstract.

This thesis makes use of an alternative SPH formulation, the Total Lagrangian formulation, to characterise dynamic events in solids and to achieve the proposed objectives outlined in Chapter 1. The structure is as follows:

Chapter 1, Introduction, describes the motivation for this research and outlines the objectives and the structure of this thesis.

Chapter 2, SPH fundamentals, supplies the standard procedure to generate particle equations and provides a comprehensive summary of gradient approximation formulae in SPH. The discretised SPH form of the conservation laws is included here.

Chapter 3, SPH drawbacks: describes the limitations of SPH such as particle deficiency, consistency, zero energy modes, treatment of boundaries and the tensile instability problem. A rigorous stability analysis of continua and SPH particle equations is also presented in this chapter.

Chapter 4, Total Lagrangian SPH. Continuum Mechanics considerations are discussed here; detailed derivations of SPH equations in a total Lagrangian framework are given together with potential corrections to the total Lagrangian SPH equations.

Chapter 5, Total Lagrangian SPH algorithms and their implementation using FORTRAN. This chapter gives a brief introduction to explicit codes. It also provides flow charts describing the Total Lagrangian algorithms and their integration into the MCM code.

Chapter 6, Total Lagrangian SPH code validation. This chapter includes problems of varying degrees of complexity. Examples are provided to illustrate how the Total Lagrangian SPH code compares to a conventional collocational SPH code. Cases are supplied for which the analytical solution is known, and the results compared with the SPH approximations in order to show the

accuracy of the approximation. Some examples are supplied which provide a direct comparison between SPH and non linear FE results and SPH and experimental results.

Chapter 7, Alternative formulation of SPH equations and improvements to the standard MCM code: Various modifications to the standard SPH code are presented. These modifications include the implementation of subroutines that make use of an alternative approach to ensure the conservation of mass law is met locally at every particle. The introduction of XSPH to achieve further stabilisation of the code was also carried out and some examples are provided. The theory behind an alternative form of the conservation of mass equation as proposed by Belytschko [4] is explained and its implementation into the SPH code is assessed through examples. Also, an alternative formulation of SPH equations based on the general theory of mixed Lagrangian-Eulerian formulations [35] is presented: these equations could serve as the foundation for future research in this field.

Chapter 8, Conclusions are presented in this chapter.

A brief literature review is provided at the beginning of each chapter as a means of introduction to the topic and a concise summary outlines the main points discussed.

Acknowledgements.

First and foremost I would like to thank Professor Rade Vignjevic for his invaluable guidance throughout this research work. Without him this thesis would never have materialised.

Thanks also to Cranfield University for giving me the opportunity to pursue my academic objectives and for supporting me and my research work through their DTA scheme.

Dr. James Campbell, Dr. Kevin Hughes, Dr. Mustapha Gourma and Mr. James Brown have all contributed in different ways to the successful completion of this research project, thank you all.

Thanks to Mr. Alexander Lukyanov for the helpful discussions and for keeping me sane during my first year at the lonely Cranfield University campus.

I dedicate this thesis to my beloved wife, Dr. Lucy Wilson, for her endless love, encouragement and support during these challenging years. Thank you Lucy.

The birth of my daughter Amelia May during my second year as a PhD student brought great joy and encouraged me to work harder towards achieving my goal. I dedicate this research work to her as well.

I dedicate this thesis to all those who over many years have given freely of their time to teach me with no expectations in return. I hope this thesis will be a tribute to their efforts.

Dedico esta tesis a mi madre, mi hermano y hermanas, cunados y cunada por su amor y comprension. Tambien dedico este trabajo a mis sobrinas y sobrino, espero que los aliente a seguir adelante con sus estudios hasta alcanzar sus metas deseadas.

Glossary.

$\vec{\mathbf{a}}$	Acceleration
A, ψ	Any physical field
$\mathbf{B}, B$	Matrix of derivative correction terms
$\vec{\mathbf{b}}$	Body forces per unit mass
C	Speed of sound
C_i	Coefficients of the polynomial equation of state
$\mathbf{D}, \dot{\boldsymbol{\varepsilon}}, \dot{\varepsilon}$	Rate of deformation tensor
D_i	Damage parameters in the Johnson-Cook material model
$\mathbf{E}$	Green-Lagrange strain tensor
E	Young modulus
e	Specific internal energy
$\dot{\mathbf{F}}$	Material velocity gradient
$F_{i,j}, \bar{\bar{\mathbf{F}}}$	Gradient of deformation tensor
f'	Time derivative of $f(r,t)$ at a constant referential co-ordinate r
$f_{,i}$	Gradient of $f(r,t)$ with respect to referential co-ordinates r
G	Shear modulus
h_{ij}, h	Smoothing length
I, J	Particle identification sub-index
J	Jacobian, determinant of gradient of deformation tensor
$\bar{\bar{\mathbf{L}}}$	Velocity gradient
$\mathbf{L}$	Matrix of derivative correction terms
$\bar{\bar{\mathbf{P}}}, \mathbf{P}$	Second order tensor, 1st Piola-Kirchhoff stress tensor
P	Pressure, 1st Piola-Kirchhoff stress tensor in 1-D
$q = \frac{r}{h}$	Parameter that relates inter-particle distance to smoothing length
$\mathbf{R}, R, \omega$	Spin tensor
$r = \lvert\vec{\mathbf{x}} - \vec{\mathbf{x}}'\rvert = \lvert\vec{\mathbf{x}}_i - \vec{\mathbf{x}}_j\rvert$	Inter-particle distance
$\mathbf{r}$	Referential coordiantes
$\mathbf{S}, S$	Deviatoric stress, 2nd Piola-Kirchhoff stress tensor
S	Sub-domain of particle I
S_i	Coefficients of the Mie-Gruneisen equation of state
T	Scalar field such as temperature
$u,\ \vec{\mathbf{u}} = \vec{\mathbf{x}} - \vec{\mathbf{X}}$	Displacement of a material point
$\mathbf{V}_J^0$	Initial volume of particle J
$\vec{\mathbf{v}}$	Vector field such as velocity
$\mathrm{W}(r,h), \mathrm{W}(\vec{\mathbf{x}} - \vec{\mathbf{x}}', h)$	Smoothing function

$\tilde{W}\left(\vec{X}-\vec{X}',h_0\right)$ Normalised smoothing function in terms of material coordinates

$\dot{w}_i$ Difference between the velocity of a material point X and the velocity of a referential point r multiplied by the Jacobian

$\mathbf{x}, x$ Spatial or Eulerian co-ordinates

$\vec{\mathbf{X}}, X$ Lagrangian or material coordinates

γ_0 Gruneisen gamma

δ_{ij} Kronecker delta

$\delta(\mathbf{x}-\mathbf{x}')$ Dirac delta function

Δt Time step

$\dot{\hat{\varepsilon}}$ Rate of deformation written in an arbitrary referential domain

$\varepsilon_{s,t}$ Smoothing and truncation error

κ Wave number

Λ Pulse length

μ Excess compression in the polynomial equation of state

υ Poisson ratio

$\sum_{J\in S}\cdot$ Weighted sum over the S domain

$\bar{\bar{\sigma}}, \sigma$ Cauchy stress tensor

σ^{∇} Jaumann stress rate

$\varphi(X,t)$ Mapping of initial into current configuration

$\hat{\phi}(r,t)$ Mapping of referential configuration into current configuration

$\phi(X,t)$ Mapping of initial configuration into referential configuration

∇_X Nabla operator with respect to a material point X

ϖ Complex frequency

Ω Particle domain

Ω_r Referential domain

Ω_x Spatial domain

Ω_X Initial/Material configuration

$\langle\cdot\rangle$ Smoothing approximation

$\frac{\partial}{\partial t}, \frac{D}{Dt}$ Partial and material derivative operator

CONTENTS.

LIST OF FIGURES.

LIST OF TABLES.

In the language of Mathematics, equations are like poetry:
They state truths with a unique precision, convey
volumes of information in rather brief terms, and
often are difficult for the uninitiated to comprehend.
And just as conventional poetry helps us to see deep
within ourselves, mathematical poetry helps us to
see far beyond ourselves-if not all the way up to heaven,
then at least out to the brink of the visible universe.

(Michael Guillen in "Five Equations that Changed the World")

CHAPTER 1

INTRODUCTION

Smoothed Particle Hydrodynamics (SPH) is a novel numerical technique that has found widespread application in the simulation of transient dynamic events where large deformations of the problem domain need to be studied with accuracy. SPH was originally conceived for astrophysical problems and was first introduced by Lucy [58] and Gingold and Monaghan [31] independently. However, recent applications incorporate strength of materials [12, 37, 46, 51, 77, 86, 87] and the study of fluid flow [22, 33, 43, 71, 77]. These advances and the flexibility of the SPH method to incorporate new physics have made it an attractive tool to model problems in solid mechanics, problems involving fluid-solid interactions [85], phase change [65], explosive charges [74] and multi-phase flows [64], and it has recently been applied to model viscous and heat conducting flow problems [16] and conduction heat transfer [44].

In essence, SPH is a pure Lagrangian particle method that uses no underlying grid to approximate the value of a function or its derivative at a point. Instead, SPH relies on interpolation theory whereby the value of a field can be approximated by using a smoothing function (or "kernel") and by performing a weighted sum of discretised particles over the domain of interest. In addition, the kernel approximation allows spatial gradients to be determined from the value of the function at discrete points and the value of the first spatial derivative of the kernel, rather than from the value of the derivatives of the function itself. This key feature of SPH represents the main computational strength of the method and the reason SPH is regarded as meshless in nature: a rigid connectivity of nodes is not required for the approximation of the gradient terms found in a great deal of equations in physical mathematics.

In contrast, standard Eulerian and Lagrangian finite element formulations require an underlying mesh for the approximation of the spatial derivative terms, which make them computationally expensive and impractical in some scenarios such as in applications that involve free surfaces and moving boundaries [55].

1.1 The Motivation for this Research.

Meshless methods in general and the SPH method in particular should not be regarded as the panacea to every existing deficiency in modern computational mechanics. The initial excitement experienced by the computational mechanics community was brought to an end when it was discovered that, similarly to other numerical techniques, SPH also caused some unwanted effects. The numerical simulation of solids revealed that SPH suffered from certain instabilities which manifested as an unphysical clumping of particles. This condition is known in the literature as tensile instability [63, 79, 80]. In the computational characterization of solids this condition is highly undesirable since it does not allow differentiation of real fracture from numerical fracture. A number of solutions to the tensile instability problem

have been proposed, including non-collocational SPH (where stress or velocity field data is carried by a different set of interpolating particles [26]), the introduction of interparticle forces based on an interparticle contact potential or interparticle contact algorithms [63,69,70] and Lagrangian kernel based interpolation SPH [6,73]. The use of Lagrangian kernels in a Total Lagrangian framework is the avenue fully exploited in the current research. This ensures the required level of accuracy and the minimization of numerical instability effects in the characterisation of dynamic events in solids. Additionally, the different types of corrections necessary for first order consistency [9,45,74] are also addressed and introduced in the final version of the Total Lagrangian SPH code.

Kernels can incorporate a varying smoothing length, h, which is comparable to adaptive gridding in mesh-based codes [68]. This allows a better resolution in regions within the domain where a higher level of detail in the solution is required. A varying smoothing length is also very useful when large expansions occur within the material and particles become either so distant from each other that they no longer interact, or so close that a large number fall within the smoothing length. In these cases, h should be made to vary accordingly [7,68]. This is known as *adaptivity*. New algorithms will be created and incorporated to the existing code if required.

Some authors [39,40] state that a meshless Lagrangian formulation linked to a standard finite element Lagrangian formulation is a very robust tool since it makes both severe distortion and structural response applications possible within one single Lagrangian code. In this project the Total Lagrangian SPH code will be linked to an ordinary mesh based Finite Element code (DYNA 3-D) through a contact algorithm that makes use of a contact potential to define a repulsion force between SPH nodes and FE particles. This part of the dissertation is a direct extension of the algorithm proposed by [25].

In order to demonstrate the accuracy of the code, the numerical results have to be compared with experimental data and with analogous numerical techniques. Existing experimental data will be used for correlation purposes. In other cases, a direct comparison with other numerical techniques such as non-linear finite elements will be carried out. In literature, the most commonly employed tests for correlation and validation are the Taylor test [47,61], the plate impact test [18,42] and the penetration test [38,76]. Consequently these tests will be used to demonstrate the computational accuracy and robustness of the code.

The existing SPH Cranfield code (the "MCM code") was originally developed in FORTRAN. Hence several FORTRAN subroutines need to be created and many others modified in order to seamlessly integrate the Total Lagrangian SPH code into the existing MCM code. It is expected a tracking document will be required to capture the created and modified FORTRAN files. This document should outline the nature of the changes, date of last modification and level or type of modification needed.

1.2 Summary of objectives.

The objectives of this project are:

1.- To extend the capabilities of the existing Cranfield Smoothed Particle Hydrodynamic (SPH) code (MCM) into a 3-D total explicit Lagrangian SPH code integrated to the material models available in DYNA 3-D.

2.- To investigate and implement a suitable adaptivity algorithm into the SPH code if required.

3.- To demonstrate through correlation with existing experimental data and alternative numerical techniques, that large deformation in solids can be accurately modelled through the use of the SPH code resulting from this research.

4.- To explore further improvements to the SPH method.

1.3 Structure of the thesis.

This thesis makes use of an alternative SPH formulation, the Total Lagrangian formulation, to characterize dynamic events in solids and to achieve the proposed objectives outlined. The structure is as follows:

Chapter 2, SPH fundamentals, supplies the standard procedure to generate particle equations and provides a comprehensive summary of gradient approximation formulae in SPH. The discretised SPH form of the conservation laws is included here.

Chapter 3, SPH drawbacks: describes the limitations of SPH such as particle deficiency, consistency, zero energy modes, treatment of boundaries and the tensile instability problem. Techniques available to tackle these issues are discussed. A rigorous stability analysis of continua and SPH particle equations is also presented in this chapter. This permits the reader to identify the terms that yield the tensile instability condition in the ordinary SPH equations, and how these terms are no longer exhibited when the equations are derived in a Total Lagrangian framework.

Chapter 4, Total Lagrangian SPH. Continuum Mechanics considerations are discussed here. Detailed derivations of SPH equations in a total Lagrangian framework are given together with potential corrections to the total Lagrangian SPH equations.

Chapter 5, Total Lagrangian SPH algorithms and their implementation to FORTRAN. This gives a brief introduction to explicit codes. In addition, flow charts describing the Total Lagrangian algorithms and their integration into the MCM code are provided.

Chapter 6, Total Lagrangian SPH code validation. This chapter includes problems of varying degrees of complexity. Examples are provided to illustrate how the Total Lagrangian code compares to a conventional collocational SPH code. Cases are supplied for which the analytical solution is known, and the

results compared with the SPH approximations in order to show the accuracy of this method. Other examples demonstrate how certain corrections restore 1st order consistency in the approximation of derivatives. Finally, some examples are supplied which provide a direct comparison between SPH and non-linear FE results and SPH and experimental results.

Chapter 7, Alternative formulation of SPH equations and improvements to the standard MCM code: Various modifications to the standard SPH code are presented. These modifications include the implementation of subroutines that make use of an alternative approach to ensure the conservation of mass law is met locally at every particle. The introduction of XSPH to achieve further stabilization of the code was also carried out and some examples are provided. The theory behind an alternative form of the conservation of mass equation as proposed by [4] is explained and its implementation into the SPH code is assessed through examples. Also, an alternative formulation of SPH equations that make use of a moving reference frame is sketched; these equations could serve as the foundation for future research in this field.

Chapter 8, Conclusions are presented in this chapter.

In the Appendix, some Total Lagrangian input files in 1-D, 2-D, 3-D are provided and the expected results are also included as a means of code verification.

A brief literature review is provided at the beginning of each chapter as a means of introduction to the topic and a concise summary outlines the main points discussed.

CHAPTER 2

SPH FUNDAMENTALS

Chapter 1 provided a brief introduction to the SPH method, its key features and its flexibility to model a variety of physical phenomena. It was stated that one of the computational strengths of the method was that spatial derivatives can be approximated through the derivatives of the interpolating function without the need for a background mesh. When this method is applied to the conservation laws of Continuum Mechanics, which are expressed in the form of partial differential equations, these expressions are transformed into integral equations which estimate the kernel approximation of the field variables at a point. Computationally, in a fully collocational SPH scheme, information is only known at discrete points, hence integrals are evaluated as sums over neighbouring points. In this Chapter the basic ingredients of the SPH method will be provided. In addition, a detailed analysis of derivative

approximations will be carried out. Subsequently, SPH interpolating formulae will be used to derive the standard SPH equations of the conservation laws in an Eulerian form. Finally the resulting error of an SPH approximation will be evaluated and sources of error identified.

2.1 The Basic Ingredients of the SPH Method.

2.1.1 Particle discretisation and its advantages over mesh-based discretisation.

Prior to discussing mesh and meshless formulations let us first define a concept which is intimately linked to the nature of the domain discretisation: the concept of spatial and material coordinates.

The spatial coordinate , $\vec{\mathbf{x}}$, specifies the location of a point in space. These coordinates are also called Eulerian coordinates [4,60]. On the other hand, material or Lagrangian coordinates are material points that lie within a body [4,60] and move with the material domain. Each material point has a unique material coordinate which is usually regarded as its spatial coordinate during the initial configuration prior to the deformation process taking place. The mesh description depends on the choice of the independent variables used in the definition of the motion of a body, which can be described in terms of the Lagrangian or material coordinates $\vec{\mathbf{X}}$, or in terms of the Eulerian or spatial coordinates. The differences between Eulerian and Lagrangian meshes are most clearly seen in the behaviour of the nodes defining the mesh (Fig. 2.1). If the mesh is Eulerian then the Eulerian coordinates of the nodes are fixed (i.e. the nodes are coincident with spatial points). If the mesh is Lagrangian, the material coordinates of the nodes are time invariant (i.e. the nodes are coincident with material points).

The nature of complications that may arise during the solution process depend on the type of mesh selected. For instance, in a Lagrangian mesh, boundary nodes remain on the boundary throughout the evolution of a problem (which simplifies the imposition of boundary conditions in Lagrangian

meshes, for example), whereas in Eulerian meshes boundary nodes do not remain coincident with the boundary. This implies boundary conditions must be imposed at points which are not nodes. Conversely, in Lagrangian meshes the material points remain coincident with mesh points thus the mesh deforms with the material which might yield a severely distorted set of elements. It is a well known fact that computational accuracy degrades with the geometrical quality of the elements. Hence the magnitude of the distortion that can be simulated with a Lagrangian mesh is limited. By contrast, Eulerian elements remain unchanged by the deformation of the material so no degradation of accuracy occurs as a result of material deformation [4]. The ability of the Lagrangian codes to simulate problems with large deformations can be enhanced by the use of erosion algorithms [35]. These algorithms work by removing Lagrangian zones which have reached a user-specified strain, typically above 150% [37]. Erosion algorithms, however, do not attempt to model the physics of the problem. In fact, energy and mass are removed from the problem which clearly contradicts the basic conservation laws of physics.

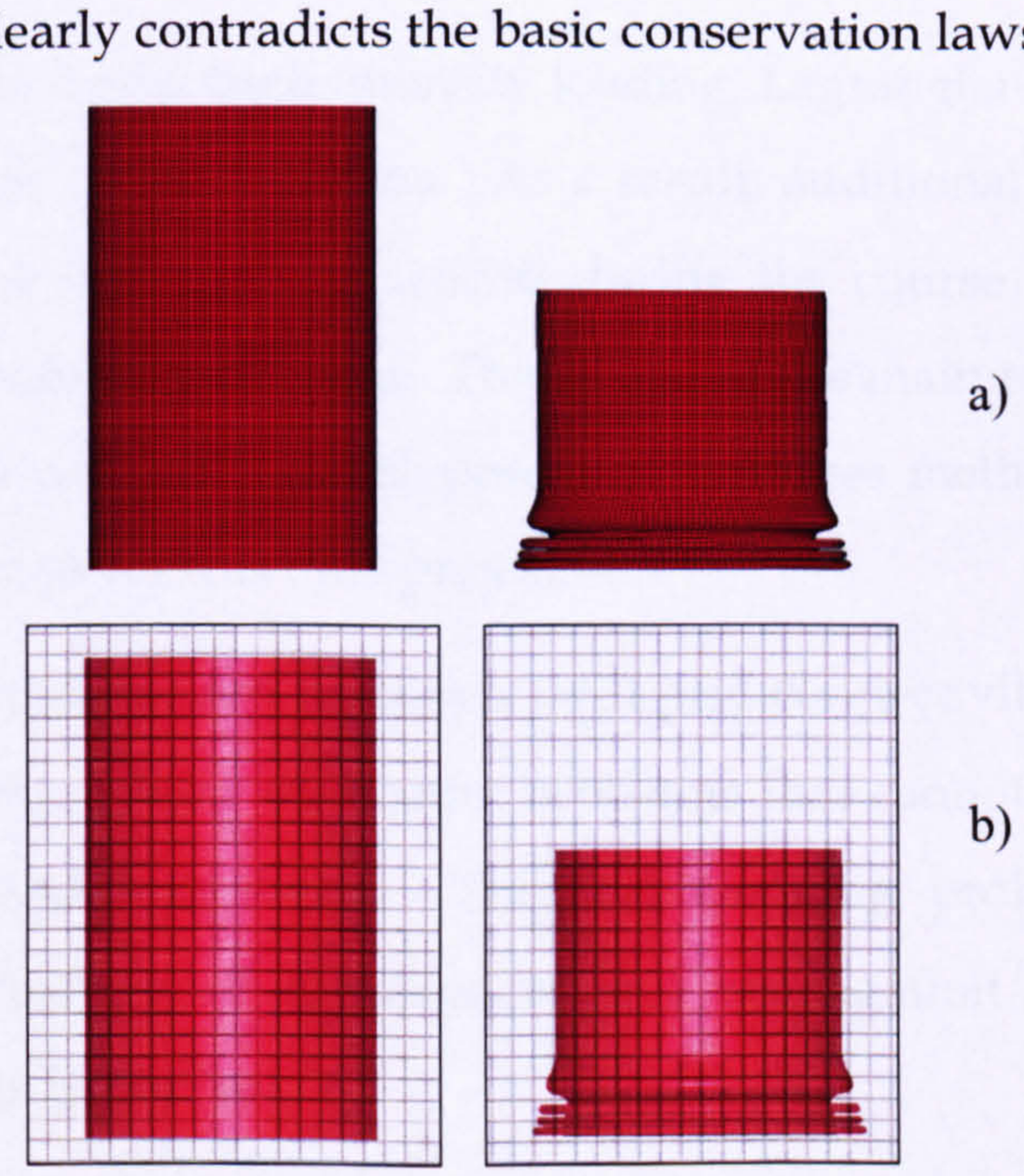

Fig. 2.1 a) represents a Lagrangian grid "etched" on the body, hence the grid deforms with the body b) represents an Eulerian grid, the deformation of the material is followed through a grid "etched" on a piece of glass.

The Lagrangian methods in which the mesh distorts with the material have the advantage of being computationally fast and give good definition of material interfaces. In addition, a good history of the events associated with each Lagrangian element can be kept. The Eulerian approximation which uses a fixed grid through which material flows, is computationally very expensive but is often better suited to modelling larger deformations such as those experienced by fluid flow. Eulerian meshes also inherently carry the problem of diffusion as the mass moves through fixed space.

Some authors describe the Lagrangian calculations as being more accurate and more efficient to run and Eulerian codes as having greater capabilities and the ability to handle large deformations well [50,61]. Later developments include the use of hybrid techniques whereby two grids are used; one Lagrangian and one Eulerian with information exchange between the two of them. These mappings add a good deal of complexity to the calculations and can also introduce inaccuracies.

As pointed out, under high intensity loading, Lagrangian mesh methods can suffer from severe mesh distortion. As a result, additional efforts such as remeshing or element deletion are needed during the course of the solution which is not computationally efficient. This is one of the main reasons research is being conducted towards the development of meshless methods and one of the fundamental reasons for this PhD project.

Meshless methods do not possess a rigid grid connectivity which makes them ideal for modelling solid mechanics problems that cannot be handled by conventional mesh-based methods. These challenging problems typically involve large deformations of the domain and propagation of cracks with arbitrary and complex paths [18].

Conversely, they are generally not as good as standard finite element methods for structural response applications [46]. Some authors suggest a meshless Lagrangian formulation linked to a standard finite element

Lagrangian formulation would be a very robust tool since it would make both severe distortion and structural response applications possible with one single Lagrangian code [1, 39, 40]. SPH is one of such meshless methods. Although the term "hydrodynamics" reflects its origin in hydrodynamic applications, material strength can also be included as has been shown by several authors [8, 50, 52, 86].

Once it has been determined that SPH is better suited than an ordinary mesh-based technique for solving a given problem, the interpolating function or kernel has to be chosen carefully. The following section will give a brief description of the main characteristics a kernel function should possess if it is to be used successfully in an SPH approximation.

2.1.2 The kernel.

One of the main issues in the SPH method is how to effectively choose or construct a proper shape function that will make use of nodes scattered in an arbitrary manner without using a predefined mesh that provides particle connectivity [54]. In an SPH approximation this function is highly relevant since it not only determines the pattern to interpolate but also defines the width of the influencing area of the particle. This so-called "smoothing function" has to satisfy certain constraints. In theory, any function that meets these constraints can be employed as an SPH smoothing kernel. Some authors have investigated a great number of kernels for accuracy and report that in practice, bell shaped (also called Gaussian) kernels perform better than any other shape functions [17].

Evidently, there exists a wide set of bell shaped functions that can be employed. The consequences of using different kernels in the SPH method are analogous to the use of different difference schemes in the finite difference method. In addition, these bell-shaped kernels could incorporate a varying smoothing length, h, which is analogous to adaptive gridding in mesh-based

codes [17, 68]. This allows a better resolution in regions within the domain where a higher level of detail in the solution is required. A varying smoothing length is also very useful when large expansions occur within the material and particles become so distant from each other that they no longer interact.

Morris [67] reports that in cases when the domain does not undergo substantial compression, a constant smoothing length is sufficient. Whereas in cases where particles become so distant that they cease to interact, or so close that a large number lie within the smoothing length, then a computational scheme incorporating a variable smoothing length should be used, such as that described by Benz [7]. Alternatively, a remeshing technique can also be used as described by Chaniotis et. al [16]. The smoothing lengths must be explicit functions of the distances between particles and the number of particles interacting with any given particle should be roughly constant. Again, referring to Morris in [67], it is mentioned that in one dimension, the number of neighbours including the particle over which the interpolating function is centred (referred to as "*I*" throughout this document) should be about 5 in one dimension, 21 in two dimensions and about 57 in three dimensions. These numbers correspond to a lattice with a smoothing length of 1.2 times the particle spacing and a kernel which extends to $2h$ such as in the case of a cubic spline.

In principle, different discretised equations can make use of different interpolating functions, although there is no evidence that any advantage is gained by that [62]. The most commonly used kernels which satisfy all conditions for an SPH interpolation are the following [7]:

1.- Gaussian Kernel. This type of kernel was originally used by Gingold and Monaghan [31]. The form of the kernel is as follows:

$$W(r,h)=\frac{1}{\pi^{3/2}h^3}e^{-q^2} \tag{2.1}$$

2.- Exponential Kernel.

$$W(r,h)=\frac{1}{8\pi h^3}e^{-q} \tag{2.2}$$

3.- Cubic Spline Kernel. This kernel has compact support which means that interaction is exactly zero for $|\vec{\mathbf{x}}-\vec{\mathbf{x}}'|\geq kh$, where k is a scaling factor:

$$W(r,h)=\frac{b}{\pi h^a}\begin{cases}1-\frac{3}{2}q^2+\frac{3}{4}q^3 & \text{if} \quad 0\leq q\leq 1\\ \frac{1}{4}(2-q)^3 & \text{if} \quad 1\leq q\leq 2\\ 0 & \text{otherwise}\end{cases} \tag{2.3}$$

in the above expression, a is the number of dimensions, b is the normalized constant with the values $\frac{2}{3},\frac{10}{7\pi},\frac{1}{\pi}$ in one, two and three dimensions respectively, $q=\frac{r}{h}$, $r=|\vec{\mathbf{x}}-\vec{\mathbf{x}}'|=|\vec{\mathbf{x}}_i-\vec{\mathbf{x}}_j|$,and the smoothing length is h. Once the smoothing length of each particle has been computed, the interaction of each particle pair must have a smoothing length associated with it. This "average" smoothing length can be obtained using one of the expressions given by Morris [67]:

$$h_{ij}=\frac{1}{2}(h_i+h_j) \tag{2.4}$$

$$h_{ij}=\min(h_i,h_j) \tag{2.5}$$

$$h_{ij}=\max(h_i,h_j) \tag{2.6}$$

$$\text{or } h_{ij}=\frac{h_i h_j}{h_i+h_j} \tag{2.7}$$

2.1.3 Kernel approximation.

In SPH, spatial derivatives are calculated by differentiation of a given interpolation function and functions are evaluated through a weighted sum. To illustrate this consider a continuum represented by a set of interacting particles. (Fig. 2.2)

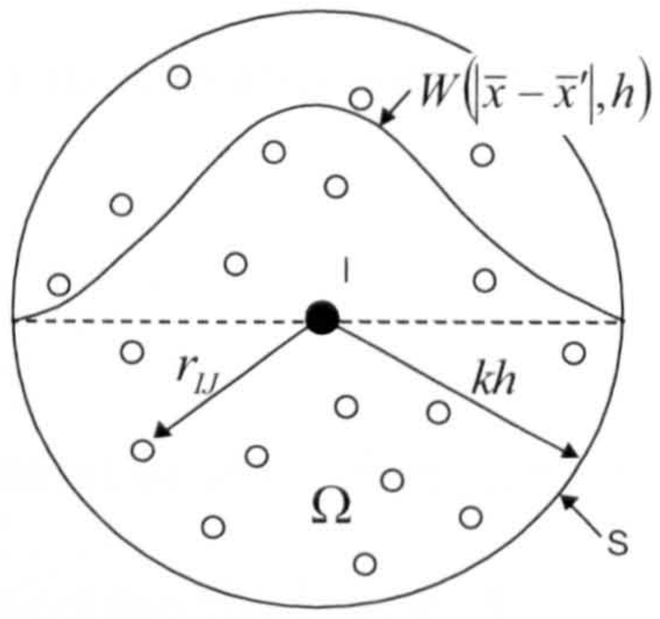

Fig.2.2 Neighbouring particles of a kernel estimate.

Each particle I interacts with all other particles J that are within a given distance (usually assumed to be $2h$) from it. The parameter h determines the spatial resolution of the calculations and it can be fixed or variable as discussed before and k is a scaling factor. One expression to calculate the value of the smoothing length is given by Gingold and Monaghan in [32] as $h_{IJ} = \frac{|\vec{\mathbf{x}}_I - \vec{\mathbf{x}}_{I\max}|}{2}$ where $\vec{\mathbf{x}}_I$ is the position vector of particle I and $\vec{\mathbf{x}}_{I\max}$ is the position vector of particle I's most distant nearest neighbour. The interaction between I and J is weighted by the smoothing function $\mathrm{W}(\vec{\mathbf{x}} - \vec{\mathbf{x}}', h)$. Using this principle, the value of a continuous function can be estimated at any particle I based on known values at surrounding particles J [37]. Likewise, a differentiable interpolant of a function can be constructed from its values at the particle by using a differentiable kernel. Derivatives of this interpolant can be obtained by ordinary differentiation which means there is no need to use finite differences or a grid.

The conventional approach used to generate SPH equations is as follows:

1st step.- Estimate the kernel approximation. For a vector function f at a point, whose position vector is $\vec{\mathbf{x}}$, in an interval Ω, the conventional kernel approximation is given by the integral interpolant :

$$\langle f(\vec{\mathbf{x}})\rangle \approx \int_{\Omega} f(\vec{\mathbf{x}}')\mathrm{W}(\vec{\mathbf{x}}-\vec{\mathbf{x}}')d\Omega \tag{2.8}$$

Where: W is the kernel function and depends upon distance $\vec{\mathbf{x}}-\vec{\mathbf{x}}'$,

$\vec{\mathbf{x}}$ is a parameter,

$\vec{\mathbf{x}}'$ is a variable,

h a width control parameter or smoothing length,

Ω is the kernel support centred at a point $\vec{\mathbf{x}}$.

A typical kernel function must satisfy the following requirements [50,53,54,80]:

$\mathrm{W}(\vec{\mathbf{x}}-\vec{\mathbf{x}}',h)=0$ when $|\vec{\mathbf{x}}-\vec{\mathbf{x}}'|\geq kh$ (i.e. the kernel should exhibit compact support).

k is a scale factor that determines the supporting area of the smoothing function $\mathrm{W}(\vec{\mathbf{x}}-\vec{\mathbf{x}}',h)\geq 0$ in the compact support area where $|\vec{\mathbf{x}}-\vec{\mathbf{x}}'|\leq kh$.

Integration of W over the entire domain is unity:

$$\int_{\Omega} f(\vec{\mathbf{x}}')\mathrm{W}(\vec{\mathbf{x}}-\vec{\mathbf{x}}')d\Omega = 1 \tag{2.9}$$

Due to the symmetrical nature of the kernel function, the following expression should hold:

$$\frac{\partial \mathrm{W}(0,h)}{\partial \vec{\mathbf{x}}'} = 0 \tag{2.10}$$

Note that the kernel has to be differentiable at least once since the kernel approximation allows spatial gradients to be determined from the values of the function and the first spatial derivative of the kernel rather than the derivatives

of the function itself. In addition, the derivative should be continuous to prevent large fluctuations in the values of the variables of particle *I*.

In the limit W equals the Dirac delta function as *h* approaches zero:

$$\lim_{h\to 0} \mathrm{W}(\vec{\mathbf{x}} - \vec{\mathbf{x}}', h) = \delta(\vec{\mathbf{x}} - \vec{\mathbf{x}}') \tag{2.11}$$

2nd step.- The second step is to convert the kernel integrals into a volume weighted sum. This is known as particle approximation. Thus

$$f_I = f(\vec{\mathbf{x}}_I) = \langle f(\vec{\mathbf{x}}_I) \rangle = \sum_{J \in S} f(\vec{\mathbf{x}}_J) \mathrm{W}(\vec{\mathbf{x}}_I - \vec{\mathbf{x}}_J, h) \frac{m_J}{\rho_J} \tag{2.12}$$

In the equation above the subscript *I* and *J* denote particle number, m_J and ρ_J the mass and the density of particle *J* respectively and *S* is the sub-domain of particle *I* .

It is important to note that although Equation (2.12) implies a summation over the entire number of particles in the domain, only a small number contribute to the summation since one of the properties of the kernel used in the approximations presented in this thesis (e.g. the cubic spline) is that it has compact support. This means that $\mathrm{W}_{IJ} = \mathrm{W}(\vec{\mathbf{x}}_I - \vec{\mathbf{x}}'_J, h)$ falls off rapidly as $|\vec{\mathbf{x}}_I - \vec{\mathbf{x}}_J| \geq h$. In order to make hydrocodes computationally more efficient, search algorithms are standard in all SPH codes which help identify the neighbours of a given particle [53,80].

In SPH, a time-dependent partial differential equation is simplified to a time dependent ordinary differential equation by:

1.- multiplying both sides of the equation with a kernel function;

2.- integrating all the products over the entire domain;

3.- linearising the integrals if needed;

4.- Integrating each term using the technique of integration by parts;

5.- dropping boundary terms (since we assume a kernel with compact support), and

6.- converting all the integrals into summation over a set of discrete particles.

The steps outlined above will be followed to derive the conservation equations in an Eulerian and a Total Lagrangian form. This will be discussed in the next chapter.

2.2 Approximation of Derivatives.

Consider the vector function $f(\vec{\mathbf{x}})$. The SPH approximation of this function can be obtained through the integral interpolant:

$$\langle f(\vec{\mathbf{x}})\rangle \approx \int_{\Omega} f(\vec{\mathbf{x}}')\mathrm{W}(\vec{\mathbf{x}}-\vec{\mathbf{x}}')d\Omega \tag{2.13}$$

If the approximation of the derivative of $f(\vec{\mathbf{x}})$ is required, then by taking the derivative of (2.13):

$$\left\langle \frac{\partial f(\vec{\mathbf{x}})}{\partial \vec{\mathbf{x}}'} \right\rangle = \int_{\Omega} \frac{\partial f(\vec{\mathbf{x}}')}{\partial \vec{\mathbf{x}}'} \mathrm{W}(\vec{\mathbf{x}}-\vec{\mathbf{x}}',h)d\Omega \tag{2.14}$$

the right hand side of (2.14) can be written as:

$$\int_{\Omega} \frac{\partial f(\vec{\mathbf{x}}')}{\partial \vec{\mathbf{x}}'} \mathrm{W}(\vec{\mathbf{x}}-\vec{\mathbf{x}}',h)d\Omega = \int_{\Omega} \frac{\partial\left(f(\vec{\mathbf{x}}')\mathrm{W}(\vec{\mathbf{x}}-\vec{\mathbf{x}}',h)\right)}{\partial \vec{\mathbf{x}}'} d\Omega - \int_{\Omega} f(\vec{\mathbf{x}}') \frac{\partial \mathrm{W}(\vec{\mathbf{x}}-\vec{\mathbf{x}}',h)}{\partial \vec{\mathbf{x}}'} d\Omega \tag{2.15}$$

Through the use of the Green-Gauss theorem [19], the first integral on the right hand side (RHS) can be written as follows:

$$\int_{\Omega} \frac{\partial\left(f(\vec{\mathbf{x}}')\mathrm{W}(\vec{\mathbf{x}}-\vec{\mathbf{x}}',h)\right)}{\partial \vec{\mathbf{x}}'} d\Omega = -\int_{\Sigma} \left(f(\vec{\mathbf{x}}')\mathrm{W}(\vec{\mathbf{x}}-\vec{\mathbf{x}}',h)\right).\vec{\mathbf{n}}d\Sigma \tag{2.16}$$

The assumption made at this point is that the solution space Ω extends far enough so that at its boundaries Σ, the kernel $\mathrm{W}(\vec{\mathbf{x}}-\vec{\mathbf{x}}',h)$ vanishes. This

assumption sets the value of the surface integral to zero, thus (2.3) can be rewritten as:

$$\int_{\Omega} \frac{\partial f(\vec{\mathbf{x}}')}{\partial \vec{\mathbf{x}}'} \mathrm{W}(\vec{\mathbf{x}} - \vec{\mathbf{x}}', h) d\Omega = -\int_{\Omega} f(\vec{\mathbf{x}}') \frac{\partial \mathrm{W}(\vec{\mathbf{x}} - \vec{\mathbf{x}}', h)}{\partial \vec{\mathbf{x}}'} d\Omega \qquad (2.17)$$

For a numerical approximation, the domain Ω needs to be discretised in a set of interpolation points and the integral on the RHS of (2.17) needs to be expressed in terms of a weighted sum as follows:

$$-\int_{\Omega} f(\vec{\mathbf{x}}') \frac{\partial \mathrm{W}(\vec{\mathbf{x}} - \vec{\mathbf{x}}', h)}{\partial \vec{\mathbf{x}}'} d\Omega \approx -\sum_{J \in S} \frac{m_J}{\rho_J} f(\vec{\mathbf{x}}_J) \frac{\partial \mathrm{W}(\vec{\mathbf{x}}_I - \vec{\mathbf{x}}_J, h)}{\partial \vec{\mathbf{x}}_J} \qquad (2.18)$$

hence the approximation of the derivative $f(\vec{\mathbf{x}})$ at a point I with position vector $\vec{\mathbf{x}}_I$ is given by:

$$\left\langle \frac{\partial f(\vec{\mathbf{x}}_I)}{\partial \vec{\mathbf{x}}_J} \right\rangle = -\sum_{J \in S} \frac{m_J}{\rho_J} f(\vec{\mathbf{x}}_J) \frac{\partial \mathrm{W}(\vec{\mathbf{x}}_I - \vec{\mathbf{x}}_J, h)}{\partial \vec{\mathbf{x}}_J} \qquad (2.19)$$

Due to the symmetric nature of the smoothing functions the previous expression can be written as follows:

$$\left\langle \frac{\partial f(\vec{\mathbf{x}}_I)}{\partial \vec{\mathbf{x}}_I} \right\rangle = \sum_{J \in S} \frac{m_J}{\rho_J} f(\vec{\mathbf{x}}_J) \frac{\partial \mathrm{W}(\vec{\mathbf{x}}_I - \vec{\mathbf{x}}_J, h)}{\partial \vec{\mathbf{x}}_I} \qquad (2.20)$$

It will be shown later that this crude approximation is not even zero order consistent, that is the derivative of a constant field could not be reproduced accurately through (2.20).

The SPH approximation of derivatives can also include density as follows:

$$\frac{\nabla A}{\rho} = \nabla\left(\frac{A}{\rho}\right) + \frac{A}{\rho^2} \nabla \rho \qquad (2.21)$$

where A is any physical field. If this expression is used, the evaluation of the SPH approximation is carried out as follows:

Multiplying (2.21) by the smoothing function and then integrating over the entire domain yields :

$$\int_{\Omega}\frac{1}{\rho}\frac{\partial A}{\partial \vec{\mathbf{x}}'}\mathrm{W}(\vec{\mathbf{x}}-\vec{\mathbf{x}}',h)d\Omega=\int_{\Omega}\frac{\partial}{\partial \vec{\mathbf{x}}'}\left(\frac{A}{\rho}\right)\mathrm{W}(\vec{\mathbf{x}}-\vec{\mathbf{x}}',h)d\Omega+\int_{\Omega}\left(\frac{A}{\rho^2}\right)\frac{\partial \rho}{\partial \vec{\mathbf{x}}'}\mathrm{W}(\vec{\mathbf{x}}-\vec{\mathbf{x}}',h)d\Omega \tag{2.22}$$

Linearisation of the second integral on the RHS of (2.22) yields:

$$\int_{\Omega}\frac{A}{\rho^2}\frac{\partial \rho}{\partial \vec{\mathbf{x}}'}\mathrm{W}(\vec{\mathbf{x}}-\vec{\mathbf{x}}',h)d\Omega=\frac{A(\vec{\mathbf{x}})}{\rho^2(\vec{\mathbf{x}})}\int_{\Omega}\frac{\partial \rho}{\partial \vec{\mathbf{x}}'}\mathrm{W}(\vec{\mathbf{x}}-\vec{\mathbf{x}}',h)d\Omega \tag{2.23}$$

which can also be written as:

$$\int_{\Omega}\frac{A}{\rho^2}\frac{\partial \rho}{\partial \vec{\mathbf{x}}'}\mathrm{W}(\vec{\mathbf{x}}-\vec{\mathbf{x}}',h)d\Omega=\frac{A(\vec{\mathbf{x}})}{\rho^2(\vec{\mathbf{x}})}\left[\int_{\Omega}\frac{\partial}{\partial \vec{\mathbf{x}}'}\left(\mathrm{W}(\vec{\mathbf{x}}-\vec{\mathbf{x}}',h)\rho\right)d\Omega-\int_{\Omega}\rho\frac{\partial \mathrm{W}(\vec{\mathbf{x}}-\vec{\mathbf{x}}',h)}{\partial \vec{\mathbf{x}}'}d\Omega\right] \tag{2.24}$$

and through the use of the Green-Gauss theorem [19] and by dropping boundary terms:

$$\int_{\Omega}\frac{A}{\rho^2}\frac{\partial \rho}{\partial \vec{\mathbf{x}}'}\mathrm{W}(\vec{\mathbf{x}}-\vec{\mathbf{x}}',h)d\Omega=-\frac{A(\vec{\mathbf{x}})}{\rho^2(\vec{\mathbf{x}})}\int_{\Omega}\rho\frac{\partial \mathrm{W}(\vec{\mathbf{x}}-\vec{\mathbf{x}}',h)}{\partial \vec{\mathbf{x}}'}d\Omega \tag{2.25}$$

the first integral on the RHS of (2.22) yields:

$$\int_{\Omega}\frac{\partial}{\partial \vec{\mathbf{x}}'}\left(\frac{A}{\rho}\right)\mathrm{W}(\vec{\mathbf{x}}-\vec{\mathbf{x}}',h)d\Omega=\int_{\Omega}\frac{\partial}{\partial \vec{\mathbf{x}}'}\left(\frac{A}{\rho}\mathrm{W}(\vec{\mathbf{x}}-\vec{\mathbf{x}}',h)\right)d\Omega-\int_{\Omega}\frac{\partial \mathrm{W}(\vec{\mathbf{x}}-\vec{\mathbf{x}}',h)}{\partial \vec{\mathbf{x}}'}\frac{A}{\rho}d\Omega=$$

$$=-\int_{\Omega}\frac{A}{\rho}\frac{\partial \mathrm{W}(\vec{\mathbf{x}}-\vec{\mathbf{x}}',h)}{\partial \vec{\mathbf{x}}'}d\Omega \tag{2.26}$$

Converting the integrals into a summation of N particles over the domain yields:

$$-\int_{\Omega}\frac{A}{\rho}\frac{\partial \mathrm{W}(\vec{\mathbf{x}}-\vec{\mathbf{x}}',h)}{\partial x'^{\beta}}d\Omega=-\sum_{J\in S}\frac{A}{\rho_J^2}m_J\nabla_{\vec{\mathbf{x}}_J}\mathrm{W}(\vec{\mathbf{x}}-\vec{\mathbf{x}}',h) \tag{2.27}$$

and:

$$-\frac{A}{\rho^2}\int_{\Omega}\rho\frac{\partial \mathrm{W}(\vec{\mathbf{x}}-\vec{\mathbf{x}}',h)}{\partial \vec{\mathbf{x}}'}d\Omega=-\frac{A_I}{\rho_I^2}\sum_j m_J\mathrm{W}(\vec{\mathbf{x}}-\vec{\mathbf{x}}',h) \tag{2.28}$$

hence:

$$\left\langle \frac{1}{\rho}\frac{\partial A(\vec{\mathbf{x}}_I)}{\partial \vec{\mathbf{x}}_J} \right\rangle = -\sum_{J\in S} m_J \left(\frac{A_I}{\rho_I^2} + \frac{A_J}{\rho_J^2} \right) \nabla_{\vec{\mathbf{x}}_J} \mathrm{W}(\vec{\mathbf{x}} - \vec{\mathbf{x}}', h) \tag{2.29}$$

which can also be written as:

$$\left\langle \frac{1}{\rho}\frac{\partial A(\vec{\mathbf{x}}_I)}{\partial \vec{\mathbf{x}}_I} \right\rangle = \sum_{J\in S} m_J \left(\frac{A_I}{\rho_I^2} + \frac{A_J}{\rho_J^2} \right) \nabla_{\vec{\mathbf{x}}_I} \mathrm{W}(\vec{\mathbf{x}} - \vec{\mathbf{x}}', h) \tag{2.30}$$

since $-\nabla_{\vec{\mathbf{x}}_J} = \nabla_{\vec{\mathbf{x}}_I}$.

2.3 Summary of the SPH Derivative Approximation Formulae

In this section, a comprehensive summary of approximation of . derivatives in SPH is provided.

1.- For a scalar function such as a temperature field, the approximation is carried out as follows:

$$\left\langle \nabla_{\vec{\mathbf{x}}_I} T(\vec{\mathbf{x}}_I) \right\rangle = -\sum_{J\in S} \frac{m_J}{\rho_J} T_J \nabla_{\vec{\mathbf{x}}_J} \mathrm{W}(\vec{\mathbf{x}}_I - \vec{\mathbf{x}}_J, h) = \sum_{J\in S} \frac{m_J}{\rho_J} T_J \nabla_{\vec{\mathbf{x}}_I} \mathrm{W}(\vec{\mathbf{x}}_I - \vec{\mathbf{x}}_J, h) \tag{2.31}$$

$$\text{since } -\nabla_{\vec{\mathbf{x}}_J} = \nabla_{\vec{\mathbf{x}}_I} \tag{2.32}$$

or in index notation:

$$\left\langle \frac{\partial T(\vec{\mathbf{x}}_I)}{\partial x_{I,\alpha}} \right\rangle = \sum_{J\in s} \frac{m_J}{\rho_J} T_J \frac{\partial \mathrm{W}(\vec{\mathbf{x}}_I - \vec{\mathbf{x}}_J, h)}{\partial x_{I,\alpha}} \tag{2.33}$$

2.- For a vector field such as a velocity field $\vec{\mathbf{v}}$, the SPH divergence approximation is computed as follows:

$$\left\langle \nabla_{\vec{\mathbf{x}}_I} \vec{\mathbf{v}}(\vec{\mathbf{x}}_I) \right\rangle = \sum_{J\in S} \frac{m_J}{\rho_J} \vec{\mathbf{v}}_J \cdot \nabla_{\vec{\mathbf{x}}_I} \mathrm{W}(\vec{\mathbf{x}}_I - \vec{\mathbf{x}}_J, h) \tag{2.34}$$

or in index notation:

$$\left\langle \frac{\partial v^\alpha(x_I)}{\partial x_{I,\alpha}} \right\rangle = \sum_{J\in s} \frac{m_J}{\rho_J} v_J^\alpha \frac{\partial \mathrm{W}(\vec{\mathbf{x}}_I - \vec{\mathbf{x}}_J, h)}{\partial x_{I,\alpha}} \tag{2.35}$$

3.- The tensor product of a gradient operator and a vector field is approximated as follows:

$$\left\langle \nabla_{\vec{\mathbf{x}}} \otimes \vec{\mathbf{v}} \right\rangle = \sum_{J \in S} \frac{m_J}{\rho_J} \vec{\mathbf{v}}_J \otimes \frac{\partial \mathrm{W}\left(\vec{\mathbf{x}}_I - \vec{\mathbf{x}}_J, h\right)}{\partial \vec{\mathbf{x}}_I} \tag{2.36}$$

or in index notation:

$$\left\langle \frac{\partial v^{\alpha}(x_I)}{\partial x_{I,\beta}} \right\rangle = \sum_{J \in S} \frac{m_J}{\rho_J} v_J^{\alpha} \frac{\partial \mathrm{W}\left(\vec{\mathbf{x}}_I - \vec{\mathbf{x}}_J, h\right)}{\partial x_{I,\beta}} \tag{2.37}$$

4.- The dot product of a gradient operator and a second order tensor such as the stress tensor $\bar{\bar{\mathbf{P}}}$ is :

$$\left\langle \nabla_{\vec{\mathbf{x}}_I} \cdot \bar{\bar{\mathbf{P}}}(\vec{\mathbf{x}}_I) \right\rangle = \sum_{J \in S} \frac{m_J}{\rho_J} \bar{\bar{\mathbf{P}}}_J \cdot \nabla_{\vec{\mathbf{x}}_I} \mathrm{W}\left(\vec{\mathbf{x}}_I - \vec{\mathbf{x}}_J, h\right) \tag{2.38}$$

or in index notation:

$$\left\langle f^{\alpha}(\vec{\mathbf{x}}_I) \right\rangle = \left\langle \frac{\partial P^{\alpha\beta}(\vec{\mathbf{x}}_I)}{\partial x_{I,\beta}} \right\rangle = \sum_{J \in S} \frac{m_J}{\rho_J} P_J^{\alpha\beta} \frac{\partial \mathrm{W}\left(\vec{\mathbf{x}}_I - \vec{\mathbf{x}}_J, h\right)}{\partial x_{I,\beta}} \tag{2.39}$$

Although the expressions above are acceptable approximations in an SPH context, a common deficiency shared by all of them is that they are not symmetric with respect to indices *I* and *J*.

In order to ensure Galilean invariance and in order to meet Newton's third law locally, the introduction of symmetry terms is required since symmetric equations tend to produce more accurate approximations. The Galilean invariance principle states that the form of the equations of motion of an isolated system should be invariant when a change of observer, consisting of a translation with a constant velocity is applied.

Symmetry terms can be obtained if the gradients of, say, a scalar field T are computed in the following way:

$$\nabla T = \frac{\left[(\nabla \rho T) - T \nabla \rho\right]}{\rho} \tag{2.40}$$

Using the expression above, equations (2.41) ,(2.42) and (2.43) can be derived:

1.- Approximation for a scalar:

$$\rho(\vec{\mathbf{x}}_I)\left\langle \nabla_{\vec{\mathbf{x}}_I} T(\vec{\mathbf{x}}_I)\right\rangle = \sum_{J\in S} m_J (T_J - T_I)\nabla_{\vec{\mathbf{x}}_I} \mathrm{W}(\vec{\mathbf{x}}_I - \vec{\mathbf{x}}_J, h) \tag{2.41}$$

where $\sum_{J\in s} m_J T_J \nabla_{\mathbf{x}_I} \mathrm{W}(\vec{\mathbf{x}}_I - \vec{\mathbf{x}}_J, h)$ is a rough approximation of $\nabla(\rho T)$ and $T_I \sum_{J\in s} m_J \nabla_{\mathbf{x}_I} \mathrm{W}(\vec{\mathbf{x}}_I - \vec{\mathbf{x}}_J, h)$ is the approximation for $T\nabla\rho$.

2.- Approximation of divergence of a vector field $\vec{\mathbf{v}}$:

$$\rho(\vec{\mathbf{x}}_I)\left\langle \nabla_{\vec{\mathbf{x}}_I} \vec{\mathbf{v}}(\vec{\mathbf{x}}_I)\right\rangle = \sum_{J\in S} m_J (\vec{\mathbf{v}}_J - \vec{\mathbf{v}}_I)\cdot \nabla_{\vec{\mathbf{x}}_I} \mathrm{W}(\vec{\mathbf{x}}_I - \vec{\mathbf{x}}_J, h) \tag{2.42}$$

The approximation for a tensor product follows exactly the same rule:

$$\rho(\vec{\mathbf{x}}_I)\left\langle \nabla_{\vec{\mathbf{x}}_I} \otimes \vec{\mathbf{v}}(\vec{\mathbf{x}}_I)\right\rangle = \sum_{J\in S} m_J (\vec{\mathbf{v}}_J - \vec{\mathbf{v}}_I)\otimes \nabla_{\vec{\mathbf{x}}_I} \mathrm{W}(\vec{\mathbf{x}}_I - \vec{\mathbf{x}}_J, h) \tag{2.43}$$

Another acceptable approximation in SPH makes use of (2.30)

An SPH approximation for a second order tensor such as the stress tensor $\bar{\bar{\mathbf{P}}}$ would be:

$$\left\langle \frac{\nabla\bar{\bar{\mathbf{P}}}(\vec{\mathbf{x}}_I)}{\rho(\vec{\mathbf{x}}_I)}\right\rangle = \sum_{J\in S}\left(\frac{\bar{\bar{\mathbf{P}}}_J}{\rho_J^2} + \frac{\bar{\bar{\mathbf{P}}}_I}{\rho_I^2}\right) m_J \cdot \nabla_{\vec{\mathbf{x}}_I} \mathrm{W}(\vec{\mathbf{x}}_I - \vec{\mathbf{x}}'_J, h) \tag{2.44}$$

Where the expression $\sum_{J\in s} \frac{\bar{\bar{\mathbf{P}}}_J}{\rho_J^2} m_J \cdot \nabla_{\vec{\mathbf{x}}_I} \mathrm{W}(\vec{\mathbf{x}}_I - \vec{\mathbf{x}}_J, h)$ is taken as the approximation of $\nabla\left(\frac{A}{\rho}\right)$.

In all the expressions above, repeated indices indicate summation over that index as per Einstein's dummy index notation.

2.4 Derivation of the Conservation Laws Particle Equations Using Standard SPH Approach.

The equations solved by the Cranfield MCM code are the conservation laws derived in an Eulerian framework. When these equations are discretised through the SPH method, certain conditions during the simulation might lead to the tensile instability problem [13, 26, 73] which results from a combination of an Eulerian kernel with an Eulerian description of motion. It will be shown in Chapter 3 that when the conservation laws are expressed in a Total Lagrangian framework, a stability analysis reveals that the resulting particle equations do not contain the terms that lead to tensile instability.

In an Eulerian referential, the conservation laws take the following form [19]:

a) Conservation of mass:

$$\frac{D\rho}{Dt} = -\rho \nabla . \vec{\mathbf{v}} \tag{2.45}$$

b) Conservation of momentum:

$$\rho \frac{D\vec{\mathbf{v}}}{Dt} = -\nabla \bar{\bar{\boldsymbol{\sigma}}} \tag{2.46}$$

c) Conservation of Energy:

$$\frac{De}{Dt} = -\frac{\bar{\bar{\boldsymbol{\sigma}}}}{\rho} : \nabla \otimes \vec{\mathbf{v}} \tag{2.47}$$

The dependent variables are density ρ and specific internal energy e, the velocity $\vec{\mathbf{v}}$ and the stress tensor component $\bar{\bar{\boldsymbol{\sigma}}}$ which is the Cauchy stress tensor. The independent variables are the spatial coordinates $\vec{\mathbf{x}}$ and time t.

Whereas in field based approximations (such as the element-free Galerkin method) the discrete equations are obtained from a weak form, in a fully collocational SPH scheme the particle equations are obtained from the strong form of the equations by collocation, i.e. the governing equations are

enforced at each particle. The next section makes use of the SPH formulae supplied in Section 2.2 and the strong form of the conservation equations (i.e. (2.45),(2.46) and (2.47)).

2.4.1 Conservation of mass in an SPH framework

To approximate the value of density in SPH, it is acceptable, albeit not always advisable, to sum over the particles according to:

$$\rho(\vec{\mathbf{x}}_I) = \sum_{J \in S} m_J \mathrm{W}(\vec{\mathbf{x}}_I - \vec{\mathbf{x}}_J, h) \tag{2.48}$$

This expression, however, yields incorrect results at the free boundaries, resulting in particles with underestimated density (refer to Chapter 3 in this thesis). For example, it is reported that for fluids such as water, the density falls to zero at the surface. The equation of state will in turn introduce incorrect pressures and degrade the calculation. To overcome this, approximating the rate of change of density rather than the value of the density at a point is preferred. In this case, all particles are assigned the same initial density which only changes when particles are in relative motion.

Let us work with the form of the conservation of mass equation supplied in the previous section which makes use of the value of the change in density:

$$\int_{\Omega} \frac{D\rho}{Dt} \mathrm{W}(\vec{\mathbf{x}} - \vec{\mathbf{x}}', h) d\Omega = -\int_{\Omega} \rho \frac{\partial \vec{\mathbf{v}}}{\partial \vec{\mathbf{x}}'} \mathrm{W}(\vec{\mathbf{x}} - \vec{\mathbf{x}}', h) d\Omega \tag{2.49}$$

Making use of the expression for approximation of divergence of a vector field $\vec{\mathbf{v}}$:

$$\left\langle \nabla_{\vec{\mathbf{x}}_I} \vec{\mathbf{v}}(\vec{\mathbf{x}}_I) \right\rangle = \sum_{J \in S} \frac{m_J}{\rho_J} \vec{\mathbf{v}}_J \cdot \nabla_{\vec{\mathbf{x}}_I} \mathrm{W}(\vec{\mathbf{x}}_I - \vec{\mathbf{x}}_J, h) \tag{2.50}$$

the conservation of mass equation can be written as follows:

$$\left\langle \frac{D\rho(\vec{\mathbf{x}}_I)}{Dt} \right\rangle = \rho_I \sum_{J \in S} \frac{m_J}{\rho_J} (\vec{\mathbf{v}}_I - \vec{\mathbf{v}}_J) \cdot \nabla_{\vec{\mathbf{x}}_I} \mathrm{W}(\vec{\mathbf{x}}_I - \vec{\mathbf{x}}_J, h) \tag{2.51}$$

or in index notation as:

$$\left\langle \frac{D\rho_I}{Dt} \right\rangle = \rho_I \sum_{J \in S} \frac{m_J}{\rho_J} \left(v_I^\beta - v_J^\beta \right) \frac{\partial \mathrm{W}\left(\vec{\mathbf{x}}_I - \vec{\mathbf{x}}_J, h \right)}{\partial x_I^\beta} \tag{2.52}$$

2.4.2 Conservation of momentum.

The conservation of momentum equation can be expressed as a kernel estimate in the following way:

$$\int_\Omega \mathrm{W}\left(\vec{\mathbf{x}} - \vec{\mathbf{x}}', h \right) \frac{D\vec{\mathbf{v}}}{Dt} d\Omega = -\int_\Omega \frac{1}{\rho} \frac{\partial \bar{\bar{\boldsymbol{\sigma}}}}{\partial \vec{\mathbf{x}}'} \mathrm{W}\left(\vec{\mathbf{x}} - \vec{\mathbf{x}}', h \right) d\Omega \tag{2.53}$$

using (2.44) , the following expression can be obtained:

$$\left\langle \frac{D\vec{\mathbf{v}}\left(\vec{\mathbf{x}}_I \right)}{Dt} \right\rangle = -\sum_{J \in S} m_J \left(\frac{\bar{\bar{\boldsymbol{\sigma}}}_I}{\rho_I^2} + \frac{\bar{\bar{\boldsymbol{\sigma}}}_J}{\rho_J^2} \right) \nabla_{\vec{\mathbf{x}}_I} \mathrm{W}\left(\vec{\mathbf{x}}_I - \vec{\mathbf{x}}_J, h \right) \tag{2.54}$$

or in index notation:

$$\left\langle \frac{Dv_I{}^\alpha}{Dt} \right\rangle = -\sum_{J \in S} m_J \left(\frac{\sigma_I^{\alpha\beta}}{\rho_I^2} + \frac{\sigma_J^{\alpha\beta}}{\rho_J^2} \right) \frac{\partial \mathrm{W}\left(\vec{\mathbf{x}}_I - \vec{\mathbf{x}}_J, h \right)}{\partial x_I^\beta} \tag{2.55}$$

2.4.3 Conservation of energy.

In order to carry out the SPH approximation, the energy equation is re-written as:

$$\frac{De}{Dt} = -\frac{\bar{\bar{\boldsymbol{\sigma}}}}{\rho^2} : \rho \nabla \otimes \vec{\mathbf{v}} \tag{2.56}$$

The conservation of energy equation can be expressed in terms of a kernel estimate as follows:

$$\int_\Omega \frac{De}{Dt} \mathrm{W}\left(\vec{\mathbf{x}} - \vec{\mathbf{x}}', h \right) d\Omega = -\int_\Omega \frac{\bar{\bar{\boldsymbol{\sigma}}}}{\rho^2} : \rho \nabla \otimes \vec{\mathbf{v}} \mathrm{W}\left(\vec{\mathbf{x}} - \vec{\mathbf{x}}', h \right) d\Omega \tag{2.57}$$

The integral on the RHS of (2.57) can be approximated as:

$$-\int_\Omega \frac{\bar{\bar{\boldsymbol{\sigma}}}}{\rho^2} : \rho \nabla \otimes \vec{\mathbf{v}} \mathrm{W}\left(\vec{\mathbf{x}} - \vec{\mathbf{x}}', h \right) d\Omega = -\frac{\bar{\bar{\boldsymbol{\sigma}}}\left(\vec{\mathbf{x}} \right)}{\rho^2\left(\vec{\mathbf{x}} \right)} : \int_\Omega \rho \nabla \otimes \vec{\mathbf{v}} \mathrm{W}\left(\vec{\mathbf{x}} - \vec{\mathbf{x}}', h \right) d\Omega \tag{2.58}$$

using the approximation $\rho(\vec{\mathbf{x}}_I)\left\langle \nabla_{\vec{\mathbf{x}}_I} \otimes \vec{\mathbf{v}}(\vec{\mathbf{x}}_I) \right\rangle = \sum_{J \in S} m_J (\vec{\mathbf{v}}_J - \vec{\mathbf{v}}_I) \otimes \nabla_{\vec{\mathbf{x}}_I} \mathrm{W}(\vec{\mathbf{x}}_I - \vec{\mathbf{x}}_J, h)$ for the term inside the integral we obtain:

$$\left\langle \frac{De(\vec{\mathbf{x}}_I)}{Dt} \right\rangle = \frac{\bar{\bar{\sigma}}_I}{\rho^2{}_I} : \sum_{J \in S} m_J (\vec{\mathbf{v}}_I - \vec{\mathbf{v}}_J) \otimes \nabla_{\vec{\mathbf{x}}_I} \mathrm{W}(\vec{\mathbf{x}}_I - \vec{\mathbf{x}}_J, h) \tag{2.59}$$

or in index notation:

$$\left\langle \frac{De_I}{Dt} \right\rangle = \frac{\sigma^{\alpha\beta}{}_I}{\rho^2{}_I} \sum_{J \in S} m_J \left(v_I^\alpha - v_J^\alpha \right) \frac{\partial \mathrm{W}(\vec{\mathbf{x}}_I - \vec{\mathbf{x}}_J, h)}{\partial x_I^\beta} \tag{2.60}$$

2.4.4 Rate of deformation tensor in SPH.

An important kinematic measure in the Eulerian formalism is the rate of deformation, hence the SPH equation of the rate of deformation tensor is also here.

The rate of deformation tensor has the following form:

$$\bar{\bar{\mathbf{D}}} = \frac{1}{2}(\nabla \otimes \vec{\mathbf{v}} + \vec{\mathbf{v}} \otimes \nabla) \tag{2.61}$$

The approximation of $\nabla \otimes \vec{\mathbf{v}}$ is readily obtained using (2.36):

$$D_I^{\alpha\beta} = \frac{1}{2} \sum_{J \in S} \frac{m_J}{\rho_J} \left[\left(v_J^\alpha - v_I^\alpha \right) \frac{\partial \mathrm{W}(\vec{\mathbf{x}}_I - \vec{\mathbf{x}}_J, h)}{\partial x_I{}^\beta} + \left(v_J^\beta - v_I^\beta \right) \frac{\partial \mathrm{W}(\vec{\mathbf{x}}_I - \vec{\mathbf{x}}_J, h)}{\partial x_I{}^\alpha} \right] \tag{2.62}$$

The stress tensor can be defined in terms of an isotropic part which is the pressure P and a traceless symmetric deviatoric stress S. The expression for the complete stress tensor is as follows:

$$\sigma^{\alpha\beta} = P\delta^{\alpha\beta} + S^{\alpha\beta} \tag{2.63}$$

The pressure is normally computed using an equation of state having functional form $P = P(\rho, E)$ such as the Mie-Gruneisen equation for solids or the gamma law for gases (the expressions can be found in [50]).

For the deviatoric (or anisotropic) part of the stress tensor the following equation can be written:

$$\dot{S}^{\alpha\beta} = \mu D^{p,\alpha\beta} = \mu\left(D^{\alpha\beta} - \frac{1}{3}\delta^{\alpha\beta} D^{P,\kappa\kappa} \right) \tag{2.64}$$

where μ is the shear modulus $D^{p,\alpha\beta}$ is the traceless rate of strain and $D^{\alpha\beta}$ is the total strain rate tensor. This expression isn't material frame independent which means that the material response will depend, in an unphysical way, on rotation, translation and on the observer describing those two motions. As an example take a bar which is pre-stressed at its initial configuration. If that bar undergoes rigid body motion, the state of stress within the bar is frozen in time, i.e. an observer riding with the bar will see no changes in the state of stresses within the bar. However, when viewed from a space fixed coordinate system (as is the case in the Eulerian approach), the components of the Cauchy stress will change during the rigid body motion (take rotation as an example). Therefore, although the state of stress within the material is frozen in time, the derivative of the stress is non-zero. To account for this apparent inconsistency, frame independent or objective stress rates have been formulated and they are widely in use. The most commonly adopted is the Jaumann rate [1, 15, 50]. By making use of the definition of Jaumann rate we can write the following expression for the stress rate:

$$\overset{\nabla}{S}^{\alpha\beta} = 2\mu\left(D^{\alpha\beta} - \frac{1}{3}\delta^{\alpha\beta} D^{\gamma\gamma} \right) + S^{\alpha\gamma} R^{\beta\gamma} + S^{\gamma\beta} R^{\alpha\gamma} \tag{2.65}$$

where **R** is the antisymmetric part of the velocity gradient tensor and is known as rotation rate or spin tensor and is defined by:

$$R^{\alpha\beta} = \frac{1}{2}\left(\frac{\partial v^{\alpha}}{\partial x^{\beta}} - \frac{\partial v^{\beta}}{\partial x^{\alpha}} \right) \tag{2.66}$$

The approximation to the spin tensor is identical to the SPH approximation for the strain rate tensor which has been obtained before with the plus sign replaced by a minus sign as follows:

$$R_I^{\alpha\beta} = \frac{1}{2}\sum_{J\in S}\frac{m_J}{\rho_J}\left[\left(v_J^\alpha - v_I^\alpha\right)\frac{\partial \mathrm{W}\left(\vec{\mathbf{x}}_I - \vec{\mathbf{x}}_J, h\right)}{\partial x_I{}^\beta} - \left(v_J^\beta - v_I^\alpha\right)\frac{\partial \mathrm{W}\left(\vec{\mathbf{x}}_I - \vec{\mathbf{x}}_J, h\right)}{\partial x_I{}^\alpha}\right] \quad (2.67)$$

All the SPH expressions above can be rewritten in terms of the derivatives of the smoothing function $\mathrm{W}\left(\vec{\mathbf{x}} - \vec{\mathbf{x}}', h\right)$ with respect to the $\vec{\mathbf{x}}_J$ coordinates bearing in mind that $-\nabla_{\vec{\mathbf{x}}_J} = \nabla_{\vec{\mathbf{x}}_I}$. The derivative of the smoothing function is obtained through the chain rule as follows:

$$\frac{\partial \mathrm{W}\left(\vec{\mathbf{x}} - \vec{\mathbf{x}}', h\right)}{\partial x_I^\alpha} = \frac{x_I^\alpha - x_J^\alpha{}'}{r}\frac{\partial \mathrm{W}}{\partial r} = -\frac{\partial \mathrm{W}\left(\vec{\mathbf{x}} - \vec{\mathbf{x}}', h\right)}{\partial x_J^\alpha} \quad (2.68)$$

where $r = \left|\vec{\mathbf{x}} - \vec{\mathbf{x}}'\right|$

2.5 SPH Approximation Error.

In SPH there are two types of errors, namely truncation errors and smoothing errors. Some researchers have also identified an error due to the particle disorder within the SPH domain which is directly linked to the truncation error [49]. In this section the analysis will be restricted to a 1-D case as in this case an expression for error estimation is much simpler to develop and it aids in understanding the potential source of error when using SPH. Initially, the smoothing error is dealt with and subsequently a similar development is shown for the estimation of truncation errors.

The general idea for calculating the smoothing error is to find an expression that yields the difference between the evaluation of a function, or the derivative of a function at a given point in space, versus the value of the smoothed function at the same point. In other words, the main idea is to find

$$\varepsilon_s = f(x) - < f(x) > \quad (2.69)$$

The approximation of a function f is given by (2.13):

Equation (2.13) can be expanded as a Taylor series as follows:

$$\int_{\Omega} f(x')\mathrm{W}(x-x',h)dx' = f(x)\Big|_{x'=x}\int_{\Omega}\mathrm{W}(x-x',h)dx' +$$

$$+\frac{\partial f(x')}{\partial x'}\Big|_{x'=x}\int_{\Omega}(x-x')\mathrm{W}(x-x',h)dx' + \frac{\partial^2 f(x')}{\partial x'^2}\Big|_{x'=x}\int_{\Omega}\frac{(x-x')^2}{2}\mathrm{W}(x-x',h)dx' + \ldots \qquad (2.70)$$

In order to approximate the derivative of the function f rather than the function f itself, the following Taylor series expansion is performed (note at this stage the derivatives of the function have not yet been replaced by the derivative of the smoothing function on the right hand side of Eq (2.70)):

$$-\int_{\Omega} f(x')\frac{\partial \mathrm{W}(x-x',h)}{\partial x'}dx' = \frac{\partial f(x')}{\partial x'}\Big|_{x'=x}\int_{\Omega}\mathrm{W}(x-x',h)dx' + \frac{\partial^2 f(x')}{\partial x'^2}\Big|_{x'=x}\int_{\Omega}(x-x')\mathrm{W}(x-x',h)dx' +$$

$$+\frac{\partial^3 f(x')}{\partial x'^3}\Big|_{x'=x}\int_{\Omega}\frac{(x-x')^2}{2}\mathrm{W}(x-x',h)dx' + \ldots \qquad (2.71)$$

From the properties of the normalized kernel : $\int_{s}\mathrm{W}(x-x',h)dx' = 1$

and it will be shown in Chapter 4, Eq (4.41), that: $\int_{s}(x-x')\mathrm{W}(x-x',h)dx' = 0$

hence, (2.71) can be written as:

$$-\int_{\Omega} f(x')\frac{\partial \mathrm{W}(x-x',h)}{\partial x'}dx' - \frac{\partial f(x')}{\partial x'}\Big|_{x'=x} = \frac{\partial^3 f(x')}{\partial x'^3}\Big|_{x'=x}\int_{\Omega}\frac{(x-x')^2}{2}\mathrm{W}(x-x',h)dx' + \ldots \qquad (2.72)$$

Eq (1.74) can be written:

$$-\int_{\Omega} f(x')\frac{\partial \mathrm{W}(x-x',h)}{\partial x'}dx' - \frac{\partial f(x')}{\partial x'}\Big|_{x'=x} = \frac{h^2}{2}\frac{\partial^3 f(x')}{\partial x'^3}\Big|_{x'=x}\int_{\Omega}\frac{(x-x')^2}{h^2}\mathrm{W}(x-x',h)dx' + \ldots \qquad (2.73)$$

Equation (2.73) is the contribution to error due to smoothing approximation. The preceding expression can be written as:

$$-\int_{\Omega} f(x')\frac{\partial \mathrm{W}(x-x',h)}{\partial x'}dx' - \left.\frac{\partial f(x')}{\partial x'}\right|_{x'=x} = \frac{h^2}{2}\left.\frac{\partial^3 f(x')}{\partial x'^3}\right|_{x'=x}\int_{\Omega}\frac{(x-x')^2}{h^2}\mathrm{W}(x-x',h)dx' + O(h^4) \tag{2.74}$$

which is of second-order in h. The preceding derivation can be found in [72].

The next source of error is introduced by the numerical discretisation of the integral in Eq (2.70). This type of error is called truncation error [49] and is induced by the accuracy of the nodal integration. The truncation error is expressed as follows:

$$\varepsilon_t = < f(x) > -\sum_{J\in S}\frac{m_J}{\rho_J}f_J \mathrm{W}_{IJ} \tag{2.75}$$

Again, if the 1-D case is considered, the kernel function must satisfy (2.9) and (4.41) However, this only holds for continuous forms. The discretised forms of (2.9) and (4.41) are $-\sum_{J\in S}\frac{m_J}{\rho_J}f_J \mathrm{W}_{IJ}$ and $-\sum_{J\in S}(x_I - x_J)\frac{m_J}{\rho_J}f_J \mathrm{W}_{IJ}$ respectively and the numerical values of these two approximations may not necessarily be exactly 1 and 0 as is expected in the continuous forms (i.e. the continuous form of conditions (2.9) and (4.41) may not be valid after the SPH discretisation has taken place).

The truncation error is dependent on the accuracy of the nodal integration employed and on the particle distribution [49]. For an orderly and even distribution of particles, the truncation error is of order h^2 or higher [49]. For a disordered but evenly distributed particle arrangement, the average truncation error is of order $h\left|\ln h\right|^{\frac{n-1}{2}}$ [49].

Summary.

The basic components of the SPH method have been provided in this chapter. A comprehensive compilation of SPH formulae and the standard

methodology to obtain these expressions have been supplied. Subsequently, the conservation laws of continuum mechanics have been discretised in space using the resulting interpolating formulae. Finally, the main two sources of error of the SPH method, namely truncation and smoothing errors, have been identified and expressions to evaluate these errors have been provided. In this chapter, the following notation was enforced: T for scalar fields, $\bar{\mathbf{v}}$ for vector fields and $\bar{\bar{\mathbf{P}}}$ for second order tensors. This has been done to emphasise that equations that look the same will generate particle equations with entirely different properties depending on the nature of the field under consideration. In subsequent chapters, this notation is dropped under the assumption that the reader is familiar with the continuous forms of the conservation laws and with basic concepts of Continuum Mechanics.

CHAPTER 3

SPH DRAWBACKS

It is well known that the conventional SPH method initially proposed by Lucy and Gingold and Monaghan [31,58] has a number of shortcomings including inconsistency and rank deficiency [73] (which is related to a type of spurious instability present in the particle equations) as well as tensile and material instability. Later it will be shown that rank deficiency and tensile instability are the result of the type of discretisation carried out in SPH: the former is related to the cut-off wave number whereas the latter refers to the effect of the product of the second derivative of the smoothing function and the value of stress. The material instability present in the particle equations is desirable since it is also present in the continuum equations.

Further limitations inherent in SPH which still hamper the full exploitation of the method are the treatment of boundary conditions and spurious zero energy modes [7]; these shortcomings will be briefly described before the stability of particle equations is dealt with rigorously.

3.1 Particle Deficiency.

The basic SPH approximations are derived for interior nodes which assume there is a full distribution of neighbouring nodes. When the distribution of nodes is not full, inaccuracies in the computations are introduced. These inaccuracies can be minimized by the introduction of normalized kernels which are also very effective when the nodes are distributed in non-uniform arrangements [46].

As an example, consider an equally-spaced distribution of interpolation points. If the kernel used has compact support then the effect of particles outside this support will be zero. If the particles have uniform density then the particles at the interior of the domain will feel the effect of neighbouring particles on two sides, while particles at the boundaries will appear underdense as the contribution comes from particles on one side only. The normalization of the kernel restores particle deficiency at the boundaries.

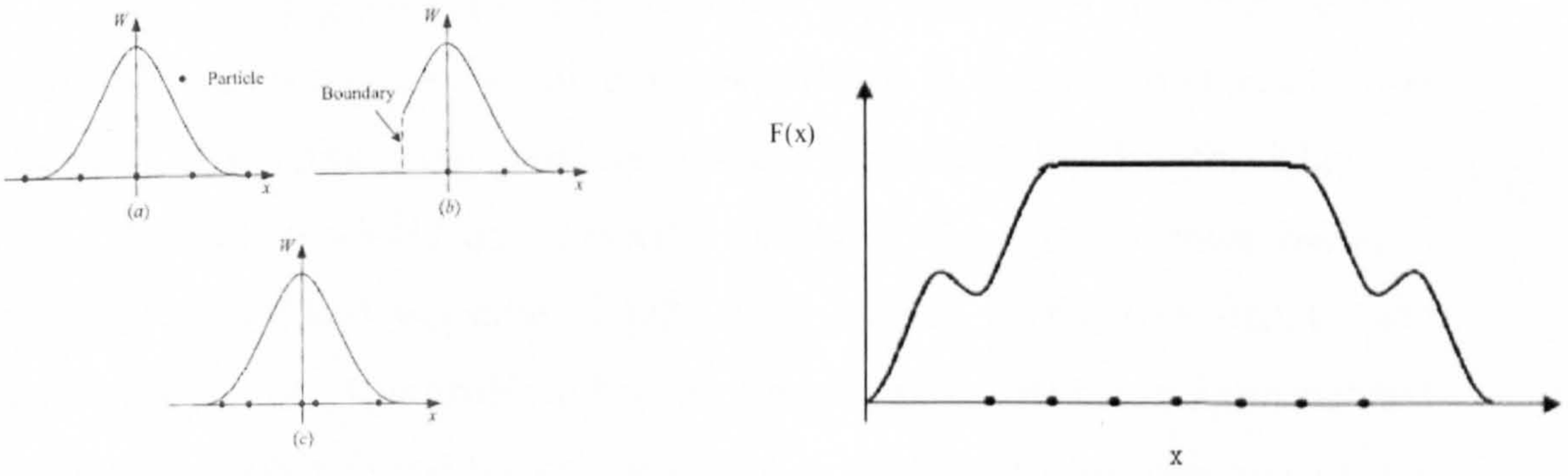

Fig. 3.1 An example of kernel approximation of F(x) in interior particles with complete support and in boundary particles.

This avenue is fully exploited in the present thesis. The numerical examples presented in Chapter 6 demonstrate the advantages of kernel normalization.

3.2 Consistency of SPH Equations.

This problem has been briefly described in Chapter 2. Consistency (or completeness) of the SPH equations refers to the highest order polynomial the method is capable of reproducing accurately. In is most basic form, standard SPH equations are not even zero order consistent. This deficiency in the method implies that a constant field will not be interpolated accurately if the standard form of the SPH equations is to be used. This problem can easily be tackled by introducing symmetry terms into the discretised equations. With symmetric terms (Refer to Chapter 2, Section 2.3) the interpolation becomes zero order consistent for all interior particles which possess complete support. However for particles that lie close to the boundary or at the boundary, the one sided contribution of particles still introduces inaccuracies in some practical cases despite the symmetry terms.

3.3 Boundary Conditions in SPH.

When dealing with free surfaces, boundary conditions in SPH have been successfully ignored since the value of stress drops to zero at a distance $2h$ due to the lack of neighbouring particles outside the smoothing length. This one sided contribution yields approximate results at the solid surface because, although stresses and velocities might drop to zero at the free surface, the density should not. The problem becomes more noticeable when a normalized form of the kernel is introduced since kernel normalization compensates for the lack of neighbours outside physical boundaries [45, 74]. In the normalized SPH case, both free and traction boundaries have to be imposed rigorously at the

surface. One way in which boundary conditions are treated is through the introduction of so-called ghost particles [34,50]. The ghost particle method uses artificial particles lying within a specified distance from the real boundaries. These are mirroring particles which have the same density and value of stress as real particles lying within a $2h$ distant of the boundary but with opposite velocity.

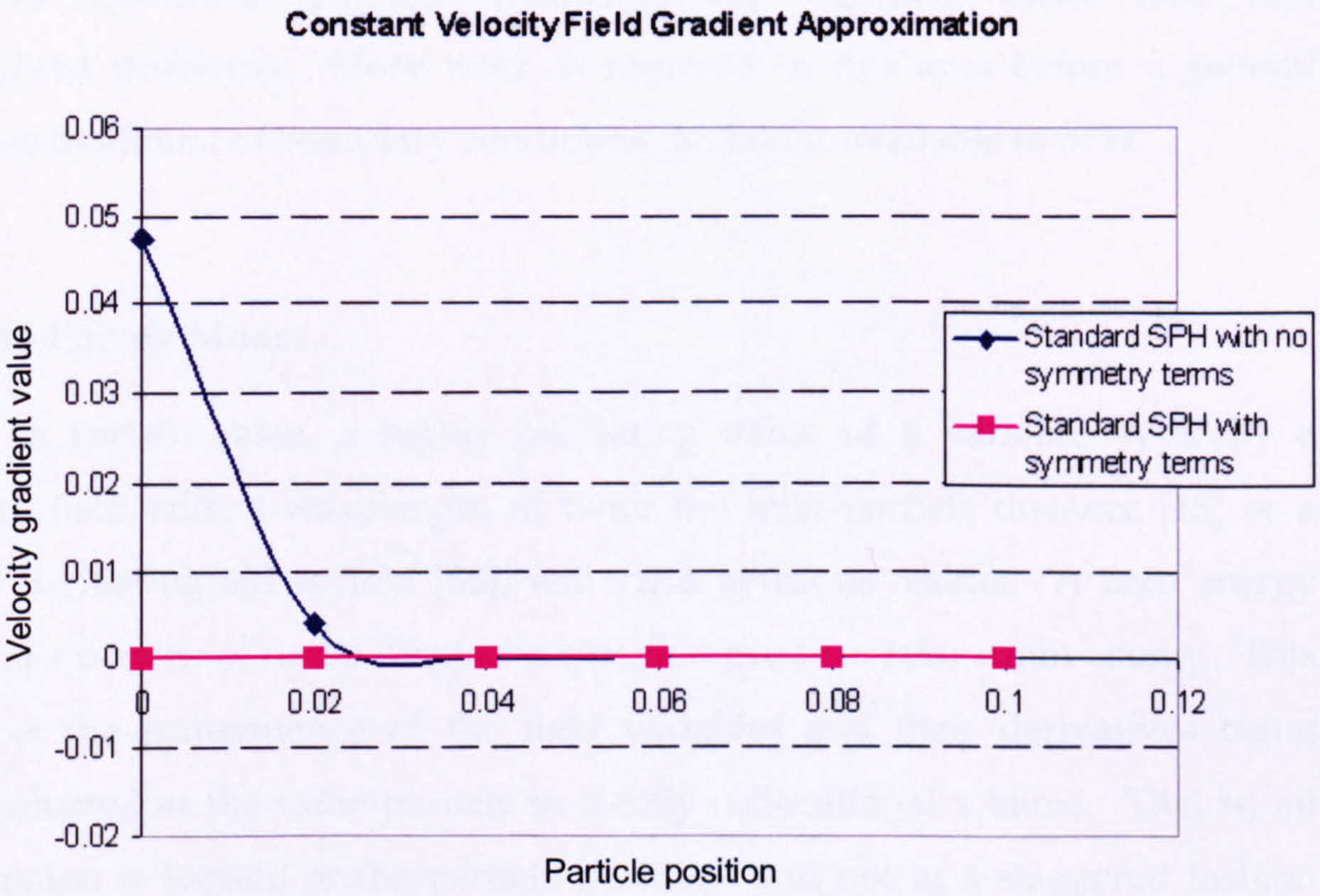

Fig. 3.2 Two SPH schemes are used to approximate the gradient of a constant velocity field. The standard SPH with no symmetry terms uses $\nabla v_I = -\sum_{J \in S} \frac{m_J}{\rho_J} v_J \nabla W_{IJ}$ to approximate the gradient whereas $\nabla v_I = \sum_{J \in S} \frac{m_J}{\rho_J} (v_I - v_J) \nabla W_{IJ}$ contains symmetry terms.

The effect of these fictitious particles is included explicitly in the summations of field and gradients [34]. It has been reported by Liu and Liu [53] that mirroring ghost particles of this kind are not enough to prevent real particles from penetrating the boundary. Monaghan [66] suggested introducing a line of virtual particles located right on the solid boundary to generate a highly repulsive, non-physical potential that increases as the real particles get

closer to the virtual ones, thus preventing unphysical penetration at the boundaries. Campbell [14] has suggested introducing the boundary terms into the SPH particle equations. It is the author's experience that when trying to implement boundary terms into an SPH code, one is faced with a density term at the boundary, which, in the author's opinion has little or no physical meaning. The introduction of ghost particles increases the complexity of the numerical code significantly. In addition, the introduction of boundary terms in SPH equations, although mathematically rigorous, poses new and unresolved problems. More work is required in this area before a general purpose treatment of boundary conditions method is available in SPH.

3.4 Zero Energy Modes.

In certain cases, a highly oscillating value of a variable, typically a velocity field with a wavelength of twice the inter-particle distance [15] or a highly oscillating stress field [80], will yield spurious results. A zero energy mode is a pattern of nodal displacements that produce zero strain energy. This mode is the consequence of the field variables and their derivatives being approximated at the same particle in a fully collocational scheme. That is; all information is located at the particle positions and not in a staggered fashion [80]. As an example, take a distribution of 3 particles in 1-D where the odd particles have the same value and sign of stress, whereas even particles have a different value (Refer to Fig.3.3). When the value of stress of the neighbouring particles is introduced into the momentum equation, the resulting value of acceleration for particle I will be zero and consequently so will the value of the velocity irrespective of the value of stress of particle I

In our example, the 1-D momentum equation for 3 evenly distributed $(\Delta x = 2h)$ particles with the same density is written as:

$$\ddot{x}_I = \frac{1}{\rho}\left(\sigma_{I-1}\mathrm{W}'(-\Delta x) + \sigma_I \mathrm{W}'(x_I) + \sigma_{I+1}\mathrm{W}'(\Delta x)\right)$$

but the derivative of a bell shaped function is anti-symmetric, hence:

$$\mathrm{W}'(-\Delta x) = -\mathrm{W}'(\Delta x)$$

and $\mathrm{W}'(x_i) = 0$.

This equation will produce no acceleration if the stresses at the odd particles *I-1* and *I+1* have the same value, regardless of the value of stress at particle *I*. The approximation for acceleration at particle *I* using a fully collocational SPH scheme is therefore $\ddot{x}_i = 0$.

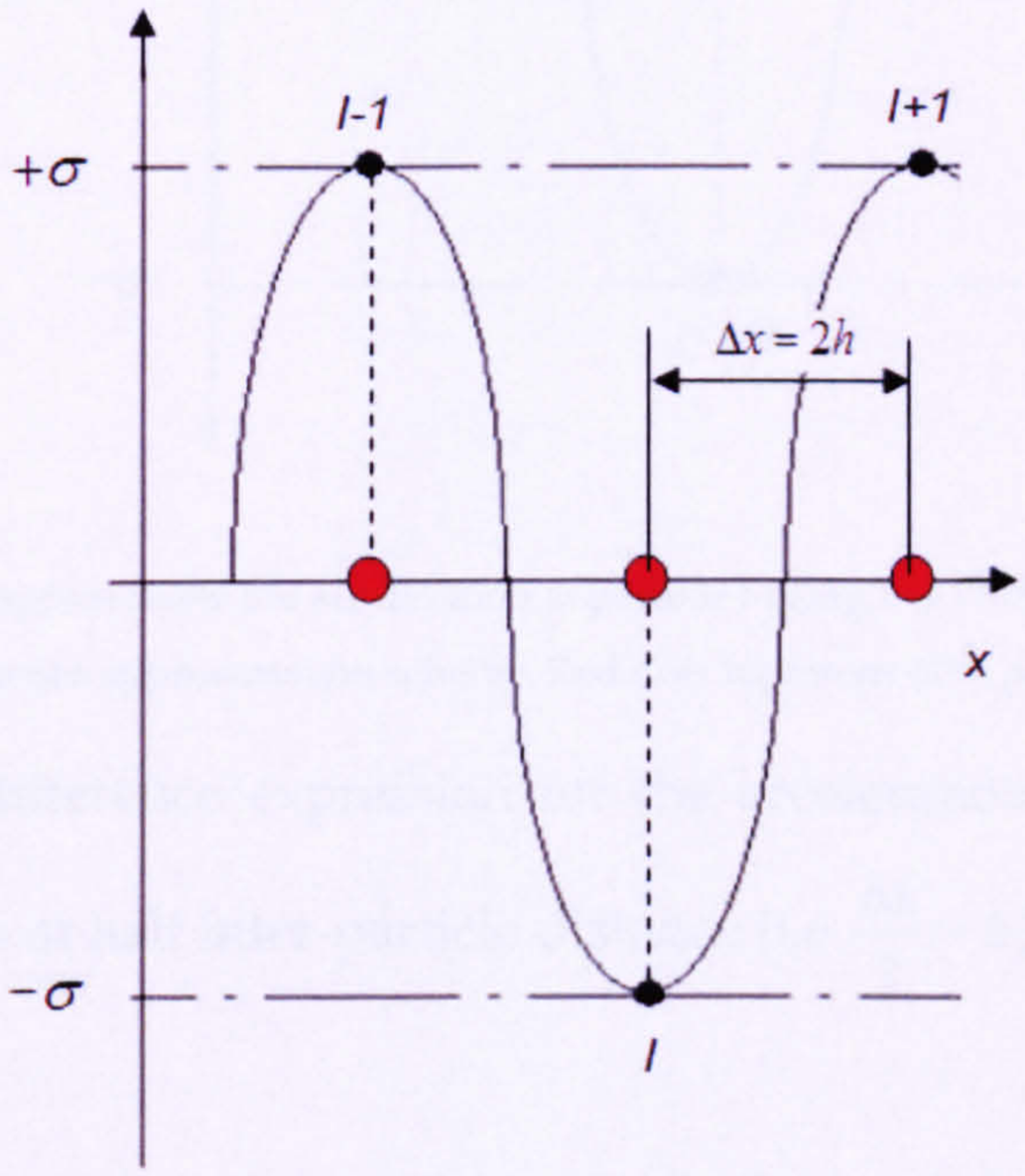

Fig.3.3 Spurious zero energy mode at particle *I* caused by a highly oscillating stress field. Red dots represent SPH particles.

If the acceleration in the problem above gets approximated through a staggered centred difference algorithm such as the Von Neumann-Richtmyer (VNR) scheme (as quoted by Swegle et al. in [80]), the resulting acceleration will

be non-zero. In this scheme, the material particles carry position, velocity and acceleration but all other quantities are located at the mesh centres between particles (Refer to Figure 3.4).

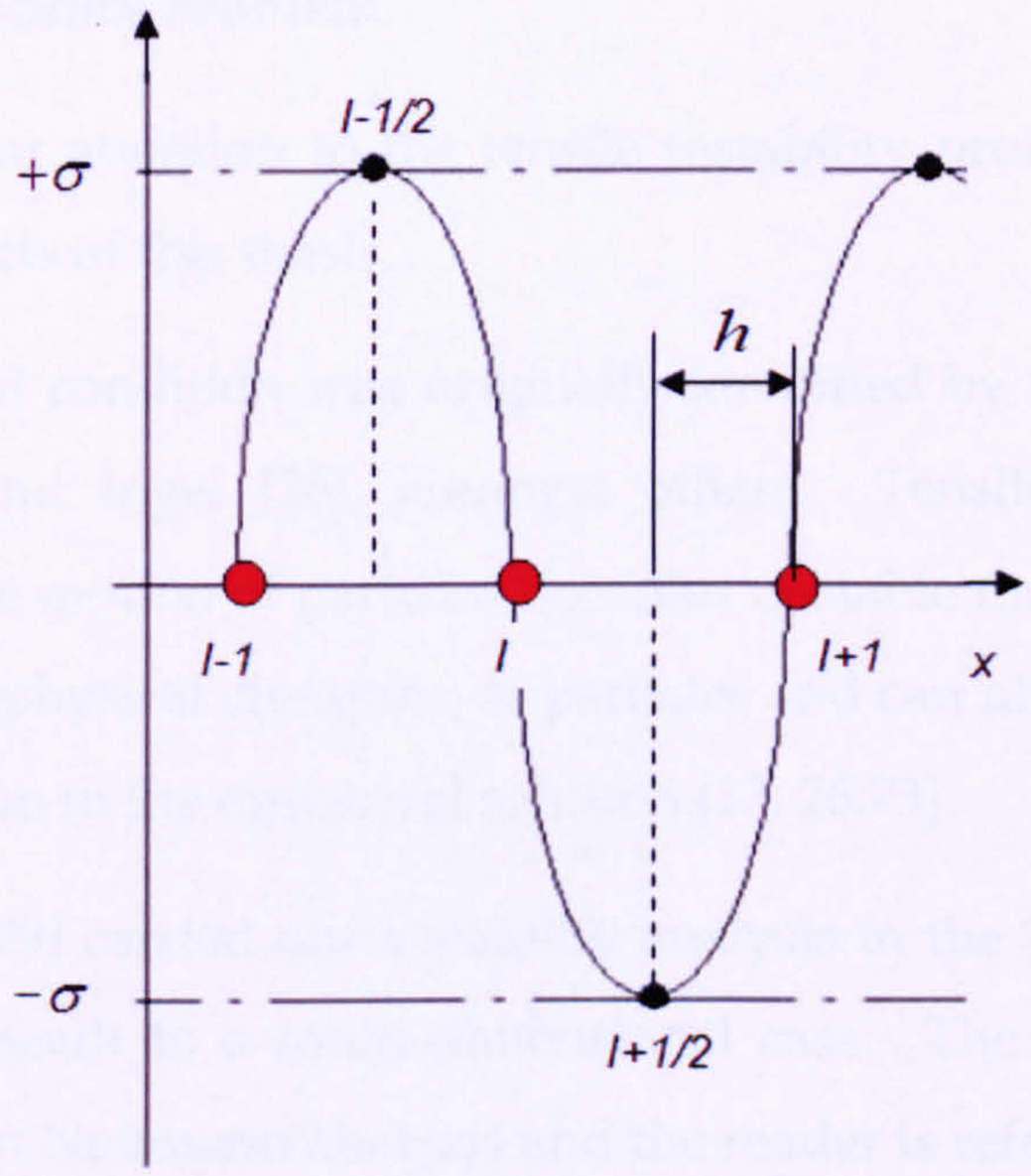

Fig.3.4 Set-up used to approximate the acceleration at particle I using the VNR staggered centred finite difference approximation scheme. Red dots represent SPH particles.

The finite-difference expression for the acceleration of node I uses the values of the stress at half inter-particle distance (i.e. $\frac{\Delta x}{2} = h$) and is expressed as follows:

$$\ddot{x}_I = \frac{1}{\rho}\left(\frac{\sigma_{I+1/2} - \sigma_{I-1/2}}{h}\right)$$

This yields a non-zero value for the acceleration at particle I.

The spurious SPH mode presented above is known as "zero energy". It is a condition carried not only by particle methods but also by standard finite element methods. The fundamental problem is that all information is carried by a single material point [80]. One potential solution is the introduction of

stress points as proposed by Dyka and Ingel [26]. This idea was later extended to 3-D by Vignjevic et.al. [78].

3.5 The Tensile Instability Problem.

Let us turn our attention to the tensile instability problem since this is one of the main aspects of this thesis.

This numerical condition was originally identified by Swegle et al [80], Balsara [2], Dyka and Ingel [26], amongst others. Tensile instability is a situation in which the motion of particles becomes unstable under tensile stress. It manifests as an unphysical clumping of particles and can ultimately lead to a premature termination in the numerical solution [13, 26,73].

Swegle et al [79] carried out a stability analysis in the 1D equations and then extended this result to a multi-dimensional case. The stability analysis carried out was a Von Neumann analysis and the reader is referred to Swegle et al. [80] for a detailed explanation of this technique.

In their analysis, Swegle et al found out that the tensile instability neither depends on the artificial viscosity nor on the time integration scheme. The sufficient condition for unstable growth is a combination of the derivative of the gradient of the kernel and the stress at the particle. Mathematically this condition can be expressed as follows: $W''\sigma > 0$. This condition implies that as long as the product of the second derivative of the smoothing function and the stress at a particle is greater than zero, unstable growth will take place.

Consider the next case as an example. In 1D standard SPH method, the first neighbour particle is found at h (the smoothing length) from particle I. The smoothing function used by the Lagrangian code generated for this dissertation makes use of a cubic spline smoothing function. From Figure 3.5 it can be observed that the gradient of the spline has its minimum at 2/3 of h which indicates that from the first neighbour to the boundary of the support,

the second derivative of the kernel will always result in a positive value. We can therefore conclude that under tension (i.e. stress value greater than zero) the standard SPH method is unstable.

Several remedies have been proposed to alleviate or avoid such tensile instability. Morris [67] suggested using special smoothing functions since the instability is closely related to the second derivative of the kernel. These special kernels proved to be successful only in a few specific cases and did not always yield satisfactory results.

Dyka and Ingel [26] introduced stress points into SPH and concluded that stress points diminish the effect of tensile instability. Belytschko et. al. [5] point out that whilst better stability of the method can be achieved using stree points, Eulerian kernels in combination with stress points cannot fully rid the method of its inherent stability. Instead, they proposed using Lagrangian kernels and proved that the method becomes more stable at the expense of the magnitude of the deformation that can be modelled.

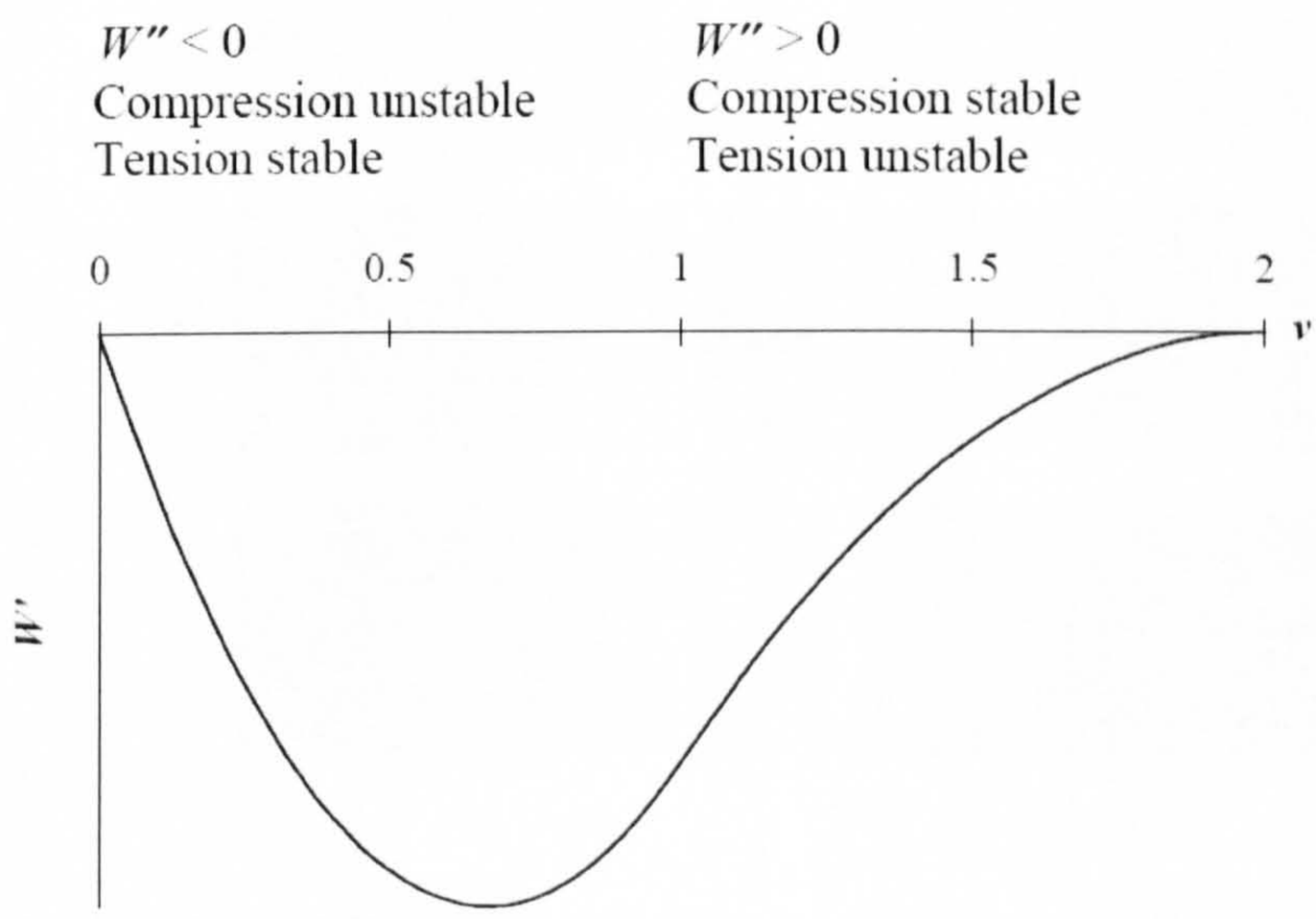

Fig. 3.5 Value of first derivative of a cubic spline.

3.6 Stability Analysis of Continua and SPH Equations.

The linear stability analysis of continua provides reliable guidelines with regard to the type of instabilities expected when analysing particle equations. Initially, a general stability analysis of the conservation equations based on the Von Neumann approach is carried out [51, 73]. An alternative stability analysis can be found in [34].

The simplifications introduced are as follows: the analysis is carried out in a Total Lagrangian Framework and the process is considered to be isothermal and adiabatic which implies that the energy equation is irrelevant as stated by Rabczuk et. al. [73]. The conservation of mass has a simple algebraic form, hence only the momentum equation will be dealt with. In spite of these simplifications, the results provide a great deal of information on continua stability and provide a solid foundation for a clear understanding of the stability analysis of SPH particle equations.

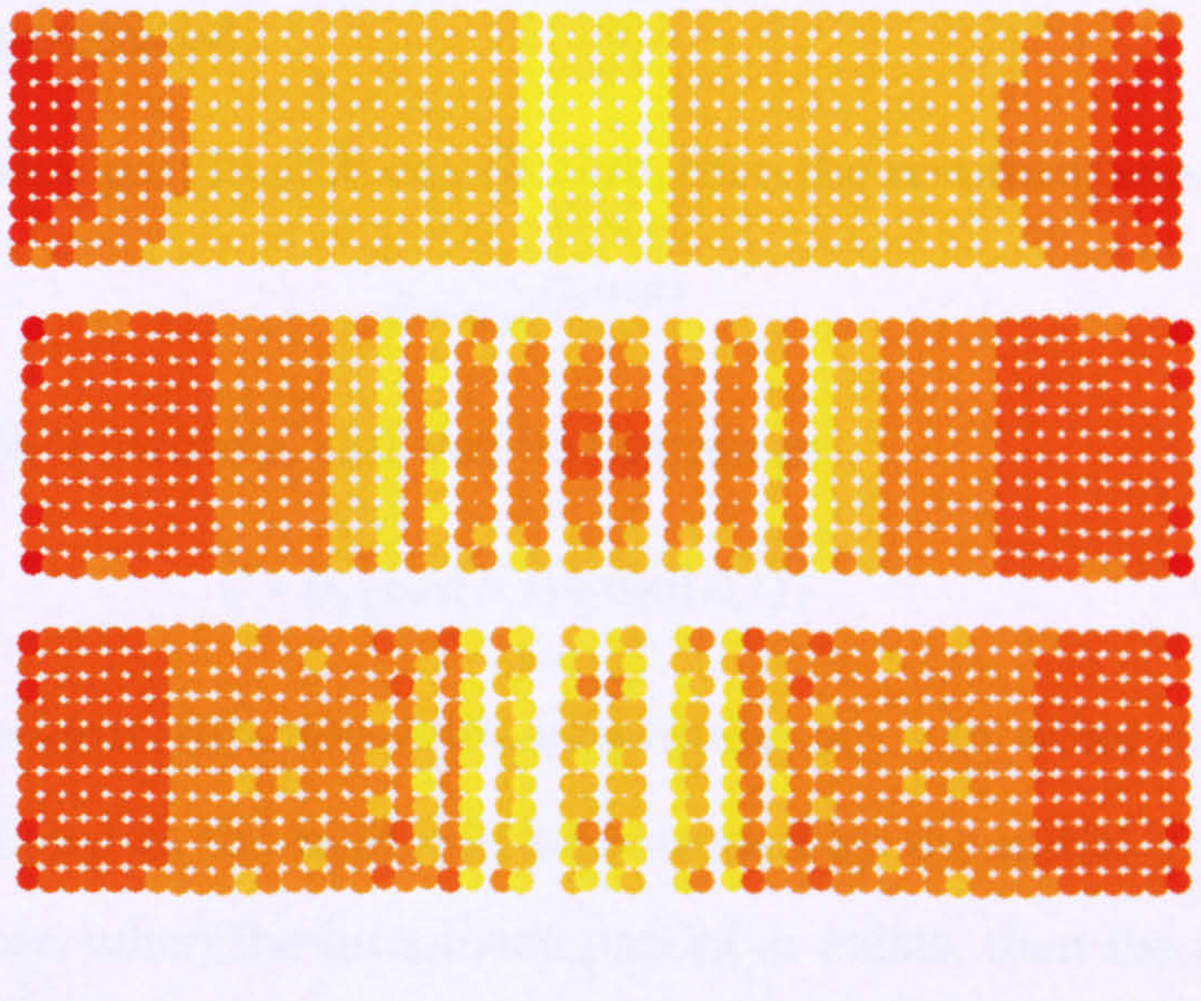

Fig.3.6 Typical collocated Eulerian SPH behaviour under tension. Although the linear elastic model was used for this simulation (i.e. no fracture is included in the constitutive model), unphysical fracture of the 2-D specimen occurs as a consequence of numerical instability in areas of high tensile stresses.

The type of perturbation introduced in this analysis has the following form, irrespective of the field in which the perturbation gets introduced:

$$\tilde{\psi} = \psi_0 e^{i(\varpi t + \kappa X)} \tag{3.1}$$

Where κ is known as the wave number, ϖ is the complex frequency, t is time. The complex frequency can be expressed a function of its real and imaginary terms:

$$\varpi = \omega_r + i\omega_i \tag{3.2}$$

hence.(3.1) can be written as:

$$\tilde{\psi} = \psi_0 e^{-\omega_i t}\left(e^{i(\omega_r t + \kappa X)}\right) \tag{3.3}$$

The main question to answer is: if a perturbation such as (3.1) is introduced in the system of governing equations, will the perturbation decay or grow as time progresses. Equation (3.3) can provide a good deal of information regarding the stability of continua and particle equations when a perturbation of the type (3.1) is introduced.

If the imaginary part in (3.3) equals zero, then the resulting expression is:

$$\tilde{\psi} = \psi_0 e^{i(\omega_r t + \kappa X)} \tag{3.4}$$

which, through Euler's formula, can also be written as:

$$\tilde{\psi} = \psi_0\left[\cos(\omega_r t) + i\sin(\omega_r t)\right] \tag{3.5}$$

This is a periodic function with amplitude ψ_0. In other words, the perturbation introduced in the field will be bounded by the initial value of the amplitude. However, when the imaginary part of ω exists, then the amplitude in equation (3.3) is bounded by $\psi_0 e^{-\omega_i t}$. It is therefore the imaginary part of the complex frequency that drives the stability of the solution. The conditions for stable or unstable growth are summarized as follows:

Condition 1.- If $\omega_i > 0$ in equation (3.3), the system remains stable since $\psi_0 e^{-\omega_i t}$ decays as t grows.

Condition 2.- If $\omega_i < 0$, the system becomes unstable since $\psi_0 e^{-\omega_i t}$ grows as time grows.

Condition 3.- When the complex frequency $\varpi = 0$,the threshold for instability is present.

The first step in the analysis of the continuum laws written in a Total Lagrangian referential involves the linearisation of the momentum equation. Perturbations are assumed over the displacement, which have the following form:

$$\bar{\mathbf{u}} = \mathbf{u} + \tilde{\mathbf{u}} \tag{3.6}$$

where $\tilde{u}$ denotes the displacement perturbation.

In order to obtain the value of the perturbation over the 1st Piola-Kirchhoff stress tensor **P** and the perturbation solution, the conservation of momentum in a Total Lagrangian framework needs to be considered first:

$$\rho_0 \frac{\partial^2 \mathbf{u}}{\partial t^2} = \nabla \mathbf{P} \tag{3.7}$$

and when the perturbation of the type in (3.6) is introduced, (3.7) becomes:

$$\rho_0 \frac{\partial^2 \bar{\mathbf{u}}}{\partial t^2} = \nabla \bar{\mathbf{P}} \tag{3.8}$$

or:

$$\rho_0 \frac{\partial^2 (\mathbf{u} + \tilde{\mathbf{u}})}{\partial t^2} = \nabla \bar{\mathbf{P}} \tag{3.9}$$

The relation between the 1st Piola-Kirchhoff stress **P** and the 2nd Piola-Kirchhoff **S** is found in [60]:

$$\mathbf{P} = \mathbf{S}\mathbf{F}^T \tag{3.10}$$

where **F** is the gradient of deformation tensor. It assumed that:

$$\bar{\mathbf{P}} = \bar{\mathbf{S}}\bar{\mathbf{F}}^T \tag{3.11}$$

where:

$$\bar{\mathbf{S}} = \mathbf{S} + \tilde{\mathbf{S}} \tag{3.12}$$

$$\bar{\mathbf{F}} = \mathbf{F} + \tilde{\mathbf{F}} \tag{3.13}$$

with (3.13) and (3.12) into (3.10):

$$\bar{\mathbf{P}} = \mathbf{S}\mathbf{F}^T + \mathbf{S}\tilde{\mathbf{F}}^T + \tilde{\mathbf{S}}\mathbf{F}^T + \tilde{\mathbf{S}}\tilde{\mathbf{F}}^T \tag{3.14}$$

which results in:

$$\tilde{\mathbf{P}} = \bar{\mathbf{P}} - \mathbf{P} = \mathbf{S}\tilde{\mathbf{F}}^T + \tilde{\mathbf{S}}\mathbf{F}^T \tag{3.15}$$

where the $\tilde{\mathbf{S}}\tilde{\mathbf{F}}^T$ has been neglected.

Subtracting (3.7) from (3.8) yields the equations that govern the perturbation solution:

$$\rho_0 \frac{\partial^2 \tilde{\mathbf{u}}}{\partial t^2} = \nabla \tilde{\mathbf{P}} \tag{3.16}$$

where $\tilde{\mathbf{P}}$ is given by (3.15)

The constitutive model that relates the 2nd Piola-Kirchhoff stress to the Green-Lagrange stress tensor is:

$$\mathbf{S} = \mathbf{C} : \mathbf{E} \tag{3.17}$$

where **C** is the material tangent modulus.

The perturbed constitutive equation can be written as:

$$\tilde{\mathbf{S}} = \mathbf{C} : \tilde{\mathbf{E}} \tag{3.18}$$

The Green-Lagrange strain tensor perturbation $\tilde{\mathbf{E}}$ is obtained as follows:

Green-Lagrange strain is defined as [60]:

$$\mathbf{E} = \frac{1}{2}\left(\mathbf{F}^T\mathbf{F} - \mathbf{I}\right) \tag{3.19}$$

The perturbed equation is written as:

$$\bar{\mathbf{E}} = \frac{1}{2}\left(\bar{\mathbf{F}}^T\bar{\mathbf{F}} - \mathbf{I}\right) \tag{3.20}$$

with $\bar{\mathbf{F}}$ as defined in (3.13)

Equation (3.20) yields

$$\bar{\mathbf{E}} = \frac{1}{2}\left(\mathbf{F}^T\mathbf{F} + \mathbf{F}^T\tilde{\mathbf{F}} + \tilde{\mathbf{F}}^T\mathbf{F} - \mathbf{I}\right) \tag{3.21}$$

where the $\tilde{\mathbf{F}}^T\tilde{\mathbf{F}}$ term has been neglected.

Subtracting (3.19) from (3.21) results in:

$$\tilde{\mathbf{E}} = \bar{\mathbf{E}} - \mathbf{E} = \frac{1}{2}\left(\mathbf{F}^T\tilde{\mathbf{F}} + \tilde{\mathbf{F}}^T\mathbf{F}\right) \tag{3.22}$$

Assuming $\mathbf{F}^T\tilde{\mathbf{F}}$ to be symmetric (3.22) adopts the following final form:

$$\tilde{\mathbf{E}} = \tilde{\mathbf{F}}^T\mathbf{F} \tag{3.23}$$

$$\text{or } \tilde{\mathbf{E}} = \mathbf{F}^T\tilde{\mathbf{F}} \tag{3.24}$$

(3.24) in (3.18) yields:

$$\tilde{\mathbf{S}} = \mathbf{C}:\tilde{\mathbf{E}} = \mathbf{C}:\left(\mathbf{F}^T\tilde{\mathbf{F}}\right) \tag{3.25}$$

(3.25) in (3.15) yields:

$$\tilde{\mathbf{P}} = \mathbf{C}:\left(\mathbf{F}^T\tilde{\mathbf{F}}\right)\mathbf{F}^T + \mathbf{S}\tilde{\mathbf{F}}^T \tag{3.26}$$

Equation (3.26) can be written in index notation following the next procedure:

The product in brackets in (3.26) can be expressed as:

$$\mathbf{F}^T\tilde{\mathbf{F}} = F^T_{ar}\tilde{F}_{rb} \tag{3.27}$$

The double contraction with the material tangent modulus can be expressed as:

$$\mathbf{C}:\left(\mathbf{F}^T\tilde{\mathbf{F}}\right)=C_{ikab}F^T_{ar}\tilde{F}_{rb} \tag{3.28}$$

Hence, the first tensor product in (3.26) is expressed as:

$$\mathbf{C}:\left(\mathbf{F}^T\tilde{\mathbf{F}}\right)\mathbf{F}^T=C_{ikab}F^T_{ar}\tilde{F}_{rb}F^T_{kj} \tag{3.29}$$

and the second term in (3.26) can be written as:

$$\mathbf{S}\tilde{\mathbf{F}}^T=S_{ib}\tilde{F}^T_{bj} \tag{3.30}$$

hence (3.26) can be written in index notation as:

$$\tilde{P}_{ij}=C_{ikab}F^T_{ar}\tilde{F}_{rb}F^T_{kj}+S_{ib}\tilde{F}^T_{bj} \tag{3.31}$$

Note that once the proper indices have been identified, we can pre- or post-multiply each one of these components since each term in (3.31) is now a scalar. The first term in (3.31) can be expressed as:

$$C_{ikab}F^T_{ar}\tilde{F}_{rb}F^T_{kj}=F_{ar}F_{jk}C_{ikab}F^T_{ar}\tilde{F}_{rb} \tag{3.32}$$

the second term in (3.31) can be expressed as:

$$S_{ib}\tilde{F}^T_{bj}=S_{ib}\delta_{jr}\tilde{F}_{rb} \tag{3.33}$$

Note in (3.33) that $S_{ib}\delta_{jr}\tilde{F}_{rb}$ only yields a value different from zero when $r=j$ which is consistent with the original second term in (3.31).

Typically, (3.31) is written as:

$$\tilde{P}_{ij}=A^0_{ijrb}\tilde{F}_{rb} \tag{3.34}$$

$$\text{where } A^0_{ijrb}=F_{ra}F_{jk}C_{ikab}+S_{ib}\delta_{jr} \tag{3.35}$$

is the elasticity tensor.

By substituting (3.34) in (3.16) the following governing perturbation equation is obtained:

$$\rho_0 \frac{\partial^2 \tilde{u}_i}{\partial t^2} = \frac{\partial \left(A^0_{jirb} \tilde{F}_{rb} \right)}{\partial X_j} = \frac{\partial}{\partial X_j} \left(A^0_{jirb} \frac{\partial \tilde{u}_r}{\partial X_b} \right) \tag{3.36}$$

In the previous equation the 1st Piola-Kirchhoff stress tensor has been written in terms of the displacement perturbation and the elasticity tensor.

It is now assumed that the perturbation of the displacements uses the classical Fourier representation form:

$$\tilde{\mathbf{u}} = \mathbf{g} e^{\varpi t + i\kappa \mathbf{n}^0 \cdot \mathbf{X}} \tag{3.37}$$

where $\mathbf{g}$ is a vector, κ is known as the wave number, $\mathbf{n}^0$ is the unit vector normal to the wave front, ϖ is the complex frequency, t is time. Alternatively κ and $\mathbf{n}^0$ can be combined as $\kappa \mathbf{n}^0$ which is termed the wave vector.

Substitution of (3.37) into the right hand side of (3.36) yields:

$$\tilde{F}_{rb} = \frac{\partial \tilde{u}_r}{\partial X_b} = \frac{\partial \left(g_r e^{\varpi t + i\kappa n^0_b X_b} \right)}{\partial X_b} \tag{3.38}$$

bearing in mind that $\frac{\partial \left(\kappa n^0_i X_i \right)}{\partial X_i} = \kappa n^0_i$ (3.39) yields:

$$\tilde{F}_{rb} = \frac{\partial \tilde{u}_r}{\partial X_b} = i\kappa g_r n^0_b e^{\varpi t + i\kappa \mathbf{n}^0 \mathbf{X}} \tag{3.40}$$

The derivative on the right hand side of (3.36) can be written as:

$$\frac{\partial}{\partial X_j} \left(A^0_{jirb} \tilde{F}_{rb,b} \right) = A^0_{jirb} \frac{\partial F_{rj}}{\partial X_j} \tag{3.41}$$

$$\frac{\partial \tilde{F}_{rj}}{\partial X_j} = \left(i\kappa g_r n^0_b \right) \left(i\kappa n^0_j \right) e^{\varpi t + i\kappa \mathbf{n}^0 \cdot \mathbf{X}} \tag{3.42}$$

Hence (3.41) becomes:

$$\frac{\partial}{\partial X_j}\left(A^0_{jirb}\tilde{F}_{rb,b}\right) = -\kappa^2 A^0_{jirb} n^0_b n^0_j g_r e^{\varpi t + i\kappa \mathbf{n}^0 \cdot \mathbf{X}} \tag{3.43}$$

The second order derivative on the left hand side of Eq (3.36) is straightforwardly calculated as:

$$\frac{\partial^2 \tilde{u}_i}{\partial t^2} = g_i \varpi^2 e^{\varpi t + i\kappa \mathbf{n}^0 \cdot \mathbf{X}} \tag{3.44}$$

Equation s (3.43) and (3.44) in (3.36) yields:

$$\rho_0 \varpi^2 g_i + \kappa^2 A^0_{jirb} n^0_b n^0_j g_r e^{\varpi t + i\kappa \mathbf{n}^0 \cdot \mathbf{X}} = 0 \tag{3.45}$$

which is known as the dispersion relation equation [27]. This is an equation that expresses the relation between the frequency and the wave number.

Equation (3.45) is generally expressed as:

$$\left(\frac{\varpi^2}{\kappa^2}\delta_{ir} + \frac{A^0_{ir}}{\rho_0}\right) g_r = 0 \tag{3.46}$$

with $A^0_{ir} = A^0_{jirb} n^0_b n^0_j$

Thus the characteristic equation is written as:

$$\det\left|A - \lambda I\right| = 0 \tag{3.47}$$

where:

$$A = \frac{A^0_{ir}}{\rho_0} \tag{3.48}$$

and:

$$\lambda = -\frac{\varpi^2}{\kappa^2} \tag{3.49}$$

From Equations (3.46), (3.48) and (3.49) , the continuum is stable if the solution for the complex frequency ϖ is an imaginary number, i.e when the

complex frequency ϖ takes the form $\omega_i i$ with $\omega_i \Rightarrow R^+$. This implies that all Eigen values of A are positive, in other words A needs to be positive definite. From Equation (3.28) it can be seen that the material tangent modulus is a component of the A matrix, hence A could lose its positive definiteness if C loses its definiteness. We can therefore conclude that the stability of the system in the Total Lagrangian framework is closely related to the stability of the continuum itself.

Equation (3. 39) can also be used to obtain the stability of the continuum in the current configuration when the reference and the current configurations coincide (Refer to section 2.1.1 and Chapter 4 for a detailed explanation). In this case the spatial coordinates $\vec{\mathbf{x}}$ and material coordinates $\vec{\mathbf{X}}$ coincide ($\vec{\mathbf{x}} = \vec{\mathbf{X}}$) and the gradient of deformation tensor is the identity matrix, $\mathbf{F} = \mathbf{I}$. The 2nd Piola-Kirchhoff stress tensor and the Cauchy stress tensor are related in the following way [4]:

$$\mathbf{S} = J\mathbf{F}^{-1}\boldsymbol{\sigma}\mathbf{F}^{-T} \tag{3.50}$$

which results in $\mathbf{S} = \boldsymbol{\sigma}$ when the reference and the current configurations coincide. In the current configuration, the material tangent modulus C becomes $C^{\sigma\tau}$, where $C^{\sigma\tau}$ is the modulus relating the objective Truesdell rate of the Cauchy stress tensor to the rate of deformation tensor. The Truesdell rate is derived by considering the time derivative of the 2nd Piola-Kirchhoff stress when the reference and the current configuration coincide [4], hence $\dot{\mathbf{S}} = \boldsymbol{\sigma}^{\nabla\tau}$.

With all of the above in mind Eq.(2.35) transforms into:

$$A_{ijrb} = C^{\sigma\tau}_{ikab} + \sigma_{ib}\delta_{jr} \tag{3.51}$$

thus equation (3.46) adopts the following form:

$$\left(\frac{\varpi^2}{\kappa^2}\delta_{ir} + \frac{A_{ir}}{\rho_0}\right)g_r = 0 \tag{3.52}$$

$$\text{with} \quad A_{ir} = A_{jirb} n_b n_j \tag{3.53}$$

For additional simplicity it is assumed that the domain is simply 1-D in which case equation (3.7) becomes:

$$\rho_0 \ddot{\tilde{u}} = \frac{\partial P}{\partial X} \tag{3.54}$$

In 1-D, equation (3.10) and the time derivative of equation (3.17) become:

$$P = SF \tag{3.55}$$

$$\text{and} \quad \dot{S} = C\dot{E} \tag{3.56}$$

respectively.

Since E is defined by Eq. (3.19), with $F^T F$ assumed to be symmetrical, equation (3.56) can be written as:

$$\dot{S} = CF\dot{F} \tag{3.57}$$

since in 1-D, $F^T = F$

The 1-D perturbed equations corresponding to (3.16) and (3.31) become:

$$\rho_0 \ddot{\tilde{u}} = \frac{\partial \tilde{P}}{\partial X} \tag{3.58}$$

$$\text{and} \quad \tilde{P} = CF\tilde{F}F + S\tilde{F} = \bar{C}\tilde{F} \tag{3.59}$$

$$\text{respectively, with } \bar{C} = CF^2 + S \tag{3.60}$$

Comparing equation (3.34) with (3.59) it is deduced that the elasticity tensor A is equal to $\bar{C}$, therefore the governing equation in 1-D follows from (3.36):

$$\rho_0 \frac{\partial^2 \tilde{u}_i}{\partial t^2} = \bar{C} \frac{\partial^2 \tilde{u}}{\partial X^2} \tag{3.61}$$

with a perturbed solution of the form:

$$\tilde{u} = ge^{i\kappa X + i\varpi t} \tag{3.62}$$

Equation (3.61) yields:

$$\varpi^2 = \frac{\bar{C}\kappa^2}{\rho_0} \tag{3.63}$$

and the solution becomes unstable when $\bar{C} \leq 0$, hence the threshold for unstable behaviour occurs when:

$$\bar{C} = CF^2 + S = 0 \tag{3.64}$$

The stability conditions for the current configuration are obtained from equation (3.59) and equation (3.63). $\tilde{F}$ in (3.59) has to be expressed in current configuration as follows:

$\tilde{F} = \frac{\partial \tilde{u}}{\partial X} = \frac{\partial \tilde{u}}{\partial x}\frac{\partial x}{\partial X}$ (3.65) which yields $\left(\frac{\partial x}{\partial X}\right)^{-1}\frac{\partial \tilde{u}}{\partial x} = \tilde{F}_c$

and from (3.60):

$$\bar{C}^{\sigma\tau} = C^{\sigma\tau} + \sigma \tag{3.66}$$

hence equation (3.59) yields:

$$\tilde{P} = \bar{C}^{\sigma\tau}\tilde{F}_c \tag{3.67}$$

The stability of the system is still governed by equation (3.63) with $\bar{C} = \bar{C}^{\sigma\tau}$, hence the stability threshold for the current configuration is:

$$\sigma + C^{\sigma\tau} = 0 \tag{3.68}$$

It is clear from (3.63) and conditions (3.66) and (3.68) that the solution becomes unstable under two situations.

1.- when $\bar{C}^{\sigma\tau} \leq 0$, which could occur when $C \leq 0$ becomes sufficiently negative. This corresponds to the material instability induced by strain softening [73].

2.- when $\sigma \leq 0$ and $|\sigma| = C^{\sigma\tau}$, in other words, material instabilities manifest under compressive stresses when the stress achieves a certain negative value.

3.7 Stability Analysis of Particle Equations.

3.7.1 Lagrangian SPH equations.

In a 1-D domain, the Total Lagrangian SPH momentum equation with nodal integration is written as follows when external and body forces are neglected:

$$m_I \ddot{u}_I = -\sum_{J \in S} \frac{m_J}{\rho_{0J}} \mathrm{W}'(X_I - X_J, h_0) P_J \tag{3.69}$$

The perturbed SPH equation is obtained by discretising (3.58):

$$m_I \ddot{\tilde{u}}_I = -\sum_{J \in S} \frac{m_J}{\rho_{0J}} \mathrm{W}'(X_I - X_J, h_0) \tilde{P}_J \tag{3.70}$$

Where $\tilde{P}_J$ is given by Eq. (3.59) which can be written as follows in 1-D:

$$\tilde{P}_J = \bar{C} \tilde{F}_J \tag{3.71}$$

and $\tilde{F}_J$ can be discretised as follows:

$$\tilde{F}_I = -\sum_{J \in S} \mathrm{W}'(X_I - X_J, h_0) \tilde{u}_J \tag{3.72}$$

Equation (3.71) can be written as follows:

$$\tilde{P}_J = -\bar{C} \sum_{K \in S} \mathrm{W}'(X_J - X_K, h_0) \tilde{u}_K = \bar{C} \sum_{K \in S} \mathrm{W}'(X_K - X_J, h_0) \tilde{u}_K \tag{3.73}$$

Equation (3.73) in (3.70) yields:

$$m_I \ddot{\tilde{u}}_I = -\sum_{J \in S} \frac{m_J}{\rho_{0J}} \mathrm{W}'(X_I - X_J, h_0) \bar{C} \sum_{K \in S} \mathrm{W}'(X_K - X_J, h_0) \tilde{u}_K \tag{3.74}$$

Substituting (3.37) into (3.74) yields:

$$m_I \varpi^2 g_I e^{i\kappa X_I} = \sum_{J \in S} \frac{m_J}{\rho_{0J}} \mathrm{W}'(X_I - X_J, h_0) \bar{C} \sum_{K \in S} \mathrm{W}'(X_K - X_J, h_0) g_K e^{i\kappa X_K} \tag{3.75}$$

Multiplication of $e^{-i\kappa X_I}$ by (3.75) yields:

$$m_I \varpi^2 g_I = \sum_{J \in S} \frac{\mathrm{m_J}}{\rho_{0J}} \mathrm{W}'(X_I - X_J, h_0) \bar{C} \sum_{K \in S} \mathrm{W}'(X_K - X_J, h_0) g_K e^{i\kappa (X_K - X_I)} \tag{3.76}$$

Equating only the real part of the left hand side of (3.76) and assuming that $g_I = g_K = g$:

$$\omega_r^{\,2} = \frac{1}{m_I} \sum_{J \in S} \frac{m_J}{\rho_{0J}} \mathrm{W}'(X_I - X_J, h_0) \bar{C} \sum_{K \in S} \mathrm{W}'(X_K - X_J, h_0) e^{i\kappa (X_K - X_I)} \tag{3.77}$$

Note that in spite of having considered only the real part of the complex frequency ϖ, ω_r as defined by equation (3.77) can still result in an imaginary number. Equation (3.69) can be re-written as:

$$\omega_r^{\,2} = \frac{1}{m_I} \sum_{J \in S} \frac{m_J}{\rho_{0J}} \mathrm{W}'(X_I - X_J, h_0) \bar{C} \sum_{K \in S} \mathrm{W}'(X_K - X_J, h_0) \cos\left(\kappa (X_K - X_I)\right) \tag{3.78}$$

For a distribution of particles equally spaced and with equal mass, equation (3.78) can be rewritten as:

$$\omega_r^{\,2} = \frac{\bar{C}}{\rho_{0J}} \sum_{J \in S} \mathrm{W}'(X_I - X_J, h_0) \sum_{K \in S} \mathrm{W}'(X_K - X_J, h_0) \cos\left(\kappa (X_K - X_I)\right) \tag{3.79}$$

From (3.79) it is concluded that the particle equations present a so-called spurious singular mode when the particle wave number $\kappa = \dfrac{\pi}{2(X_K - X_I)}$ which also represents the cut-off wave number for a regular particle spacing equal to $X_K - X_I = \Delta X$. This singular mode is present irrespective of the value of stress S contained implicitly in $\bar{C}$.

The other instance in which the particle equations become unstable is when $\bar{C}$ becomes zero which could happen when C in (3.64) loses its positive definiteness, which is intimately related to the so-called material instability. This is desirable since the continuum equations also present this type of

material instability (Equation (3.63)), in other words, the particle and the continuum equations present the same stability properties when representing material behaviour.

For an imaginary frequency below zero, i.e. $\omega_i \Rightarrow R^-$, the conservation of momentum particle equation becomes unstable (Condition 2).

3.7.2 Eulerian SPH equations.

For the analysis of SPH equations in current configuration, the following 1-D SPH momentum equation with nodal integration is considered:

$$m_I \ddot{u}_I = -\sum_{J \in S} V_J \mathrm{W}_I'(x_I - x_J, h)\sigma_J \tag{3.80}$$

where V_J is the current volume of particle J and σ_J is the Cauchy stress of particle J. In order to introduce the displacement perturbation on the right hand side of (3.80), the current volume V_J needs to be expressed in terms of the particle mass and density as follows:

$$V_J = \left.\frac{m}{\rho}\right|_J \tag{3.81}$$

and the current density in (3.81) can be expressed as:

$$\rho = J^{-1}\rho_0 \tag{3.82}$$

and since, in a 1-D analysis $J = F$, equation (3.82) and equation (3.81) in equation (3.80) yield:

$$m_I \ddot{u}_I = -\sum_{J \in S} \frac{m_J}{\rho_0} \mathrm{W}_I'(x_I - x_J, h) F_J \sigma_J \tag{3.83}$$

In (3.83), the deformation gradient needs to be expressed in the current configuration hence:

$$F_I = \left.\frac{\partial x}{\partial X}\right|_I = \left.\frac{\partial u}{\partial X}\right|_I + 1 \tag{3.84}$$

$$\left.\frac{\partial x}{\partial X}\right|_I = \frac{\partial u}{\partial x}\left.\frac{\partial x}{\partial X}\right|_I + 1 \tag{3.85}$$

$$F_I = \left.\frac{\partial x}{\partial X}\right|_I = \frac{1}{1 - \left.\frac{\partial u}{\partial x}\right|_I} \tag{3.86}$$

In expressions (3.83) through to (3.86), u is the particle displacement, x and X are the spatial and the material coordinates as defined in section 2.1.1 of Chapter 2.

Similar to the linearisation carried out in (3.6), linearised variables are introduced in (3.83):

$$m_I \ddot{\bar{u}}_I = -\sum_{J \in S} \frac{m_J}{\rho_0} \mathrm{W}_I'(\bar{x}_I - \bar{x}_J, h)\bar{F}_J \bar{\sigma}_J \tag{3.87}$$

$$m_I \ddot{\bar{u}}_I = -\sum_{J \in S} \frac{m_J}{\rho_0} \mathrm{W}_I'(\bar{x}_I - \bar{x}_J, h)(\sigma + \tilde{\sigma})\left(F + \tilde{F}\right) \tag{3.88}$$

which yields:

$$m_I \ddot{\bar{u}}_I = -\sum_{J \in S} \frac{m_J}{\rho_0} \mathrm{W}_I'(\bar{x}_I - \bar{x}_J, h)\left(\sigma_J F_J + \sigma_J \tilde{F}_J + \tilde{\sigma}_J F_J\right) \tag{3.89}$$

in (3.89) the product $\tilde{\sigma}\tilde{F}$ has been neglected.

When disturbances are introduced, the smoothing function can be written as:

$$\mathrm{W}(\bar{x}_I - \bar{x}_J, h) = \mathrm{W}\left((x_I + \tilde{x}_I) - (x_J + \tilde{x}_J)\right) \tag{3.90}$$

with $\tilde{x}_I = \tilde{u}_I$ and $\tilde{x}_J = \tilde{u}_J$

Equation (3.90) can be written as:

$$\mathrm{W}\left((x_I + \tilde{x}_I) - (x_J + \tilde{x}_J)\right) = \mathrm{W}\left((x_I - x_J) + (\tilde{u}_I - \tilde{u}_J)\right) \tag{3.91}$$

Upon expanding in Taylor's series:

$$\mathrm{W}(\bar{x}_I - \bar{x}_J, h) = \mathrm{W}(x_I - x_J) + \Delta x\, \mathrm{W}'(x_I - x_J) \tag{3.92}$$

where $\Delta x = \tilde{u}_I - \tilde{u}_J$ (3.93)

For the derivative of (3.92) the following expression can be written:

$$\mathrm{W}'(\bar{x}_I - \bar{x}_J, h) = \mathrm{W}'(x_I - x_J) + \Delta x\, \mathrm{W}''(x_I - x_J) \tag{3.94}$$

hence:

$$\mathrm{W}'(\bar{x}_I - \bar{x}_J, h) - \mathrm{W}'(x_I - x_J) = (\tilde{u}_I - \tilde{u}_J)\mathrm{W}''(x_I - x_J) = \tilde{\mathrm{W}}'(x_I - x_J, h) \tag{3.95}$$

Subtracting equation (3.83) from (3.89) yields:

$$m_I \ddot{\tilde{u}}_I = -\sum_{J \in S} \frac{m_J}{\rho_{0J}} \mathrm{W}_I'(\bar{x}_I - \bar{x}_J, h)\left(\sigma_J F_J + \sigma_J \tilde{F}_J + \tilde{\sigma}_J F_J\right) + \sum_{J \in S} \frac{m_J}{\rho_{0J}} \mathrm{W}_I(x_I - x_J, h)\sigma_J F_J \tag{3.96}$$

Rearranging:

$$m_I \ddot{\tilde{u}}_I = \sum_{J \in S} \frac{m_J}{\rho_{0J}} \left(-\mathrm{W}_I'(\bar{x}_I - \bar{x}_J, h) + \mathrm{W}_I(x_I - x_J, h)\right)\sigma_J F_J - \sum_{J \in S} \frac{m_J}{\rho_{0J\ J}} \mathrm{W}_I'(\bar{x}_I - \bar{x}_J, h)\left(\sigma_J \tilde{F}_J + \tilde{\sigma}_J F_J\right) \tag{3.97}$$

equation (3.95) in (3.97):

$$m_I \ddot{\tilde{u}}_I = -\sum_{J \in S} \frac{m_J}{\rho_{0J}} \left[\left(\tilde{\mathrm{W}}_I'(\tilde{x}_I - \tilde{x}_J, h)\right)\sigma_J F_J + \mathrm{W}_I'(\bar{x}_I - \bar{x}_J, h)\left(\sigma_J \tilde{F}_J + \tilde{\sigma}_J F_J\right)\right] \tag{3.98}$$

from equation (3.65) and (3.67) in current configuration:

$$\tilde{\sigma}_I = \bar{C}^{\sigma\tau} F_I^{-1} \tilde{F}_I \tag{3.99}$$

With all these ingredients the resulting dispersion relation for the current configuration is expressed as follows, the reader is referred to [51, 73] for a detailed explanation:

$$\omega^2 = \frac{\bar{C}^{\sigma\tau}}{\rho}\left[\sum_{J \in S} \mathrm{W}'(j\Delta x)\sin(\kappa \Delta x)\right]^2 - \frac{\sigma}{\rho}\left\{\sum_{J \in S} \mathrm{W}''(j\Delta x)\left[1 - \cos(\kappa j \Delta x)\right] - \left[\sum_{J \in S} \mathrm{W}'(j\Delta x)\sin(\kappa j \Delta x)\right]^2\right\} \tag{3.100}$$

Upon inspection of equation (3.100) it is immediately clear that the three terms contained herein yield three different conditions for stability:

1) When the material becomes unstable. In other words, when $\bar{C}^{\sigma\tau}$ vanishes, which corresponds to the material instability of the continuum

(Equation (3.63). This implies (3.100) could have two possible solutions: $\omega = \pm i\sqrt{x}$, the negative solution would yield Condition 2 outlined above.

2) At the cutoff wave number $\kappa = \frac{\pi}{\Delta x}$, $j = -1$, this is the onset of stability for the particle equations in current configuration for an equally spaced particle arrangement. In this case, the first term on the right hand side of equation (3.100) vanishes. Again, two possible solutions exist: $\omega = \pm i\sqrt{x}$, the negative solution would yield Condition 2.

3) When $\sigma > 0$ and $\bar{C}^{\sigma\tau} \neq 0$, which is the tensile instability identified by Swegle [80]. The second term inside the brackets on the right hand side is always positive, hence, if only $\frac{\bar{C}^{\sigma\tau}}{\rho}\left[\sum_{J\in S} W'(j\Delta x)\sin(\kappa\Delta x)\right]^2$ and $\left(\sum_{J\in S} W'(j\Delta x)\sin(\kappa j\Delta x)\right)^2$ existed, the particle equation would be unconditionally stable (i.e. the only possible solution for ω is a positive real). However, if $\sum_{J\in S} W''(j\Delta x)\left[1-\cos(\kappa j\Delta x)\right]$ is sufficiently positive and $\sigma > 0$, the product of what is in brackets in equation (3.100) and σ would yield a negative value, hence $\omega = \pm i\sqrt{x}$ and again, the negative solution would yield Condition 2. This condition is given by Swegle et al [80,81] as $\sigma W'' > 0$ which defines the onset of tensile instability of the SPH equations with nodal integration [21,25].

Note that stability condition 1) is desirable as it represents the stability of continuum equations. Conditions 2) and 3) are the result of the type of discretisation carried out in SPH. From this analysis it is clear why some special smoothing functions can reduce or eliminate the tensile instability altogether: as long as the smoothing function is carefully selected, the second derivative might yield a negative value which can restore stability in the particle equation. For the cubic spline, (widely employed for SPH approximations, and also used in this thesis work) the value of the second derivative of the smoothing function

at a distance Δx from particle I ispositive (Refer to Fig 3.6). Therefore, the onset of tensile instability is defined by $\sigma W'' > 0$ [80].

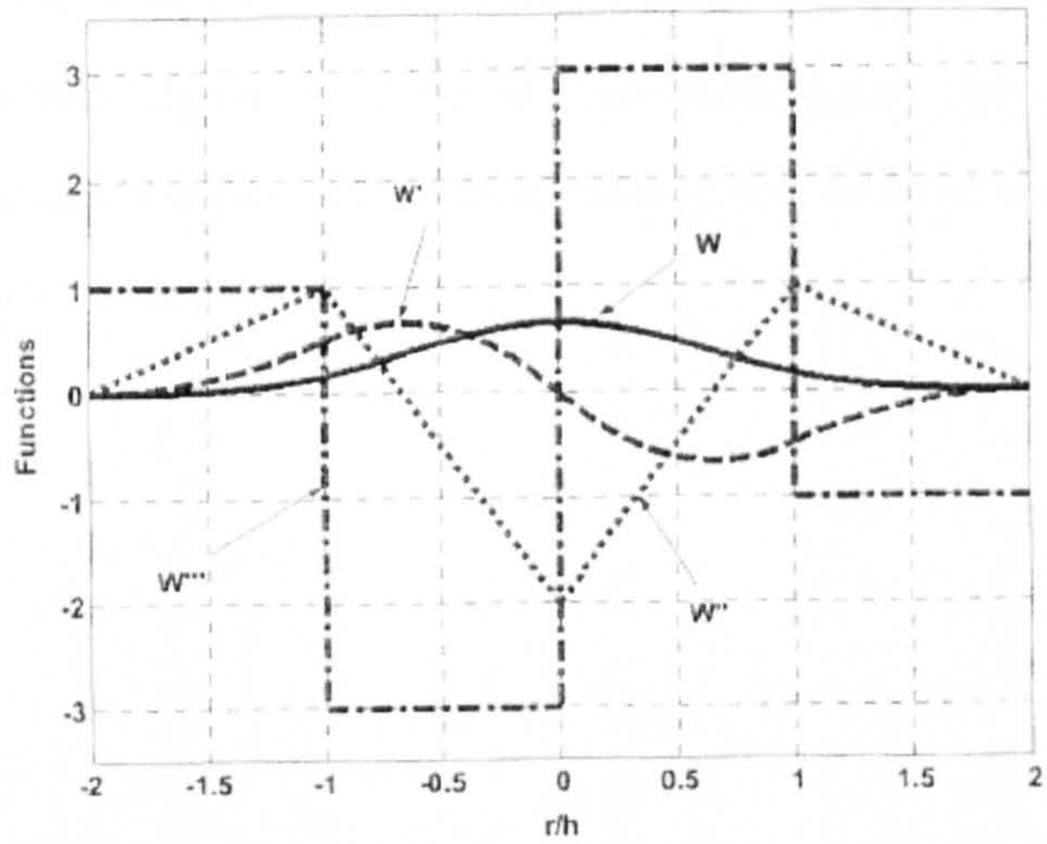

Fig.3.7. Value of first, second and third derivatives of a cubic spline.

Summary.

The main drawbacks of the ordinary SPH method, namely zero energy modes, particle deficiency, incompleteness, the treatment of boundary conditions and the tensile instability problem, have been identified. Potential solutions have also been discussed and their effectiveness and ease of implementation in a numerical code assessed. A comprehensive analysis of both continuum and particle equations has been developed by means of a standard Von Neumann stability analysis in which a perturbation of the form $\tilde{\psi} = \psi_0 e^{i(\varpi t + \kappa X)}$ is introduced in the field of interest.

The stability analysis of the Eulerian SPH equations has revealed that the stability of the system is governed by three terms: a material stability term, which is desirable since this term is also present in the continuum equations, and two more terms which are the result of the type of discretisation carried out, namely the spurious singular mode term and the tensile instability term.

Based on the analysis of continuum and particle equations it can be concluded that the stability of the system in the Total Lagrangian formulation is closely related to the stability of the continuum itself. In other words, the Total Lagrangian particle equations and the continuum equations exhibit similar stability properties when representing material behaviour, the only difference being the spurious singular mode corresponding to the cut-off wavelength term present in particle equations.

CHAPTER 4

TOTAL LAGRANGIAN SPH

SPH provides an excellent tool for simulating the physics of dynamic events in solids and fluids where large deformations of the problem domain are expected. It is particularly well suited to problems in computational solid mechanics that result in complex fracture paths, since in a random distribution of nodes there is no preferential path to crack propagation. These features have made SPH a robust tool in the simulation of dynamic fracture and fragmentation of brittle solids [50,75]. This method, however, suffers from certain conditions that yield unstable growth (which have been identified in the preceding chapter). When simulating the behaviour of a solid the most critical type of instability is the tensile instability. This instability manifests as a clumping of particles within the problem domain; a condition which is clearly

unacceptable when simulating fracture as this instability makes it impossible to differentiate real from numerical fracture. As an example, let us consider the case where a specimen is subject to tension (Fig.4.1).

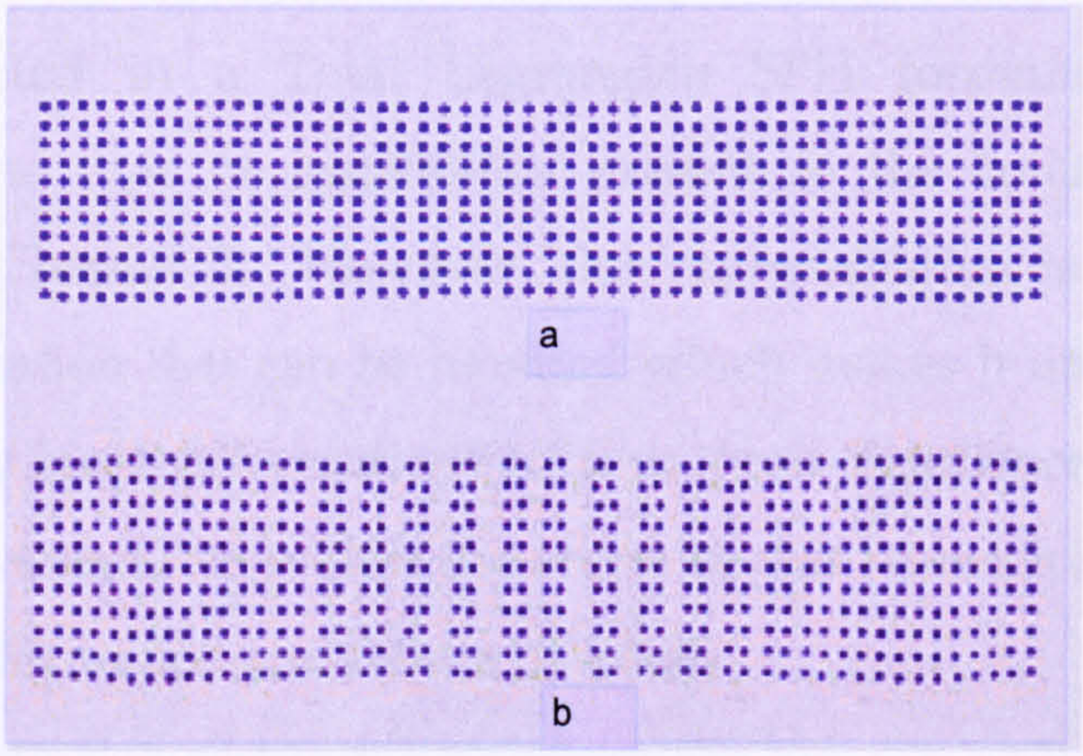

Fig.4.1 Simple 2-D case of specimen under tension to illustrate the stability achieved with Lagrangian Kernels (a) vs Eulerian Kernels (b) in conventional SPH . (b) appears to fracture due to the tensile instability condition.

Under a tensile stress state, the domain appears to fracture by yielding areas with high particle density while other areas are left with virtually no particles. The unphysical fracture generated is the result of numerical instability rather than the loading process [Refer to Chapter 3]. This condition will be prevented in a real solid by repulsive intermolecular forces ensuring that no material interpenetration takes place. This force has been implemented successfully in SPH in the form of a potential whereby the molecular forces generated between any two particles are inversely proportional to the distance between them. It has been reported that this approach eliminates the tensile instability problem under certain conditions [63].

It is clear from the preceding example that the computational simulation of solids in general and of fracture in particular requires the numerical method

to be stable. Only when such stability is achieved can dynamic events and fracture be modelled and predicted accurately.

The representation of the kernel in terms of material coordinates provides a more consistent procedure when simulating material fracture because instabilities will not occur due to numerical artifacts [5,73]. The instabilities expected in a Total Lagrangian SPH formulation are more consistent with the type of instabilities present in the continuum itself as demonstrated in Chapter 3. However, this representation is limited by the amount of deformation that can be handled which makes it unsuitable for the study of extremely large deformations such as those experienced in fluid flow. This limitation is acceptable within the scope of this research since the prime concern is with deformation and failure of solids.

The following sections will deal with the fundamental aspects of Continuum Mechanics required to formulate particle equations in a total Lagrangian framework.

4.1 Conservation Equations in the Total Lagrangian Formalism.

In order to describe the motion of a continuum, the conservation of mass, momentum and energy equations and the constitutive laws have to be integrated. Usually, when using a Total Lagrangian approach the initial state of the domain of interest is regarded as the reference state. In this analysis the same assumption was made, hence the conservation and constitutive equations will be expressed in terms of material coordinates which are referred to the initial configuration of the domain. This implies that when the Spatial and Material reference frames are coincident (refer to section 2.1.1 for a detailed explanation on spatial and material coordinates), the mapping that transforms material into spatial coordinates at time t=0 is the identity mapping:

$$\vec{\mathbf{x}} = \phi(\mathbf{X},0) = \mathbf{I}\cdot\vec{\mathbf{X}} = \vec{\mathbf{X}} \tag{4.1}$$

At any other instant of time, the motion is described by $\vec{\mathbf{x}} = \phi(\vec{\mathbf{X}},t)$. The displacement of a material point is thus given by the difference between its current position and its original position. This is expressed as:

$$\vec{\mathbf{u}}(\vec{\mathbf{X}},t) = \phi(\vec{\mathbf{X}},t) - \phi(\vec{\mathbf{X}},0) = \phi(\vec{\mathbf{X}},t) - \vec{\mathbf{X}} = \vec{\mathbf{x}} - \vec{\mathbf{X}} \tag{4.2}$$

Usually this expression is written as:

$$\vec{\mathbf{u}} = \vec{\mathbf{x}} - \vec{\mathbf{X}} \tag{4.3}$$

or in index notation as:

$$u_i = x_i - X_i. \tag{4.4}$$

The kinematic or strain-displacement equations describe how the strains (i.e. the stretching and distortion) within a loaded body relate to displacements (Fig.4.2). If all points within the domain experience the same displacement, the body moves as a rigid entity. For deformation to occur, the points of the body must experience different displacements. An important variable in the description of body kinematics is the deformation gradient, **F**. This mathematical entity is also a key element of the total Lagrangian Hydrocode since it provides the basic ingredient in the formulation of strains.

The deformation gradient $\overline{\overline{\mathbf{F}}}$ is the Jacobian of the matrix of the motion $\phi(\vec{\mathbf{X}},t)$ and it can be expressed as follows:

$$\overline{\overline{\mathbf{F}}} = \begin{bmatrix} \frac{\partial x_1}{\partial X_1} & \frac{\partial x_1}{\partial X_2} & \frac{\partial x_1}{\partial X_3} \\ \frac{\partial x_2}{\partial X_1} & \frac{\partial x_2}{\partial X_2} & \frac{\partial x_2}{\partial X_3} \\ \frac{\partial x_3}{\partial X_1} & \frac{\partial x_3}{\partial X_2} & \frac{\partial x_3}{\partial X_3} \end{bmatrix} \tag{4.5}$$

$$\text{and} \quad J = \det\left(\overline{\overline{\mathbf{F}}}\right) \tag{4.6}$$

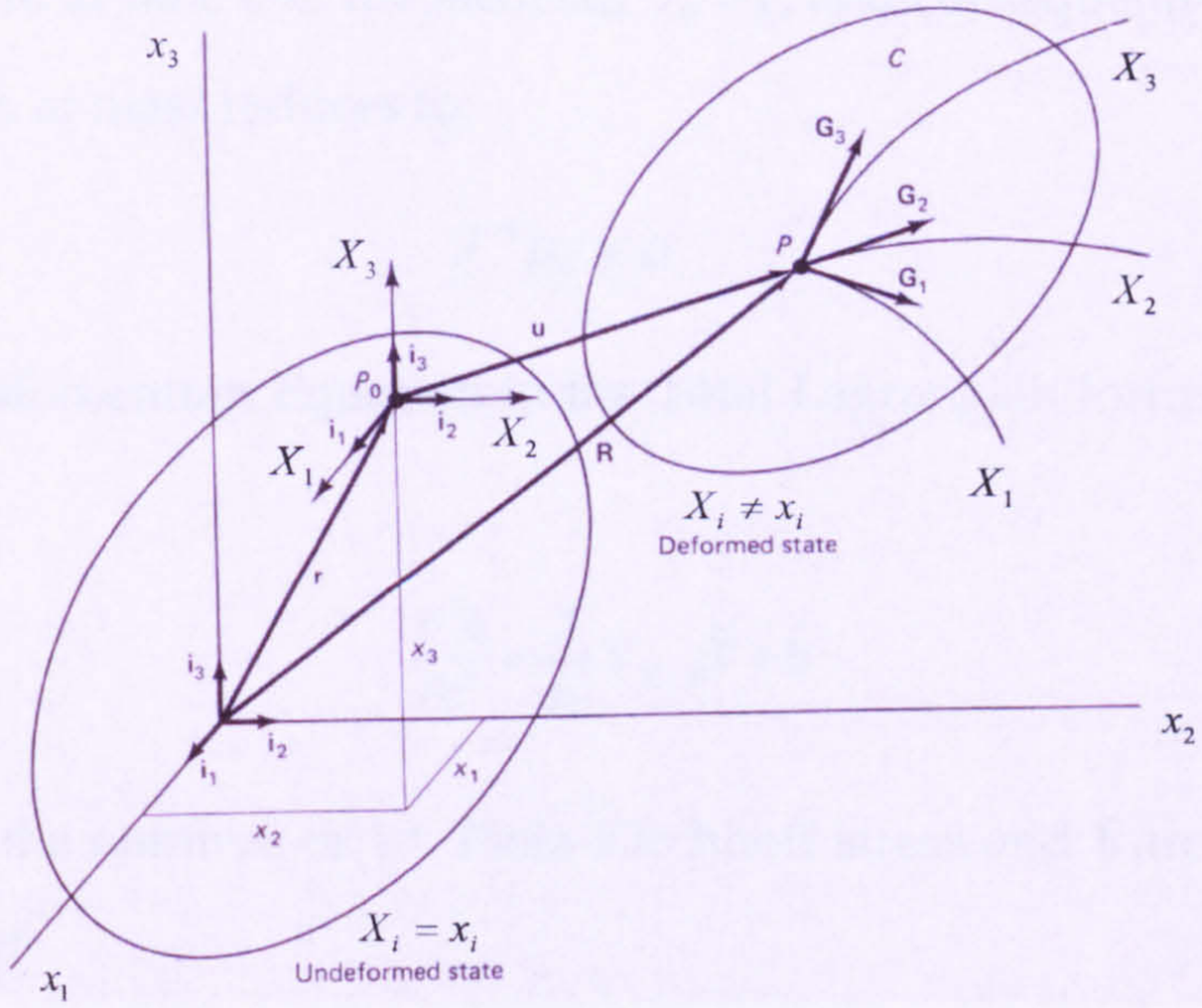

Fig. 4.2 The typical reference frames and reference and current configurations considered in the study of kinematics of deformable bodies.

It is clear from the definition above that the deformation gradient can also be related to the displacements $\vec{\mathbf{u}}$ in the following way:

$$\bar{\bar{\mathbf{F}}} = \frac{\partial \vec{\mathbf{x}}}{\partial \vec{\mathbf{X}}} = \frac{\partial\left(\vec{\mathbf{u}} + \vec{\mathbf{X}}\right)}{\partial \vec{\mathbf{X}}} \tag{4.7}$$

or in index notation:

$$F_{ij} = \frac{\partial u_i}{\partial X_j} + \delta_{ij} \tag{4.8}$$

The Jacobian J provides a key parameter for computing the updated density of a material particle. In a Total Lagrangian formulation, the conservation of mass adopts the following algebraic form [4, 60]:

$$J_0 \rho_0 = J \rho \tag{4.9}$$

In the special case where the material and the spatial reference frames are coincident at time t=0, the Jacobian $J_0 = 1$, and consequently the equation of conservation of mass reduces to:

$$J^{-1}\rho_0 = \rho \tag{4.10}$$

The Momentum Equation in the Total Lagrangian formalism is given by [4, 60]:

$$\frac{\partial^2 \vec{\mathbf{u}}}{\partial t^2} = \frac{\mathbf{1}}{\rho_0}\nabla_{\vec{\mathbf{x}}_{,0}}\bar{\bar{\mathbf{P}}} + \vec{\mathbf{b}} \tag{4.11}$$

where $\bar{\bar{\mathbf{P}}}$ is the nominal or 1st Piola-Kirchhoff stress and $\vec{\mathbf{b}}$ are the body forces per unit mass.

Finally, the conservation of energy is given by:

$$\frac{\partial e}{\partial t} = \frac{\mathbf{1}}{\rho_0}\dot{\mathbf{F}} : \bar{\bar{\mathbf{P}}} \tag{4.12}$$

where $\frac{\partial e}{\partial t}$ is the rate of change of internal energy and $\dot{\mathbf{F}}$ is the material velocity gradient.

4.1.1 Green-Lagrange Strain

In non-linear continuum mechanics there are several measures of strain. The measure of strain has to meet two necessary conditions: a) it has to yield a zero value of strain under pure rigid body motion, and b) its value has to increase as the deformation increases. The definition of Green strain (or Green-Lagrange) meets these two key conditions. In order to define the change in length in the Green-Lagrange strain tensor, the expression for the difference of the square of the length of an infinitesimal line segment *s* in the current

(deformed) configuration and the reference (undeformed) configuration S is used [19].

The statement above is expressed as [60]:

$$ds^2 - dS^2 = d\vec{\mathbf{x}}\, d\vec{\mathbf{x}} - d\vec{\mathbf{X}}\, d\vec{\mathbf{X}} = (\bar{\bar{\mathbf{F}}} d\vec{\mathbf{x}})(\bar{\bar{\mathbf{F}}} d\vec{\mathbf{x}}) - d\vec{\mathbf{X}}\, d\vec{\mathbf{X}} = d\vec{\mathbf{X}}(\bar{\bar{\mathbf{F}}}^T \bar{\bar{\mathbf{F}}} - \mathbf{I}) d\vec{\mathbf{X}}$$

Typically, the Green strain tensor is expressed in terms of displacement gradients:

$$\bar{\bar{\mathbf{E}}} = \frac{1}{2}\left((\nabla_{\vec{\mathbf{X}}} \vec{\mathbf{u}})^T + \nabla_{\vec{\mathbf{X}}} \vec{\mathbf{u}} + \nabla_{\vec{\mathbf{X}}} \vec{\mathbf{u}} (\nabla_{\vec{\mathbf{X}}} \vec{\mathbf{u}})^T \right) \tag{4.13}$$

where the nabla operator is given in terms of the material coordinates. However, it is generally more convenient to make use of the definition of gradient of deformation for computing strains. The expression for Green-Lagrange strain in terms of the gradient of deformation is as follows [60]:

$$\bar{\bar{\mathbf{E}}} = \frac{1}{2}\left(\bar{\bar{\mathbf{F}}}^T \bar{\bar{\mathbf{F}}} - \mathbf{I} \right) \tag{4.14}$$

Eq (4.14) provides the foundation upon which the Lagrangian code is built.

The conservation equations described above, together with the strain-displacement relations contain vital concepts to mechanics of materials but do not provide an insight into the behaviour of the material itself. The kinematic equations relate strains to displacement gradients and the momentum equation relates stress gradients to accelerations. However, the role of the material in the deformation process has been neglected up to this point.

When dealing with three dimensional problems, the resulting system of nine equations (six strain-displacement and three momentum) contains fifteen variables: three displacements, six strains and six stresses. Six more equations are required to close the system and these are provided by the material's constitutive relations. These are mathematical models which supply six additional expressions that relate stresses to strains.

The constitutive models employed by the SPH code developed at Cranfield University [15, 25, 34] ,MCM, are fully compatible with the constitutive models available in DYNA 3-D. Since DYNA code is written in an Eulerian form, the constitutive equations are formulated in rate form for large deformations. Stress rates are therefore given in terms of Jauman (co-rotational) rates which are frame invariant.

The strain rate required for updating stresses must be expressed in a compatible form, namely rate of deformation tensor $\bar{\bar{\mathbf{D}}}$ (also termed velocity strain). This implies that before the Green strain rate tensor can be employed to update stresses in the hydrocode, some transformations are required. First we employ the definition of velocity gradient $\bar{\bar{\mathbf{L}}}$:

$$\bar{\bar{\mathbf{L}}} = \frac{\partial \vec{\mathbf{v}}}{\partial \vec{\mathbf{x}}} = \frac{\partial \vec{\mathbf{v}}}{\partial \vec{\mathbf{X}}} \frac{\partial \vec{\mathbf{X}}}{\partial \vec{\mathbf{x}}} \tag{4.15}$$

From the definition of gradient of deformation we can rewrite $\bar{\bar{\mathbf{L}}}$ as:

$$\bar{\bar{\mathbf{L}}} = \dot{\mathbf{F}} \bar{\bar{\mathbf{F}}}^{-1} \tag{4.16}$$

By splitting the velocity gradient in its symmetric and skew-symmetric components, the rate of deformation can be written as:

$$\bar{\bar{\mathbf{D}}} = \frac{\mathbf{1}}{\mathbf{2}} \left(\bar{\bar{\mathbf{L}}} + \bar{\bar{\mathbf{L}}}^{\mathbf{T}} \right) \tag{4.17}$$

Taking the derivative with respect to time of the Green-Lagrange strain tensor yields:

$$\dot{\mathbf{E}} = \frac{\mathbf{1}}{\mathbf{2}} \left(\bar{\bar{\mathbf{F}}}^{\mathbf{T}} \dot{\mathbf{F}} + \dot{\mathbf{F}}^{\mathbf{T}} \bar{\bar{\mathbf{F}}} \right) \tag{4.18}$$

From the definition of velocity gradient in terms of the gradient of deformation we have:

$$\dot{\mathbf{F}} = \bar{\bar{\mathbf{L}}} \bar{\bar{\mathbf{F}}} \tag{4.19}$$

$$\text{and } \dot{\mathbf{F}}^{\mathrm{T}} = \bar{\bar{\mathbf{F}}}^{\mathrm{T}}\bar{\bar{\mathbf{L}}}^{\mathrm{T}} \tag{4.20}$$

From the expressions above and Green-Lagrange strain rate we obtain:

$$\bar{\bar{\mathbf{D}}} = \bar{\bar{\mathbf{F}}}^{-\mathrm{T}}\dot{\mathbf{E}}\bar{\bar{\mathbf{F}}}^{-1} \tag{4.21}$$

which is the measure of strain rate we employ to update stresses.

The stress is integrated incrementally in time:

$$\sigma_{ij}(t+dt) = \sigma_{ij}(t) + \dot{\sigma}_{ij}dt = \sigma_{ij}(t) + (\sigma_{ij}^{\nabla} + \sigma_{ik}R_{kj} + \sigma_{jk}R_{ki})dt \tag{4.22}$$

where the dot denotes the material derivative, R is the spin tensor and $\sigma_{ij}^{\nabla} = C_{ijkl}D_{kl}$ is the Jaumann stress rate.

To integrate the conservation of momentum equation, Cauchy stress is transformed into Nominal stress using the following transformation:

$$\bar{\bar{\mathbf{P}}} = \left(J\bar{\bar{\mathbf{F}}}^{-1}\bar{\bar{\boldsymbol{\sigma}}}\right) \tag{4.23}$$

Eq. (4.23) is used to calculate the accelerations of a particle in the conservation of momentum equation (4.11).

4.2 SPH Discretisation of the Total Lagrangian Conservation Laws.

In order to update the density in the conservation of mass equation, the value of the Jacobian J is required at every time step in the integration process. The Jacobian is obtained from the determinant of the gradient of deformation tensor $\mathbf{F}$ which is in turn calculated using expression (4.7). The discretisation of $\mathbf{F}$ is achieved by applying the rules supplied in Chapter 2 for discretising the tensor product of a gradient operator and a vector field. The resulting expression is as follows:

$$\left\langle \bar{\bar{\mathbf{F}}}_I \right\rangle = -\sum_{J \in S} (\vec{\mathbf{u}}_J - \vec{\mathbf{u}}_I) \otimes \nabla_{\vec{\mathbf{x}}_J} \mathrm{W}\left(\vec{\mathbf{X}}_I - \vec{\mathbf{X}}_J, h_0\right) \mathbf{V}_J^0 + \mathbf{I} \tag{4.24}$$

Note that the smoothing function W and the differential operator $\nabla_{\vec{\mathbf{x}}_J}$ are given in terms of the material coordinates at the reference configuration and $\mathbf{V}_J^0$ is the initial volume of particle J (i.e. the volume of the particle calculated with the intial density and the mass of the particle in the reference state when time $t=0$).

The Total Lagrangian Conservation of Momentum equation can be discretised using the approximation for a dot product of a gradient operator and a second order tensor. The resulting expression, ignoring body forces, is as follows:

$$\left\langle \vec{\mathbf{a}}_I \right\rangle = -\sum_{J \in S} \left(\bar{\bar{\mathbf{P}}}_J - \bar{\bar{\mathbf{P}}}_I \right) \otimes \nabla_{\vec{\mathbf{x}}_J} \mathrm{W}\left(\vec{\mathbf{X}}_I - \vec{\mathbf{X}}_J, h_0\right) \mathbf{V}_J^0 \tag{4.25}$$

Alternatively, the SPH Momentum Equation can be obtained considering the approximation of $\frac{\nabla A}{\rho} = \nabla\left(\frac{A}{\rho}\right) + \frac{A}{\rho^2}\nabla\rho$ as supplied in Chapter 2, where A is a second order tensor. The resulting expression has the following form:

$$\left\langle \vec{\mathbf{a}}_I \right\rangle = -\sum_{J \in S} \left(\frac{\bar{\bar{\mathbf{P}}}_J}{\rho_J^2} + \frac{\bar{\bar{\mathbf{P}}}_I}{\rho_I^2} \right) m_J \cdot \nabla_{\vec{\mathbf{x}}_J} \mathrm{W}\left(\vec{\mathbf{X}}_I - \vec{\mathbf{X}}_J, h_0\right) \tag{4.26}$$

The velocity gradient used in the conservation of energy equation can be calculated using the SPH approximation for the tensor product of a gradient operator and a vector field:

$$\left\langle \dot{\bar{\mathbf{F}}}_I \right\rangle = -\sum_{J \in S} (\vec{\mathbf{v}}_J - \vec{\mathbf{v}}_I) \otimes \nabla_{\vec{\mathbf{x}}_J} \mathrm{W}\left(\vec{\mathbf{X}}_I - \vec{\mathbf{X}}_J, h_0\right) \mathbf{V}_J^0 \tag{4.27}$$

Following the procedure outlined in Chapter 2, the following expression for the conservation of energy can be obtained:

$$\langle \dot{e}_I \rangle = -\frac{\bar{\bar{\mathbf{P}}}_I}{\rho_I^2} : \sum_{J \in S} m_J \left(\vec{\mathbf{v}}_J - \vec{\mathbf{v}}_I \right) \otimes \nabla_{\vec{\mathbf{X}}_J} \mathrm{W}\left(\vec{\mathbf{X}}_I - \vec{\mathbf{X}}_J, h_0 \right) \mathbf{v}_J^0 \tag{4.28}$$

4.3 Normalised, Corrected and Normalised-Corrected SPH

The recent improvements of the conventional SPH method which have given the method first order consistency [9,46] have been achieved by modifying the properties of the kernel function itself [56,57] or by introducing some corrections to the interpolation integral [9,83]. In this section we refer to three methods termed normalisation, correction, and normalisation and correction. These terms are used interchangeably in literature but we adhere to the following convention: normalisation refers to the improvement which gives zero order consistency to the interpolation method while correction refers to the improvement of the approximation of the gradient and gives the interpolation scheme first order consistency. The term normalised-corrected refers to the corrected gradient approximation combined with normalised smoothing function.

The conditions for zero order completeness (i.e. the exact reproducibility of a constant field) for an approximation using Lagrangian kernels are:

$$\sum_{J \in S} \phi_J \left(\vec{\mathbf{X}} \right) = 1 \tag{4.29}$$

$$\sum_{J \in S} \nabla_0 \phi_J \left(\vec{\mathbf{X}} \right) = 0 \tag{4.30}$$

where $\vec{\mathbf{X}}$ are material coordinates, ∇_0 is the differential operator in terms of material coordinates and $\phi_J \left(\vec{\mathbf{X}} \right) = \mathrm{W}\left(\vec{\mathbf{X}}_I - \vec{\mathbf{X}}_J, h_0 \right) V_J$ is the shape function.

It is therefore evident that the ordinary SPH method yields zero-order completeness when applied to interior particles since the integration of W over the entire domain is unity (with its associated truncation error as explained in

Chapter 2). The second property is fulfilled due to the symmetric nature of the interpolating function (Fig.4.3). However for boundary particles, the constant reproducing conditions are violated even for uniformly spaced particles (Fig.4.4).

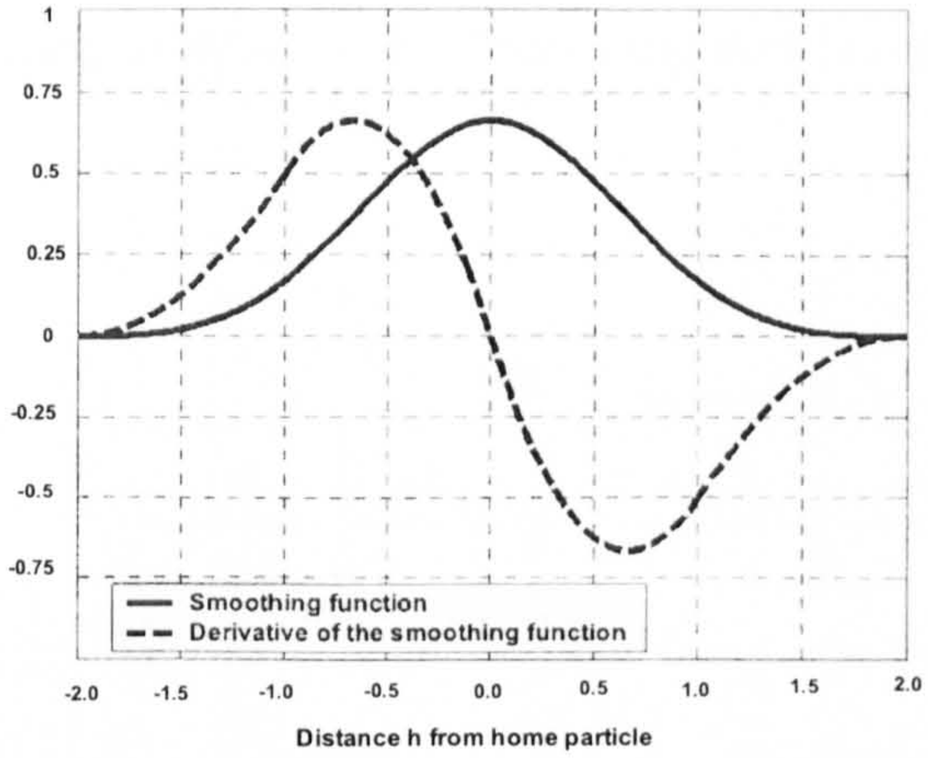

Fig.4.3 Typical smoothing function and its derivative for a complete set of interpolating particles.

This results from the truncation of the smoothing function by the boundary due to the unbalanced particle contribution in the discretised summation (Fig. 4.4). Some procedures have been developed for restoring consistency; [54] gives a general approach to restore consistency based on Taylor series expansions. Other methods like the reproducing particle kernel (RPKM) were developed even earlier [56].

The conditions for 1st order completeness in $\Re^3$ are as follows:

$$\sum_{J \in S} \mathrm{W}(X^{\alpha}{}_{I} - X^{\alpha}{}_{J}, h_0) \frac{m_J}{\rho_J} X^{\alpha}{}_{J} = X^{\alpha} \tag{4.31}$$

where X^{α} ($\alpha = 1, 2 \text{ or } 3$ dimensions) are the material co-ordinates in a Cartesian co-ordinate system. Expression 4.31 above provides the smoothed approximation of a linear field Refer to expression 4.37 and 4.38 in this chapter for a more detailed explanation.

Later on, it will be described how 1st order completeness (e.g. the reproducibility of a linear field) can be introduced in SPH and some examples will be given in Chapter 6 to prove that the correction works well. Suffice to say at this stage that the method implemented in the MCM hydrocode relies on normalisation of the kernel, symmetrisation and correction of the derivatives. This will be described in detail in the following section of this dissertation.

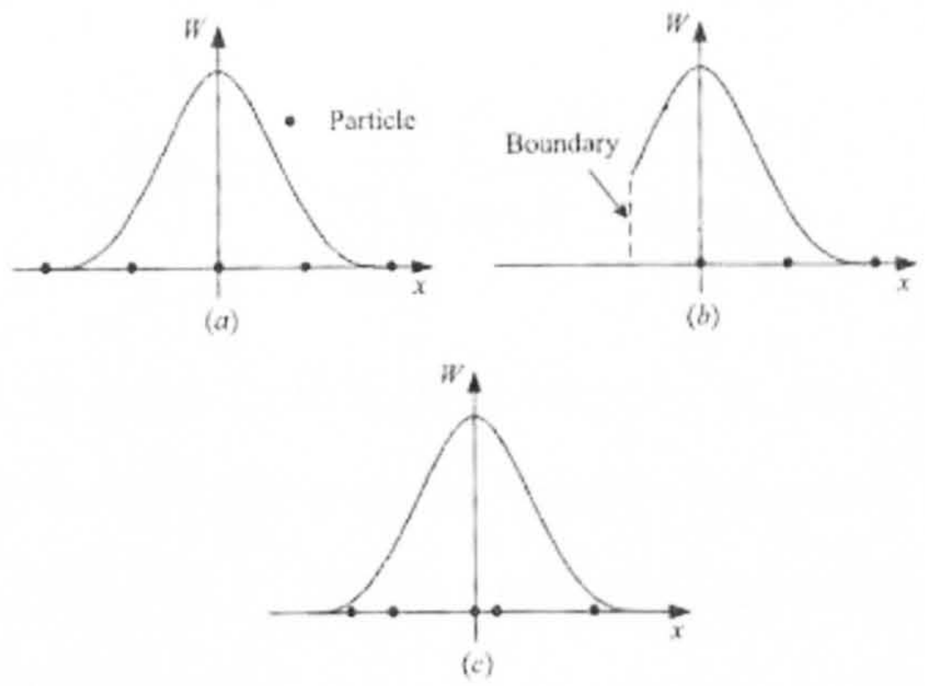

Fig.4.4 a) interior particle , b)boundary particle and c)non uniform particle arrangement.

4.3.1 Kernel Normalisation.

Normalisation or kernel correction is aimed at restoring the boundary particle inconsistency resulting from the truncation of the interpolation function at the boundaries (Fig.4.4). One of the first attempts at SPH normalisation was carried out by Johnson et. al. [45, 46]. Their approach consists of adjusting the standard smoothing functions for every node such that the normal strain rates are computed exactly for conditions of constant strain rates, i.e. this correction allows a constant strain rate to be approximated when a linear velocity distribution in the particle domain is imposed. Their algorithm generally improves the accuracy for non-uniform strain rates as well. The normalisation of the smoothing function ensures that:

$$\sum_{J\in S}\phi_J\left(\vec{\mathbf{X}}\right)=1 \tag{4.32}$$

$$\text{with } \phi_J\left(\vec{\mathbf{X}}\right)=\mathrm{W}\left(\vec{\mathbf{X}}_I-\vec{\mathbf{X}}_J,h_0\right)V_J \tag{4.33}$$

over the entire domain.

The normalised smoothing function which correctly reproduces a constant field is known as the Shepard function and is given by:

$$\tilde{\mathrm{W}}\left(\vec{\mathbf{X}}_I-\vec{\mathbf{X}}_J,h_0\right)=\frac{\mathrm{W}\left(\vec{\mathbf{X}}_I-\vec{\mathbf{X}}_J,h_0\right)}{\sum_{J\in S}\frac{m_J}{\rho_J}\mathrm{W}\left(\vec{\mathbf{X}}_I-\vec{\mathbf{X}}_J,h_0\right)} \tag{4.34}$$

Equation (4.34) is zero order consistent. It can be viewed as the particular case of the general approach to ensure first order consistency in the SPH approximations [45, 70]. In the general approach, the normalised smoothing function is given by:

$$\tilde{\mathrm{W}}\left(\vec{\mathbf{X}}_I-\vec{\mathbf{X}}_J,h_0\right)=\mathrm{W}\left(\vec{\mathbf{X}}_I-\vec{\mathbf{X}}_J,h_0\right)\alpha\left(\vec{\mathbf{X}}_I\right)\left[1+\beta\left(\vec{\mathbf{X}}_I\right).\left(\vec{\mathbf{X}}_I-\vec{\mathbf{X}}_J\right)\right] \tag{4.35}$$

hence, functions are now approximated as:

$$\left\langle\psi\left(\vec{\mathbf{X}}_I\right)\right\rangle=\sum_{J\in S}\psi\left(\vec{\mathbf{X}}_J\right)\frac{m_J}{\rho_J}\tilde{\mathrm{W}}\left(\vec{\mathbf{X}}_I-\vec{\mathbf{X}}_J,h_0\right) \tag{4.36}$$

The α and β parameters in Eq (4.35) are the correction factors which are calculated to make $\tilde{\mathrm{W}}\left(\vec{\mathbf{X}}_I-\vec{\mathbf{X}}_J,h_0\right)$ first order consistent. Using $\tilde{\mathrm{W}}\left(\vec{\mathbf{X}}_I-\vec{\mathbf{X}}_J,h_0\right)$, a linear function of the form $c_0+c_1\vec{\mathbf{X}}'=\psi\left(\vec{\mathbf{X}}'\right)$ can be approximated as:

$$\psi\left(\vec{\mathbf{X}}\right)=\int_{\Omega}\left(c_0+c_1\vec{\mathbf{X}}'\right)\tilde{\mathrm{W}}\left(\vec{\mathbf{X}}-\vec{\mathbf{X}}',h_0\right)d\Omega=c_0+c_1\vec{\mathbf{X}} \tag{4.37}$$

This equation can be simplified as:

$$\int_{\Omega}\vec{\mathbf{X}}'\tilde{\mathrm{W}}\left(\vec{\mathbf{X}}-\vec{\mathbf{X}}',h_0\right)d\Omega=\vec{\mathbf{X}} \tag{4.38}$$

Equally, the following must be true to satisfy the kernel normality condition:

$$\int_{\Omega}\tilde{W}\left(\vec{X}-\vec{X}',h_0\right)d\Omega=1 \tag{4.39}$$

Multiplying both sides of Eq. (4.39) by $\vec{X}$ yields:

$$\int_{\Omega}\vec{X}\tilde{W}\left(\vec{X}-\vec{X}',h_0\right)d\Omega=\vec{X} \tag{4.40}$$

By subtracting Eq. (4.38) from Eq. (4.40) one obtains:

$$\int_{\Omega}\left(\vec{X}-\vec{X}'\right)\tilde{W}\left(\vec{X}-\vec{X}',h_0\right)d\Omega=0 \tag{4.41}$$

which can be approximated as a weighted sum:

$$\sum_{J\in S}\frac{m_J}{\rho_J}\left(\vec{X}_I-\vec{X}_J\right)\tilde{W}\left(\vec{X}_I-\vec{X}_J,h_0\right)=0 \tag{4.42}$$

By substituting the expression for corrected kernel (Eq. 4.35) into the expression above, $\beta(x)$ can be defined as (in discrete form):

$$\beta\left(\vec{X}_I\right)=\left[\sum_{J\in S}\frac{m_J}{\rho_J}\left(\vec{X}_I-\vec{X}_J\right)\otimes\left(\vec{X}_I-\vec{X}_J\right)W\left(\vec{X}_I-\vec{X}_J,h_0\right)\right]^{-1}\sum_{J\in S}\frac{m_J}{\rho_J}W\left(\vec{X}_I-\vec{X}_J,h_0\right) \tag{4.43}$$

Similarly, once $\beta\left(\vec{X}_I\right)$ has been defined, $\alpha\left(\vec{X}_I\right)$ can be determined by substitution of Eq. (4.43) into Eq. (4.35) and use of the kernel normality condition, i.e:

$$\sum_{J\in S}\frac{m_J}{\rho_J}\tilde{W}\left(\vec{X}_I-\vec{X}_J,h_0\right)=1 \tag{4.44}.$$

The resulting expression for α is:

$$\alpha\left(\vec{X}_I\right)=\frac{1}{\sum_{J\in S}\frac{m_J}{\rho_J}W\left(\vec{X}_I-\vec{X}_J,h_0\right)\left[1+\beta\left(\vec{X}_I\right)\left(\vec{X}_I-\vec{X}_J\right)\right]} \tag{4.45}$$

It is clear that to achieve zero order consistency of the smoothing

function rather than first order consistency, it is sufficient to set the value of $\beta\left(\vec{\mathbf{X}}_I\right)$ to zero, which leads to $\tilde{\mathrm{W}}\left(\vec{\mathbf{X}}_I-\vec{\mathbf{X}}_J,h_0\right)=\dfrac{\mathrm{W}\left(\vec{\mathbf{X}}_I-\vec{\mathbf{X}}_J,h_0\right)}{\sum_{J\in S}\frac{m_J}{\rho_J}\mathrm{W}\left(\vec{\mathbf{X}}_I-\vec{\mathbf{X}}_J,h_0\right)}$, i.e. Shepard functions.

4.3.2 Correction of derivatives.

A simple correction technique involves modification of the kernel gradient by introducing a correction matrix denoted by **L** [9] or **B** [75] in literature. These corrections are aimed at restoring 1st order consistency.

There are several ways in which this correction can be obtained, two derivations are presented here.

First let us start by considering a function $\psi(x')$ in a 1-D space which is assumed to be sufficiently smooth in the domain that contains x. Performing the Taylor series expansion for $\psi(x')$ in the vicinity of x yields:

$$\psi(x')=\psi(x')\big|_{x'=x}+(x'-x)\left.\frac{\partial\psi(x')}{\partial x'}\right|_{x'=x}+\frac{(x'-x)^2}{2}\left.\frac{\partial^2\psi(x')}{\partial x'^2}\right|_{x'=x}+\ldots \tag{4.46}$$

Multiplying both sides of the equation by a smoothing function W and integrating over the sub-domain S:

$$\int_S\psi(x')\mathrm{W}(x')dx'=\psi(x')\big|_{x'=x}\int_S\mathrm{W}(x-x',h)dx'+\left.\frac{\partial\psi(x')}{\partial x'}\right|_{x'=x}\int_S(x'-x)\mathrm{W}(x-x',h)dx'+$$
$$+\left.\frac{\partial^2\psi(x')}{\partial x'^2}\right|_{x'=x}\int_S\frac{(x'-x)^2}{2}\mathrm{W}(x-x',h)dx'+\ldots \tag{4.47}$$

In order to approximate the derivative of the function ψ rather than the

function ψ itself, the function W can be replaced by the derivative of the function W in the above expression as follows:

$$\int_S \psi(x')\frac{\partial W(x-x',h)}{\partial x'}dx' = \psi(x')\Big|_{x'=x}\int_S \frac{\partial W(x-x',h)}{\partial x'}dx' + \frac{\partial \psi(x')}{\partial x'}\Big|_{x'=x}\int_S (x'-x)\frac{\partial W(x-x',h)}{\partial x'}dx' + \frac{\partial^2 \psi(x')}{\partial x'^2}\Big|_{x'=x}\int_S \frac{(x'-x)^2}{2}\frac{\partial W(x-x',h)}{\partial x'}dx' + \ldots \quad (4.48)$$

from where the corrected expression for the first derivative, neglecting higher order terms, is given by:

$$\frac{\partial \psi(x)}{\partial x'} = \frac{\int_S (\psi(x')-\psi(x))\frac{\partial W(x-x',h)}{\partial x'}dx'}{\int_S (x'-x)\frac{\partial W(x-x',h)}{\partial x'}dx'} \quad (4.49)$$

A discrete form of the expression above is given by:

$$\left\langle \frac{\partial \psi(x_I)}{\partial x'} \right\rangle = \frac{\sum_{J\in S}\frac{m_J}{\rho_J}(\psi_J-\psi_I)\frac{\partial W_{IJ}}{\partial x'}}{\sum_{J\in S}\frac{m_J}{\rho_J}(x_J-x_I)\frac{\partial W_{IJ}}{\partial x'}} \quad (4.50)$$

where $W_{IJ} = W(x_I - x_J, h)$.

Eq. (4.50) is the discretised expression for the gradient correction of a function $\psi(x')$. The numerator is the kernel approximation for the first derivative of a function and the denominator acts as the correction factor. It is easy to extend the procedure to 2-D and 3-D.

From the above expression it is not entirely clear how the 1st order consistency of the method gets restored. An alternative approach to derivation of the correction of the derivatives may provide additional insight. To this end one can consider approximation of a linear function based on SPH framework.

Let us consider a linear velocity field in 1-D defined as:

$$v = \mathrm{a} + \mathrm{b}x' \tag{4.51}$$

where a and b are constants. The approximation of the gradient of velocity L based on corrected SPH is:

$$L = \frac{\partial v}{\partial x'} = \left(-\sum_{J \in S} \frac{m_J}{\rho_J} (v_J - v_I) \frac{\partial \mathrm{W}_{IJ}}{\partial x'_J} . B \right) \tag{4.52}$$

By substituting (4.51) into the LHS of (4.52) and into v_J and v_I, B can be readily obtained as:

$$B = \left(-\sum_{J \in S} \frac{m_J}{\rho_J} (x_J - x_I) \nabla_J \mathrm{W}_{IJ} \right)^{-1} \tag{4.53}$$

Correction factor B is equivalent to the expression in the denominator in Eq. (4.50). The above derivation has been extended to 3-D by Randles and Libersky (1996) [75]. The tensor form of the correction can be written as follows:

$$\mathbf{B} = \left(-\sum_{J \in S} \frac{m_J}{\rho_J} (\vec{\mathbf{x}}_J - \vec{\mathbf{x}}_I) \otimes \nabla_J \mathrm{W}_{IJ} \right)^{-1} \tag{4.54}$$

or in index notation:

$$\mathrm{B}_{\alpha\beta} = \left(-\sum_{J \in S} \frac{m_J}{\rho_J} \left(x^{\alpha}{}_J - x^{\alpha}{}_I \right) \frac{\partial \mathrm{W}_{IJ}}{\partial x_J{}^{\beta}} \right)^{-1} \tag{4.55}$$

4.4 Normalised-Corrected Total Lagrangian SPH Interpolation.

In the Total Lagrangian formalism the neighbourhood of particle I remains fixed throughout the simulation. The interpolation correction used in this formalism is a direct extension of the correction methods developed for the ordinary SPH equations presented in the previous section [82].

In the Total Lagrangian formulation the smoothing function is given in terms of the material co-ordinates $\vec{\mathbf{X}}$. Therefore the normalised kernel can be expressed as follows:

$$\tilde{\mathrm{W}}\left(\vec{\mathbf{X}}_I - \vec{\mathbf{X}}_J, h_0\right) = \frac{\mathrm{W}\left(\vec{\mathbf{X}}_I - \vec{\mathbf{X}}_J, h_0\right)}{\sum_{J \in S} \frac{m_J}{\rho_J} \mathrm{W}\left(\vec{\mathbf{X}}_I - \vec{\mathbf{X}}_J, h_0\right)} \tag{4.56}$$

Since the denominator of the above expression remains constant, the derivative of the normalised kernel can be evaluated as:

$$\nabla \tilde{\mathrm{W}}\left(\vec{\mathbf{X}}_I - \vec{\mathbf{X}}_J, h_0\right) = \frac{1}{C} \nabla \mathrm{W}\left(\vec{\mathbf{X}}_I - \vec{\mathbf{X}}_J, h_0\right) \tag{4.57}$$

$$\text{where} \quad C = \sum_{J \in S} \frac{m_J}{\rho_J} \mathrm{W}\left(\vec{\mathbf{X}}_I - \vec{\mathbf{X}}_J, h_0\right) \tag{4.58}$$

The expression for the gradient correction term is given by:

$$\mathbf{B} = \left(-\sum_{J \in S} \frac{m_J}{\rho_J} \left(\vec{\mathbf{X}}_J - \vec{\mathbf{X}}_I\right) \otimes \nabla_{\vec{\mathbf{X}}_J} \tilde{\mathrm{W}}\left(\vec{\mathbf{X}}_I - \vec{\mathbf{X}}_J, h_0\right) \right)^{-1} \tag{4.59}$$

The gradient correction **B** operates over the gradient of the smoothing function. Hence, the final expression for the corrected gradient of deformation, in a Total Lagrangian framework is:

$$\left\langle \bar{\bar{\mathbf{F}}}_I \right\rangle = \left(-\sum_{J \in S} \left(\vec{\mathbf{u}}_J - \vec{\mathbf{u}}_I\right) \otimes \nabla_{\vec{\mathbf{X}}_J} \tilde{\mathrm{W}}_{IJ} \mathbf{V}_J^0 \right) \mathbf{B} + \mathbf{I} \tag{4.60}$$

The corrected momentum equation is:

$$\left\langle \vec{\mathbf{a}}_I \right\rangle = \left(-\sum_{J \in S} \left(\mathbf{P}_J - \mathbf{P}_I\right) \otimes \nabla_{\vec{\mathbf{X}}_J} \tilde{\mathrm{W}}_{IJ} \mathbf{V}_J^0 \right) : \mathbf{B} \tag{4.61}$$

and the corrected conservation of energy equation is expressed as:

$$\left\langle \dot{e}_I \right\rangle = \mathbf{P}_J : \left[\left(-\sum_{J \in S} \frac{m_J}{\rho_I \rho_J} \left(\vec{\mathbf{v}}_J - \vec{\mathbf{v}}_I\right) \otimes \nabla_{\vec{\mathbf{X}}_J} \tilde{\mathrm{W}}_{IJ} \mathbf{V}_J^0 \right) \mathbf{B} \right] \tag{4.62}$$

The Total Lagrangian corrected equations are much simpler for numerical implementation than their Eulerian corrected SPH counterparts. Some numerical examples are supplied in Chapter 6 as a means of comparison with the Eulerian SPH code and with the Total Lagrangian SPH algorithms.

Summary.

The significance of a robust and stable numerical tool for the study of dynamic events in solids has been emphasised. The fundamental aspects of continuum mechanics that permit the total Lagrangian description of continuum media have been considered. The resulting equations in strong form have been discretised using the approach outlined in Chapter 2. Deficiencies such as particle incompleteness and zero and first order consistency have been considered and corrections have been introduced into the Total Lagrangian SPH equations, eliminating such shortcomings. The derivations presented in this chapter provide the foundation of the MCM Total Lagrangian SPH code.

PAGE NUMBERING AS ORIGINAL

CHAPTER 5

TOTAL LAGRANGIAN SPH ALGORITHMS AND THEIR IMPLEMENTATION USING FORTRAN

With the advent of powerful computing capabilities and the continuing development of robust numerical schemes, complex physics can be simulated accurately in a cost-effective manner. In many cases, computer simulations provide a complement to physical testing [85] and under some extreme scenarios they are the only means available to predict the behaviour of dynamic systems [76] through virtual test environments. Whatever their intended purpose, numerical computations provide insightful information into the physics of a given problem. More specifically, when these methods are used in the simulation of deformable media, they yield invaluable data that result in an improved understanding of the dynamic deformation processes of materials.

The computer codes employed to carry out the simulation of dynamic events in solids are commonly referred to as hydrocodes. These are numerical solvers which incorporate strain, strain rate, temperature dependency and failure for the characterisation of material behaviour.

The basic components of these codes are:

1.-Conservation equations: Mass, Momentum and Energy.

2.-Constitutive equations: These equations describe the material behaviour in elastic, plastic and shock regimes. They link stress with strain, strain rate and often temperature. These relations are based on experiments and vary from purely phenomenological (i.e. based purely on experiments) to microstructurally based predictions which rely on a physical understanding of underlying principles. Some examples of constitutive models that describe the elasto-plastic regime are: Johnson-Cook, Zerilli-Armstrong, MTS.

For shock response an equation of state is used to calculate the spherical part of the stress tensor. Commonly employed equations of state are Mie-Gruneisen, Gamma law, Tillotson [61] etc.

3.- Damage models: these models usually describe the evolution of damage due to shear, tension and compression. A number of formulations are currently in use, the most common are: void growth, DFRACT, Cochran-Banner, Johnson-Cook model with damage, etc [42, 61].

The basic inputs required in any hydrocode are the initial values for all variables at all positions at the initial time (i.e. initial conditions) and the boundary values for all variables at the boundary positions at all times (Fig. 5.1, page 81). The task of our solver is to calculate this information at all positions throughout the response time of interest.

The complexity of the numerical code depends on the type of application they are intended for. For example, plane shock wave propagation problems are treated in one-dimensional codes (for instance, spallation), axisymmetric

problems such as normal impact of cylinders, rods, spheres etc. are successfully computed with two-dimensional codes, whereas the more complex problems such as incline impact require three-dimensional codes.

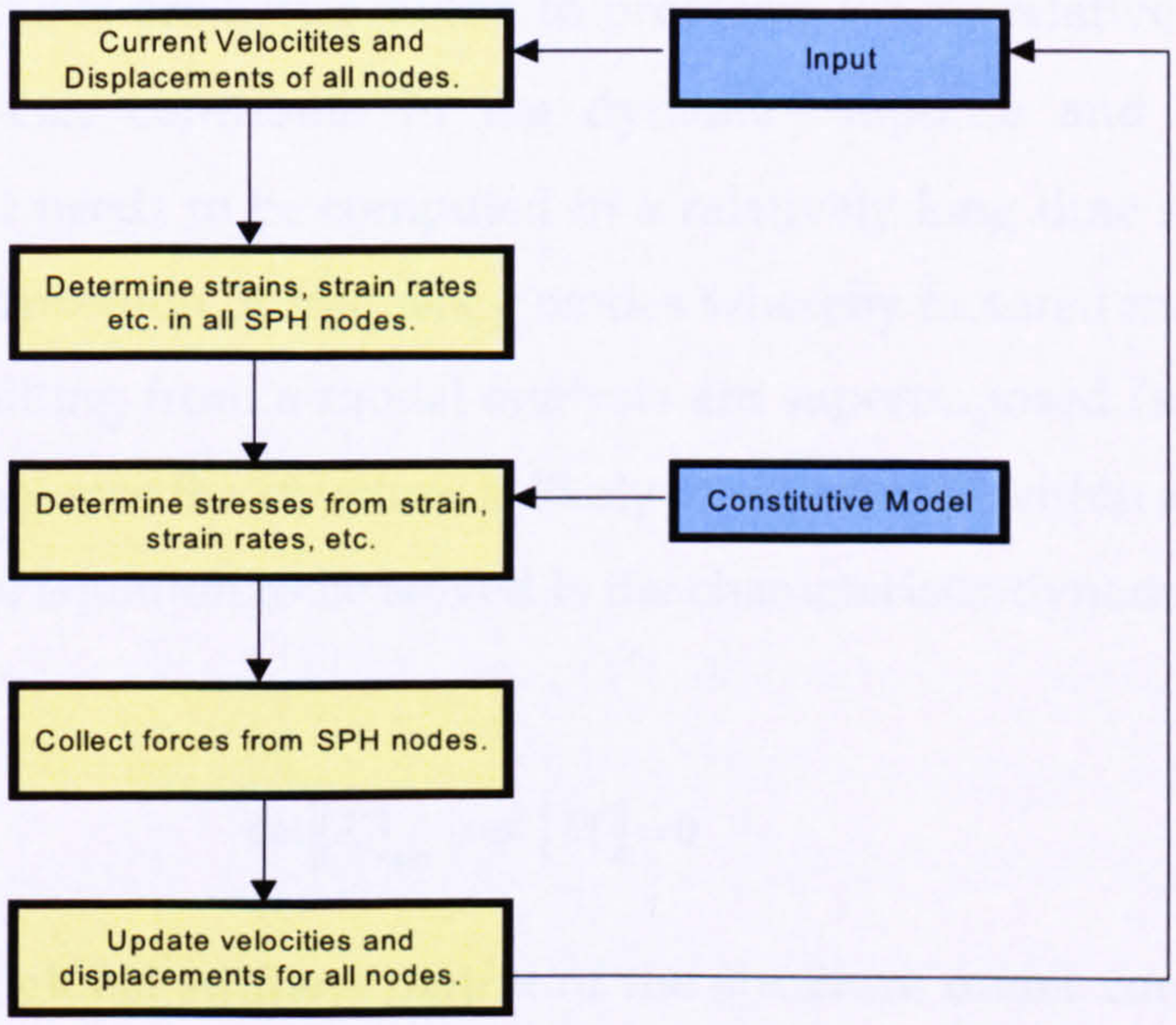

Fig.5.1 Basic steps within a time integration loop.

5.1 The MCM SPH Code.

In the characterisation of solids under dynamic loading conditions, a transient analysis is required in order to reach the solution. A transient problem can be solved in the time domain where the numerical solutions of the governing equations are obtained as a function of time, or in the frequency domain where the solution is worked out by splitting the problem into components of frequency, which is an approach not generally used in the solution of impact problems.

Within the scope of time domain solutions, there exist modal superposition methods and direct integration methods. The choice depends on whether the problem under consideration is wave propagation or structural dynamic in nature and the time span of interest. For example, modal superposition methods are better suited to problems where relatively few and only low frequencies contribute in the dynamic response and where the solution of interest needs to be computed in a relatively long time span. They are based on superposition of frequency modes whereby factored mode shapes (eigenvectors) resulting from a modal analysis are superimposed (summed) to characterise the response the structure is likely to experience within a frequency range. The general equation to be solved is the characteristic dynamic equation of the system [3]:

$$\det\left|[K]_{glo} - \omega^2 [M]\right| = 0 \tag{5.1}$$

where $[K]_{glo}$ is the global stiffness matrix of the structure under consideration, $[M]$ is the mass matrix of the system and ω is the angular frequency.

In contrast, if the structural excitation is governed by high frequencies such as those resulting from an explosive blast or impact, then the analysis is categorised as a wave propagation problem. In this type of problem the propagation of waves is of interest and the response is integrated over relatively short timespans. This is the domain of interest of hydrocodes such as SPH-MCM. Within the direct integration methods two techniques are commonly employed: Implicit integration schemes and explicit schemes.

Implicit integration schemes assume a constant average acceleration over each time step, between t_n and t_{n+1}. The value t_n is time at the beginning of each time step and the value t_{n+1} is the time at the end of that time step. The governing equation is evaluated and the resulting accelerations and velocities at t_{n+1} are calculated. Then the unknown displacements at t_{n+1} are determined.

Explicit integration schemes assume a linear change in displacement over each time step.

The major difference between the two techniques is that whereas the implicit solution method requires a matrix inversion of the structural stiffness matrix, the explicit solution does not. However, unlike the implicit solution scheme, which is unconditionally stable for large time steps, the explicit scheme is stable only if the time step size is smaller than the critical time step size for the structure being simulated. The SPH software uses the Courant-Friederichs-Levy condition to calculate the smallest time step that will allow the code to behave in a stable manner [35].

In summary, the Total Lagrangian SPH-MCM hydrocode is an explicit code for the numerical solution of the intial-boundary value problems defined by the partial differential equations which describe the conservation laws of mass, momentum and energy plus constitutive relations that characterise material behaviour.

5.2 Total Lagrangian SPH Algorithms.

Three algorithms are presented here for the integration of the conservation laws in a total Lagrangian framework. They form the foundation of the FORTRAN 90 subroutines implemented in the MCM Cranfield SPH code. These algorithms are presented in flow chart format in figure 5.2 (Pages 95-98), which provides the graphic sequential execution of the MCM code.

The first algorithm is fully Lagrangian and therefore requires the computation of the Green-Lagrange strain tensor for the integration of the constitutive model. The stress tensor resulting out of our constitutive model is the 2nd Piola-Kirchhoff stress tensor. This tensor has to be converted into Nominal Stress which is in turn introduced into the momentum equation for the computation of the acceleration of particle *I*.

The second algorithm introduces a minor modification whereby the rate of the Green-Lagrange strain tensor is used to compute the Rate of Deformation tensor **D**. The Rate of Deformation tensor is introduced in the existing constitutive model to obtain the full Cauchy (or true) stress tensor. Subsequently, some transformations have to be carried out to convert the true stress into Nominal Stress.

Finally, the third algorithm introduces normalisation and correction terms into the SPH equations.

These three procedures are better illustrated by the algorithms in the following section.

5.2.1 Algorithm 1: Total Lagrangian formulation algorithm.

Variables known at time step n:

$$x^n, v^{n-1/2}, a^{n-1}, \Delta t^n, \Delta t^{n+1}, \rho^n, P^{n-1}, u^n$$

1) Calculate the derivative of the kernel with respect to the material co-ordinates at time step n (this is done only once and the result stored).

2) Obtain displacement u of particle I at time step *n-1/2*. These have to be calculated for every component (x_1, x_2, x_3) of the displacement vector $\vec{\mathbf{u}}$:

$$\vec{\mathbf{u}}^{n-1/2} = \vec{\mathbf{u}}^n - \frac{1}{2}\vec{\mathbf{v}}^{n-1/2}\Delta t^n \tag{5.2}$$

3) Calculate deformation gradient at particle I at time step *n-1/2* [73]:

$$\left\langle \vec{\vec{\mathbf{F}}}_I^{n-1/2} \right\rangle = -\sum_{J \in S} \left(\vec{\mathbf{u}}_J^{n-1/2} - \vec{\mathbf{u}}_I^{n-1/2} \right) \otimes \nabla_{\vec{\mathbf{X}}_J} \mathrm{W}\left(\vec{\mathbf{X}}_I - \vec{\mathbf{X}}_J, h_0 \right) \mathbf{V}_J^0 + \mathbf{I} \tag{5.3}$$

Or in index notation:

$$F_{\alpha\beta}^{n-1/2}(X_I) = -\sum_J \left(u_{\alpha,J}^{n-1/2} - u_{\alpha,I}^{n-1/2} \right) \mathrm{V}_J^0 \frac{\partial \mathrm{W}(X_I - X_J, h)}{\partial X_J^\beta} + \delta_{\alpha\beta} \tag{5.4}$$

4) Calculate velocity gradient at time step *n-1/2* , this is calculated with respect to the initial co-ordinates $\vec{\mathbf{X}}$, $\dot{\mathbf{F}} = \dot{\overline{\overline{\mathbf{L}}}}\overline{\overline{\mathbf{F}}}$, $\dot{\mathbf{F}} = \frac{\partial \vec{\mathbf{v}}}{\partial \vec{\mathbf{x}}}\frac{\partial \vec{\mathbf{x}}}{\partial \vec{\mathbf{X}}} = \frac{\partial \vec{\mathbf{v}}}{\partial \vec{\mathbf{X}}}$:

$$\left\langle \dot{\mathbf{F}}_I^{n-1/2} \right\rangle = -\sum_{J \in S} \left(\vec{\mathbf{v}}_J^{n-1/2} - \vec{\mathbf{v}}_I^{n-1/2} \right) \otimes \nabla_{\vec{\mathbf{X}}_J} \mathrm{W}\left(\vec{\mathbf{X}}_I - \vec{\mathbf{X}}_J, h_0 \right) \mathbf{V}_J^0 \tag{5.5}$$

Or in index notation:

$$\dot{F}_{\alpha\beta}^{n-1/2}(X_I) = -\sum_J \left(v_{\alpha,J}^{n-1/2} - v_{\alpha,I}^{n-1/2} \right) \mathrm{V}_J^0 \frac{\partial \mathrm{W}(X_I - X_J, h_0)}{\partial X_J^\beta} \tag{5.6}$$

5) Update the density of particle *J* at time step *n+1*. Prior to updating the density of each particle, the gradient of deformation has to be computed at time step *n* and the Jacobian estimated:

$$J = \det \left| \overline{\overline{\mathbf{F}}}^n \right| \tag{5.7}$$

Then, the particle density can be updated at *n+1* using Eq.(5.8):

$$\rho_J^{n+1} = J^{-1} \rho_{oJ} \tag{5.8}$$

6) Calculate stress rate at *n-1/2*:

6a) First calculate the strain rate tensor **D** at time step *n-1/2*, the Green-Lagrange strain tensor at particle *I* is given by [4]:

$$\overline{\overline{\mathbf{E}}}^{n-1/2}\left(\vec{\mathbf{X}}_I \right) = \frac{1}{2}\left(\overline{\overline{\mathbf{F}}}^{\mathrm{T}} \overline{\overline{\mathbf{F}}} - \mathbf{I} \right)^{n-1/2} \tag{5.9}$$

the time derivative is therefore given by:

$$\dot{\mathbf{E}}^{n-1/2}\left(\vec{\mathbf{X}}_I \right) = \frac{1}{2}\left(\dot{\mathbf{F}}^{\mathrm{T}} \overline{\overline{\mathbf{F}}} + \overline{\overline{\mathbf{F}}}^{\mathrm{T}} \dot{\mathbf{F}} \right)^{n-1/2} \tag{5.10}$$

6b) with the following constitutive equation we can calculate the 2nd Piola-Kirchhoff stress rate tensor at time step *n-1/2* [4]:

$$\dot{S}_{ij}^{n-1/2} = C_{ijkl} \dot{E}_{kl}^{n-1/2} \tag{5.11}$$

where C is the material tangent modulus, and $\dot{\mathbf{E}}$ is the whole Green-Lagrange strain rate tensor.

7) Apply the following finite difference equation to calculate 2nd Piola-Kirchhoff at time step n:

$$\mathbf{S}^n = \mathbf{S}^{n-1} + \dot{\mathbf{S}}^{n-1/2}\Delta t^n \tag{5.12}$$

8) Transform 2nd Piola-Kirchhoff into 1st Piola-Kirchhoff at time step n [21]:

$$\bar{\bar{\mathbf{P}}}^n = \left(\bar{\bar{\mathbf{S}}}\bar{\bar{\mathbf{F}}}^{\mathrm{T}}\right)^n \tag{5.13}$$

9) Transpose 1st Piola-Kirchhoff to obtain nominal stress and calculate internal forces at n using the SPH momentum equation:

$$f(X_I)_\alpha^n = -\sum_J \left[m_J \left(\frac{P_{\alpha\beta}(X_I)}{\rho_0^2(X_I)} + \frac{P_{\alpha\beta}(X_J)}{\rho_0^2(X_J)} \right) \frac{\partial \mathrm{W}(X_I - X_J, h_0)}{\partial X_J^\beta} \right] \tag{5.14}$$

10) Calculate acceleration at time step n:

$$\frac{\partial v(X_I)_\alpha^n}{\partial t} = a(X_I)_\alpha^n = f(X_I)_\alpha^n \tag{5.15}$$

11) Calculate critical time for code stability and update time interval:

$$\Delta t^{n+1} = m * \Delta t_{crit}^{n+1} \tag{5.16}$$

where m is a time scale factor.

12) Update total integration time:

$$t^{n+1} = t^n + \Delta t^{n+1} \tag{5.17}$$

13) Known variables at the end of time step n:

$$v^{n+1/2}, a^n, \Delta t^n, \Delta t^{n+1}, \rho^{n+1}, P^n, u^{n+1}$$

5.2.2 *Algorithm 2: Rate of Deformation tensor* **D** *as a strain measure.*

Variables known at time step n:

$$x^n, v^{n-1/2}, a^{n-1}, \Delta t^n, \Delta t^{n+1}, \rho^n, P^{n-1}, u^n$$

1) Calculate the derivative of the kernel with respect to the material coordinates at time step n (this is done only once and the result stored).

2) Obtain displacement u of particle I at time step n-1/2, these have to be calculated for every component (x_1, x_2, x_3) of the displacement vector $\vec{\mathbf{u}}$:

$$\vec{\mathbf{u}}^{n-1/2} = \vec{\mathbf{u}}^n - \frac{1}{2}\vec{\mathbf{v}}^{n-1/2}\Delta t^n \tag{5.18}$$

3) Calculate deformation gradient at particle I at time step *n-1/2* [73]:

$$\left\langle \bar{\bar{\mathbf{F}}}_I^{n-1/2} \right\rangle = -\sum_{J \in S} \left(\vec{\mathbf{u}}_J^{n-1/2} - \vec{\mathbf{u}}_I^{n-1/2} \right) \otimes \nabla_{\vec{\mathbf{X}}_J} \mathrm{W}\left(\vec{\mathbf{X}}_I - \vec{\mathbf{X}}_J, h_0 \right) \mathbf{V}_J^0 + \mathbf{I} \tag{5.19}$$

Or in index notation:

$$F_{\alpha\beta}^{n-1/2}(X_I) = -\sum_J \left(u_{\alpha,J}^{n-1/2} - u_{\alpha,I}^{n-1/2} \right) V_J^0 \frac{\partial \mathrm{W}(X_I - X_J, h_0)}{\partial X_J^\beta} + \delta_{\alpha\beta} \tag{5.20}$$

4) Calculate velocity gradient at time step *n-1/2* [73]:

$$\left\langle \dot{\mathbf{F}}_I^{n-1/2} \right\rangle = -\sum_{J \in S} \left(\vec{\mathbf{v}}_J^{n-1/2} - \vec{\mathbf{v}}_I^{n-1/2} \right) \otimes \nabla_{\vec{\mathbf{X}}_J} \mathrm{W}\left(\vec{\mathbf{X}}_I - \vec{\mathbf{X}}_J, h_0 \right) \mathbf{V}_J^0 \tag{5.21}$$

Or index notation:

$$\dot{F}_{\alpha\beta}^{n-1/2}(X_I) = -\sum_J \left(v_{\alpha,J}^{n-1/2} - v_{\alpha,I}^{n-1/2} \right) V_J^0 \frac{\partial \mathrm{W}(X_I - X_J, h_0)}{\partial X_J^\beta} \tag{5.22}$$

5) Update the density of particle J at time step $n+1$:

$$\rho_J^{n+1} = J^{-1} \rho_{oJ} \tag{5.23}$$

Where the Jacobian is the determinant of the gradient of deformation tensor at timestep n:

$$J = \det\left|\bar{\bar{\mathbf{F}}}^{n}\right| \tag{5.24}$$

6) Calculate stress rate at *n-1/2*:

7) First calculate the strain rate tensor **D** at time step *n-1/2* at particle X_I, the Green-Lagrange strain tensor is given by [4]:

$$\bar{\bar{\mathbf{E}}}^{n-1/2}\left(\vec{\mathbf{X}}_I\right) = \frac{1}{2}\left(\bar{\bar{\mathbf{F}}}^{\mathrm{T}}\bar{\bar{\mathbf{F}}} - \mathbf{I}\right)^{n-1/2} \tag{5.25}$$

the time derivative is therefore given by:

$$\dot{\mathbf{E}}^{n-1/2}\left(\vec{\mathbf{X}}_I\right) = \frac{1}{2}\left(\dot{\mathbf{F}}^{\mathrm{T}}\bar{\bar{\mathbf{F}}} + \bar{\bar{\mathbf{F}}}^{\mathrm{T}}\dot{\mathbf{F}}\right)^{n-1/2} \tag{5.26}$$

where $\dot{\mathbf{F}}$ is known at *n-1/2*, $\dot{\mathbf{F}} = \bar{\bar{\mathbf{L}}}\bar{\bar{\mathbf{F}}}$, $\dot{\mathbf{F}} = \frac{\partial \vec{\mathbf{v}}}{\partial \vec{\mathbf{x}}}\frac{\partial \vec{\mathbf{x}}}{\partial \vec{\mathbf{X}}} = \frac{\partial \vec{\mathbf{v}}}{\partial \vec{\mathbf{X}}}$ as calculated in step 4.

7a) A slight modification would be to convert the Green-Lagrange strain rate tensor at *n* into the rate of deformation tensor at *n* as follows [4]:

$$\left(\bar{\bar{\mathbf{F}}}^{T}\bar{\bar{\mathbf{D}}}\bar{\bar{\mathbf{F}}}\right)^{n-1/2} = \dot{\mathbf{E}}^{n-1/2}, \tag{5.27}$$

$$\text{Hence } \bar{\bar{\mathbf{D}}}^{n-1/2} = (\bar{\bar{\mathbf{F}}}^{-\mathrm{T}}\dot{\mathbf{E}}\bar{\bar{\mathbf{F}}}^{-1})^{n-1/2} \tag{5.28}$$

And calculate Spin tensor at *n-1/2* from:

$$\bar{\bar{\mathbf{L}}}^{n-1/2} = \bar{\bar{\mathbf{D}}}^{n-1/2} + \bar{\bar{\mathbf{W}}}^{n-1/2} \tag{5.29}$$

7b) with the following constitutive equation we can calculate the True stress rate tensor at time step *n-1/2* [35]:

$$\dot{\sigma}_{ij}{}^{n-1/2} = C_{ijkl}D_{kl}{}^{n-1/2} \tag{5.30}$$

where C is the material tangent modulus , and D is the Rate of Deformation tensor.

7c) Update strength model to time step *n*:

$$\boldsymbol{\sigma}^n = \boldsymbol{\sigma}^{n-1} + \dot{\boldsymbol{\sigma}}^{n-\frac{1}{2}} \Delta t^n \tag{5.31}$$

8) Transform true stress into 1st Piola-Kirchhoff at time step n. [21]:

$$\overline{\overline{\mathbf{P}}}^n = \left(J \overline{\overline{\mathbf{F}}}^{-1} \overline{\overline{\boldsymbol{\sigma}}} \right)^n \tag{5.32}$$

9) Calculate internal forces at n [73] using the SPH momentum equation:

$$f(X_I)_\alpha^n = -\sum_J \left[m_J \left(\frac{P_{\alpha\beta}(X_I)}{\rho_0^2(X_I)} + \frac{P_{\alpha\beta}(X_J)}{\rho_0^2(X_J)} \right) \frac{\partial W(X_I - X_J, h_0)}{\partial X_J^\beta} \right] \tag{5.33}$$

10) Calculate acceleration at time step n:

$$\frac{\partial v(X_I)_\alpha^n}{\partial t} = a(X_I)_\alpha^n = f(X_I)_\alpha^n \tag{5.34}$$

11) Calculate critical time for code stability and update time interval:

$$\Delta t^{n+1} = m * \Delta t_{crit}^{n+1} \tag{5.35}$$

where m is a time scale factor.

12) Update total integration time:

$$t^{n+1} = t^n + \Delta t^{n+1} \tag{5.36}$$

13) Known variables at the end of time step n:

$$v^{n+\frac{1}{2}}, a^n, \Delta t^n, \Delta t^{n+1}, \rho^{n+1}, P^n, u^{n+1}$$

When fracture is simulated, regardless of the fracture criterion employed, the variable values at the particles are set to zero and they no longer contribute in the interpolation.

5.2.3 Algorithm 3: Normalised-Corrected SPH algorithm.

Variables known at time step n:

$$x^n, v^{n-1/2}, a^{n-1}, \Delta t^n, \Delta t^{n+1}, \rho^n, P^{n-1}, u^n$$

1) Calculate normalised derivative of the kernel with respect to the material co-ordinates at time step n (this is done only once and the result stored):

$$\tilde{\mathrm{W}}\left(\vec{\mathbf{X}}_J - \vec{\mathbf{X}}_I, h_0\right) = \frac{\mathrm{W}\left(\vec{\mathbf{X}}_J - \vec{\mathbf{X}}_I, h_0\right)}{\sum_{J \in S} \frac{m_J}{\rho_J} \mathrm{W}\left(\vec{\mathbf{X}}_J - \vec{\mathbf{X}}_I, h_0\right)} \tag{5.37}$$

and:

$$\nabla_{\vec{\mathbf{X}}_J} \tilde{\mathrm{W}}_{IJ} = \frac{1}{C} \nabla_{\vec{\mathbf{X}}_J} \mathrm{W}_{IJ} \tag{5.38}$$

where:

$$C = \sum_{J \in S} \frac{m_J}{\rho_J} \mathrm{W}\left(\vec{\mathbf{X}}_I - \vec{\mathbf{X}}_J, h_0\right) \tag{5.39}$$

2) Calculate derivative correction factor **B** :

$$\mathbf{B} = \left(-\sum_{J \in S} \frac{m_J}{\rho_J} \left(\vec{\mathbf{X}}_J - \vec{\mathbf{X}}_I\right) \otimes \nabla_{\vec{\mathbf{X}}_J} \tilde{\mathrm{W}} \right)^{-1} \tag{5.40}$$

or in index notation:

$$B_{\alpha\beta} = \left(-\sum_{J \in S} \frac{m_J}{\rho_J} \left(X_J^\alpha - X_I^\alpha\right) \frac{\partial \tilde{\mathrm{W}}_{IJ}}{\partial X_J^\beta} \right)^{-1} \tag{5.41}$$

3) Obtain displacement u of particle I at time step *n-1/2*. These have to be calculated for every component (x_1, x_2, x_3) of the displacement vector $\vec{\mathbf{u}}$:

$$\vec{\mathbf{u}}^{n-1/2} = \vec{\mathbf{u}}^n - \frac{1}{2} \vec{\mathbf{v}}^{n-1/2} \Delta t^n \tag{5.42}$$

4) Calculate deformation gradient at particle I at time step *n-1/2* :

$$\left\langle \bar{\bar{\mathbf{F}}}_I^{n-1/2} \right\rangle = \left[-\sum_{J \in S} \left(\vec{\mathbf{u}}_J{}^{n-1/2} - \vec{\mathbf{u}}_I{}^{n-1/2} \right) \otimes \nabla_{\vec{\mathbf{X}}_J} \mathrm{W}\left(\vec{\mathbf{X}}_I - \vec{\mathbf{X}}_J, h_0\right) \mathbf{V}_J^0 \right] \mathbf{B} + \mathbf{I} \tag{5.43}$$

Or in index notation:

$$F_{\alpha\beta}^{n-1/2}(X_I) = -\sum_J \left(u_{\alpha,J}^{n-1/2} - u_{\alpha,I}^{n-1/2}\right) V_J^0 \frac{\partial \tilde{\mathbf{W}}(X_I - X_J, h_0)}{\partial X_J^\gamma} B_{\gamma\beta} + \delta_{\alpha\beta} \tag{5.44}$$

5) Calculate velocity gradient at time step *n-1/2* :

$$\left\langle \dot{\mathbf{F}}_I^{n-1/2} \right\rangle = \left[-\sum_{J \in S} \mathbf{V}_J^0 \left(\bar{\mathbf{v}}_J^{n-1/2} - \bar{\mathbf{v}}_I^{n-1/2} \right) \otimes \nabla_{\bar{\mathbf{X}}_J} \mathrm{W}\left(\bar{\mathbf{X}}_I - \bar{\mathbf{X}}_J, h_0 \right) \right] \mathbf{B} \tag{5.45}$$

Or index notation:

$$\dot{F}_{\alpha\beta}^{n-1/2}(X_I) = -\sum_J \left(v_{\alpha,J}^{n-1/2} - v_{\alpha,I}^{n-1/2}\right) V_J^0 \frac{\partial \mathrm{W}(X_I - X_J, h_0)}{\partial X_J^\gamma} B_{\gamma\beta} \tag{5.46}$$

6) Update the density of particle *J* (from 1 to np) at time step *n*+1:

$$\rho_J^{n+1} = J^{-1} \rho_{oJ} \tag{5.47}$$

Where the Jacobian is the determinant of the gradient of deformation tensor at timestep *n*:

$$J = \det \left| \bar{\bar{\mathbf{F}}}^n \right| \tag{5.48}$$

7) Calculate stress rate at *n*-1/2:

7a) First calculate the strain rate tensor $\bar{\bar{\mathbf{D}}}$ at time step *n-1/2* at particle $\bar{\mathbf{X}}_I$, the Green-Lagrange strain tensor is given by [4]:

$$\bar{\bar{\mathbf{E}}}^{n-1/2}\left(\bar{\mathbf{X}}_I\right) = \frac{1}{2}\left(\bar{\bar{\mathbf{F}}}^{\mathrm{T}} \bar{\bar{\mathbf{F}}} - \mathbf{I}\right)^{n-1/2} \tag{5.49}$$

the time derivative is therefore given by:

$$\dot{\mathbf{E}}^{n-1/2}\left(\bar{\mathbf{X}}_I\right) = \frac{1}{2}\left(\dot{\mathbf{F}}^{\mathrm{T}} \bar{\bar{\mathbf{F}}} + \bar{\bar{\mathbf{F}}}^{\mathrm{T}} \dot{\mathbf{F}}\right)^{n-1/2} \tag{5.50}$$

where $\dot{\mathbf{F}}$ is known at *n*-1/2, $\dot{\mathbf{F}} = \bar{\bar{\mathbf{L}}} \bar{\bar{\mathbf{F}}}$, $\dot{\mathbf{F}} = \frac{\partial \vec{\mathbf{v}}}{\partial \vec{\mathbf{x}}} \frac{\partial \vec{\mathbf{x}}}{\partial \vec{\mathbf{X}}} = \frac{\partial \vec{\mathbf{v}}}{\partial \vec{\mathbf{X}}}$ as calculated at step 4.

7b) A slight modification would be to convert the Green-Lagrange strain rate tensor at n into the rate of deformation tensor at *n* as follows [4]:

$$\left(\bar{\bar{\mathbf{F}}}^{T}\bar{\bar{\mathbf{D}}}\bar{\bar{\mathbf{F}}}\right)^{n-1/2} = \dot{\mathbf{E}}^{n-1/2}, \tag{5.51}$$

$$\text{Hence } \bar{\bar{\mathbf{D}}}^{n-1/2} = (\bar{\bar{\mathbf{F}}}^{-T}\dot{\mathbf{E}}\bar{\bar{\mathbf{F}}}^{-1})^{n-1/2} \tag{5.52}$$

And calculate Spin tensor at n-1/2 from:

$$\bar{\bar{\mathbf{L}}}^{n-1/2} = \bar{\bar{\mathbf{D}}}^{n-1/2} + \bar{\bar{\mathbf{W}}}^{n-1/2} \tag{5.53}$$

7c) with the following constitutive equation we can calculate the true stress rate tensor at time step *n-1/2* [35]:

$$\dot{\sigma}_{ij}{}^{n-1/2} = C_{ijkl}D_{kl}{}^{n-1/2} \tag{5.54}$$

where C is the material tangent modulus , and D is the Rate of Deformation tensor.

7d) Update strength model to time step n [35]:

$$\bar{\bar{\boldsymbol{\sigma}}}^{n} = \bar{\bar{\boldsymbol{\sigma}}}^{n-1} + \dot{\boldsymbol{\sigma}}^{n-1/2}\Delta t^{n} \tag{5.55}$$

8) Transform True stress into 1st Piola-Kirchhoff **P** at time step n. [21]:

$$\bar{\bar{\mathbf{P}}}^{n} = \left(J\bar{\bar{\mathbf{F}}}^{-1}\bar{\bar{\boldsymbol{\sigma}}}\right)^{n} \tag{5.56}$$

9) Calculate internal forces at n using the SPH momentum equation:

$$f(X_I)_{\alpha}^{n} = -\sum_{J}\left[m_J\left(\frac{P_{\alpha\beta}(X_I)}{\rho_0^2(X_I)} + \frac{P_{\alpha\beta}(X_J)}{\rho_0^2(X_J)}\right)\frac{\partial\tilde{W}(X_I - X_J, h_0)}{\partial X_J^{\gamma}}B_{\gamma\beta}\right] \tag{5.57}$$

10) Calculate acceleration at time step n:

$$\frac{\partial v(X_I)_{\alpha}^{n}}{\partial t} = a(X_I)_{\alpha}^{n} = f(X_I)_{\alpha}^{n} \tag{5.58}$$

11) Calculate critical time for code stability and update time interval:

$$\Delta t^{n+1} = m * \Delta t_{crit}^{n+1} \tag{5.59}$$

where m is a time scale factor.

12) Update total integration time:

$$t^{n+1} = t^n + \Delta t^{n+1} \tag{5.60}$$

13) Known variables at the end of time step n:

$$v^{n+1/2}, a^n, \Delta t^n, \Delta t^{n+1}, \rho^{n+1}, P^n, u^{n+1}$$

5.3 Time Integration of the SPH Equations.

The SPH method allows partial differential equations to be discretised in space. A further discretisation is required to solve transient dynamic problems and to advance the solution in time. A typical integration scheme is the standard leap-frog algorithm.

When the integration process commences (during the first step of the simulation), the time step at *n+1* is regarded as the time step at n ($\Delta t^n = \Delta t^{n+1}$) for carrying out the pull-back operation of the particle positions [3].

$$\vec{\mathbf{u}}^{n-1/2} = \vec{\mathbf{u}}^n - \frac{1}{2}\vec{\mathbf{v}}^{n-1/2}\Delta t^n \tag{5.61}$$

At this stage, particle position and velocities are known at *n-1/2*. The Deformation Gradient and the Green-Lagrange strain rate tensor are calculated. After that, the particle positions are updated with the following push-forward operation:

$$\vec{\mathbf{u}}^n = \vec{\mathbf{u}}^{n-1/2} + \frac{1}{2}\vec{\mathbf{v}}^{n-1/2}\Delta t^n \tag{5.62}$$

The Deformation gradient is calculated again for the purposes of calculating the Jacobian at time step n.

The stress rate is calculated at *n-1/2* and the stress tensor gets updated using the following expression:

$$\mathbf{S}^n = \mathbf{S}^{n-1} + \dot{\mathbf{S}}^{n-1/2}\Delta t^n \tag{5.63}$$

or by using an objective rate. In any case, the new updated stress tensor is calculated at time *n*. Accelerations are calculated at time *n* with the momentum equation.

The velocities are advanced in time to *n+1/2* using the following expression:

$$\vec{\mathbf{v}}^{n+1/2} = \vec{\mathbf{v}}^{n-1/2} + \Delta t^* \vec{\mathbf{a}}^n \tag{5.64}$$

$$\text{where } \Delta t^* = \frac{1}{2}\left(\Delta t^n + \Delta t^{n+1}\right) \tag{5.65}$$

Note that only during the first time step:

$$\Delta t^* = \frac{1}{2}\left(\Delta t^{n+1}\right) = \frac{1}{2}\left(\Delta t^n\right) \tag{5.66}$$

subsequently $\Delta t^* = \frac{1}{2}\left(\Delta t^n + \Delta t^{n+1}\right)$ is used.

Finally, the new particle position gets updated with the new velocity:

$$\vec{\mathbf{u}}^{n+1} = \vec{\mathbf{u}}^n + \vec{\mathbf{v}}^{n+1/2}\Delta t^{n+1} \tag{5.67}$$

New time variables are assigned:

$$\Delta t^n = \Delta t^{n+1} \tag{5.68}$$

and the new time step at *n+1* is calculated using:

$$\Delta t^{n+1} = \Delta t_{crit} * m \tag{5.69}$$

where *m* is the time step scale factor and:

$$\Delta t_{crit} = \frac{h_i}{c_i + |v_i|} \tag{5.70}$$

$$\Delta t_{crit} = \frac{minimum\ \ interparticle\ \ distance}{c_i + |v_i|} \tag{5.71}$$

This is the parameter that controls the stability of the time integration (Courant-Friederichs-Levy condition).

5.4 Implementation Flow Charts.

Figure 5.2 provides a flow chart of the algorithms in section 5.2., it represents graphically the sequential execution of FORTRAN subroutines as the solution is advanced in time.

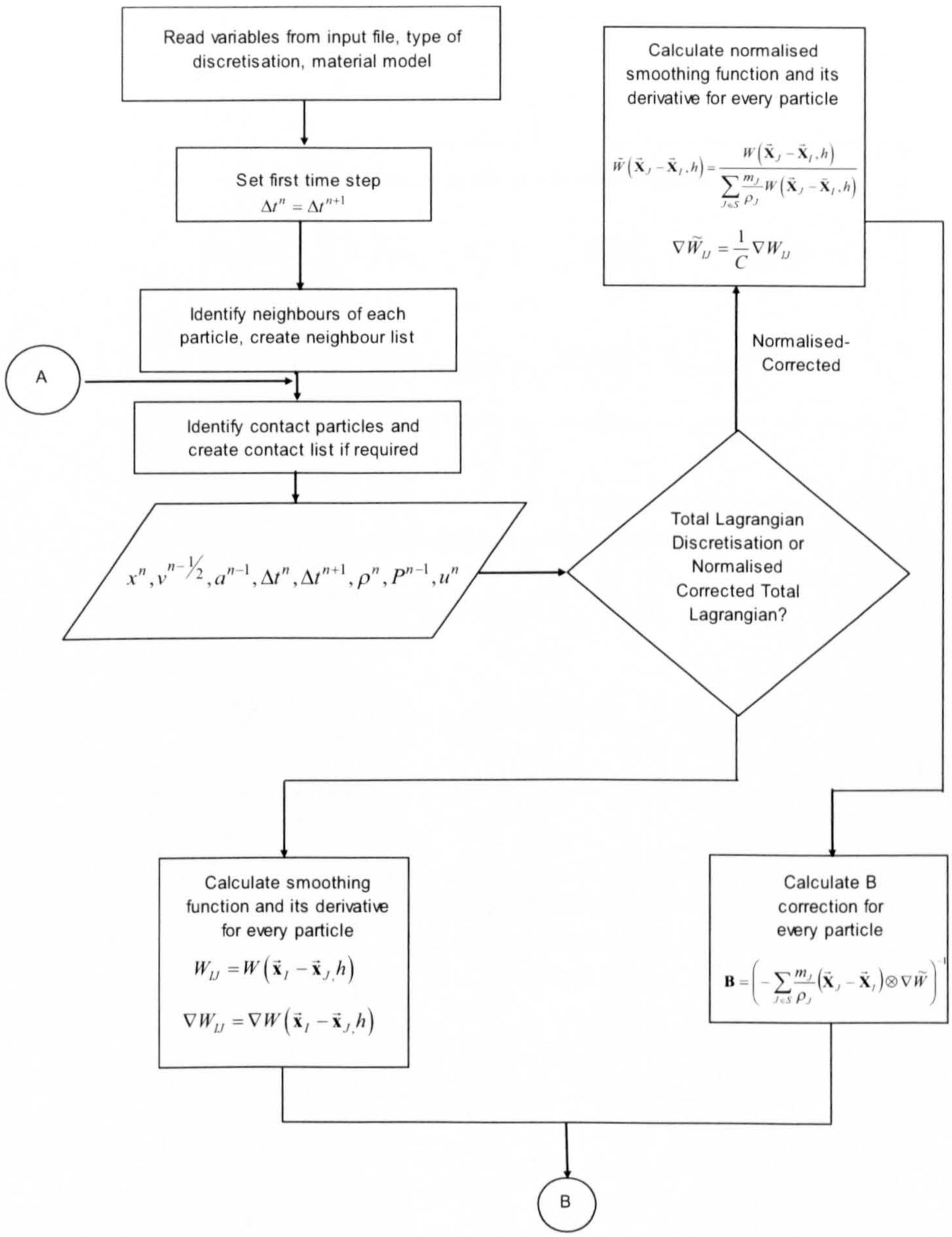

Fig. 5.2 Total Lagrangian SPH code flow chart.

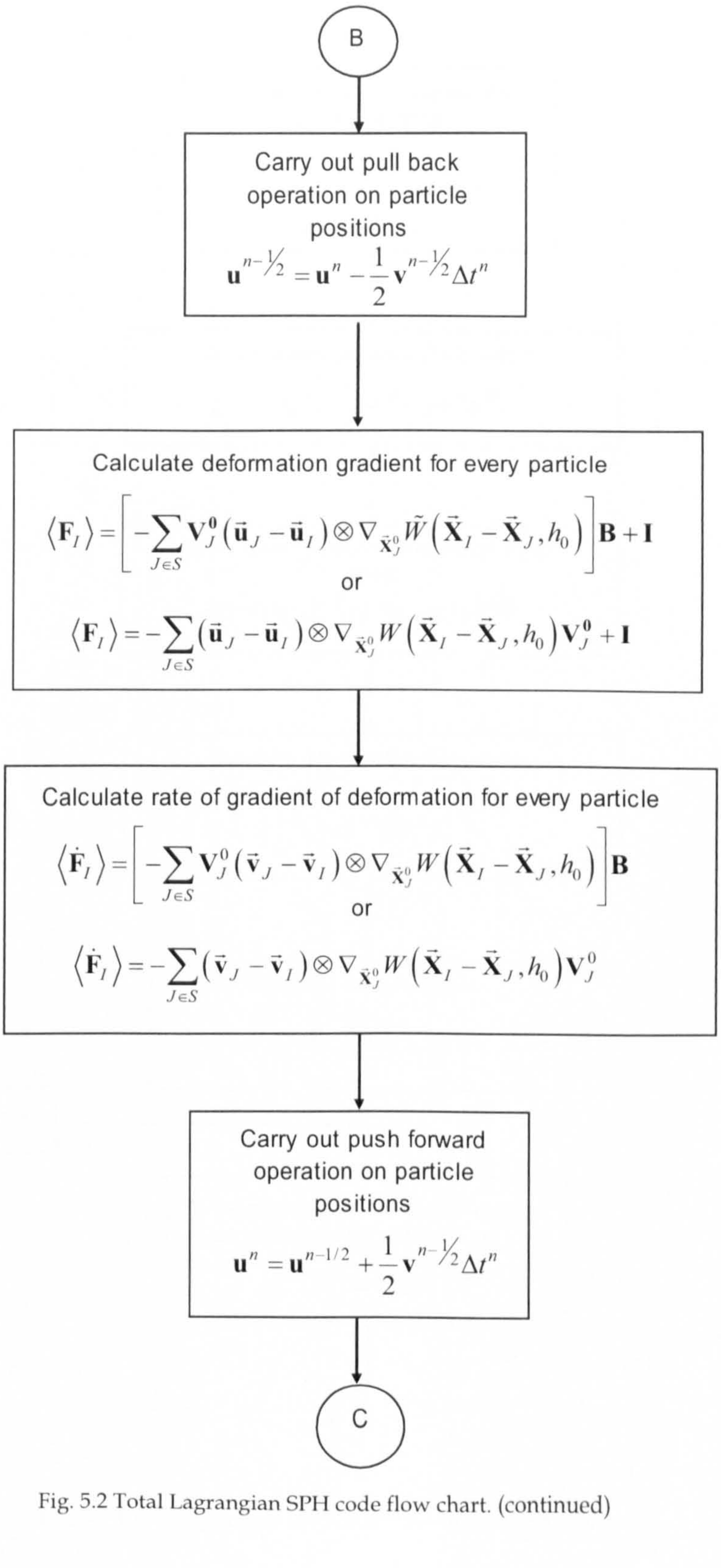

Fig. 5.2 Total Lagrangian SPH code flow chart. (continued)

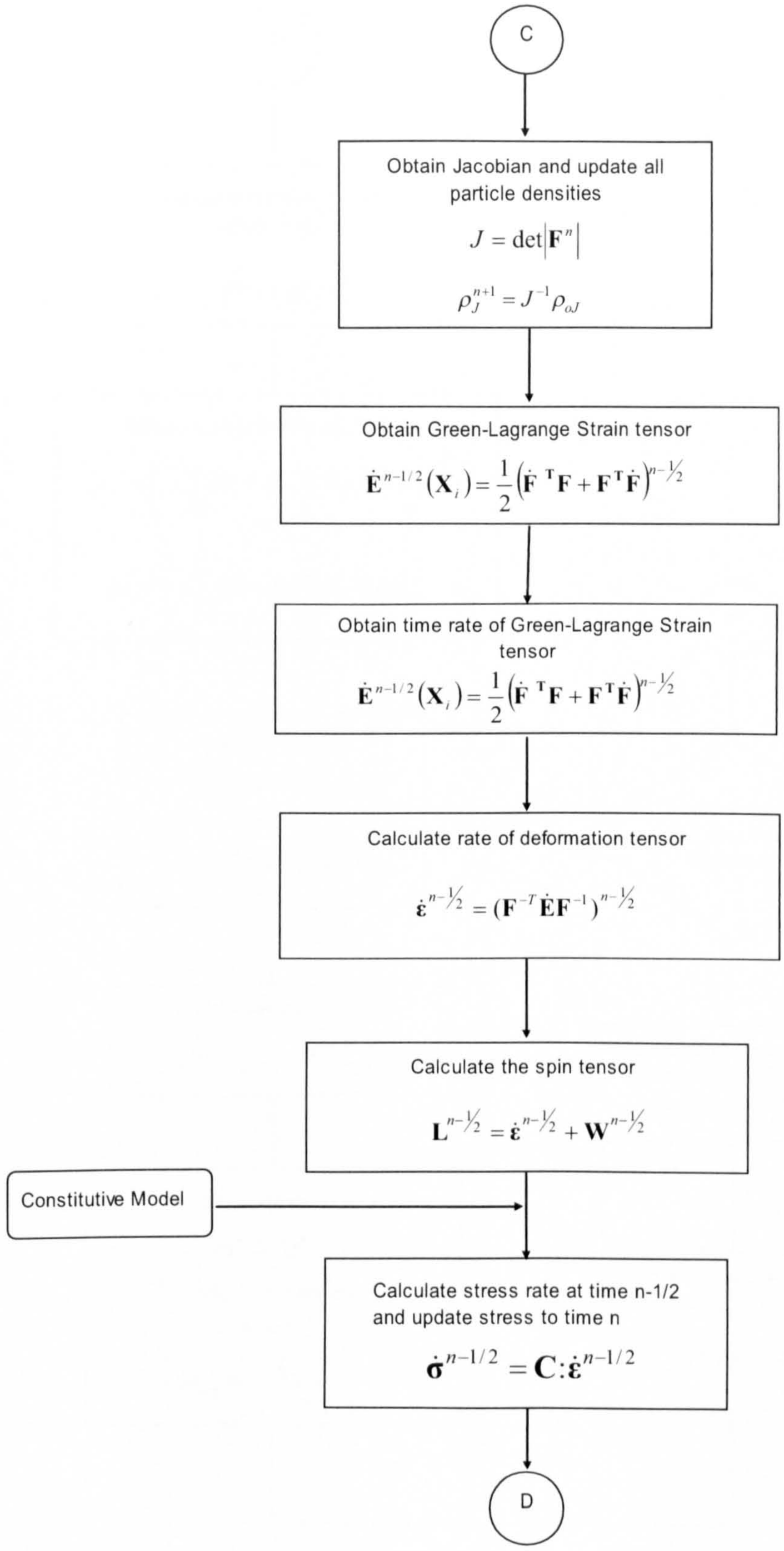

Fig. 5.2 Total Lagrangian SPH code flow chart. (continued)

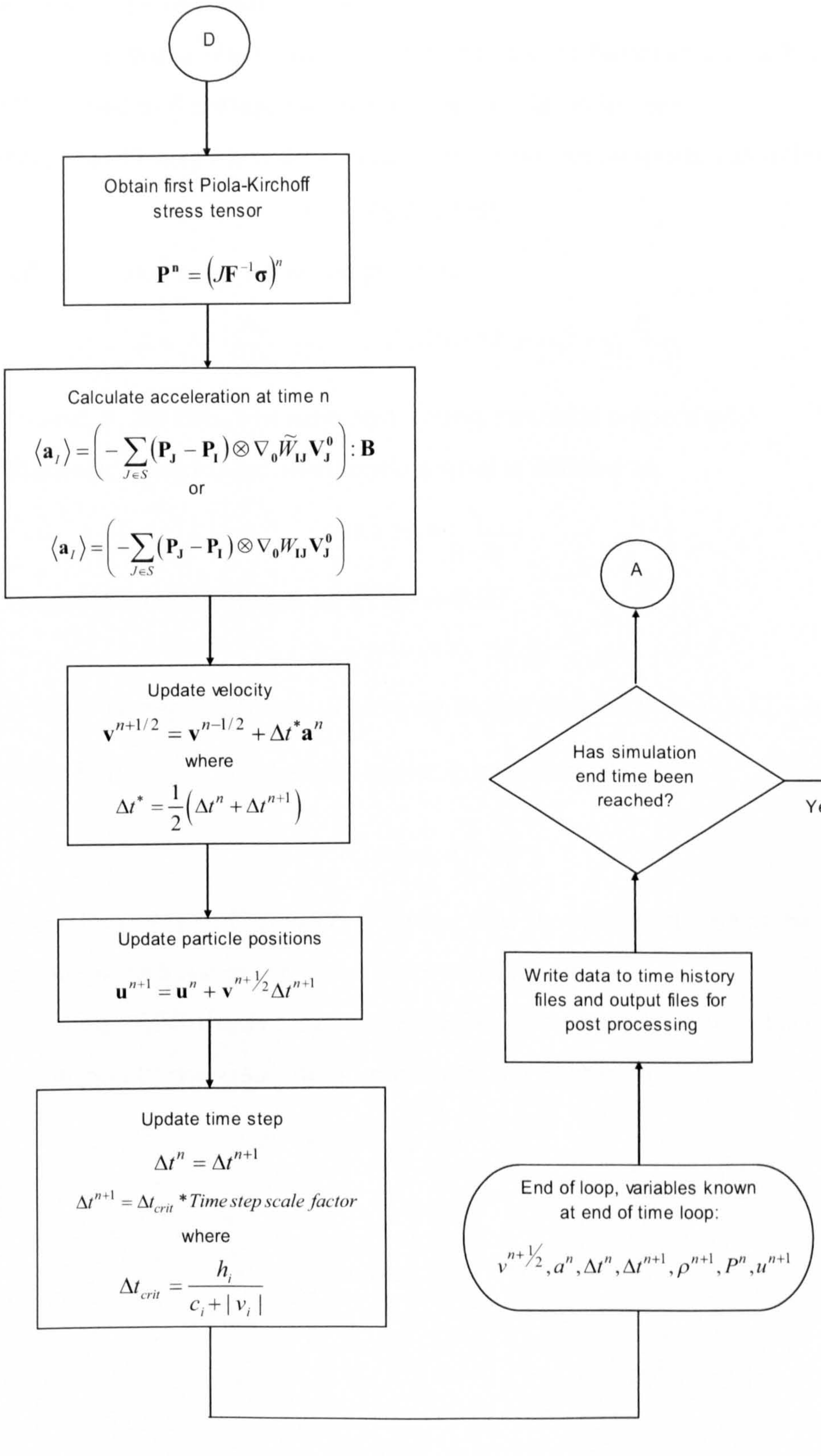

Fig. 5.2 Total Lagrangian SPH code flow chart.(continued)

5.5 Integration of Constitutive Models.

A simple linear elastic model (Material model Number 1 in DYNA 3-D [35]) will be used to illustrate how stresses get updated in time.

The generalised Hooke's law for an elastic material can be written as follows:

$$\sigma_{ij} = \lambda D_{kk}\delta_{ij} + 2\mu D_{ij} \tag{5.72}$$

Where λ and μ are Lame's constants:

$$\lambda = \frac{E\upsilon}{(\upsilon+1)(1-2\upsilon)} \quad (5.73) \text{ and } \mu = G = \frac{E}{2(\upsilon+1)} \tag{5.74}$$

where υ and E are Poissons ratio and Young modulus respectively.

The bulk modulus for an elastic material is defined as:

$$3\lambda + 2\mu = \frac{E}{1-2\upsilon} \tag{5.75}$$

Contraction of indices in Eq (5.72) yields:

$$\sigma_{ii} = 3P = (3\lambda + 2\mu)D_{ii} \tag{5.76}$$

where P is the average pressure. The stress tensor defined by Eq (5.72) can be split in its spherical $\frac{1}{3}\sigma_{kk}\delta_{ij}$ and deviatoric S_{ij} part as follows:

$$\sigma_{ij} = \frac{1}{3}\sigma_{kk}\delta_{ij} + S_{ij} \tag{5.77}$$

From Eq (5.76) and Eq (5.77) it is clear that the spherical part of the stress tensor contains the average pressure in its main diagonal.

From Eq. (5.76) the average pressure can be computed if the trace of the symmetrical part of the gradient of velocity tensor is known:

$$P = \frac{3\lambda + 2\mu}{3} D_{ii} \tag{5.78}$$

where :

$$\frac{D_{ii}}{\Delta t} = trace\, D = \frac{\partial v_i}{\partial x_i} = \nabla . \vec{\mathbf{v}} \tag{5.79}$$

and :

$$\bar{\bar{\mathbf{D}}} = \frac{1}{2}\left(\bar{\bar{\mathbf{L}}} + \bar{\bar{\mathbf{L}}}^T\right) \tag{5.80}$$

Eq. (5.80) is the rate of deformation tensor and $\bar{\bar{\mathbf{L}}}$ is the gradient of velocity tensor:

$$L_{ij} = \frac{\partial v_i}{\partial x_j} \tag{5.81}$$

The procedure for updating the stress tensor is as follows:

1) The rate of deformation tensor $\bar{\bar{\mathbf{D}}}$ is known. Compute the trace of $\bar{\bar{\mathbf{D}}}$, Eq. (5.79)
2) Calculate material bulk modulus using Eq. (5.75)
3) Calculate the pressure increment at n time step, Eq (5.78) and Eq (5.79):

$$P_{inc} = \frac{(3\lambda + 2\mu)}{3} D_{ii} = \frac{(3\lambda + 2\mu)}{3} \left(\frac{\partial v_i}{\partial x_i} \right) \Delta t \tag{5.82}$$

4) Split **D** into its spherical and deviatoric components:

$$D = D^s + D^d \tag{5.83}$$

where:

$$D^s = \frac{trace\, D}{3} \mathbf{I} \tag{5.84}$$

hence:

$$D^d = D - \frac{trace\, D}{3} \tag{5.85}$$

5) Update stress according to Eq. (5.72) as follows:

$$\begin{aligned}
\sigma_{11}{}^n &= \sigma_{11}{}^{n-1} + P_{inc} + 2G\Delta t \left(D_{11} - \frac{trace\, D}{3} \right) \\
\sigma_{22}{}^n &= \sigma_{22}{}^{n-1} + P_{inc} + 2G\Delta t \left(D_{22} - \frac{trace\, D}{3} \right) \\
\sigma_{33}{}^n &= \sigma_{33}{}^{n-1} + P_{inc} + 2G\Delta t \left(D_{33} - \frac{trace\, D}{3} \right) \\
\sigma_{12}{}^n &= \sigma_{12}{}^{n-1} + 2G\Delta t\, D_{12} \\
\sigma_{13}{}^n &= \sigma_{13}{}^{n-1} + 2G\Delta t\, D_{13}
\end{aligned} \tag{5.86}$$

$$\sigma_{23}^{\,n} = \sigma_{23}^{\,n-1} + 2G\,\Delta t\,D_{23}$$

6) End subroutine and go to (D) in the flow chart, figure 5.2.

Summary.

A brief description of current techniques used for solving wave propagation in solids is given in this chapter. Within the scope of numerical techniques with direct time integration SPH is categorised as an explicit method for the solution of initial-boundary value problems where the timespan of interest is typically from a few micro to milliseconds.

Three algorithms for the integration of the conservation and constitutive equations have been derived. Algorithm 1, the basic total Lagrangian algorithm, uses the 1st and 2nd Piola-Kirchhoff stress tensors and the Green-Lagrange strain tensor in the solution of the governing equations. Algorithm 2, transforms the Green-Lagrange strain rate tensor into the rate of deformation tensor and uses an objective stress rate and the true stress tensor to update the momentum equation. Finally, algorithm 3, provides the normalised-corrected version of algorithm 2.

The flow charts illustrate how, through the use of the SPH method, the spatial numerical approximation of the scalar and vector fields of interest is achieved at every time step. In addition, the flow charts illustrate how this spatial approximation is in turn advanced in time by means of the central finite difference leap frog algorithm.

PAGE NUMBERING AS ORIGINAL

CHAPTER 6

TOTAL LAGRANGIAN SPH CODE VALIDATION

In this chapter some numerical examples are provided which demonstrate the suitability of the Total Lagrangian SPH code to model solids under dynamic loading. The results presented in this Chapter are given sequentially for one, two and three dimensions. In every case an example is given which demonstrates the superior stability qualities of the new code when compared to the Eulerian SPH code.

Firstly, Problems 1, 5 and 7 address the tensile instability deficiency of Eulerian SPH. In these problems no attempt was made to quantify the levels of stress, wave propagation times, plastic deformation sustained by or fracture of the specimen. The objective was to qualitatively demonstrate that when the

conservation laws in a Total Lagrangian form are discretised in a Lagrangian SPH framework, the resulting code is more stable and consequently better suited to the simulation of dynamic events in solids than its Eulerian counterpart.

Secondly, some examples for which the analytical solutions are known are used as a means of validation of the total Lagrangian SPH code. Problem 2 deals with a 1-D elastic wave propagating within a plate as a result of a uniaxial state of strain (two plate impact). The analytical solution is provided for the value of velocity after impact, the stress wave amplitude and pulse duration and for the pulse length and the elapsed time to reach the back end of the target plate. SPH time histories are also presented and compared with the analytical solution. Problem 4 presents the numerical and analytical solutions of a linear elastic rod under longitudinal vibrations. A case is presented in which one end of the rod is clamped and one is free to vibrate. A linear velocity field was imposed on the SPH particles as the initial condition, a situation which could only be analysed when normalisation and correction terms are introduced in the Total Lagrangian SPH particle equations. Problem 6 deals with the Taylor test simulation of a 2-D specimen. The Total Lagrangian SPH code (with the symmetry planes option included) and a standard non-linear finite element code have been used for simulating this impact scenario. The resulting effective plastic strain experienced by the specimens is depicted for both the FE (LS-DYNA) and the SPH simulations. The validation of the normalised-corrected scheme used by the Total Lagrangian SPH code is considered in Problem 3. In this problem, a set of discrete points in a 1-D space with a constant and linear distribution of velocity is analysed through different SPH schemes, namely: a) SPH scheme with no correction and no symmetry terms, b) SPH scheme with no correction and with symmetry terms, c) SPH scheme with the standard normalisation and correction terms and without symmetry terms, d) SPH scheme with normalisation and correction and with symmetry terms, e) a new correction term used in the Total Lagrangian SPH formulation without

symmetry terms and finally f) a new correction term used in the Total Lagrangian SPH formulation with symmetry terms.

Finally, problems 8, 9 and 10 are real engineering problems that deal with hard debris impact, spall fracture of OFHC copper specimens and hard debris impact and penetration of a steel sphere on an aluminium target. The results obtained in this set of examples are either compared to finite element simulation or to experimental results whenever available.

6.1 One-Dimensional Problems

6.1.1 1-D Stability test (This problem addresses the tensile instability condition in the collocational Eulerian SPH code)

Problem 1.-The symmetric impact of two 1-D elastic rods travelling at the same speed in opposite directions was simulated using both the Eulerian and the Total Lagrangian SPH codes. The constitutive model employed was the linear isotropic elastic material model [35] with a Young modulus of 7 E10 Pa, the Poisson ratio is 0.3 and material density is $2700\frac{\text{kg}}{\text{m}}$ (1-D domain). The speed of the rods was set to $10\frac{\text{m}}{\text{s}}$ with opposite directions along the longitudinal axis of the rods.

Objective.- The aim of this numerical experiment is to qualitatively demonstrate that when the conservation laws are expressed in a Total Lagrangian form and discretised in a Total Lagrangian SPH framework, the tensile instability condition discussed in Chapter 3 is removed .

SPH formulation used.- The 1-D domain was discretised into 2000 particles. Two fully collocational SPH schemes were used for the numerical simulation of this problem: The Eulerian SPH and the Total Lagrangian SPH schemes. The smoothing function used was the cubic spline and the smoothing length was 2.4E-2 m. Both schemes used the symmetrised form of the particle

equations.

Results.- The results show that both the Eulerian code and the Total Lagrangian code are capable of simulating a compressive wave propagating towards the free ends of the rods. Once the wave gets reflected by the free surface and the stress wave changes from compressive to tensile, the Eulerian SPH simulation exhibits the effect of tensile instability in the form of numerical fracture causing computations to stop prematurely.

The Total Lagrangian SPH simulations do not exhibit this effect regardless of the value and sign of the computed stress. (Refer to figures 6.1 and 6.2). The colours in Fig. 6.1 and 6.2 represent the two different domains: the red particles belong to the rod travelling to the left and the green particles belong to the rod travelling to the right. The colour scale on the right shows the values of stress achieved during the solution process.

Fig. 6.1 Problem 1.Particles clump with specimen under tension, Eulerian Kernel. Only a few particles are shown.

Fig. 6.2 Problem 1. Inter-particle distance is maintained under tension, Lagrangian Kernel.

6.1.2 Elastic wave propagation in a uniaxial strain state: two plate impact.

Problem 2.- For the validation of the 1 dimensional code a simple case for which the analytic solution is known is considered. Consider two thin plates with thickness 0.5 and 1.5 units of length. For this problem it is assumed that the equivalent diameters of the plates are much greater than their thickness. This situation can be regarded as a planar impact case in which the thinner plate (flyer) is moving towards the thicker one (target) (Fig. 6.5). The velocity of the flyer plate v is 1.0E-01 units of length/units of time. The simulation starts when the moving plate impacts the target. The density ρ of both rods is taken as 1, the Young modulus equals 0.9 and the Poisson ratio 0.2. In the preceding properties units are irrelevant but assumed compatible. The linear elastic isotropic material [35] was used in the simulation of this problem.

Objective.- The objective if this problem is to validate the 1-D Total Lagrangian SPH code by comparing numerical and analytical results when uniaxial state of strain in a thin plate is considered.

SPH formulation used.- Fully collocational Total Lagrangian SPH was used for the numerical simulation of this problem. The smoothing function employed was the cubic spline, the smoothing length scale factor was 1.2. The symmetrised form of the particle equations was used. The 1-D domain was discretised into 2000 particles, 500 were allocated to the flyer plate and 1500 to the target plate.

Analytical solution.- For uniaxial strain, elastic waves propagate with the following velocity:

$$C_e = \sqrt{\frac{K + 4G/3}{\rho}} \tag{6.1}$$

For the given material properties:

$$K = \frac{E}{3(1-2\nu)} = \frac{0.9}{1.8} = 0.5 \quad , \quad G = \frac{E}{2(1+\nu)} = \frac{0.9}{2.4} = 0.375 \tag{6.2}$$

$$C_e = \sqrt{\frac{0.5+0.5}{1}} = 1.0$$

For the moving plate the linear momentum before the impact is expressed as: $P = \rho A_0 L V$ and after the impact $P_a = \rho A_0 \Lambda U_p$ where Λ is the pulse length given by $2L$, U_p is the velocity of the particles behind the stress wave and L is the length of the flyer. From the expressions of momentum before and after the impact we obtain the velocity of the particles after impact [61]: $U_p = \frac{V}{2}$.

The conservation of momentum states that the impulse over the target equals its change in momentum:

$$Fdt = d(mU_p) \tag{6.3}$$

For the uniaxial case we can rewrite the above expression as:

$\sigma A_0 dt = \rho A_0 dx U_p$ hence the stress can be calculated as $\sigma = \rho U_p \frac{dx}{dt}$. Note here that $\frac{dx}{dt}$ is the value of the wave velocity which we have previously expressed as C_e. With the expression for calculating stress and the expression that relates velocity after impact with velocity of particles behind the stress wave we can rewrite the expression for stress as:

$$\sigma = \frac{1}{2}\rho V C_e \tag{6.4}$$

The duration of the stress pulse at a point can be calculated through:

$$t_P = \frac{\Lambda}{C_e} = \frac{2L}{C_e}. \tag{6.5}$$

The preceding expressions are applied to the specific problem under consideration. The stress behind the elastic wave will be equal to $\sigma = 0.05$ units of stress, pulse length $\Lambda = 1$, the duration of the pulse at an arbitrary point

$t_P = 1$ units of time. The stress wave will reach the end of the stationary rod after $t = \frac{length}{C_e} = 1.5$ units of time and the velocity of particles after impact will be $U_p = 0.05$ units of length/units of time. The strain can be calculated, for the uniaxial case, as $\varepsilon = \frac{\sigma}{E}$ which results in strain= 0.055.

Results.- The numerical results are shown in Figures 6.3, 6.4 and 6.5. The agreement between analytical and numerical values obtained through the Total Lagrangian code is remarkable.

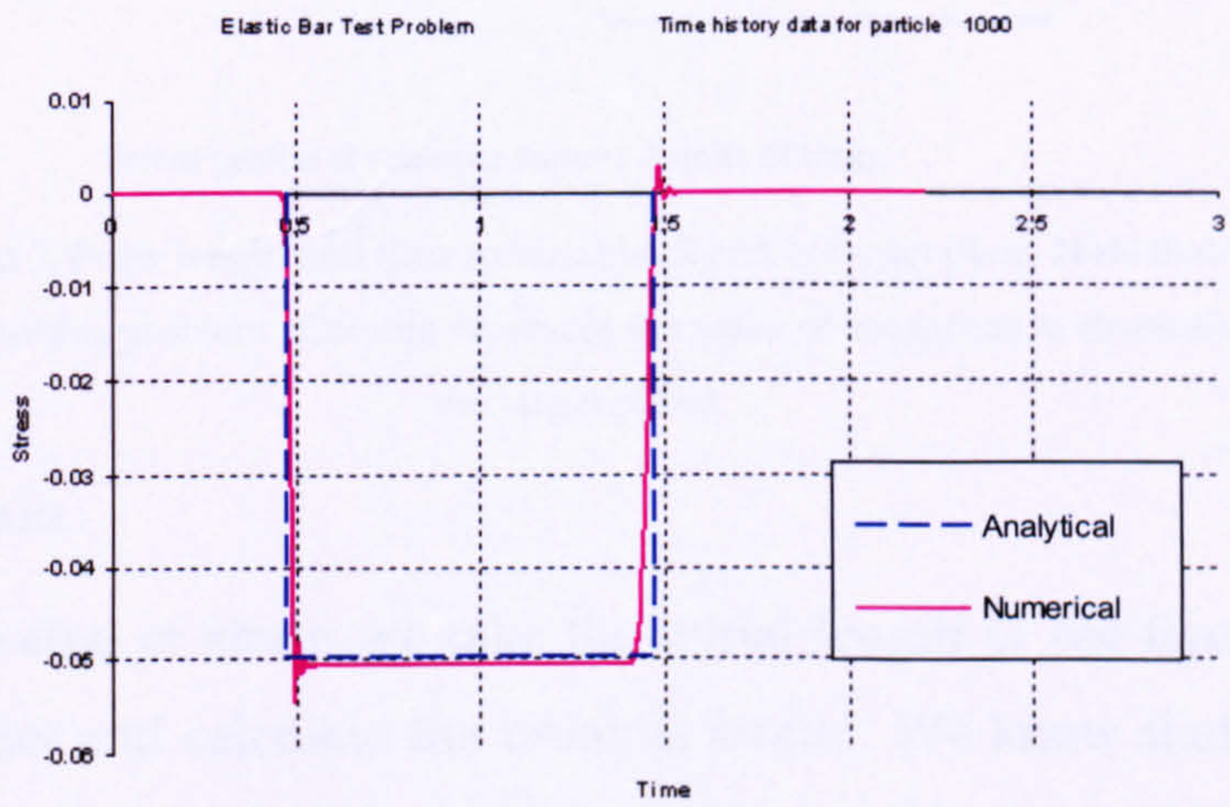

Fig 6.3 Problem 2. Stress history for uniaxial strain case wave propagation.

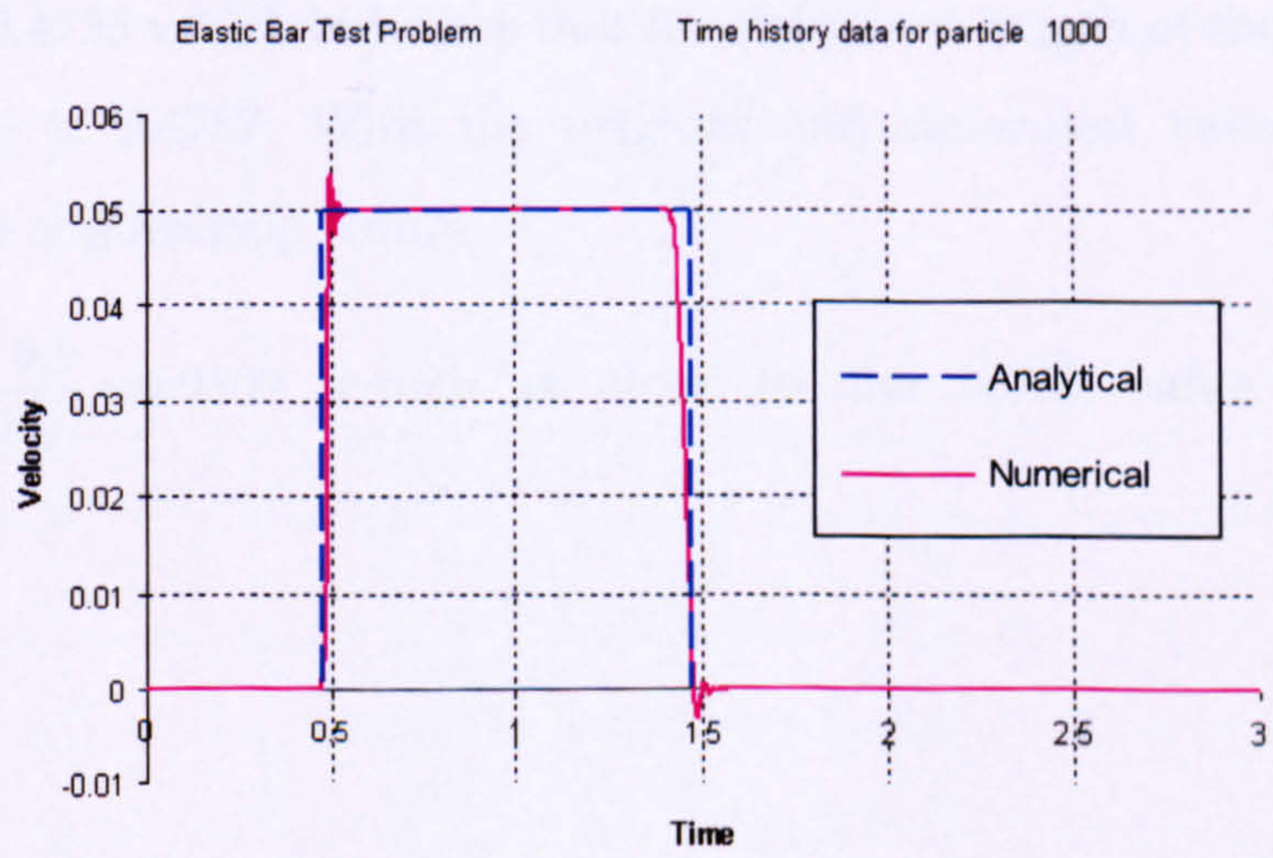

Fig 6.4. Problem 2. Velocity history for Problem 2.

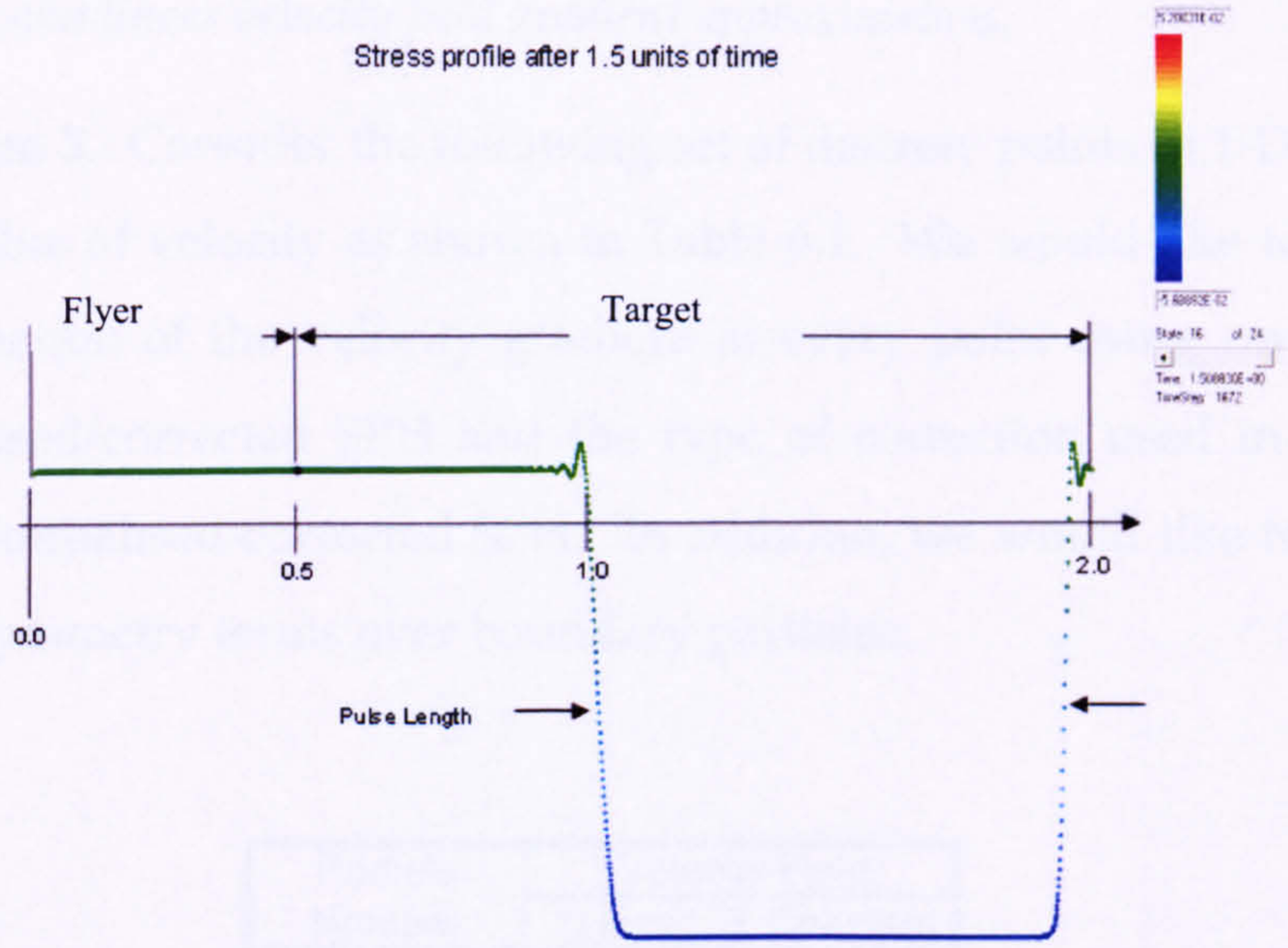

Stress profile at response time=1.5 units of time.

Fig 6.5. Problem 2. Pulse length and time to reach back end of target plate. Note that time and length units are irrelevant in this problem. Colours represent the value of compressive stress along the flyer and the target plates.

Value of strain :

For the value of strain we take the initial length of the flyer before and during impact and calculate the uniaxial strain. We know that the original plate thickness is L=0.5 units of length. After the moving plate has impacted the target plate, the measurements of the coordinates of the end points are 0.9513 and 0.4755 which indicates that the deformed length of the bar under compression is 0.4757. With the original and deformed values we can calculate the engineering strain:

$\varepsilon = \frac{0.4757 - 0.5}{0.4757} = 0.0509$ which is close to the 0.055 value calculated analytically.

6.1.3 Constant and linear velocity field gradient approximation.

Problem 3.- Consider the following set of discrete points in 1-D and their associated value of velocity as shown in Table 6.1. We would like to evaluate the approximation of the velocity gradient at every point using conventional SPH, normalised-corrected SPH and the type of correction used in the Total Lagrangian normalised-corrected SPH. In addition, we would like to evaluate the effect of symmetry terms over boundary particles.

Particle Number	Velocity Field	
	Linear	Constant
X1	-0.04	0.002
X2	-0.06	0.002
X3	-0.08	0.002
X4	-0.1	0.002
X5	-0.12	0.002
X6	-0.14	0.002

Table 6.1. Problem 3. Linear and constant velocity field values imposed over the SPH particles.

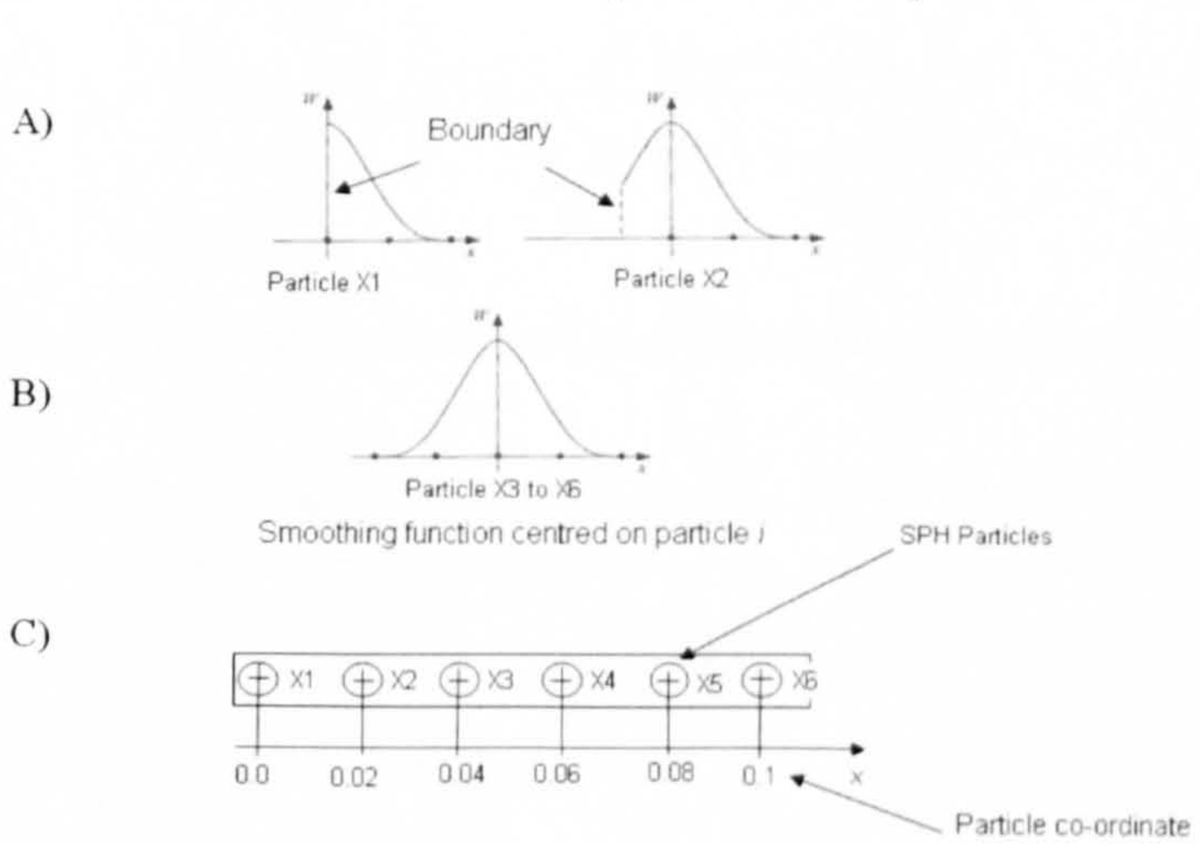

Fig. 6.6. Schematic diagram for Problem 3 C). This schematic diagram shows particles at the boundaries with a truncated smoothing function A) and internal particles with complete support B).

Objective.- The objective is to demonstrate how to restore 1st order consistency in the Total Lagrangian scheme through the introduction of correction and normalisation terms and to evaluate the effect of symmetry

terms over the value of approximated fields at boundary particles and at particles with complete supports.

SPH formulation used.-Three schemes were used for the numerical solution of this problem: Normalised SPH (with and without symmetry terms), normalised SPH in which the denominator of the smoothing function is kept constant (with and without symmetry terms), SPH without normalisation (with and without symmetry terms). The cubic spline was used as the smoothing function. The smoothing length scale factor was 1.2. The domain was discretised into 6 particles with a 0.02 m particle spacing (Fig. 6.6). The discrete values of velocity for each individual particle are shown in Table 6.1 for both the linear and the constant velocity fields (in $\frac{\mathrm{m}}{\mathrm{s}}$).

In Method A (refer to tables 6.2 and 6.3) the normalised smoothing function is expressed as follows:

$$\tilde{\mathrm{W}}\left(\vec{\mathbf{x}}_I - \vec{\mathbf{x}}_J, h\right) = \frac{\mathrm{W}\left(\vec{\mathbf{x}}_I - \vec{\mathbf{x}}_J, h\right)}{\sum_{J \in S} \mathrm{W}\left(\vec{\mathbf{x}}_I - \vec{\mathbf{x}}_J, h\right) \frac{m_J}{\rho_J}} \tag{6.6}$$

and the derivative of the normalised smoothing function is obtained as:

$$\nabla\tilde{\mathrm{W}}\left(\vec{\mathbf{x}}_I - \vec{\mathbf{x}}_J, h\right) = \frac{\nabla\mathrm{W}\left(\vec{\mathbf{x}}_I - \vec{\mathbf{x}}_J, h\right)\sum_{J \in S} \mathrm{W}\left(\vec{\mathbf{x}}_I - \vec{\mathbf{x}}_J, h\right)\frac{m_J}{\rho_J} - \mathrm{W}\left(\vec{\mathbf{x}}_I - \vec{\mathbf{x}}_J, h\right)\sum_{J \in S} \nabla\mathrm{W}\left(\vec{\mathbf{x}}_I - \vec{\mathbf{x}}_J, h\right)\frac{m_J}{\rho_J}}{\left(\sum_{J \in S} \mathrm{W}\left(\vec{\mathbf{x}}_I - \vec{\mathbf{x}}_J, h\right)\frac{m_J}{\rho_J}\right)^2} \tag{6.7}$$

In Method B, the normalised function is given as:

$$\tilde{\mathrm{W}}\left(\vec{\mathbf{X}}_J - \vec{\mathbf{X}}_I, h_0\right) = \frac{\mathrm{W}\left(\vec{\mathbf{X}}_J - \vec{\mathbf{X}}_I, h_0\right)}{\sum_{J \in S} \frac{m_J}{\rho_J} \mathrm{W}\left(\vec{\mathbf{X}}_J - \vec{\mathbf{X}}_I, h_0\right)} \tag{6.8}$$

and the derivative is approximated as:

$$\nabla_{\vec{\mathbf{X}}_J}\tilde{\mathrm{W}}_{IJ} = \frac{1}{C}\nabla_{\vec{\mathbf{X}}_J}\mathrm{W}_{IJ} \tag{6.9}$$

where:

$$C = \sum_{J\in S}\frac{m_J}{\rho_J}\mathrm{W}\left(\vec{\mathbf{X}}_I - \vec{\mathbf{X}}_J, h_0\right) \tag{6.10}$$

Note that the expression for the derivative of the smoothing function (6.9) could only be used in the Total Lagrangian SPH formalism where the neighbourhood of particle I (i.e. the denominator in (6.8)) remains constant.

Finally, in Method C the smoothing function is given by $\mathrm{W}\left(\vec{\mathbf{x}}_I - \vec{\mathbf{x}}_J, h\right)$ and its derivative is calculated as $\nabla\mathrm{W}\left(\vec{\mathbf{x}}_I - \vec{\mathbf{x}}_J, h\right)$.

Results.- The benefits of using a normalised scheme become clear in this example. Figures 6.7 through to 6.11 show the uncorrected and normalised values of the derivatives of the smoothing function for two particles with incomplete support (Particles 1 and 2) and a particle with complete support (Particle 3). The resulting values for the velocity gradient approximation can be found in Tables 6.2 and 6.3. Table 6.2 shows the approximation of a linear velocity field using three SPH schemes. In addition, the effect of symmetrisation terms over the value of the approximation is also given. SPH without normalisation (Approximation C in tables 6.2 and 6.3) is incapable of approximating the derivative, either with or without symmetrisation terms. The normalised scheme (Approximation B) can approximate the gradient only if the symmetrisation term is present in the equation whereas the scheme suggested by Vignjevic et al. , Bonet et al. [9,10,84] (Approximation A) requires no symmetrisation for the approximation of the derivatives. Table 6.3 provides the results for the approximation of a constant velocity field. All schemes can easily handle this problem, they all work well when the symmetrisation term is present and only one of them (Approximation A) provides accurate results when the symmetry term gets removed.

Note that the normalisation term suggested in scheme B could only work in the Total Lagrangian SPH formulation. In this particular case the value of the denominator in the normalised interpolating function remains constant due to the fact that the neighbourhood of each and every particle would remain unchanged throughout the numerical solution.

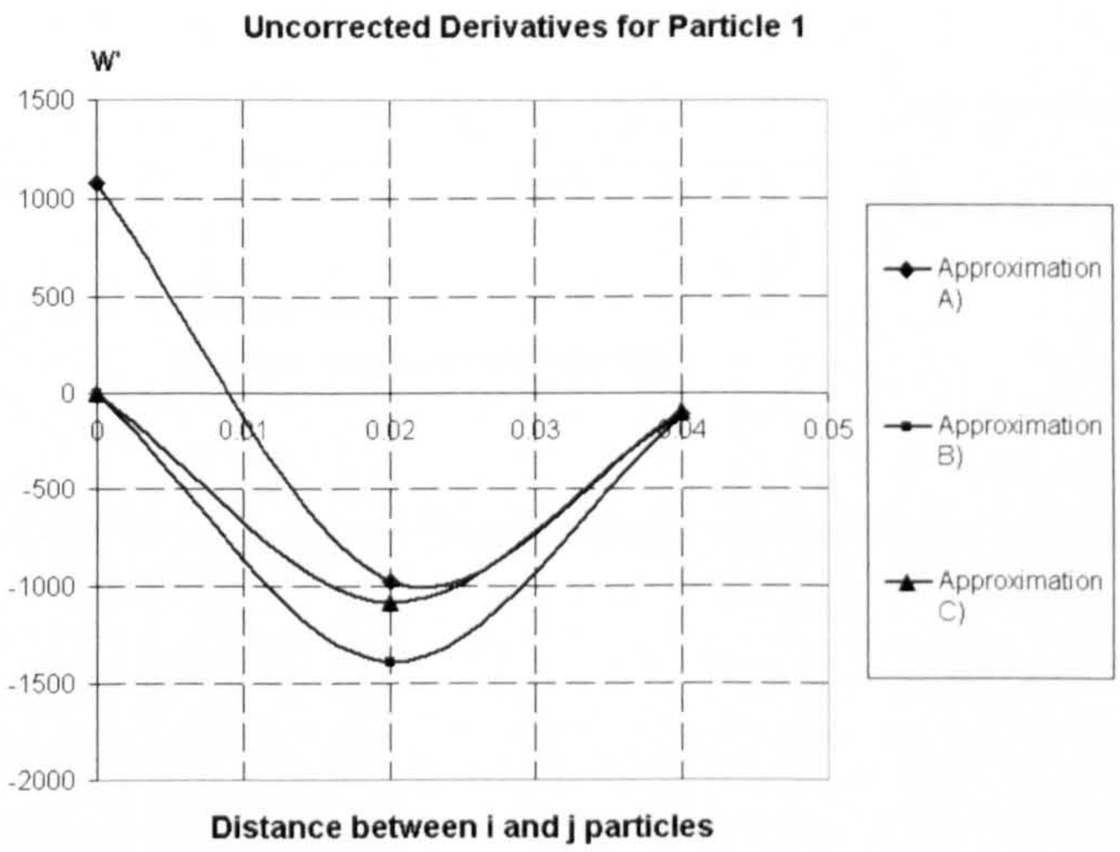

Fig 6.7. Problem 3. Uncorrected values of derivatives for particle X1, truncated support.

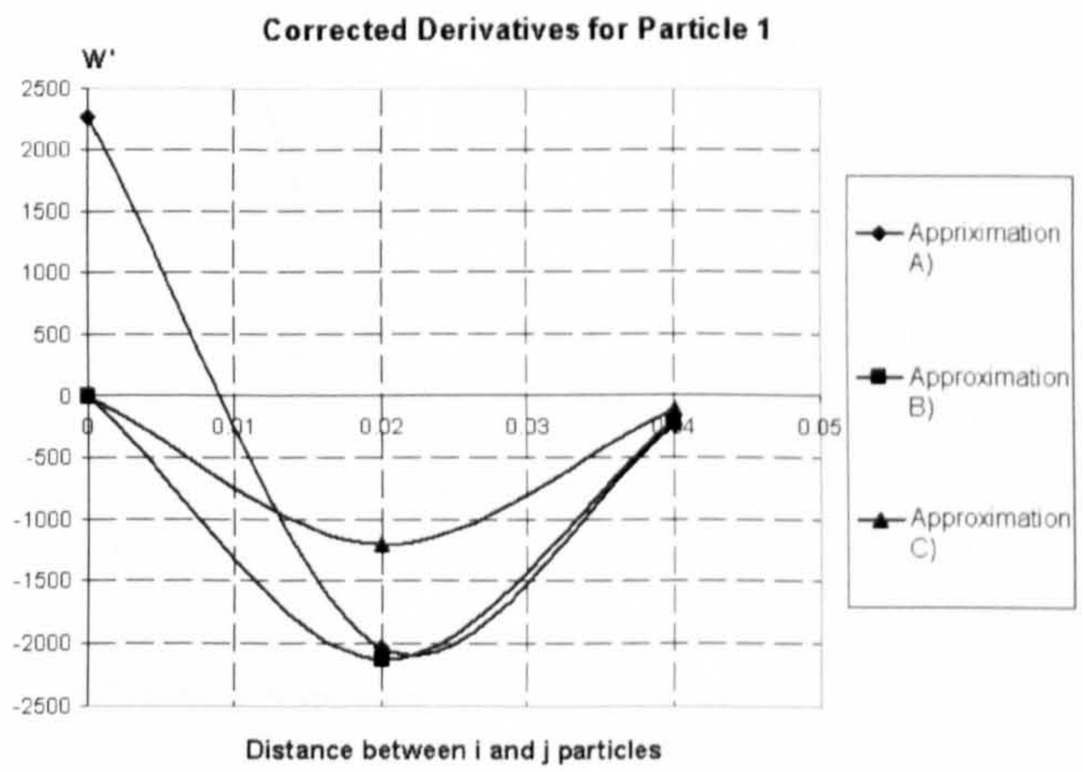

Fig 6.8. Problem 3. Corrected kernel derivative estimates for particle X1

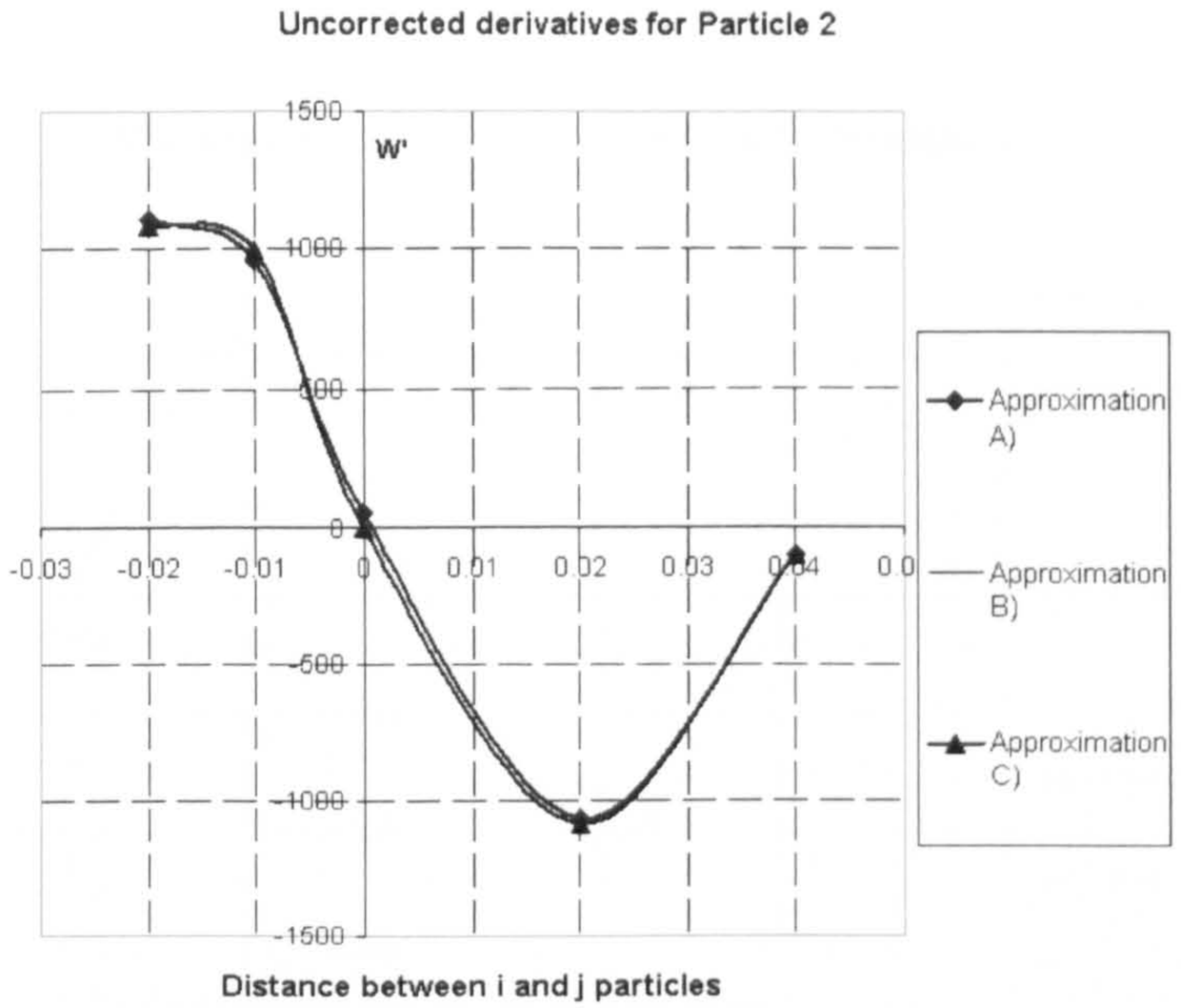

Fig 6.9. Problem 3. Uncorrected kernel derivative estimates for particle X2

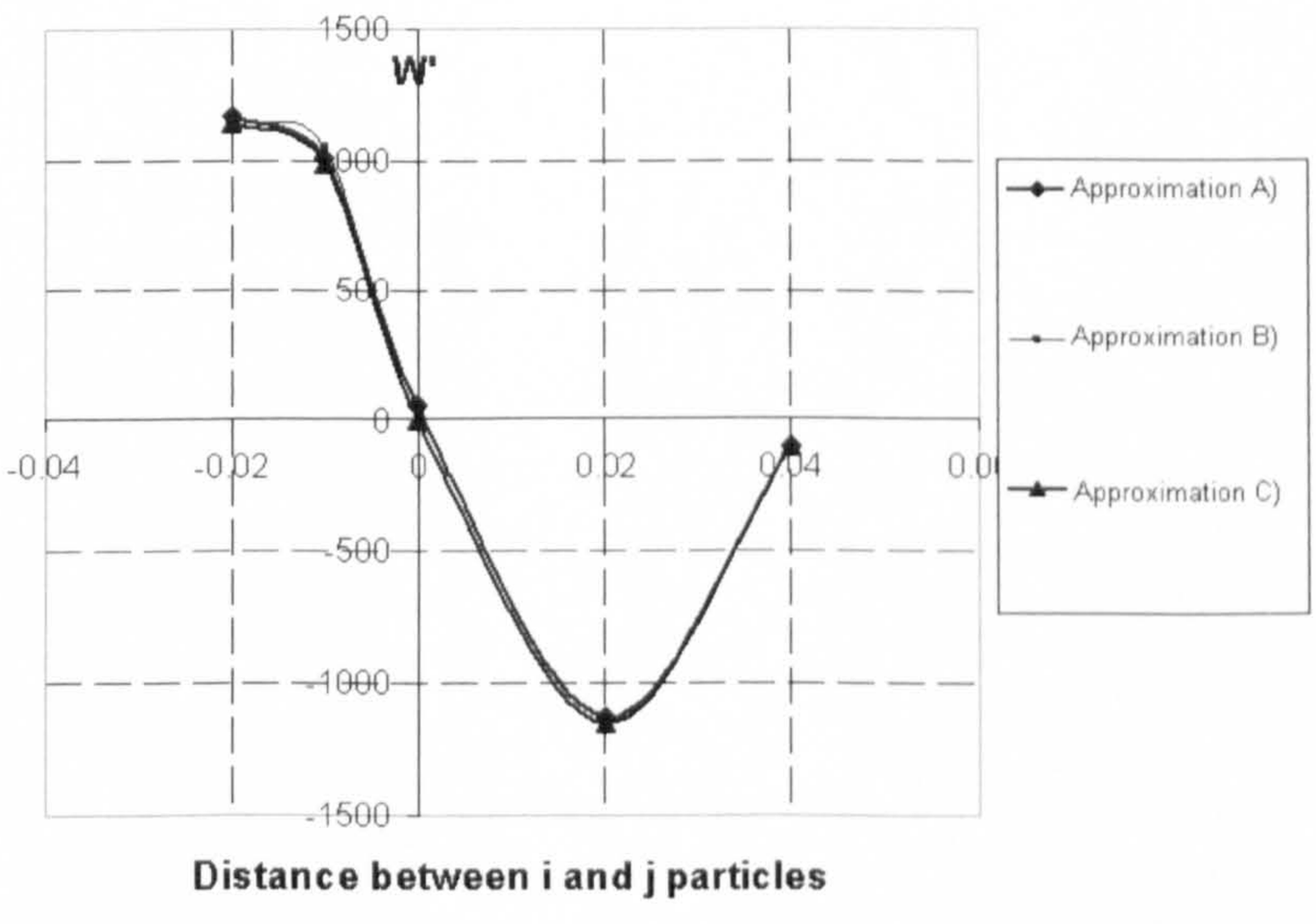

Fig 6.10. Problem 3. Corrected kernel derivative estimates for particle X2

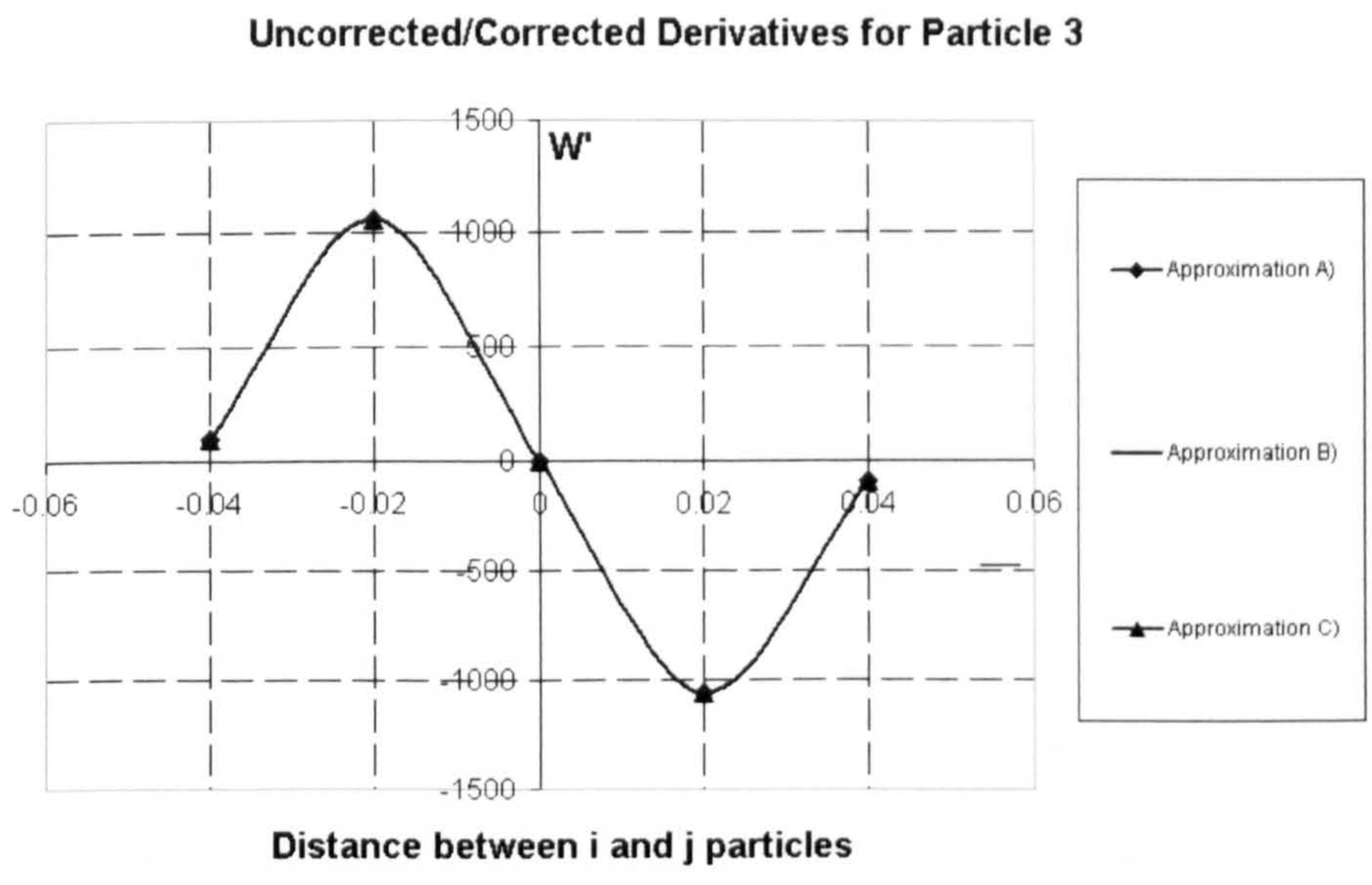

Fig 6.11. Problem 3. Corrected and uncorrected kernel derivative estimates for particle X3-X6

Method A)	$\nabla \tilde{W} = \frac{\nabla W * \sum WV - W \sum \nabla WV}{\sum WV^2}$
Mehotd B)	$\nabla \tilde{W} = \frac{1}{\sum WV} * \nabla W$
Method C)	$\nabla \quad W$

i Particle	With respect to particle	Corrected Derivative Value		
		Method A)	Method B)	Method C)
Particle 1	X2-X1	-2024.0987	-2122.5335	-1085.0600
	X3-X1	-237.8687	-188.6016	-96.4500
	X1-X1	2262.0091	0.0000	0.0000
Particle 2	X1-X2	1170.7575	1147.9624	1085.0600
	X2-X2	56.8991	0.0000	0.0000
	X3-X2	-1126.1052	-1147.9624	-1085.0600
	X4-X2	-101.5514	-102.0376	-96.4500
Particle 3	X1-X3	94.3253	94.3321	96.4500
	X2-X3	1061.8778	1061.8778	1085.0600
	X3-X3	0.0000	0.0000	0.0000
	X4-X3	-1061.8778	-1061.8778	-1085.0600
	X5-X3	-94.3253	-94.3253	-96.4500

Approximation of $\frac{\partial v}{\partial x}$ with no symmetrisation terms:

$$\nabla v_i = -\sum_{j \in S} \frac{m_j}{\rho_j} v_j \nabla W_{ij}$$

Using Method A)	Approximation for Particle 1:	0.0000
	Approximation for Particle 2:	0.0000
	Approximation for Particle 3:	0.0000
Using Method B)	Approximation for Particle 1:	0.0924
	Approximation for Particle 2:	0.0041
	Approximation for Particle 3:	0.0000
Using Method C)	Approximation for Particle 1:	0.0473
	Approximation for Particle 2:	0.0039
	Approximation for Particle 3:	0.0000

Approximation of $\frac{\partial v}{\partial x}$ with symmetrisation terms:

$$\nabla v_i = -\sum_{j \in S} \frac{m_j}{\rho_j} \left(v_j - v_i \right) \nabla W_{ij}$$

Using Method A)	Approximation for Particle 1:	0.0000
	Approximation for Particle 2:	0.0000
	Approximation for Particle 3:	0.0000
Using Method B)	Approximation for Particle 1:	0.0000
	Approximation for Particle 2:	0.0000
	Approximation for Particle 3:	0.0000
Using Method C)	Approximation for Particle 1:	0.0000
	Approximation for Particle 2:	0.0000
	Approximation for Particle 3:	0.0000

Method A)	$\nabla \tilde{W} = \frac{\nabla W * \sum WV - W \sum \nabla WV}{\sum WV^2}$
Mehotd B)	$\nabla \tilde{W} = \frac{1}{\sum WV} * \nabla W$
Method C)	$\nabla \quad W$

i Particle	With respect to particle	Corrected Derivative Value		
		Method A)	Method B)	Method C)
Particle 1	X2-X1	-2024.0987	-2122.5335	-1085.0600
	X3-X1	-237.8687	-188.6016	-96.4500
	X1-X1	2262.0091	0.0000	0.0000
Particle 2	X1-X2	1170.7575	1147.9624	1085.0600
	X2-X2	56.8991	0.0000	0.0000
	X3-X2	-1126.1052	-1147.9624	-1085.0600
	X4-X2	-101.5514	-102.0376	-96.4500
Particle 3	X1-X3	94.3253	94.3321	96.4500
	X2-X3	1061.8778	1061.8778	1085.0600
	X3-X3	0.0000	0.0000	0.0000
	X4-X3	-1061.8778	-1061.8778	-1085.0600
	X5-X3	-94.3253	-94.3253	-96.4500

Approximation of $\frac{\partial v}{\partial x}$ with no symmetrisation terms:

$$\nabla v_i = -\sum_{j \in S} \frac{m_j}{\rho_j} v_j \nabla W_{ij}$$

Using Method A)	Approximation for Particle 1:	-0.9999
	Approximation for Particle 2:	-0.9999
	Approximation for Particle 3:	-1.0004
Using Method B)	Approximation for Particle 1:	-2.8488
	Approximation for Particle 2:	-1.1224
	Approximation for Particle 3:	-0.9999
Using Method C)	Approximation for Particle 1:	-1.4564
	Approximation for Particle 2:	-1.0610
	Approximation for Particle 3:	-1.0224

Approximation of $\frac{\partial v}{\partial x}$ with symmetrisation terms:

$$\nabla v_i = -\sum_{j \in S} \frac{m_j}{\rho_j} \left(v_j - v_i \right) \nabla W_{ij}$$

Using Method A)	Approximation for Particle 1:	-0.9999
	Approximation for Particle 2:	-0.9999
	Approximation for Particle 3:	-1.0004
Using Method B)	Approximation for Particle 1:	-0.9999
	Approximation for Particle 2:	-1.0000
	Approximation for Particle 3:	-1.0004
Using Method C)	Approximation for Particle 1:	-0.5112
	Approximation for Particle 2:	-0.9452
	Approximation for Particle 3:	-1.0224

Tables 6.2 and 6.3 (right), Problem 3. The value of the normalised and not-normalised derivative of the interpolating function and the SPH approximation of the linear (right) and constant velocity fields are supplied with and without symmetry terms. The exact value should be 0.0 for the constant velocity field and 1.0 for the linear velocity field.

6.1.4 Linear elastic bar under longitudinal vibrations.

Problem 4.- The problem of axial vibrations of a 1-D rod of length L=0.006m and unit cross area is considered. The rod is clamped at x=0 and free at x=L. (see Fig. 6.12). The material is assumed to be elastic, homogeneous and isotropic [35]. The material properties are as follows: Density 4530 $\frac{kg}{m^3}$, Young Modulus 1.16 E 5 Pa , Poisson ratio 0.342. The initial conditions for this problem are given as a linear velocity field that goes from 0 at the clamped end to 6E2 $\frac{m}{s}$ at the free end as depicted in Figure 6.12. The particle displacement at time 0 s is 0 m.

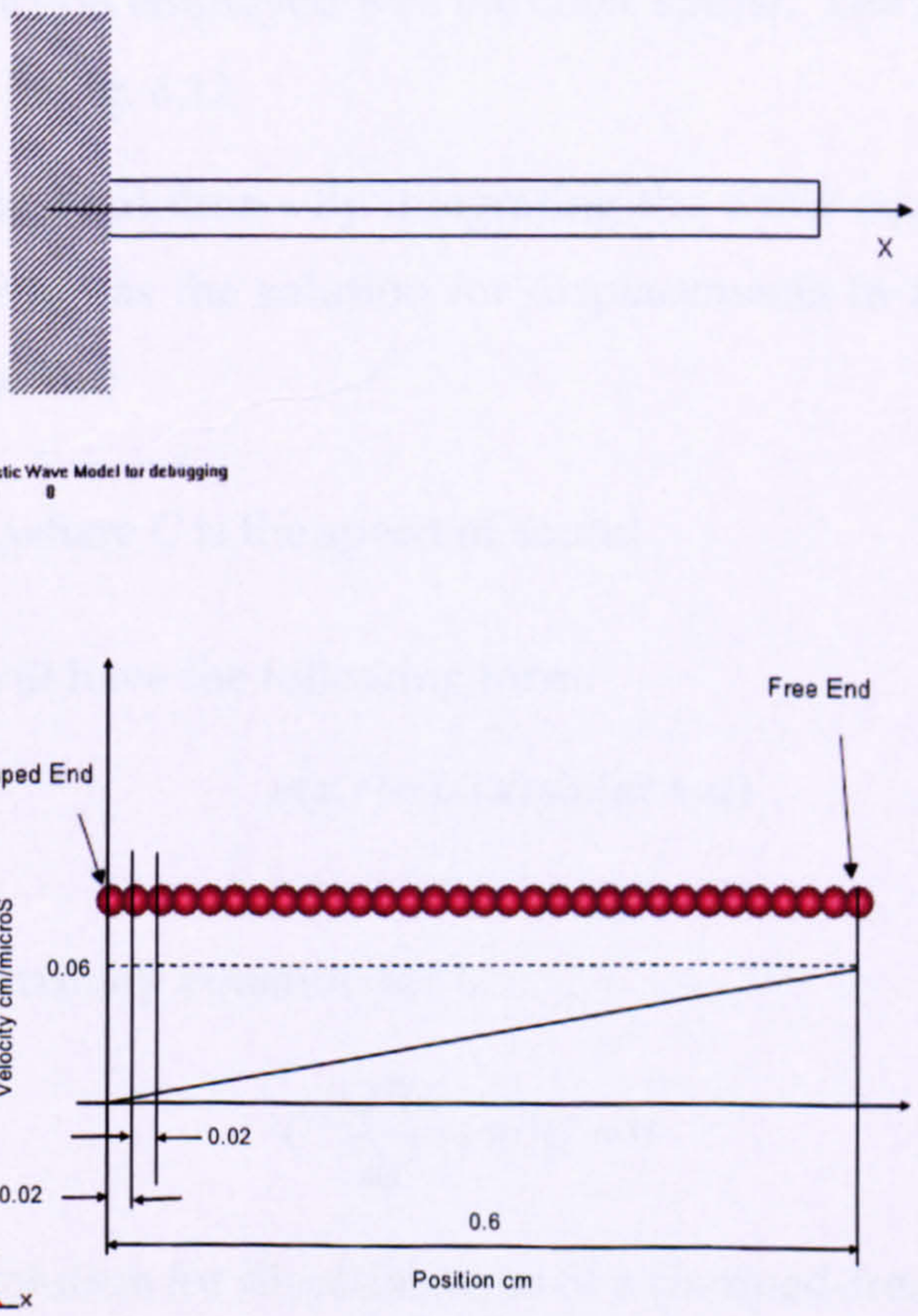

Fig 6.12. Schematic diagram for problem 8, SPH discretisation and initial conditions.

Objective.- The objective is to obtain the time response of the rod under these initial and boundary conditions. The second objective is to validate the results obtained with the normalised corrected Total Lagrangian SPH code when longitudinal vibration in a rod is generated as a consequence of a linear velocity field within the domain particles. Finally we would like to verify that 1st order consistency is restored and particle deficiency corrected.

SPH formulation used.- The normalised-corrected Total Lagrangian SPH scheme was used to simulate this problem. The rod was discretised into 31 particles and the initial condition is a linear velocity field as depicted in Fig. 6.12. The symmetrised form of the Total Lagrangian SPH equations was used for simulating this problem and the integration is fully collocational. The smoothing function employed was the cubic spline. The particle spacing is 2E-2 m as depicted in Fig. 6.12.

Analytical solution.- By integrating the wave equation we can obtain a harmonic function as the solution for displacements in the free vibration case.

The wave equation:

$\frac{\partial^2 u}{\partial x^2} = \frac{1}{C^2}\frac{\partial^2 u}{\partial t^2}$ where C is the speed of sound .

The solution will have the following form:

$$u(x,t) = U(x)\sin(\omega t + \alpha) \tag{6.11}$$

and with the auxiliary equation for U

$$C^2 \frac{d^2 U}{dx^2} + \omega^2 U = 0 \tag{6.12}$$

the complete solution for displacements of a clamped-free rod can be obtained:

$$u(x,t) = \sum_n B_n \sin\frac{(2n-1)\pi x}{2L}\sin\left[\frac{(2n-1)\pi C t}{2L} + \alpha_n\right] \tag{6.13}$$

where $n=1,2,3,\ldots$, L is the initial rod length, t is the time variable and the constants B_n and α_n are obtained for specified initial conditions:

In this specific example the initial conditions are given as follows:

$u(x,0)=0$ and $\frac{\partial u(x,0)}{\partial t}=Kx$ with $K=0.1$.

With these initial conditions, the values of the B_n and α_n constants are found to be 0.02941 and 0.0 respectively, thus the exact solution for the displacements along the rod is given by:

$$u(x,t)=0.02941\sin\left(\frac{\pi}{2L}x\right)\sin\left(\frac{\pi C}{2L}t\right) \tag{6.14}$$

with $C=\sqrt{\frac{E}{\rho}}$ (6.15) is the expression to calculate the speed of sound.

Results.- The exact and SPH solutions for particles X=0.02E-2m, X=0.03E-2m and X=0.06E-2m are provided in Fig. 6.13. It is clear from this figure that the SPH approximation is remarkably accurate since both solutions overlap. The internal and kinetic energy of the bar are shown in Fig 6.14 as a function of time As expected the value of internal energy in the bar decreases to a minimum when the kinetic energy is at a maximum and vice-versa. Two approaches to quantify the error in the period and the amplitude are provided by figures 6.15 and 6.16. The evolution of the error in the period for X=0.02E-2 m, 0.03E-2 m and 0.06E-2 m is given in Fig. 6.14. It can be noted that as the simulation progresses, the error in the period drops. Finally, the positional error of all particles within the rod is shown in Fig 6.15 for time step t=12.4 μs.

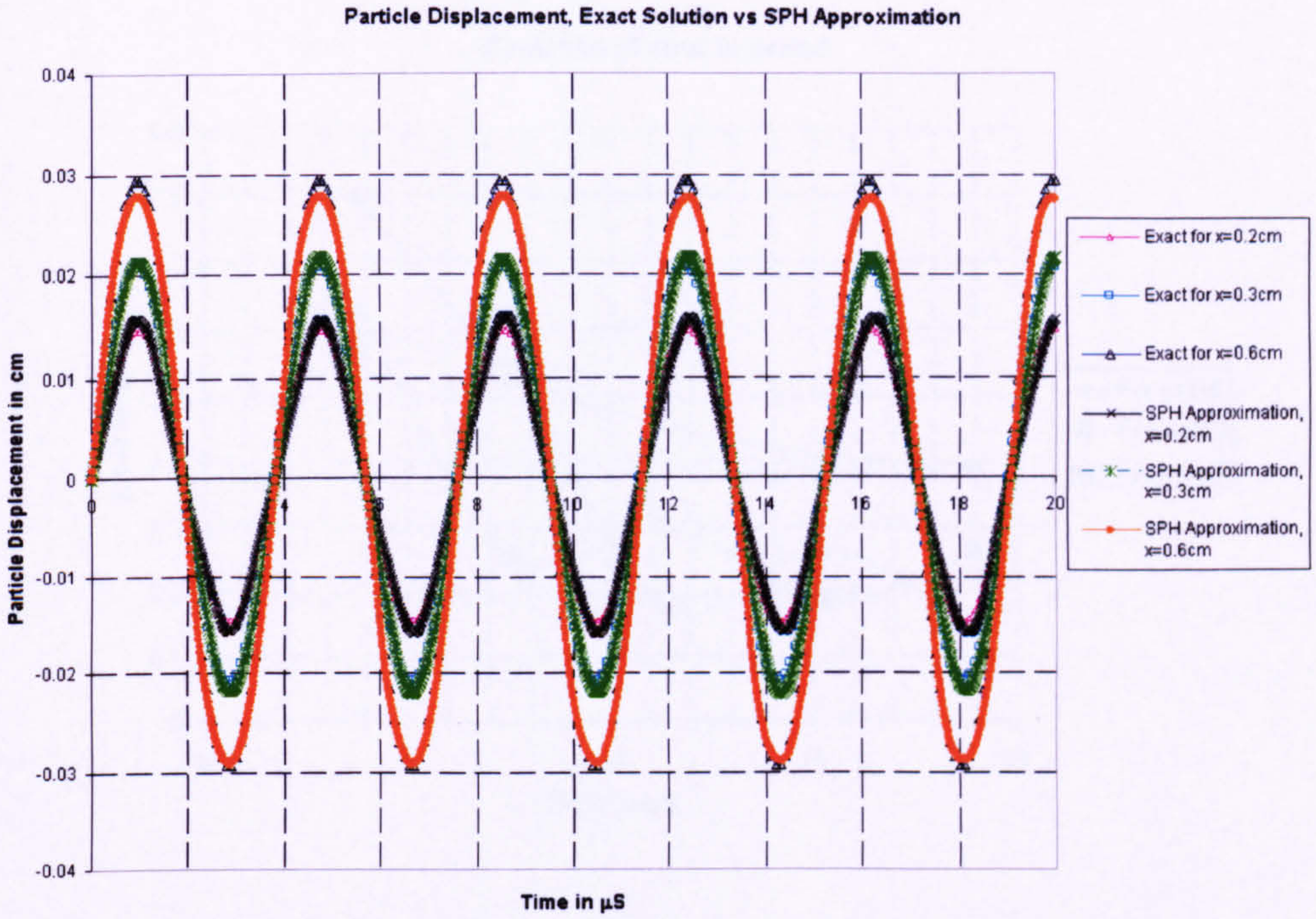

Fig. 6.13. Problem 4. Particle displacement, Exact vs SPH solution

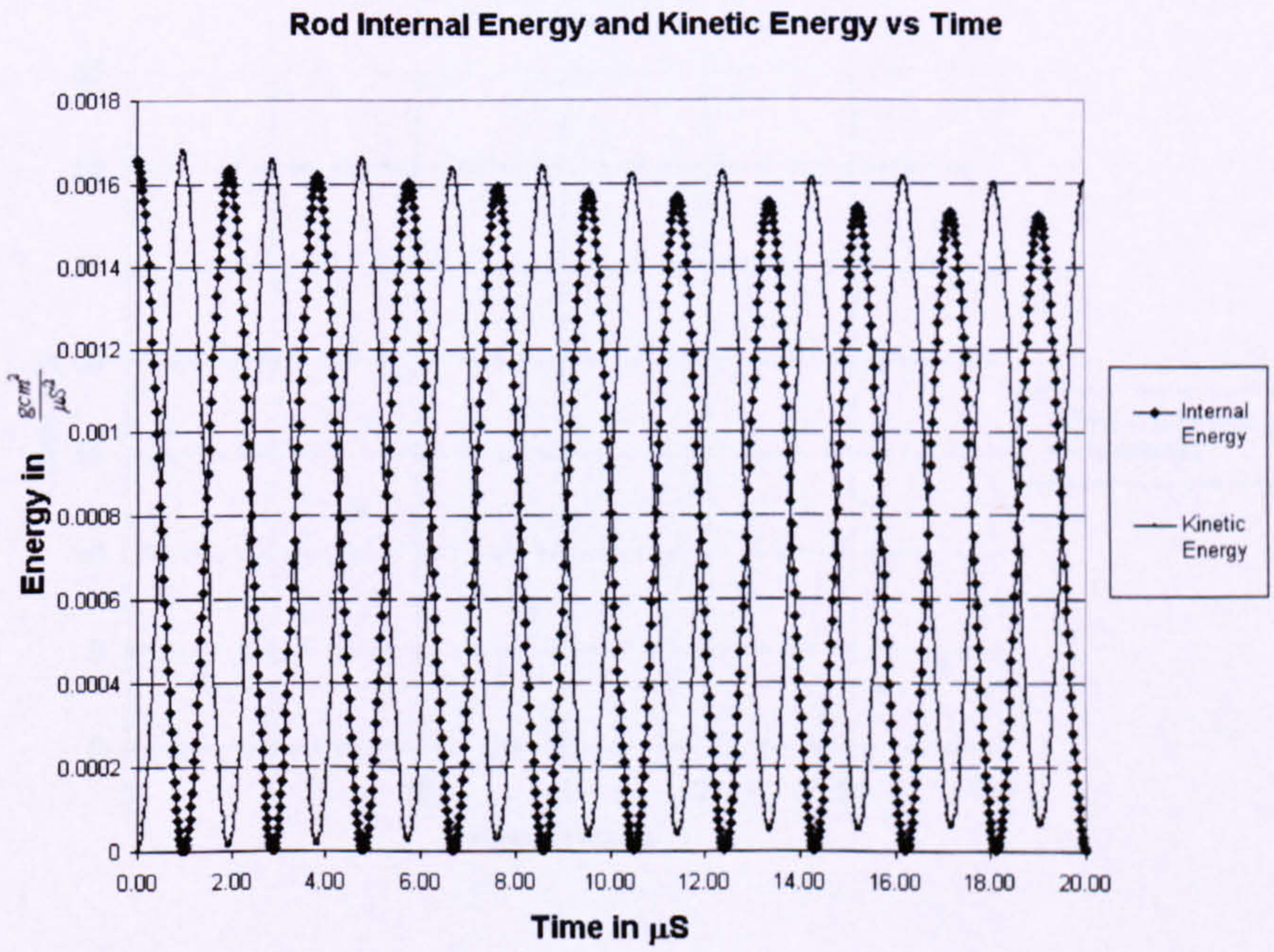

Fig.6.14. Problem 4. Kinetic Energy and Internal Energy vs Time

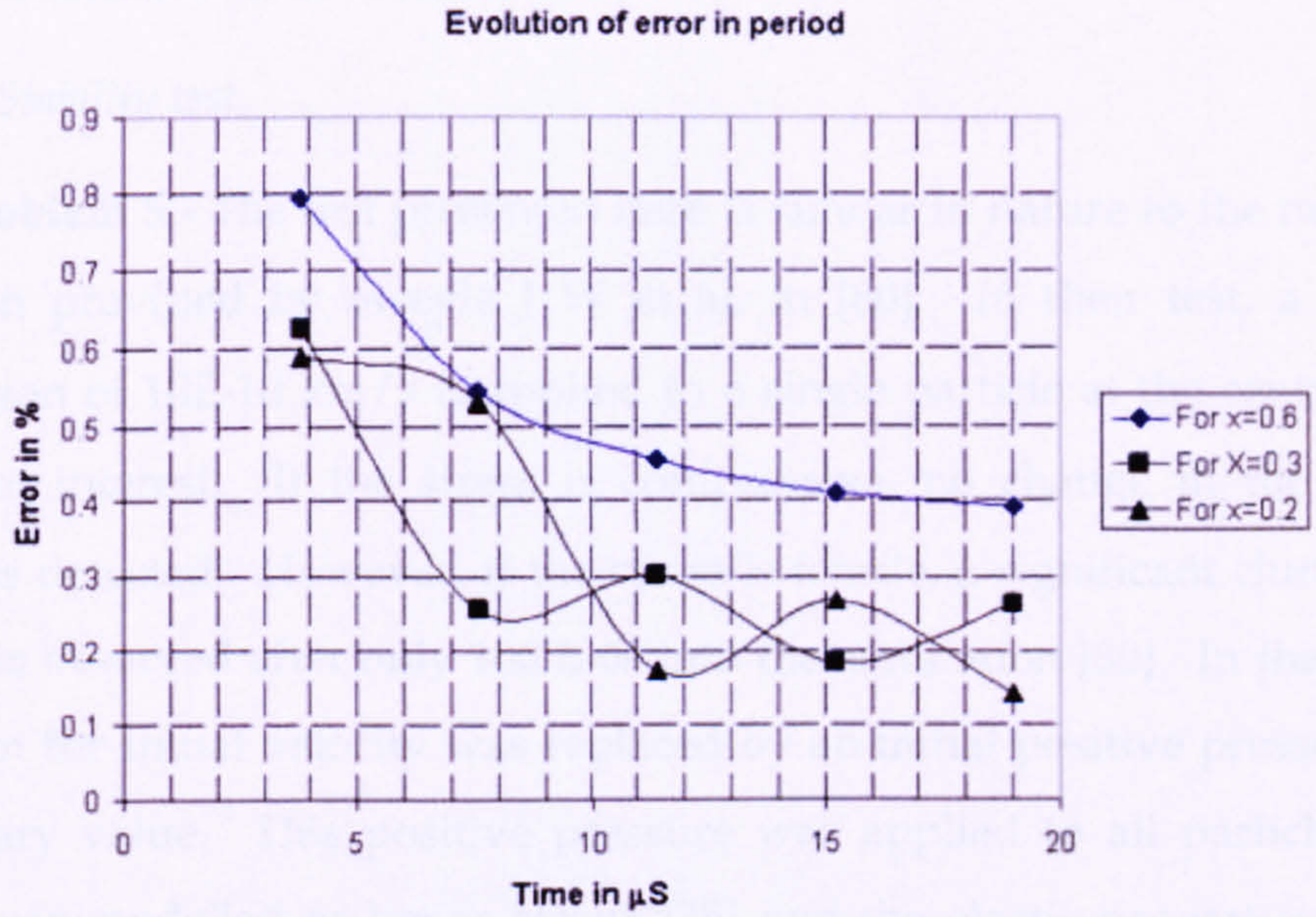

Fig. 6.15. Problem 4. Error evolution in the approximation of the period.

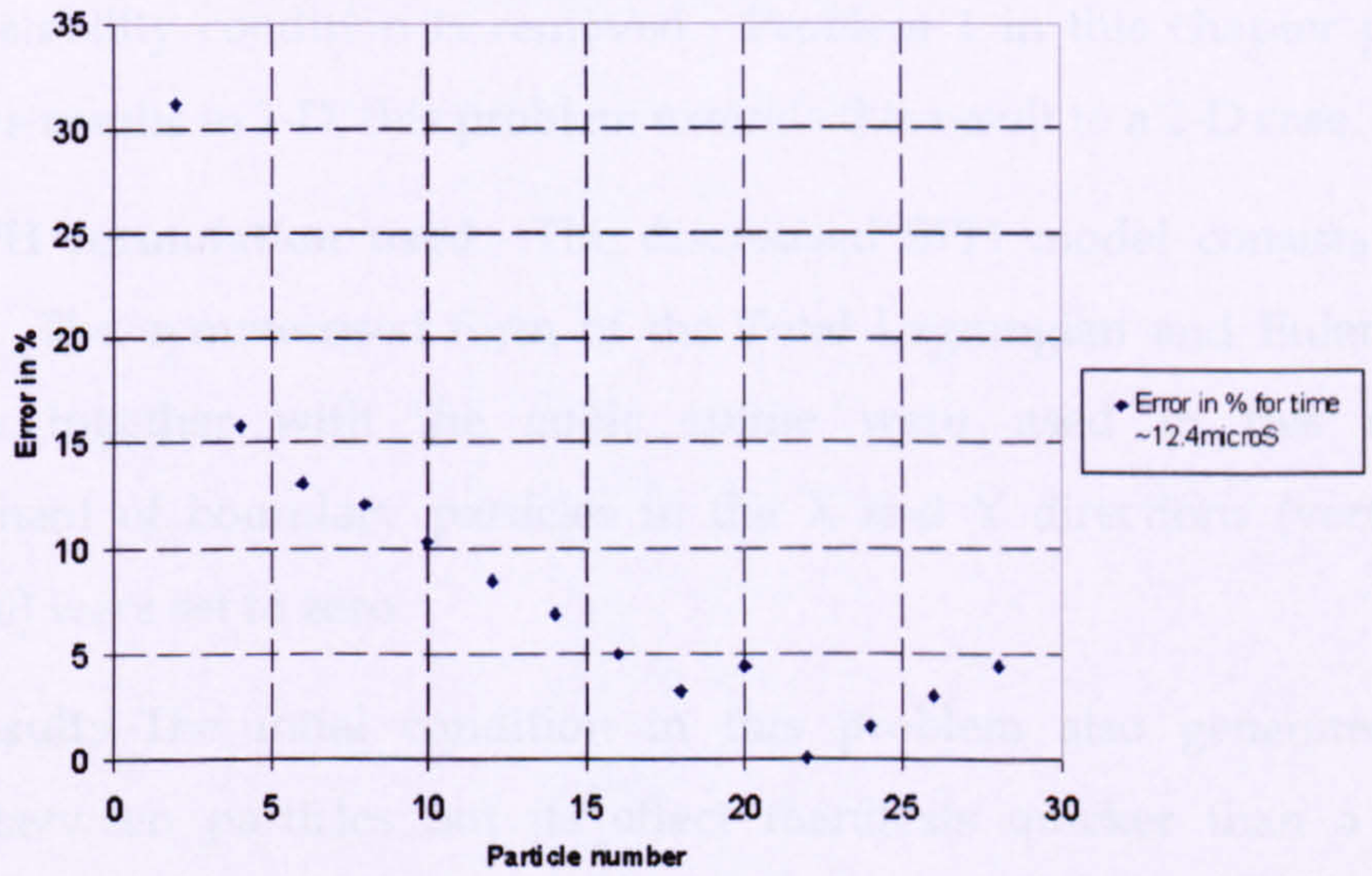

Fig. 6.16. Problem 4. Error estimate for particle amplitude at 12.4 μs.

6.2 Two-Dimensional Problems

6.2.1 2D Stability test.

Problem 5.- The test presented here is similar in nature to the numerical simulation provided by Swegle J W et al. in [80]. In their test, a velocity perturbation of 10E-10 km/s is applied to a single particle at the centre of the domain of interest. If the stress is compressive, no change in the particle position is detected. However, if the stress is tensile, a significant clumping of particles is observed after only 100 E-6s into the simulation [80]. In the present simulation the initial velocity was replaced by an initial positive pressure with an arbitrary value. This positive pressure was applied to all particles. The domain was modelled as linear elastic [35] and the elastic properties of steel were used.

Objective.- The aim of this numerical experiment is to qualitatively demonstrate that when the conservation laws are expressed in a Total Lagrangian form and discretised in an Total Lagrangian SPH framework, the tensile instability condition is removed. Problem 1 in this chapter provided qualitative results in 1-D, this problem extends this result to a 2-D case.

SPH formulation used.- The discretised SPH model consists of 2000 particles. The symmetrised form of the Total Lagrangian and Eulerian SPH equations together with the cubic spline were used in this example. Displacement of boundary particles in the X and Y directions (vertical and horizontal) were set to zero.

Results.-The intial condition in this problem also generates tensile stresses between particles but its effect manifests quicker than a velocity perturbation. The results presented here are for time t=0.6E-6s in the case of the Eulerian code (equivalent to 28 time steps) and 1.36E-5s in the case of the Total Lagrangian code (equivalent to 586 time steps). The superior stability qualities of the Total Lagrangian code become evident. The particles have clumped together when Eulerian kernels have been used. By contrast, the particles in the

Total Lagrangian SPH simulation have maintained their inter-particle distance.

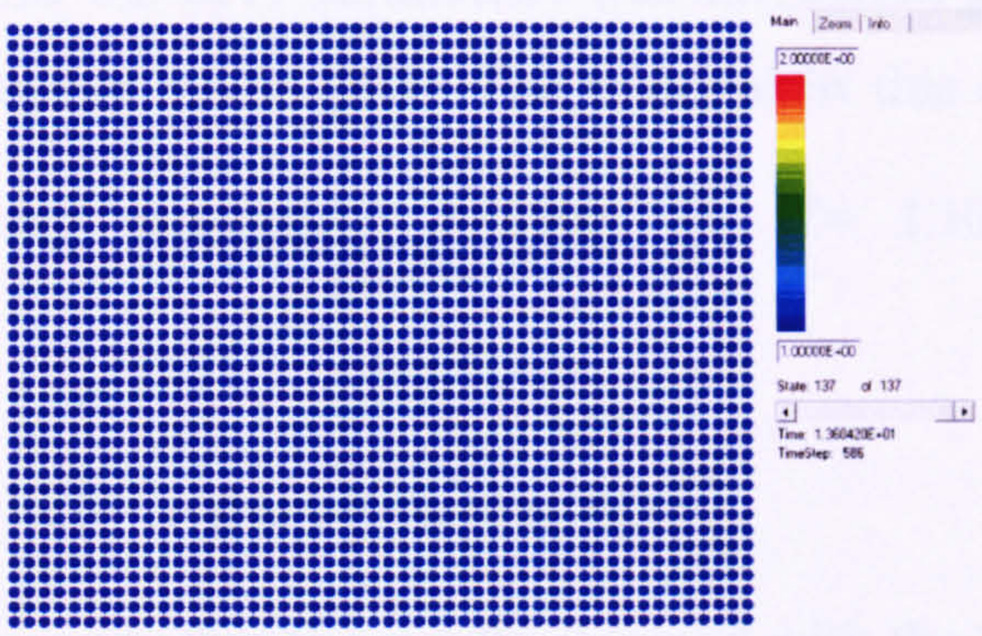

Fig. 6.17. Problem 5. An initial pressure value was assigned as an initial condition. Simulation shows result after 586 time steps, t= 13.6 μs, Lagrangian Kernel.

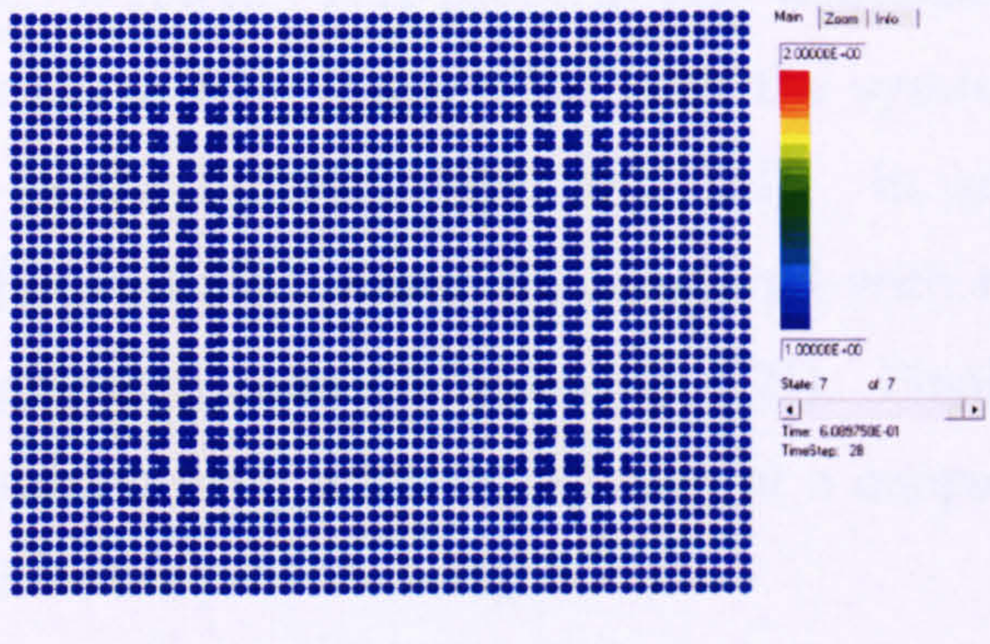

Fig. 6.18. Problem 5. An initial pressure value was assigned as an initial condition. Simulation shows result after 28 time steps, t=0.6 μs, Eulerian Kernel.

6.2.2 2-D Taylor test code validation

Problem 6.- The Taylor test is frequently used in material characterisation and validation of constitutive laws. Here the Total Lagrangian SPH results are compared to those obtained through the use of a standard non-linear explicit FE code (LS-DYNA). In addition, this problem is used to verify that the symmetry planes option in the MCM code is fully compatible with the Total Lagrangian SPH scheme. The same problem is treated in 3-D and contours of plastic deformation are presented in the results section of this problem.

In the Taylor test a small cylinder undergoes dynamic loading and, unlike a cylinder deformed quasi-statically, it experiences non-uniform deformation.

Only half a cylinder is modelled in this example. The material model employed in both the FE and the SPH simulation was the elastic-plastic with isotropic hardening constitutive model [35]. The material in this simulation is copper with the following properties: ρ=8990 $\frac{kg}{m^3}$, E= 1.10E 11 Pa, ν=0.343, σ_Y =9.00E7 Pa.

The impact velocity in this problem is 100 $\frac{m}{s}$.

Objective.- To verify that the results obtained with the 2-D Total Lagrangian SPH code correlate well with results obtained with a standard non-linear explicit FE code (LS-DYNA). This problem also demonstrates that the Total Lagrangian SPH code is fully compatible with the symmetry planes option already available in the Eulerian SPH code [34]. In addition, the results obtained with a standard SPH solver are compared with the results obtained with the Total Lagrangian code (Refer to Fig. 6.21). Finally, effective plastic strain contours resulting from a 3-D simulation of a copper cylinder with the same initial conditions are provided (Fig. 6.22).

SPH formulation used.- The discretised SPH model consists of 4000 particles. Only half of the 2-D domain was simulated in this problem and symmetry planes were imposed to ensure no unphysical particle penetration on the symmetry boundary took place. The symmetrised form of the Total Lagrangian SPH equations and the cubic spline were used in this example. The FE model consists of 1200 shell elements [35]. The symmetry boundary formulation applied makes use of the "ghost particles" method and the detailed formulation and implementation can be found in [34].

Analytical solution.-

Based on the theoretical analysis of a Taylor test as described in [61], for a copper bar of 4cm length and 0.74 cm of initial diameter travelling at 100 $\frac{m}{s}$, the expected final length and diameter after impact are 2.8cm and 1.48cm respectively . The Total Lagrangian SPH code predicts a final length of 3.01 cm

and a 1.47cm final diameter. The definition of effective plastic strain can be found in [61] as $\bar{\varepsilon}^p = \frac{\sqrt{2}}{3}\left[\left(\varepsilon_1^p - \varepsilon_2^p\right)^2 + \left(\varepsilon_1^p - \varepsilon_3^p\right)^2 + \left(\varepsilon_2^p - \varepsilon_3^p\right)^2\right]^{1/2}$ where the values of plastic strain inside the parenthesis are defined as the principal values of plastic strain.

Results.-

The resulting effective plastic strain obtained with the FE code (LS-DYNA) was compared to the Total Lagrangian SPH result with an excellent correlation observed, as depicted in Fig. 6.19 and Fig. 6.20.

The same problem was simulated using the Eulerian SPH code with the result observed in Fig. 6.21 where the computations were finished prematurely due to the presence of numerical instability.

Finally, the same problem was simulated in a 3-D domain with the result observed in Fig. 6.22. The final value of effective plastic strain in this case correlates very well to the simpler 2-D case.

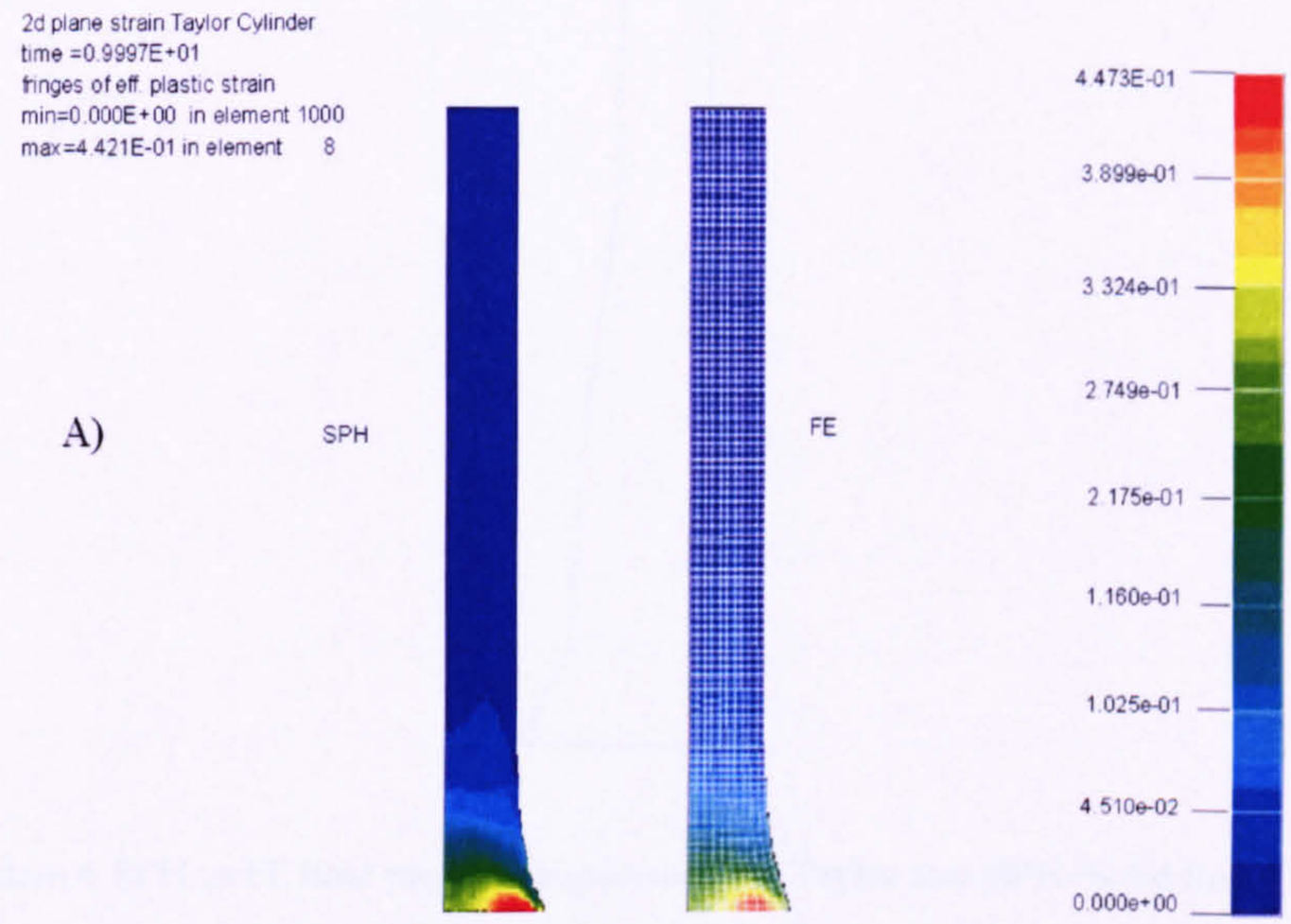

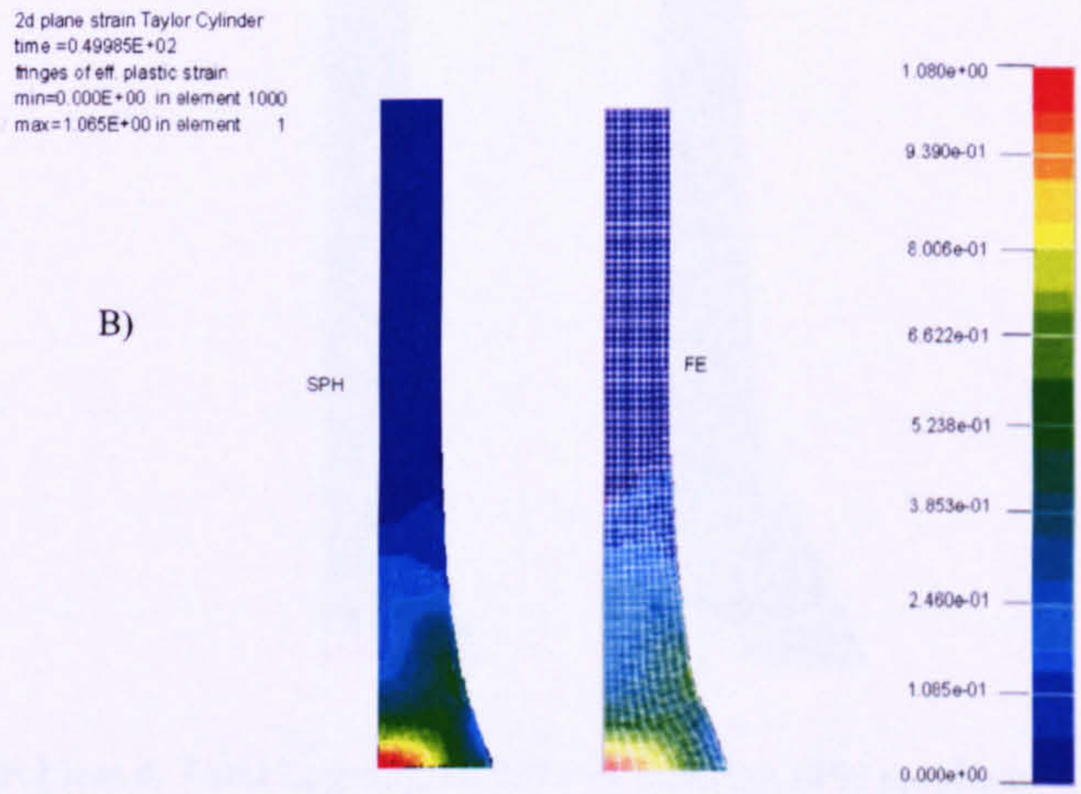

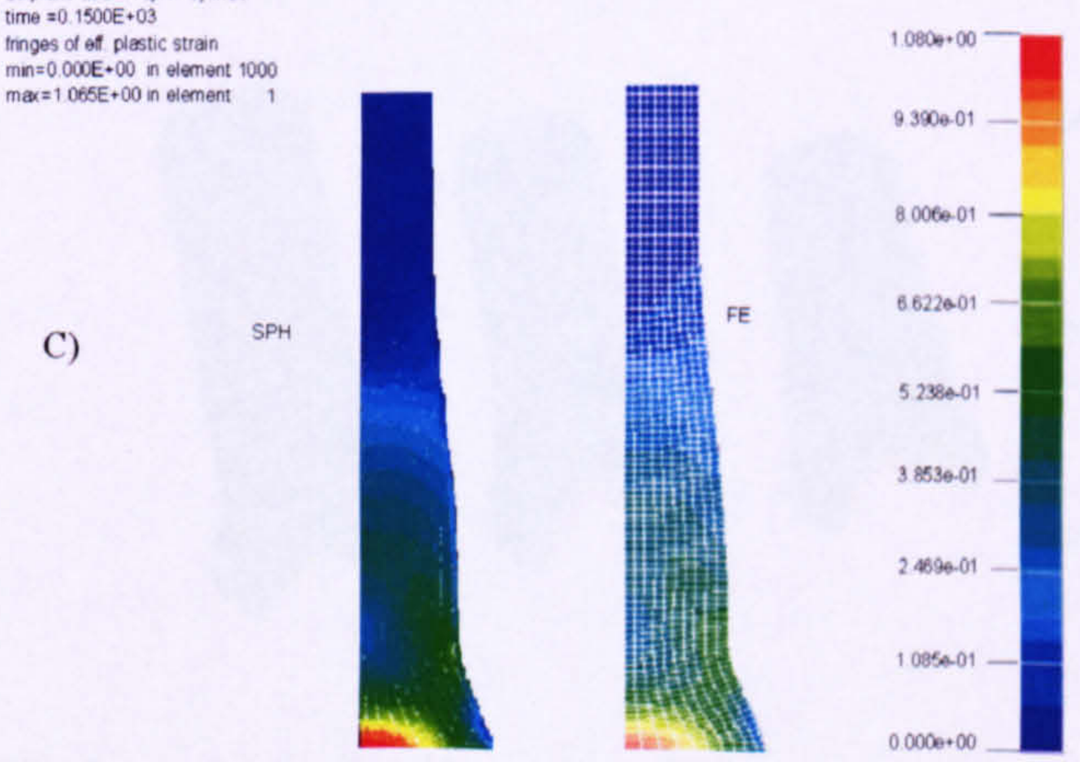

Fig. 6.19. Problem 6. 2D Taylor impact of a copper rod , 100m/s, SPH vs DYNA FE simulation using the Total Lagrangian code . Effective plastic strain shown. A) t=9.99 μs, B) t= 49.9 μs, C) t=150 μs,

Fig 6.20. Problem 6. SPH vs FE final profile comparison, 2-D Taylor test (SPH=Solid line, FE=Dashed line)

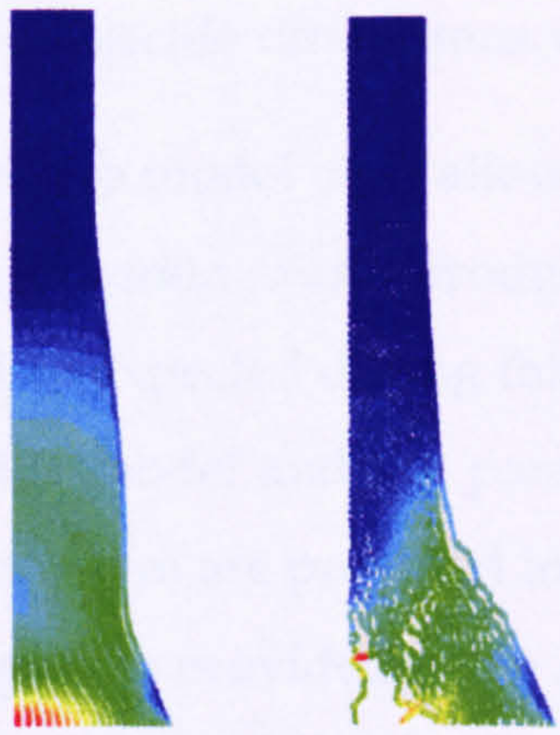

Fig 6.21. Problem 6. Total Lagrangian SPH vs Eulerian SPH results of a Taylor test.

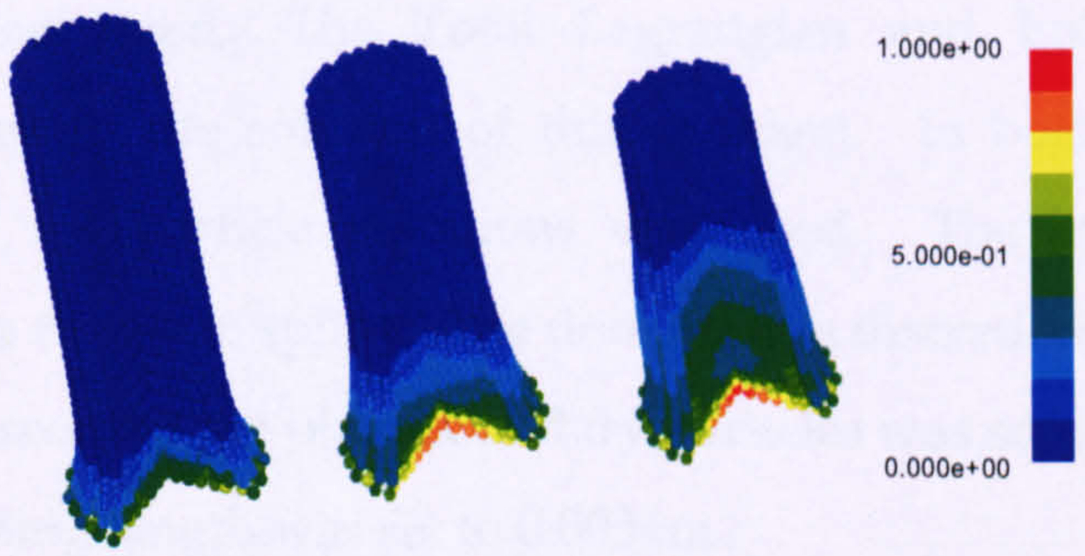

Fig 6.22 Problem 6. 3-D Taylor test using Total Lagrangian SPH with symmetry planes, 100m/s. Contours of effective plastic strain shown.

6.3 Three Dimensional Problems.

6.3.1 3D Stability test.

Problem 7.- The impact of a steel prism on an aluminium plate was used to demonstrate that the 3-D code is also stable, similarly to the 1-D and the 2-D Total Lagrangian codes. The prism was modelled as a linear elastic material [35], the plate was modelled using the Johnson-Cook material model without damage [35] and an equation of state was employed to update the pressure and allow for the capturing of shock waves [35,78]. The perimeter of the plate was fixed. The plate material used was Al7010T7651 and its dimensions were 0.30 x 0.30 m with a 0.011 m thickness. The initial velocity of the projectile was 137.00 $\frac{m}{s}$ with a 0.74 kg mass. The projectile dimensions were 0.033m by 0.033m by 0.087m in length. The constitutive model used allowed for plastic deformation of the plate but no fracture criterion was introduced. In other words, no fracture of the domain should be expected during this simulation. The material properties, detailed constitutive model and the parameters of the equation of state which characterise this problem are provided in Problem 8 in this chapter, in reference [35] and in the input file provided in the Appendix.

Objective.- The objective of this problem is to qualitatively assess the stability of the 3-D Total Lagrangian SPH code.

SPH formulation used.- The Total Lagrangian and Eulerian SPH formulations were used in the solution of this problem. In both cases, the symmetrised form of the particle equations was used. The interpolating function employed was the cubic spline. The domain was discretised into 47730 particles. The displacement of the plate boundary particles was set to zero in all directions. The smoothing length was set to 0.0034m.

Results.- The results shown in Fig. 6.23 demonstrate that whereas numerical fracture is present in the Eulerian formulation (which is the result of tensile instability) the Total Lagrangian code exhibits no numerical fracture.

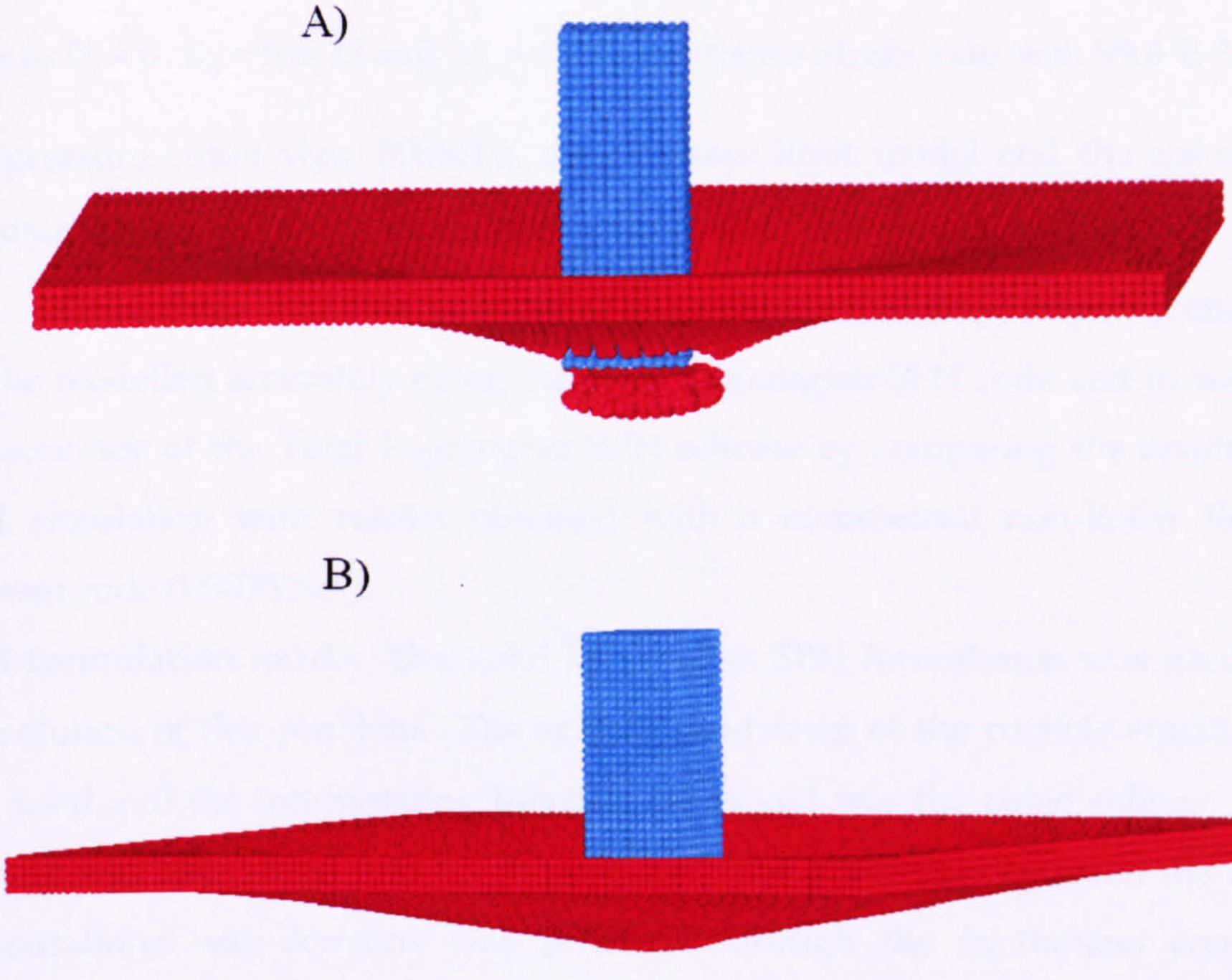

Fig. 6.23. Problem 7. A) Numerical fracture, Eulerian SPH, B) No numerical fracture, Total Lagrangian SPH

6.3.2 3-D Normal impact of a steel prism on an aluminium plate.

Problem 8.- This problem illustrates the normal impact of a prismatic projectile on a square, 0.30 x 0.30 m Al7010T7651 plate with a 0.011 m thickness. The projectile velocity is 137.00 $\frac{\text{m}}{\text{s}}$ with 0.74 kg mass and it is characterised as linear elastic [35]. The projectile dimensions are 0.033m by 0.033m by 0.087m in length. The material model employed to update the flow stress of the target plate is the Johnson-Cook Model with damage [35]. The input file for this problem can be found in the Appendix. . The non-standard material constants

used in the Johnson-Cook model were: A=479MPa, B=323MPa, n=0.410, C=0.101, m=1.80, $T_{melt} = 850\text{K}$ $T_{room} = 300\text{K}$ $D_1 = 0.450$ $D_2 = 0, D_3 = 0, D_4 = 0.0138$ and $C_1 = 68.63$, reference strain rate was 99.6 E-3 $\frac{1}{s}$, the pressure cutoff was -800MPa, the pressure limit model and the accurate iteration option for plastic strain were employed in this simulation [35].

Objective.- The objectives are to demonstrate that a real impact scenario can be modelled accurately using the Total Lagrangian SPH code and to assess the accuracy of the Total Lagrangian SPH scheme by comparing the resulting SPH simulation with results obtained with a commercial non-linear finite element code (LS-DYNA).

SPH formulation used.- The Total Lagrangian SPH formulation was used in the solution of this problem. The symmetrised form of the particle equations was used and the interpolating function employed was the cubic spline. The domain was discretised into 47730 particles. The interaction between the two computational sub-domains was achieved through the frictionless contact algorithm developed by Vignjevic et al. [84]. The displacement of the plate boundary particles was set to zero in all directions. The smoothing length was set to 0.0034m.

Analytical background.- The yield surface of the aluminium plate is described through the Johnson-Cook model:

$$\sigma_{yield} = (A + B\bar{\varepsilon}^{p^n})(1 + C\ln(\dot{\varepsilon}^*))\left[1 - (T^*)^m\right] \tag{6.16}$$

where A, B, C, n, and m are non-standard material constants, $\bar{\varepsilon}^p$ is the effective plastic strain and the temperature T^* is the homologous temperature raised to the power m in Eq. (6.16). This is given by:

$$T^* = \frac{T - T_{room}}{T_{melt} - T_{room}} \tag{6.17}$$

The Johnson-Cook model also includes damage parameters that enable element or particle deletion at a specified effective plastic strain

$$\varepsilon_f = \left[D_1 + D_2 \exp\left(D_3 \sigma^*\right)\right]\left[1 + D_4 \ln\left(\dot{\varepsilon}^*\right)\right]\left[1 + D_5 T^*\right] \tag{6.18}$$

where ε_f is the strain at failure, D_1 – D_5 are the failure parameters and σ^* is the ratio of pressure divided by the effective stress:

$$\sigma^* = \frac{P}{\bar{\sigma}} \tag{6.19}$$

where effective stress $\bar{\sigma}$ is found from:

$$\bar{\sigma} = \sqrt{\frac{3}{2} S_{ij} S_{ij}} \tag{6.20}$$

Fracture occurs when the damage parameter D:

$$D = \sum \frac{\Delta \bar{\varepsilon}^p}{\varepsilon_f} \tag{6.21}$$

reaches the value of 1.

The Johnson-Cook model requires an equation of state to be specified. The linear polynomial equation of state was used to capture shocks in the target plate and update the spherical part of the stress tensor. The polynomial equation of state is expressed as follows:

$$P = C_0 + C_1 \mu + C_2 \bar{\mu}^2 + C_3 \mu^3 + + \left(C_4 + C_5 \mu + C_6 \bar{\mu}^2\right) E \tag{6.22}$$

where E is the internal energy, C_0 – C_6 are coefficients with C_1 being the bulk modulus, and the excess compression μ is:

$$\mu = \frac{\rho}{\rho_0} - 1 \tag{6.23}$$

with ρ_0 as the initial material density.

Results.- Figures 6.24 and 6.25 show the results of the simulation using the Total Lagrangian SPH code. Figure 6.24 is a sequence of the impact of the steel prism on the aluminium target. The impact event lasts for about 1 ms from the moment of impact to prism rebound. The levels of effective plastic strain sustained by the plate are provided by figure 6.25. The maximum plastic strain levels are found at the indentations generated by the prism corners and these have values of 0.17. Figures 6.25 through to figure 6.29 provide a comparison between the SPH and the FE results (LS-DYNA). The correlation observed is remarkable.

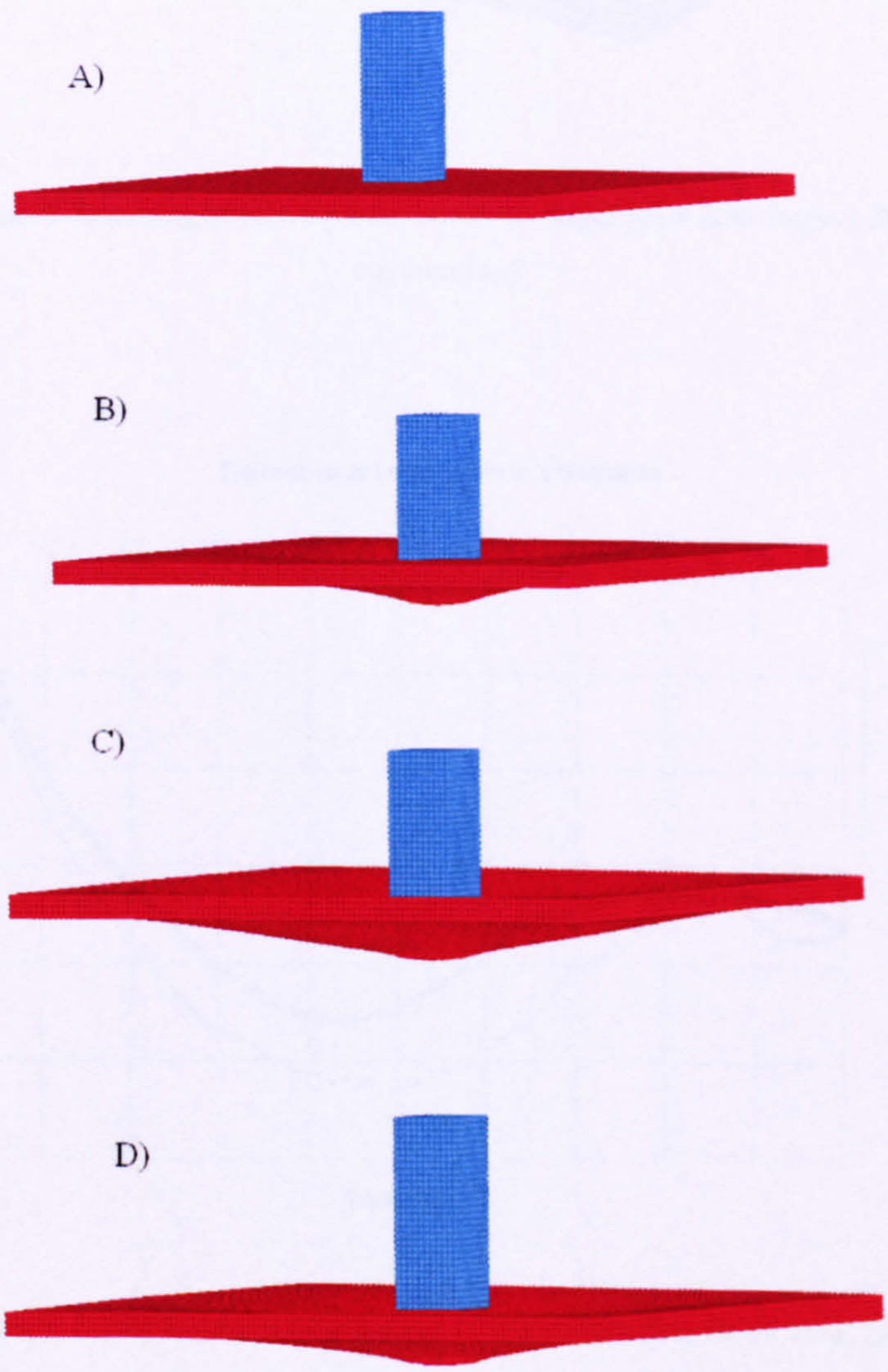

Fig. 6.24. Problem 8. Sequence of a prismatic projectile impacting a plate. A) t=0 ms, B) t=0.15 ms, C) t=0.30 ms, D) t=0.8 ms.

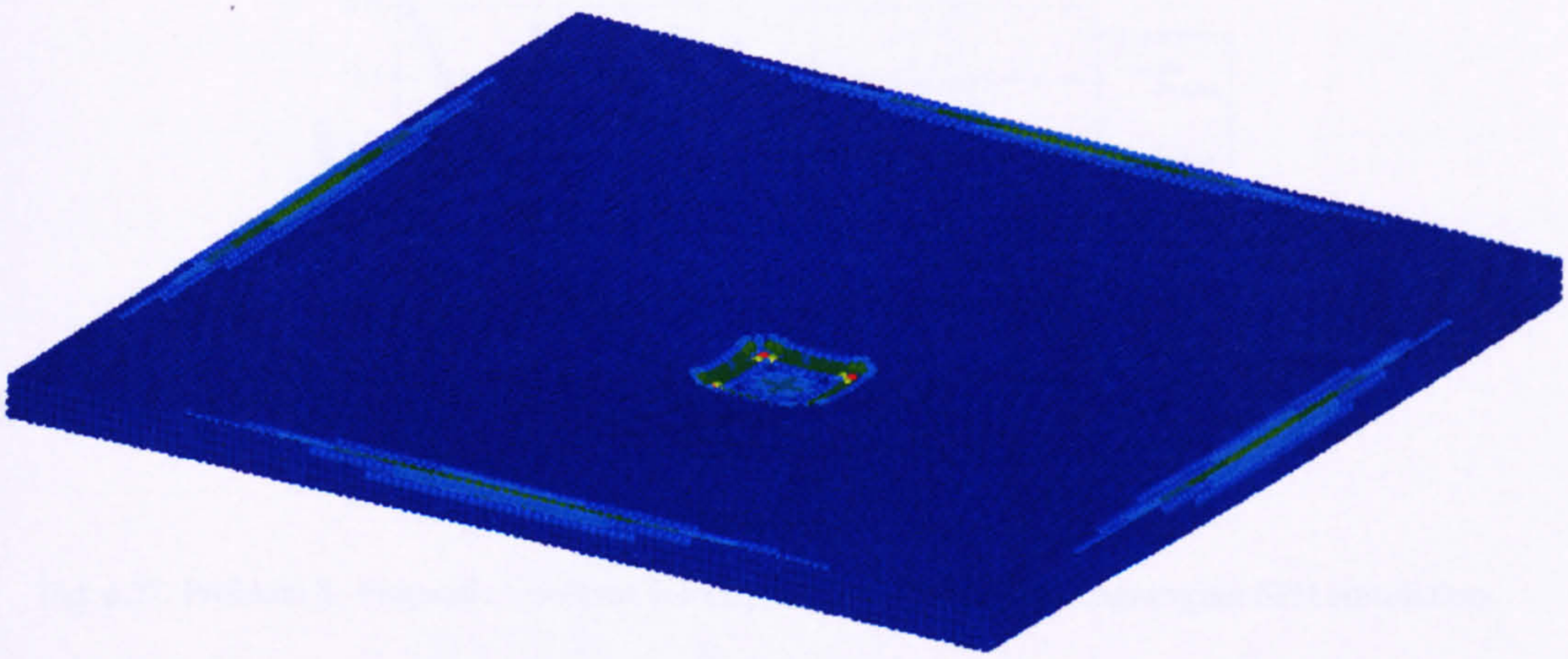

Fig. 6.25. Problem 8. Resulting effective plastic strain on target plate after impact (Refer to text for explanation).

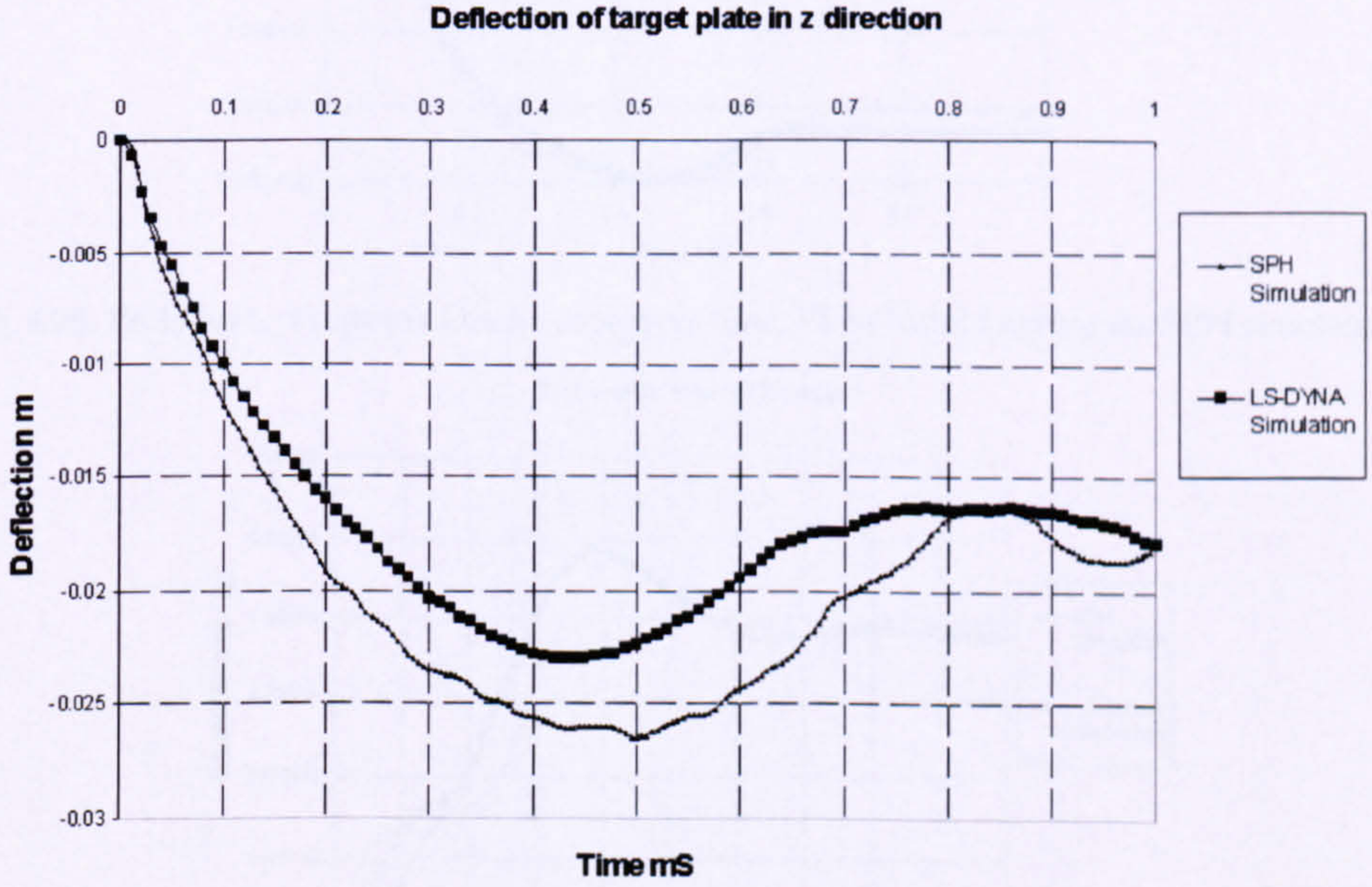

Fig. 6.26. Problem 8. Z displacement time history of the target plate, FE vs Total Lagrangian SPH simulation.

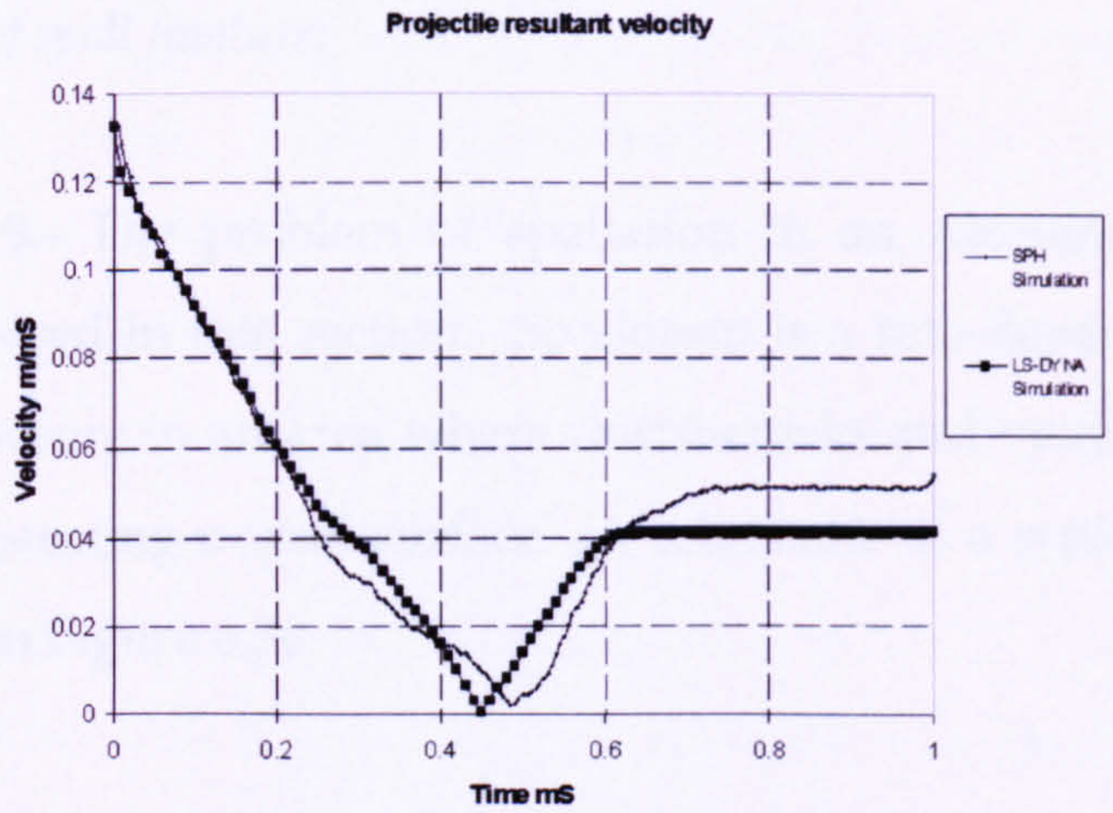

Fig. 6.27. Problem 8. Projectile resultant velocity vs time, FE vs Total Lagrangian SPH simulation.

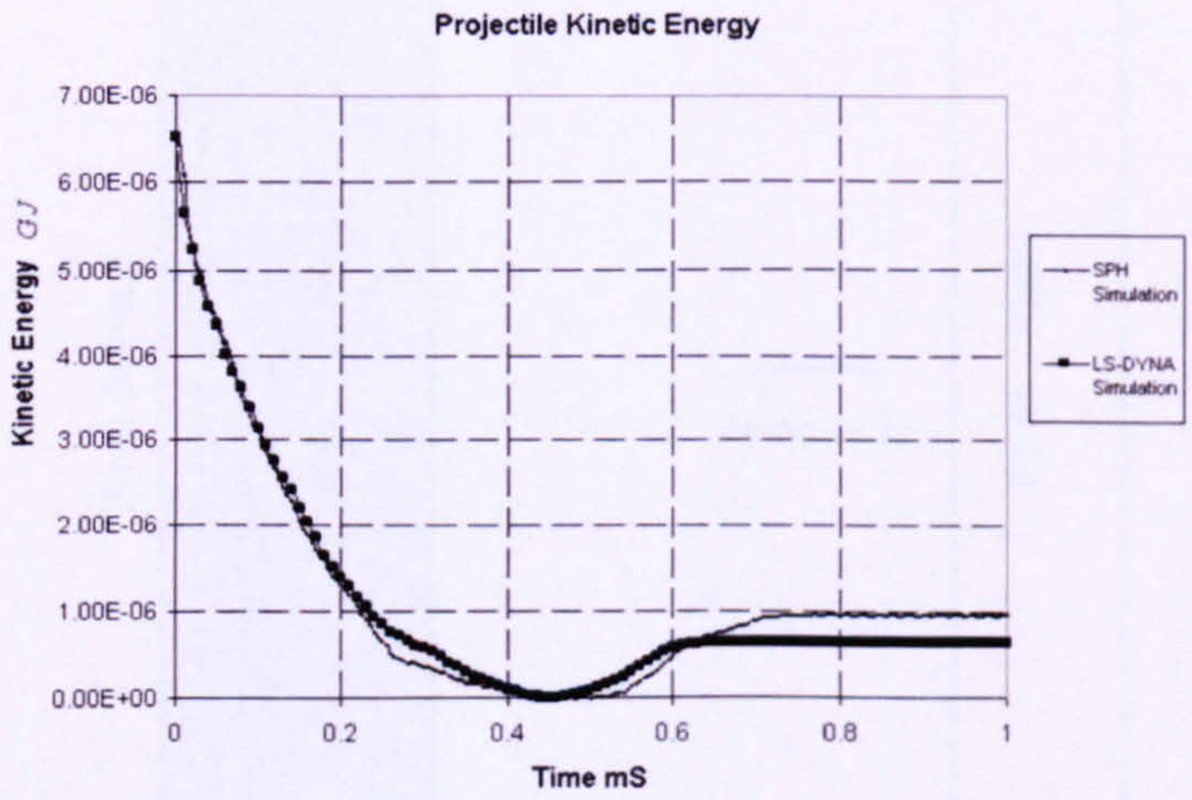

Fig. 6.28. Problem 8. Projectile kinetic energy vs time, FE vs Total Lagrangian SPH simulation.

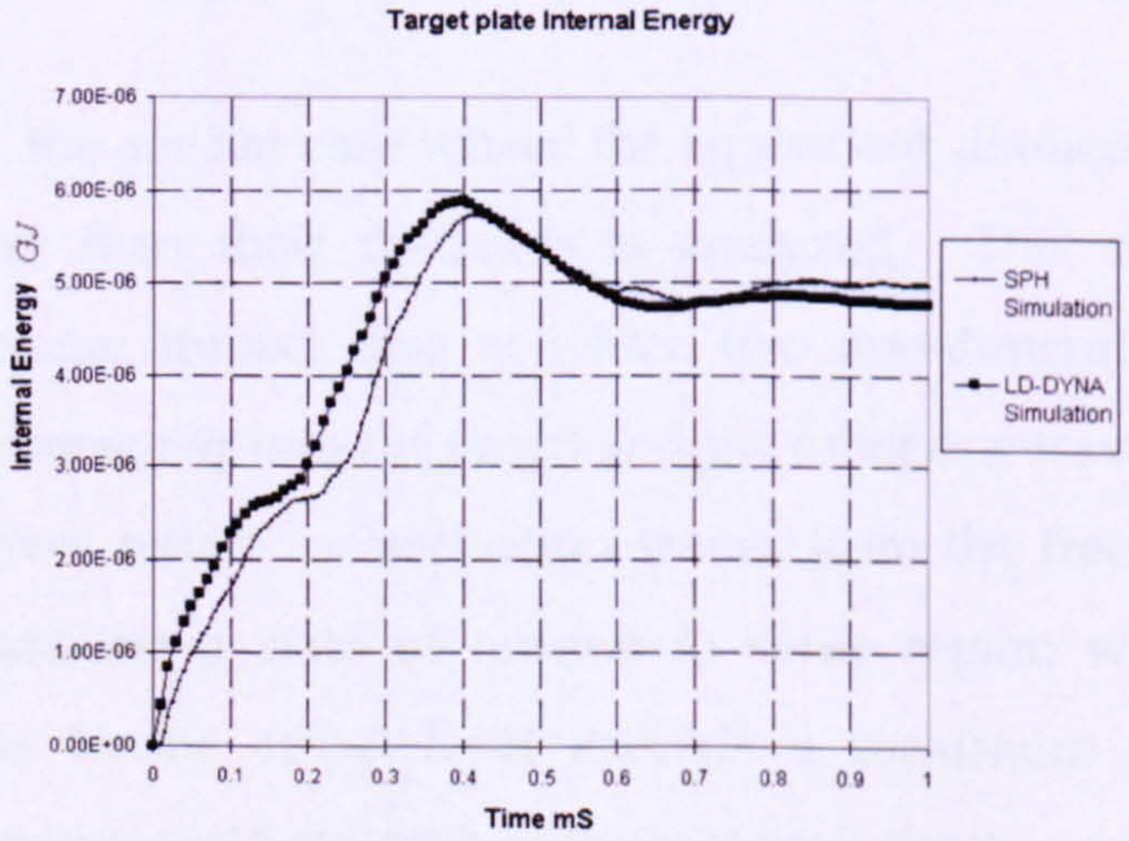

Fig. 6.29. Problem 8. Target plate internal energy vs time, FE vs Total Lagrangian SPH simulation.

6.3.3 Simulation of spall fracture.

Problem 9.- The problem of spallation in an Aluminum plate under impact is considered in this section. Spallation is a rate-dependent process in which fracture occurs in an area where micro-cracks and voids nucleate, grow and coalesce generating a spall surface. A schematic of a typical experimental set up is shown in Figure 6.30.

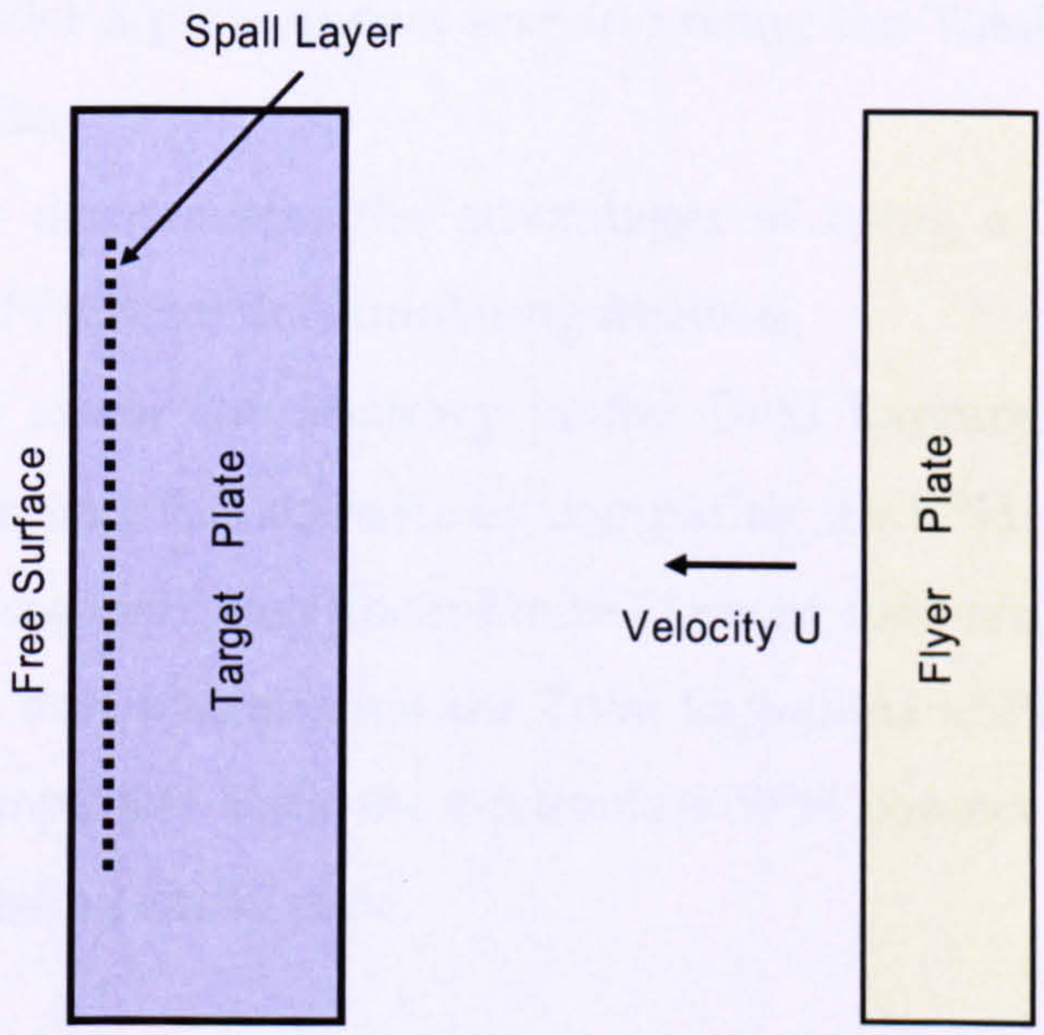

Fig.6.30. Schematic representation of a plate impact test with spall.

Typically, the special case where the equivalent diameters of the plates are much greater than their thickness is analyzed. This situation can be regarded as a planar impact case in which two one-dimensional waves are generated, one propagates into the target and the other one travels into the flyer plate. These waves reflect as rarefaction waves from the free surfaces of the target plate producing a state of tension in some region within the target domain. If this tensile stress level exceeds a maximum specified stress (typically the dynamic yield strength of the material), fracture occurs producing a scab on that section of the target. The velocity and thickness of the spalled

material depends on the pressure profile at the free surface and the yield strength of the target. One-dimensional simulations are sufficient for developing insight into the spallation process and for determining spall parameters like spall strength and spall thickness. They are also sufficient for studying the effect of variation of initial target temperature and impact pressure [42, 87].

Objectives.- The objective of this problem are:

1) To model the spall fracture of copper and aluminium specimens under a plate impact scenario using the Total Lagrangian SPH code.
2) To demonstrate the advantages of using a Total Lagrangian SPH scheme for simulating fracture.
3) To assess the accuracy of the Total Lagrangian SPH code to simulate this scenario by comparing the SPH simulation results to standard non linear Finite Element code results.
4) To demonstrate that the Total Lagrangian SPH scheme is fully compatible with the frictionless SPH contact algorithm in the existing MCM code.

Results.-

The Results section of this problem is divided as follows:

1) Under heading 6.3.4, the advantages of using the Total Lagrangian formulation to simulate spall fracture are discussed. In this section, the Total Lagrangian and the Eulerian SPH schemes are used to simulate an identical scenario whereby a compressive stress wave travels within the problem domain. A state of high tensile stress is generated after the wave reaches the back surface of the domain which induces artificial fracture in the case of the Eulerian simulation.

2) Under heading 6.3.5, spall fracture in copper is simulated using the Total Lagrangian SPH and the Johnson-Cook material model with damage. The results are compared with non-linear finite element results. The non-

standard material constants are supplied in this section as well as the SPH and FE model details.

3) Under heading 6.3.6, spall fracture is simulated using the Total Lagrangian SPH and the Johnson-Cook material model with damage. Additionally, a PMMA backing plate is also included in the numerical simulation and the stress levels are measured at the interface of the backing and the target plates. The SPH results are compared with experimental results [20].

6.3.4 Advantages of using a Total Lagrangian SPH code for the simulation of spall fracture.

For the following example, the simulation of a compressive wave within a 2-D Aluminium specimen is considered. The constitutive model used was the elastic-plastic with hardening [35] and the failure criterion employed was a prescribed maximum stress. The flyer plate material was Titanium and the target's material was Aluminium. The prescribed flyer plate velocity was $660\frac{\mathrm{m}}{\mathrm{s}}$.

Figure 6.30 shows the simulation of spall on the 2-D specimen using Eulerian kernels prior to the failure criteria being introduced. Although the particles in red have reached a prescribed critical failure value, the specimen fracture is induced by numerical instability and not by the state of stresses within the domain.

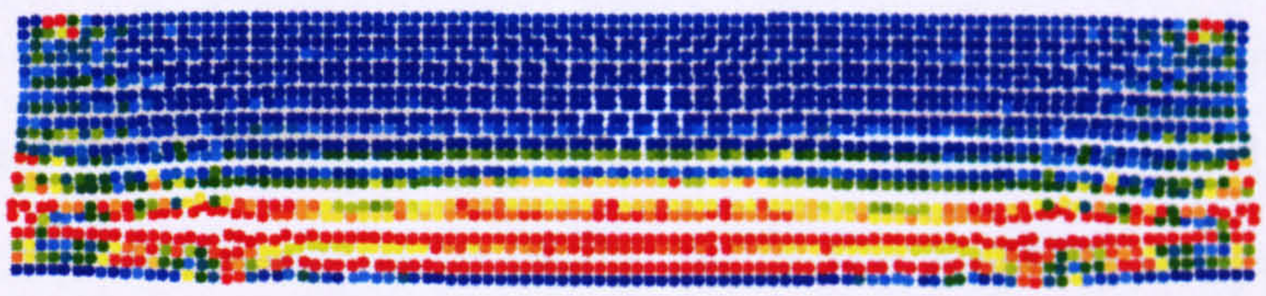

Fig. 6.31. Problem 9. Simulation of spall in a 2-D Al specimen, Eulerian kernels. Contours of effective stress shown.

Particles clump leaving areas of the domain empty which makes artificial

fracture virtually impossible to differentiate from real fragmentation. The time depicted in Fig. 6.31 is for time t =18 μs.

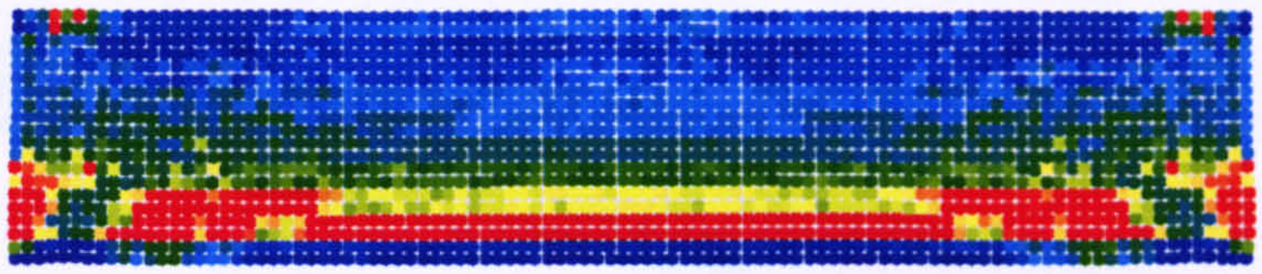

Fig. 6.32. Problem 9. Simulation of spall in a 2-D Al specimen, Lagrangian Kernels. Contours of effective stress shown.

Figure 6.32 shows the simulation of 2-D spall using Lagrangian kernels before the failure criterion is introduced. The particles in red have reached the prescribed value of failure. However, the interparticle distance is maintained and no numerical fracture is observed. The time depicted in Fig 6.30 is for t=18 μs. This simulation shows the superior stability qualities of the total Lagrangian code. Once the "failure" algorithm gets implemented, the robustness and accuracy of the Lagrangian code becomes evident. Real fracture can be modelled and predicted accurately since artificial fracture no longer takes place. This is demonstrated in the following set of results (sections 6.3.5 and 6.3.6).

6.3.5 Spall fracture simulation of OFHC Copper using Total Lagrangian SPH and Johnson-Cook model with damage.

In this example, spall fracture was simulated using a 3-D arrangement of 9375 SPH particles and 9375 FE elements as shown in Fig. 6.33 and 6.34 respectively. Symmetry planes were imposed to ensure a one-dimensional state of strain across the plate thickness. The thickness ratio between flyer and target plates is 1:2 which allows us to easily verify the location of spall within the target plate when fracture occurs (i.e the location in the target plate where a high tensile state of stress is generated which for a 1:2 ratio should be half way through the target plate).

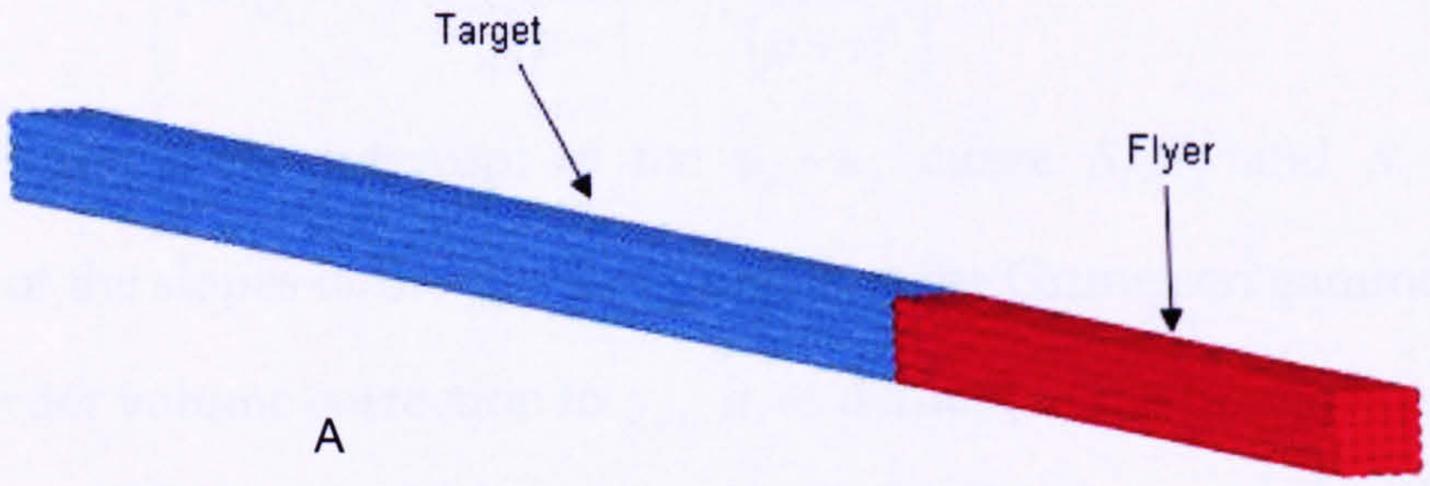

Fig 6.33. Problem 9. Schematic for spall fracture simulation of OFHC Copper, SPH discretisation.

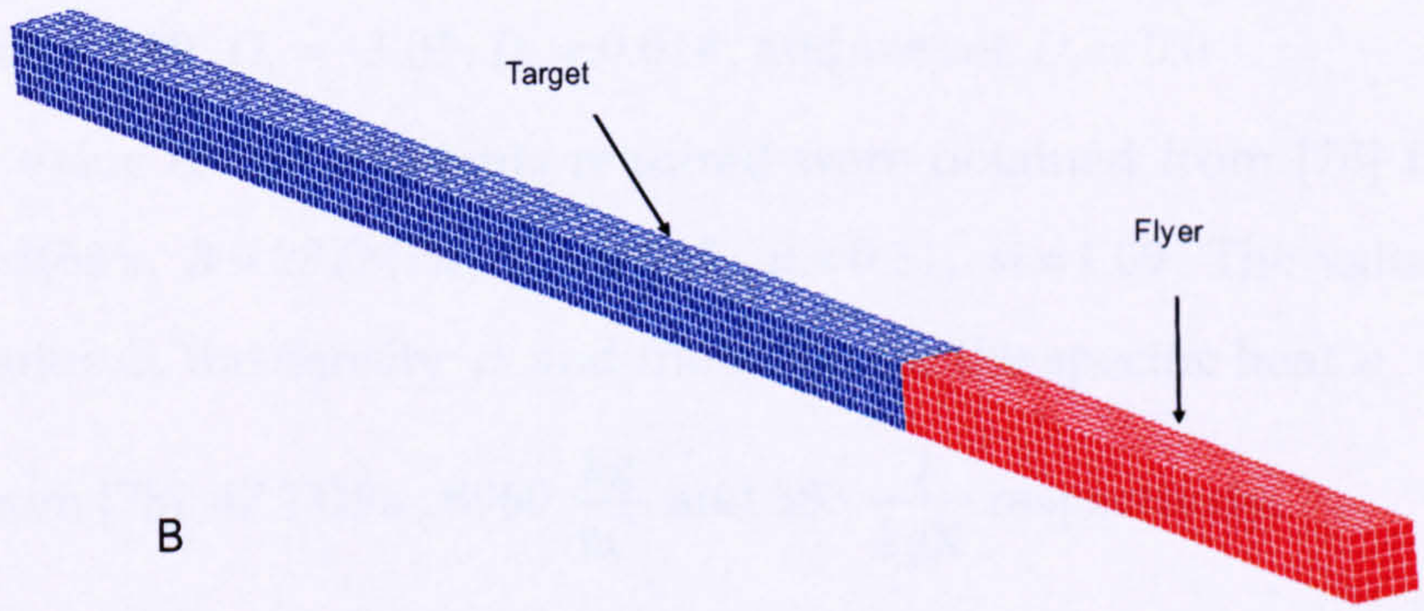

Fig 6.34. Problem 9. Schematic for spall fracture simulation of OFHC Copper, FE discretisation.

Two cases were simulated using the SPH and FE models presented in figures 6.31 and 6.33. In the first case, the flyer plate impacts the target with a 290m/s velocity. In the second case, the flyer travels at 305 m/s. A frictionless particle-to-particle contact algorithm was used to simulate the interaction of the two plates. Full details of this algorithm can be found in [24, 84]. The Johnson-Cook model together with the Gruneisen equation of state [61, 78] was used to characterise the two copper plates. The Gruneisen equation of state with cubic shock velocity-particle velocity defines pressure for a compressed material as:

$$P = \frac{\rho_0 C_0^{\,2}\mu\left[1+\left(1-\frac{\gamma_0}{2}\right)\mu-\frac{a}{2}\mu^2\right]}{\left[1-(S_1-1)\mu-S_2\frac{\mu^2}{\mu+1}-S_3\frac{\mu^3}{(\mu+1)^2}\right]^2}+(\gamma_0+a\mu)E \qquad (6.24)$$

where C_0 is the is the intercept of the u_s-u_p curve S_1, S_2 and S_3 are the coefficients of the slopes of the u_s-u_p curve, γ_0 is the Gruneisen gamma, and a is the first order volume correction to γ_0, μ as defined in the previous example.

For expanded materials the pressure is defined as:

$$P = \rho_0 C_0^{\,2}\mu+(\gamma_0+a\mu)E \qquad (6.25)$$

The damage parameters D_i required by the Johnson-Cook with damage model were obtained from [42] and are as follows:

$D_1 = 0.54, D_2 = 4.89, D_3 = -3.03, D_4 = 0.014$, and we set $D_5 = 0.0$

The value of the constants required were obtained from [78] for OFHC Copper: A=90MPa, $B = 292\text{MPa}$, $C = 0.025$, $n = 0.31$, $m = 1.09$. The values for the shear modulus G, the density ρ and the value for the specific heat c_v were also obtained from [78]: $47.7\,\text{GPa}$, $8960\ \frac{\text{kg}}{\text{m}^3}$ and $383\ \frac{\text{J}}{\text{kgK}}$ respectively.

The Gruneisen equation of state constants were obtained from [78] for OFHC Copper: $C_o = 3940\frac{\text{m}}{\text{s}}$, $S_1 = 1.489$, $S_2 = 0.0$, $S_3 = 0.0$, $\gamma_0 = 2.02$ and $b = 0.47$.

The numerical results for both the FE and SPH simulations are presented in figure 6.35 and figure 6.36. The SPH results show excellent agreement with the FE results.

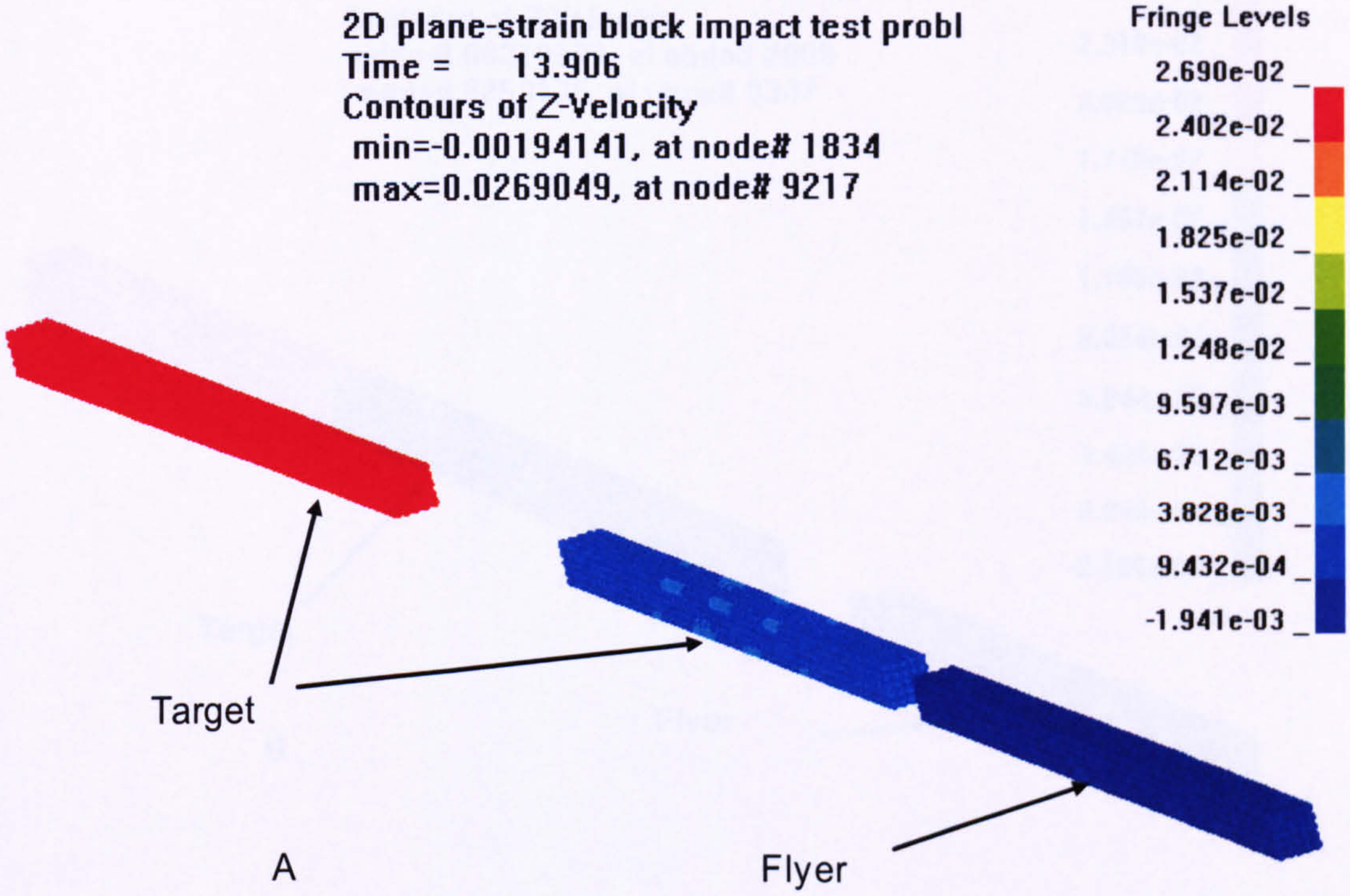
2D plane-strain block impact test probl
Time = 13.906
Contours of Z-Velocity
min=-0.00194141, at node# 1834
max=0.0269049, at node# 9217
Fringe Levels
2.690e-02
2.402e-02
2.114e-02
1.825e-02
1.537e-02
1.248e-02
9.597e-03
6.712e-03
3.828e-03
9.432e-04
-1.941e-03
Target
A
Flyer

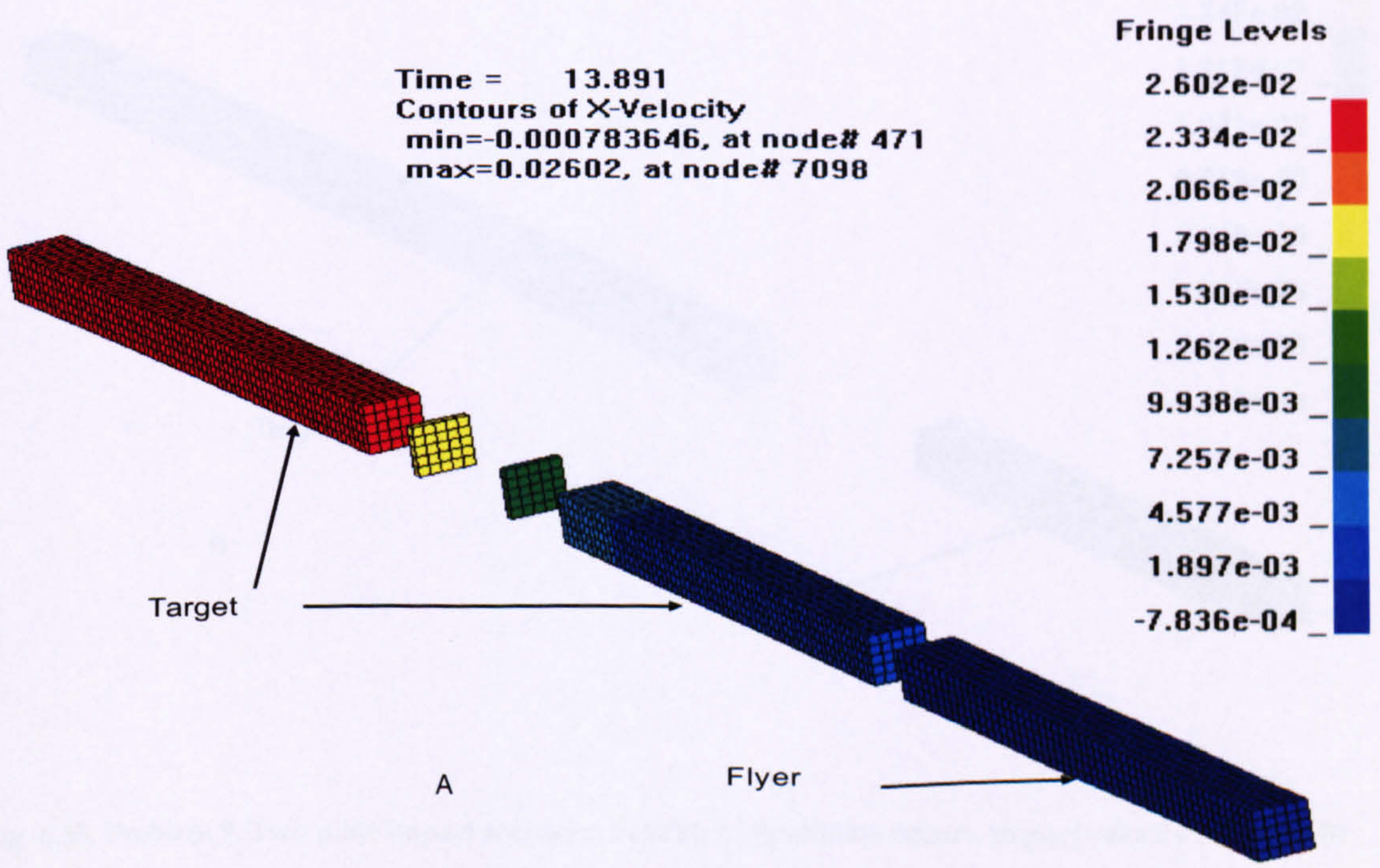
Time = 13.891
Contours of X-Velocity
min=-0.000783646, at node# 471
max=0.02602, at node# 7098
Fringe Levels
2.602e-02
2.334e-02
2.066e-02
1.798e-02
1.530e-02
1.262e-02
9.938e-03
7.257e-03
4.577e-03
1.897e-03
-7.836e-04
Target
A
Flyer

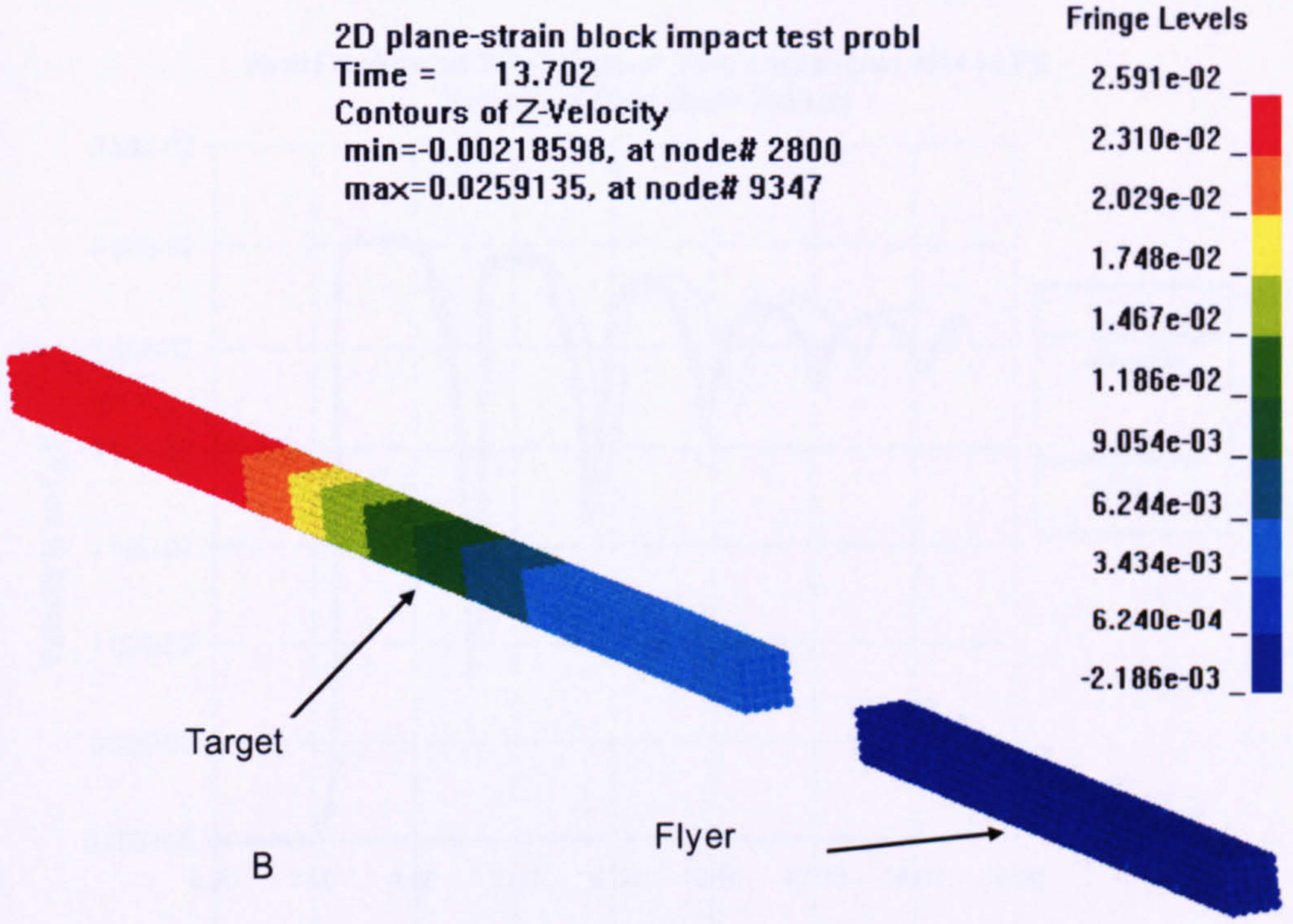

Fig. 6.35. Problem 9. Two plate impact scenarios in SPH: A) Spallation occurs, impact velocity 305 m/s. B) No spallation occurs, impact velocity 290 m/s

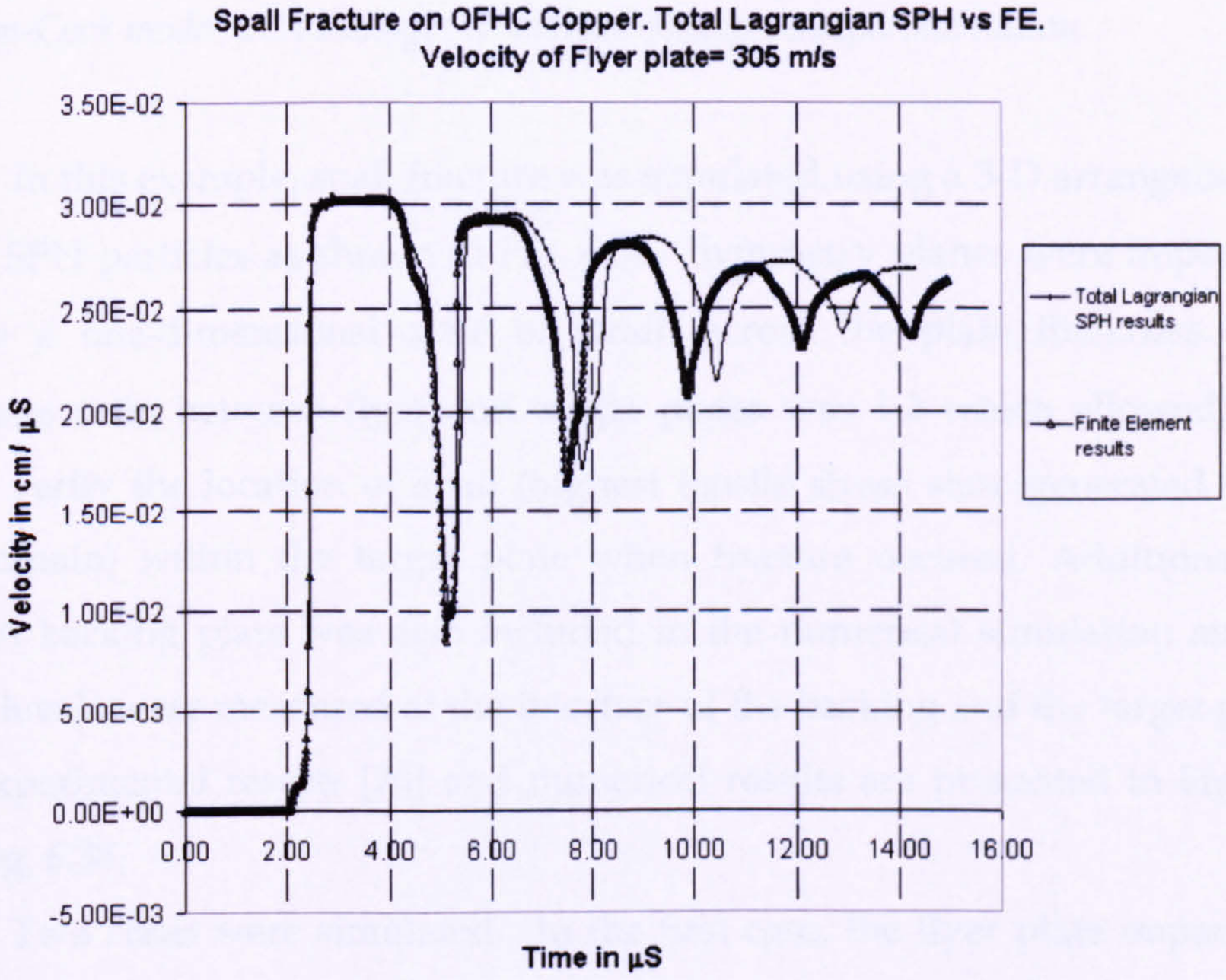

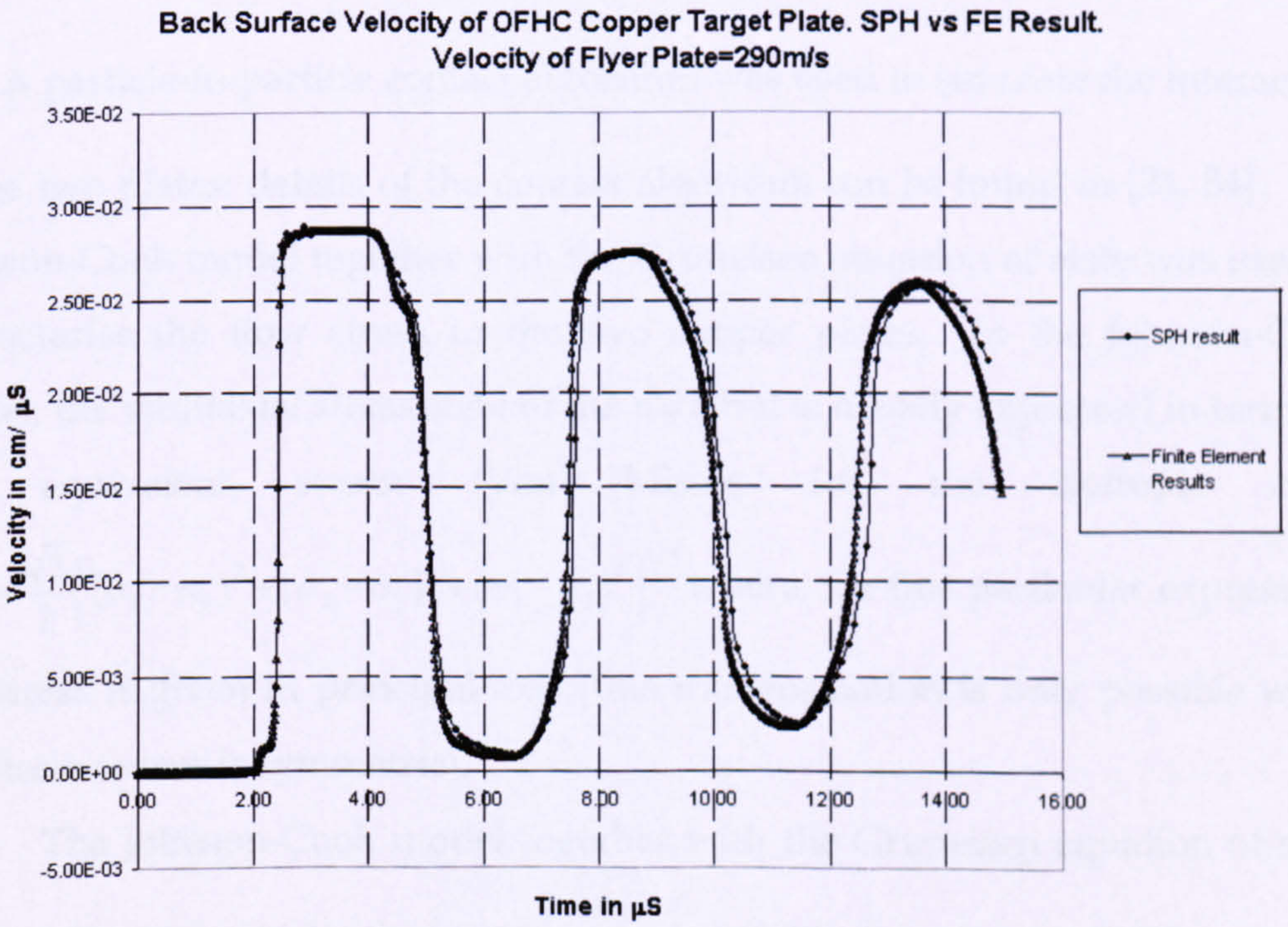

Fig. 6.36. Problem 9. Target plate back surface velocity plot. Simulations show Total Lagrangian SPH vs Finite Element results.

6.3.6 *Spall fracture simulation of OFHC Copper using total Lagrangian SPH and Johnson-Cook model with damage: Numerical results vs experimentation.*

In this example, spall fracture was simulated using a 3-D arrangement of 15625 SPH particles as shown in Fig. 6.36. Symmetry planes were imposed to ensure a one-dimensional state of strain across the plate thickness. The thickness ratio between flyer and target plates was 1:2 which allowed us to easily verify the location of spall (highest tensile stress state generated inside the domain) within the target plate when fracture occured. Additionally, a PMMA backing plate was also included in the numerical simulation and the stress levels were measured at the interface of the backing and the target plates. The experimental results [20] and numerical results are presented in Fig. 6.37 and Fig. 6.38.

Two cases were simulated. In the first case, the flyer plate impacts the target with a 200.00 $\frac{\mathrm{m}}{\mathrm{s}}$ velocity. In the second case, the flyer travels at 305.00 $\frac{\mathrm{m}}{\mathrm{s}}$. A particle-to-particle contact algorithm was used to simulate the interaction of the two plates; details of the contact algorithm can be found in [24, 84]. The Johnson-Cook model together with the Gruneisen equation of state was used to characterise the flow stress in the two copper plates. In the Johnson-Cook model, the multiaxial stress state of the material is usually expressed in terms of the equivalent stress: (Von Misses for the isotropic case) $\sigma_{eff} = \frac{\sqrt{2}}{2}\left[(\sigma_1-\sigma_2)^2+(\sigma_2-\sigma_3)^2+(\sigma_1-\sigma_3)^2\right]^{1/2}$ where, for this particular expression, the stress is given in principal axis (this transformation is only possible when the stress tensor is symmetric).

The Johnson-Cook model together with the Gruneisen equation of state was used to characterise the two copper plates: The Johnson-Cook flow stress is given by Eq. 6.16 (Page 132).

where A, B, C, n, and m are the non-standard material constants and the temperature (T^*) is the homologous temperature.

The Gruneisen equation of state with cubic shock particle velocity defines pressure for a compressed material as in Equation 6.24. Equation 6.25 is used for expanded materials.

The damage parameters D_i required by the Johnson-Cook with damage model were obtained from [42] and are as follows:

$D_1 = 0.54, D_2 = 4.89, D_3 = -3.03, D_4 = 0.014$.

The value of the constants required were obtained from [78] for OFHC Copper: $A = 90.00\,\text{MPa}$, $B = 292.00\,\text{MPa}$, $C = 0.025$, $n = 0.31$, $m = 1.09$. The values for the shear modulus G, the density ρ and the value for the specific heat c_v were also obtained from [78]: $47.70\,\text{GPa}$, $8960\ \frac{\text{kg}}{\text{m}^3}$ and $383.00\ \frac{\text{J}}{\text{kgK}}$ respectively.

The Gruneisen equation of state constants were obtained from [78] for OFHC Copper: $C_o = 3940.00\ \frac{\text{m}}{\text{s}}$, $S_1 = 1.489$, $S_2 = 0.0$, $S_3 = 0.0$, $\gamma_0 = 2.02$ and $b = 0.47$.

For the PMMA, the isotropic elastic-plastic-hydrodynamic model with an equation of state was used [35]. The required material parameters for PMMA are as follows [78]: shear modulus 2.39GPa, Yield stress 420.00 MPa, plastic modulus 300.00 MPa, Density $1180\frac{\text{kg}}{\text{m}^3}$. The Gruneisen equation of state constants are as follows: $C_o = 2180.00\ \frac{\text{m}}{\text{s}}$, $S_1 = 2.088$, $S_2 = -1.124$, $S_3 = 0.0$ and $\gamma_0 = 0.85$. Numerical results showing longitudinal stress levels are presented in Fig 6.38. Correlation with experimental results [20] is presented in Fig. 6.39 for longitudinal stress in the case where spall fracture takes place in the specimen.

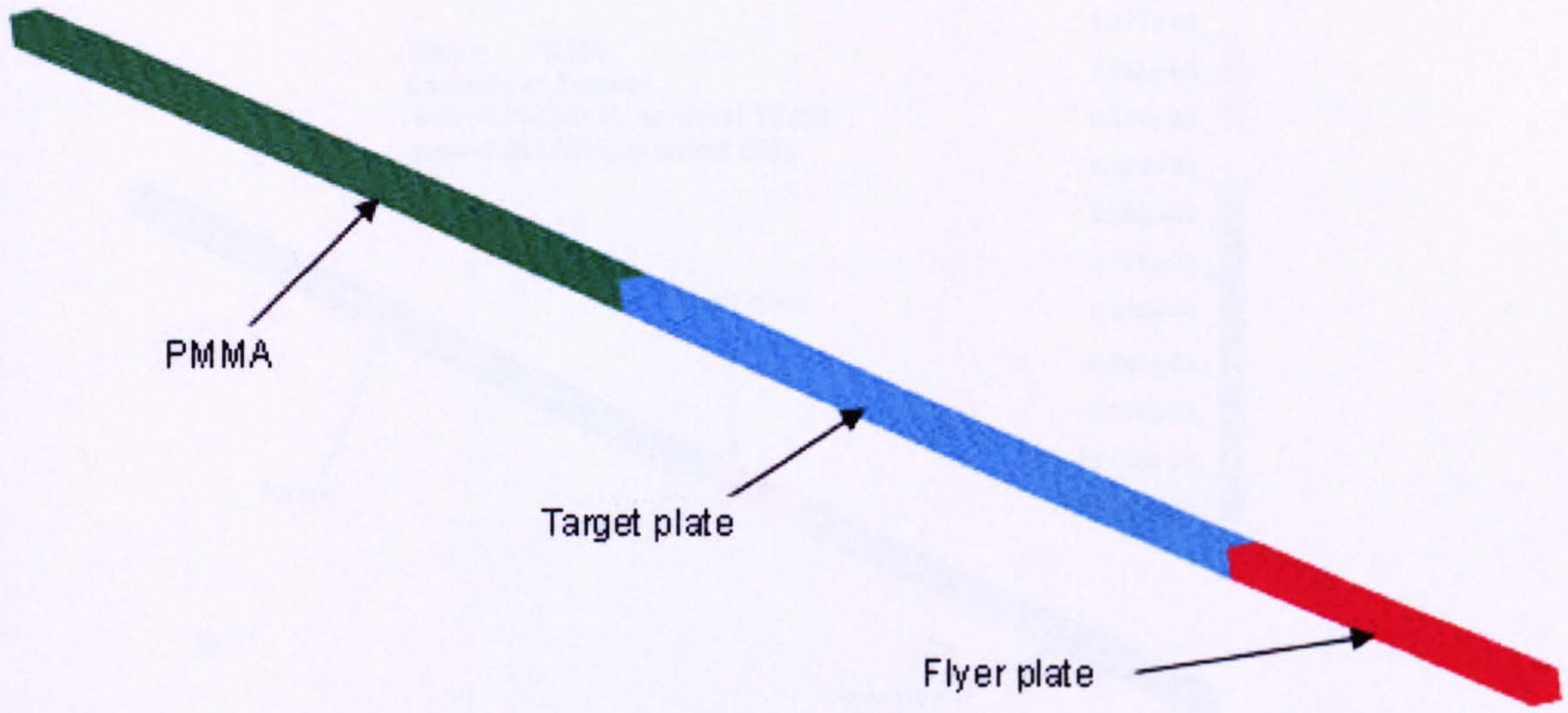

Fig. 6.37. Problem 9. Schematic diagram for spall fracture simulation of OFHC Copper, a PMMA backing plate has been included to capture stress at the PMMA-target plate interface.

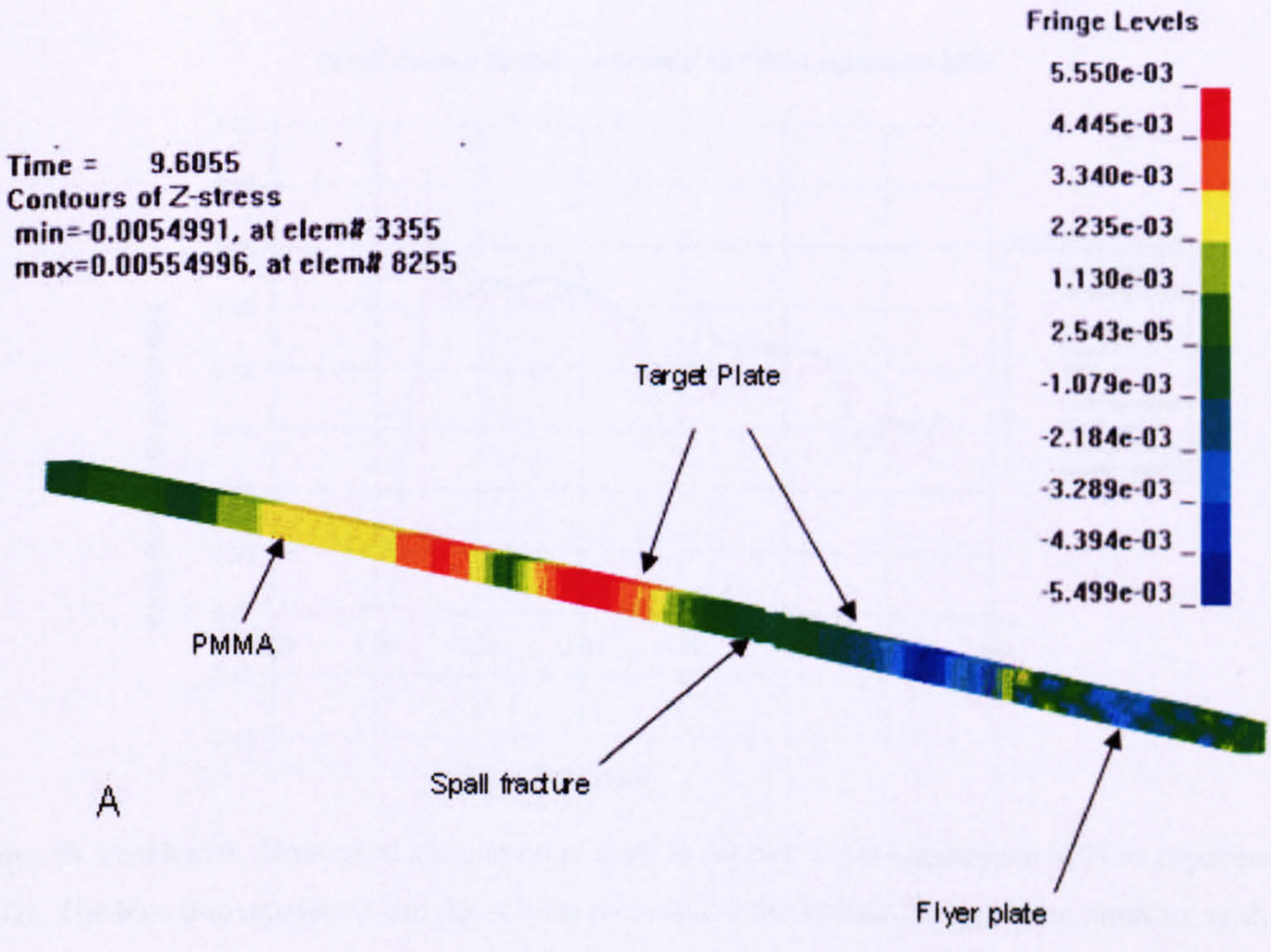

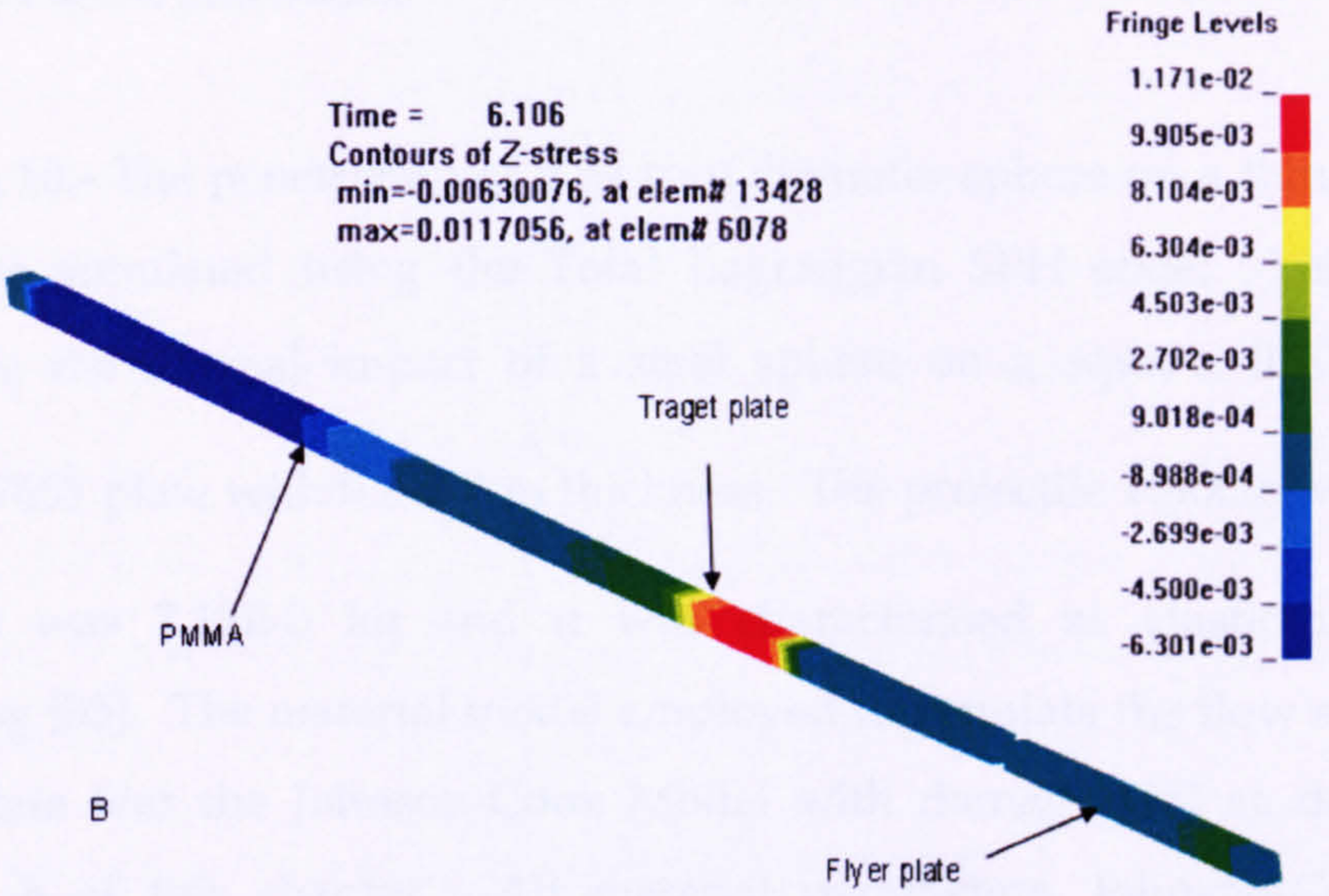

Fig. 6.38. Problem 9. Numerical simulation of spall in copper. A) depicts the Total Lagrangian SPH simulation when fracture is present, B)shows no fracture of the target. Contours of longitudinal stress shown.

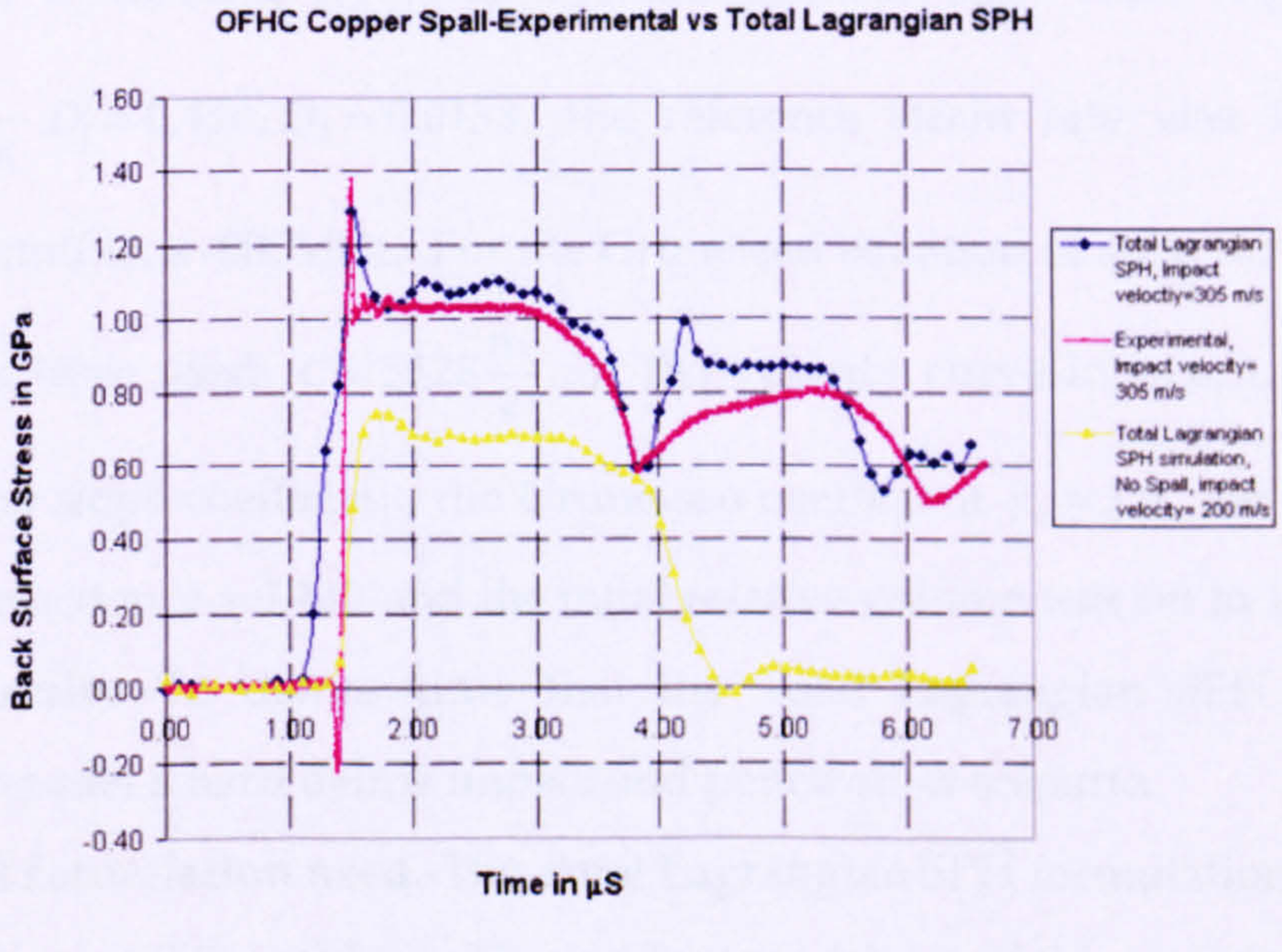

Fig 6.39. Problem 9. Numerical simulation of spall in copper. Total Lagrangian SPH vs experimental results. The blue line represents the stress level recorded at the PMMA-Target plate interface with a flyer speed of 305m/s and spall fracture is generated. The yellow line gives the stress level at the interface when the flyer travels at 200m/s and no fracture is present. The magenta line is the experimental data [20].

6.3.7 *Hard debris penetration.*

Problem 10.- The penetration of a 12 mm diameter sphere on a thin aluminum plate was simulated using the Total Lagrangian SPH code. This problem illustrates the normal impact of a steel sphere on a square, 0.10 x 0.10 m Al7010T7651 plate with 0.2 E-2 m thickness. The projectile velocity was 500 $\frac{\text{m}}{\text{s}}$, its mass was 7.12E-3 kg and it was characterised as elastic-plastic with hardening [35]. The material model employed to simulate the flow stress of the target plate was the Johnson-Cook Model with damage [35] as described in Problem 8 of this chapter. All material parameters, Johnson-Cook model parameters, elastic-plastic model parameters and the Gruneisen EOS parameters can be found in the input file in the Appendix and are reproduced here for completeness:

A=479MPa, B=323MPa, n=0.410, C=0.101, m=1.80, $T_{melt}=850\text{K}$ $T_{room}=300\text{K}$, $c_v=875\frac{\text{J}}{\text{kgK}}$ $D_1=0.450, D_4=0.0138$, the reference strain rate was 1.0 $\frac{1}{\text{s}}$, the pressure cutoff was -800MPa. For the Gruneisen equation of state the following parameters were used: $C=5328\frac{\text{m}}{\text{s}}$ for the velocity curve intercept, $S_1=1.338$ was the first slope coefficient, the Gruneisen coefficient $\gamma_0=2.0$, the first order volume correction $a=0.480$ and the intial relative volume was set to 1.

Objective.-To demonstrate that the Total Lagrangian SPH code can accurately model a hard debris impact and penetration scenario.

SPH formulation used.-The Total Lagrangian SPH formulation was used in the solution of this problem. The symmetrised form of the particle equations was used and the interpolating function employed was the cubic spline. The domain was discretised into 30912 particles. The interaction between the two computational sub-domains was achieved through the frictionless contact algorithm developed by Vignjevic et al. [84]. The displacement of the particles

at the boundaries was set to zero in all directions. The smoothing length was set to 0.12 E-2 m. Full details on the input file can be found in the Appendix.

Analytical background.- The recommended ballistic limit empirical model developed by Fish and Summers (the empirical model can be found in [29] and [36]) was used to calculate the theoretical thickness of the aluminium plate. Their model is employed to establish the penetration threshold of thin ductile metal plates for a given size of projectile and impact velocity. Below this critical thickness, penetration should occur for the same projectile velocity, shape and mass. Fish and Summers derived this equation for a single wall shield based on impact velocities ranging from $500\frac{m}{s}$ to $8500\ \frac{m}{s}$ and for a variety of metallic targets ranging from magnesium-lithium alloys to beryllium-copper [36].

The equation is as follows:

$$t = K * m^{0.352} * V^{0.875} * \rho^{1/6} \tag{6.26}$$

Where:

t=thickness in cm

K=empirically determined constant, 0.57 for aluminium alloys

m= mass of projectile in grams

V=impact velocity in $\frac{km}{s}$

ρ = projectile density in $\frac{g}{cm^3}$

For aluminium alloys K has a value of 0.57.

For a spherical steel projectile of 12 E-3 m in diameter and an impact velocity of 500 $\frac{m}{s}$, the critical thickness predicted by Eq (6.26) is t=0.879 E-2 m, in other words, the Fisher-Summers model predicts that a plate thinner than

0.879 E-2m will be penetrated by a spherical projectile with the same geometric characteristics and impact velocity. The critical thickness was verified through the use of ther Total Lagrangian SPH code and the results presented in this section are for a significanlty thinner plate for which experimental results were available. In this case, projectile penetration should be expected.

Results.-The simulation shows that penetration occurs when the thickness of the plate is reduced to 0.2 E-2 m. This has also been confirmed by projectile impact tests carried out at Cranfield University using a gas gun and a 12 E-3 m spherical steel projectile impacting on a 0.2E-2 m thick aluminium target plate (Fig 6.41). The simulation also predicts that fracture occurs when the level of effective plastic strain reaches 0.4 which is the approximate value of the first non-standard damage parameter in the Johnson-Cook model. The resulting type of fracture is typical of low velocity impacts. Fig 6.40 depicts a section of the 3-D model during impact. The bulged zone in the plate is the area where plastic deformation takes place before fracture commences, this has been corroborated by the experimental results obtained at Cranfield (Fig. 6.41). Also typical of low velocity impact penetration in ductile materials is plugging accompanied by petaling rather than fragmentation of the projectile and target plate [87]. Plugging is typical of impact by a blunt or hemispherical nose striker travelling at relatively low velocities. In this case, a nearly cylindrical slug of approximately the same diameter as the projectile is formed. This slug is shown in fig 6.40 and 6.41.

Figure 6.41 shows a sequence of the projectile impact and penetration on the aluminium plate. The images depicted correspond to response times t=0, 15.057, 53.045, 60.039, 104.02 and 179.06 μs. The variable shown is the value of effective plastic strain as defined in problem 6 in this chapter.

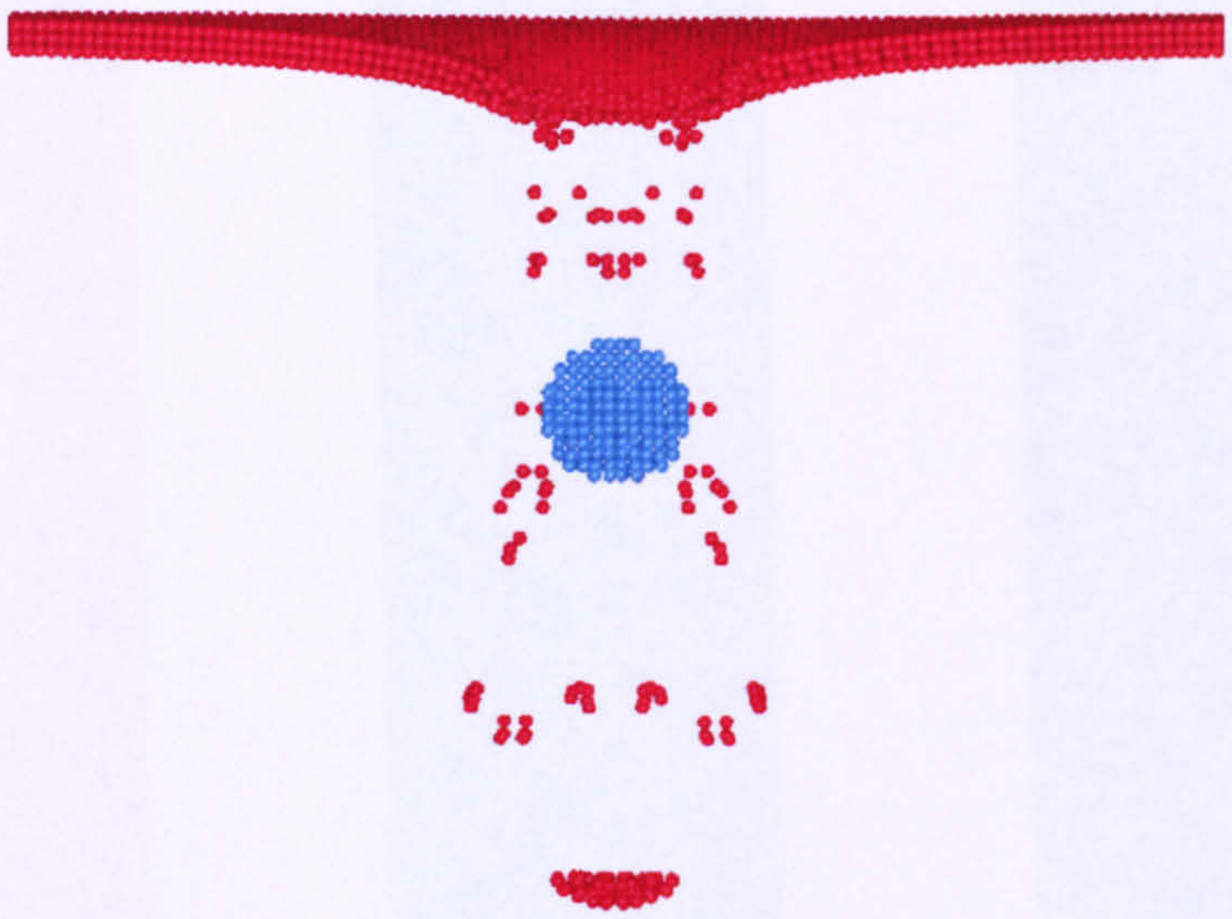

Fig. 6.40. Problem 10. Simulation of penetration of a steel sphere on an aluminium plate.

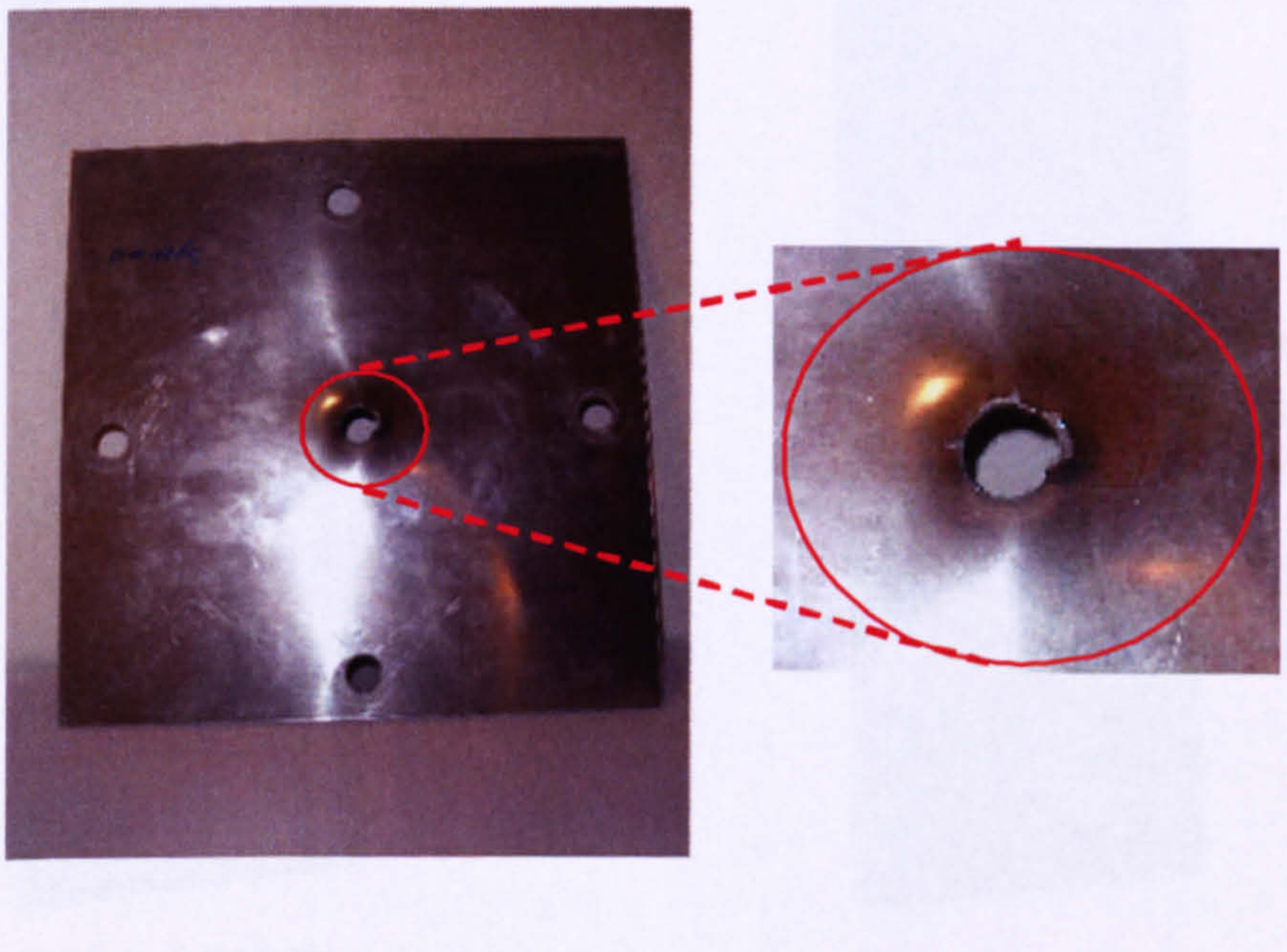

Fig. 6.41. Problem 10. Experimental results. Note the plastic deformation undergone by the specimen and the petaling typical of low velocity impacts. Projectile: 12mm diameter steel sphere. Target: 2mm thickness alumium plate, impact velocity 500 $\frac{\mathrm{m}}{\mathrm{s}}$.

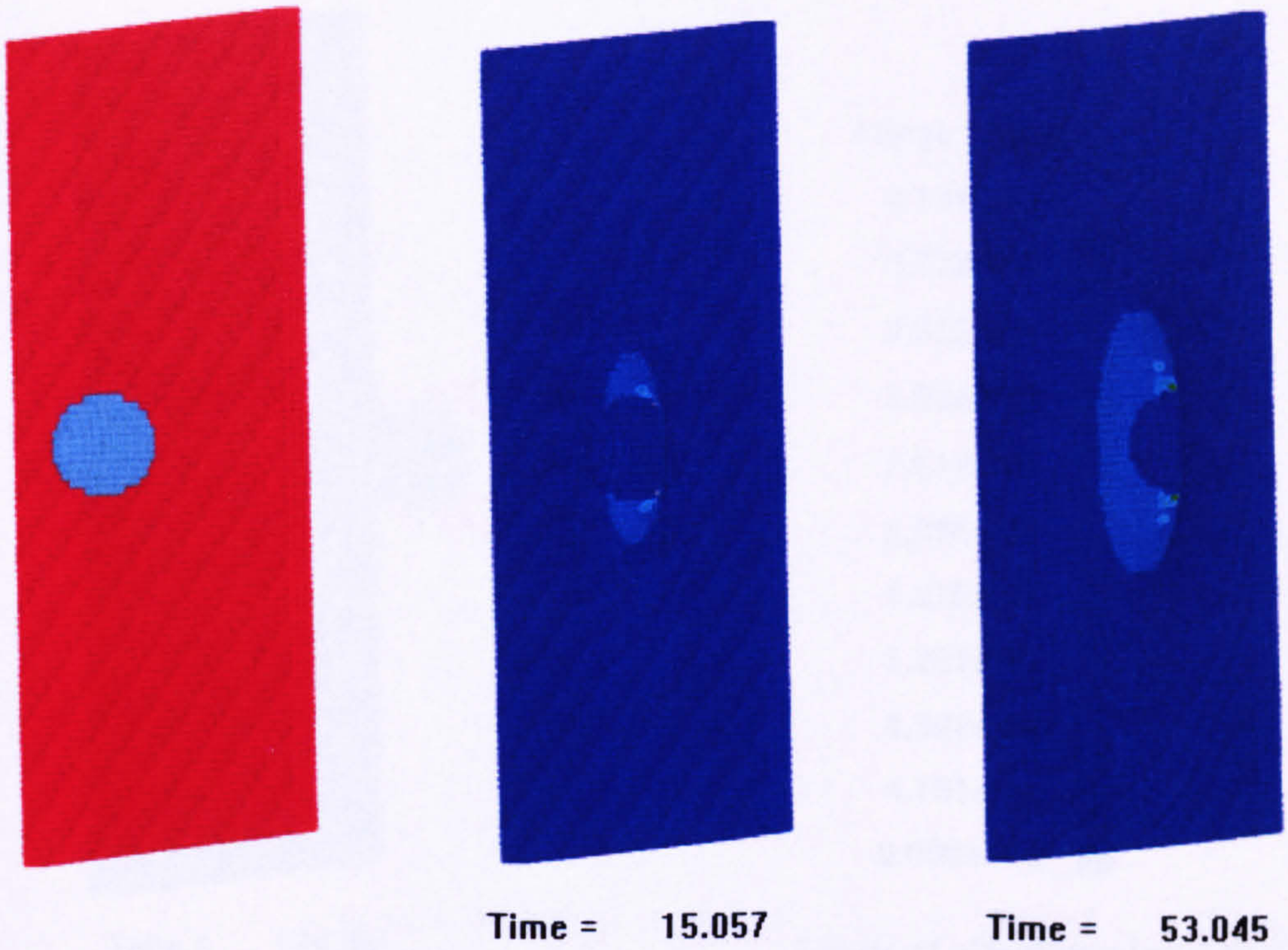

Time = 15.057

Time = 53.045

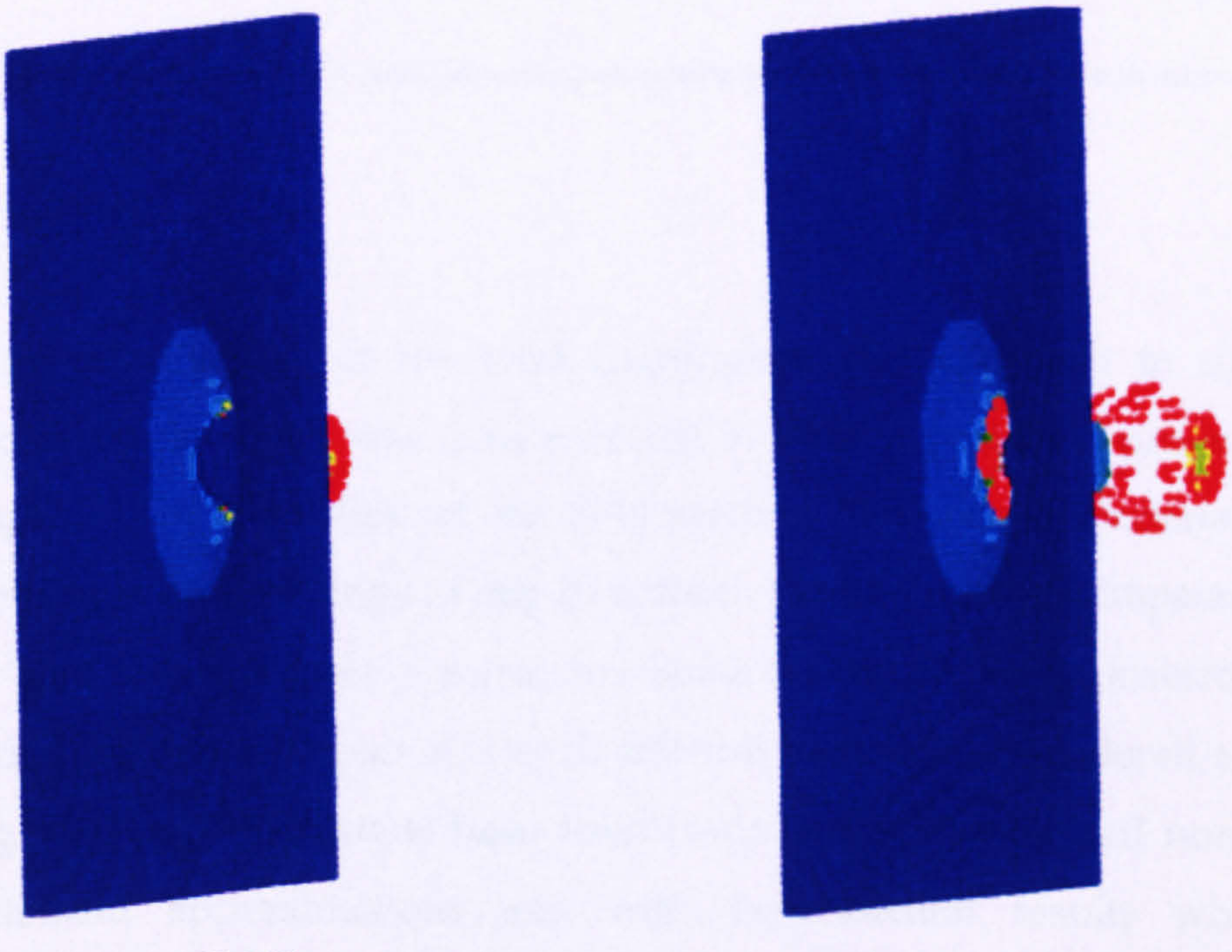

Time = 60.039

Time = 104.02

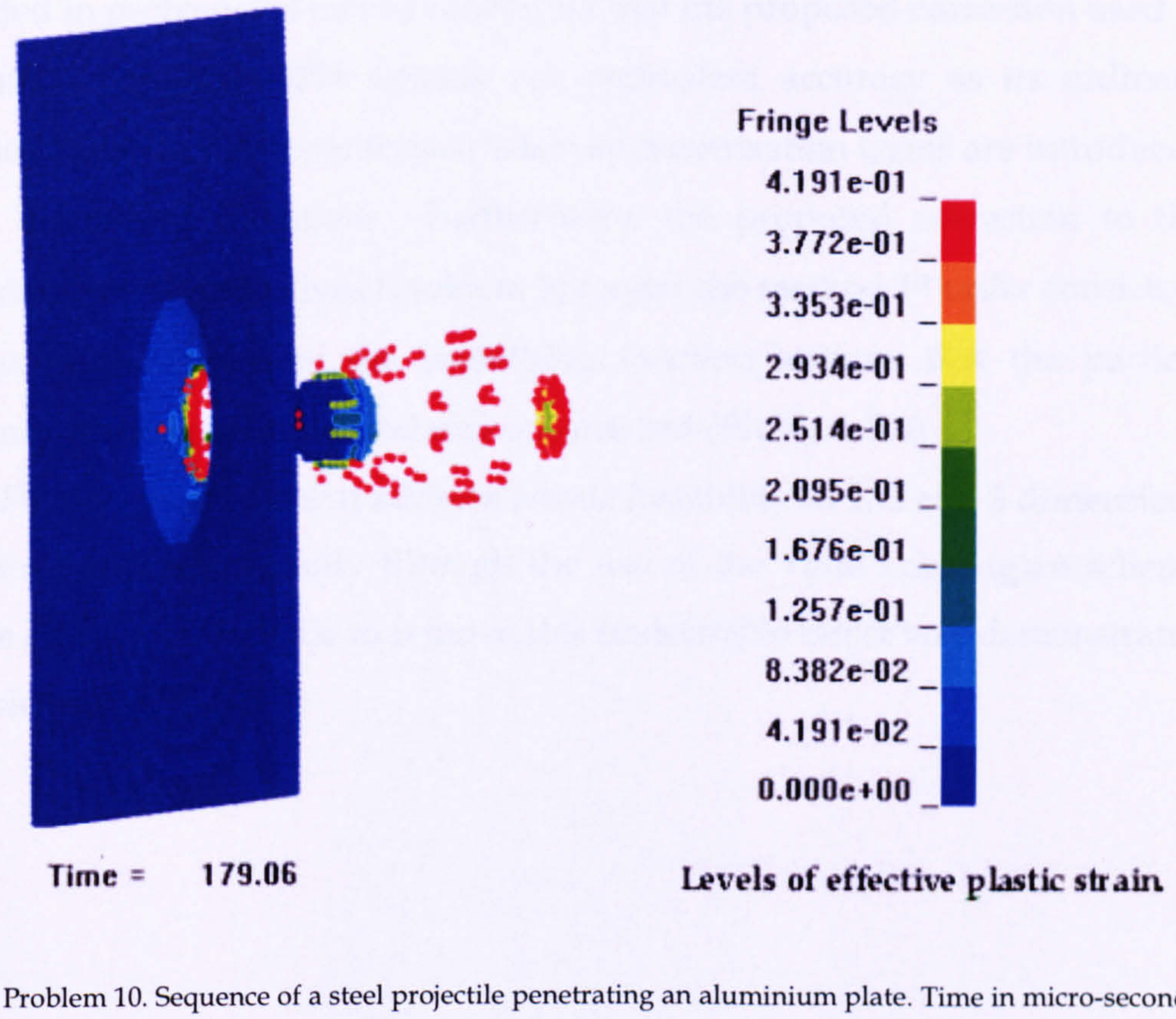

Fig. 6.42. Problem 10. Sequence of a steel projectile penetrating an aluminium plate. Time in micro-seconds

Summary.

The effectiveness of the total Lagrangian SPH approach to simulate dynamic events in solids was demonstrated in the ten problems presented in this chapter. The versatility of the SPH method has been demonstrated by characterising a diverse range of impact scenarios from the elastic impact of two rods, to hard debris impact penetration. Some real engineering problems that deal with hard debris impact and spall fracture have been considered and the resulting SPH approximations have been compared with standard non-linear finite element approximations and with experimental results whenever available (Problems 8 and 9).

A direct comparison between three SPH schemes, namely ordinary Total Lagrangian and two normalised-corrected schemes, has been carried out in problem 3. From the constant and linear velocity field approximations

presented in problem 3 it can be concluded that the proposed correction used in the Total Lagrangian SPH scheme has equivalent accuracy as its ordinary corrected Eulerian SPH counterpart when symmetrisation terms are introduced in the discretised equations. Furthermore, the proposed correction to the approximation of derivatives (Problem 3) render the method 1st order consistent and the normalisation of the smoothing function ensures that the particle deficiency problem at the boundaries is corrected (Problem 3,4)

Finally, problems that address tensile instability in 1, 2 and 3 dimensions were dealt with successfully through the use of the Total Lagrangian scheme and the efficacy of the code to remove this undesirable effect was demonstrated in problems 1, 5, 6, and 7.

PAGE NUMBERING AS ORIGINAL

CHAPTER 7

SPH: ALTERNATIVE FORMULATION AND FURTHER ENHANCEMENTS

Introduction

In Chapter 2, the conservation equations were derived using a kernel approximation based on randomly distributed interpolating nodes. A symmetry term which ensures zero order consistency was introduced based on the symmetric properties of the smoothing function. In this chapter, an attempt to explain the origin of the symmetry term is made based on the general theory of mixed Lagrangian-Eulerian descriptions [41]. An alternative form of the conservation equations in the framework of SPH is provided in this chapter. Subsequently the material form of the continuity equation as provided by

Belytschko et al. in [4] is derived and the resulting equation is discretised using the standard SPH method. The advantages of the continuity equation when derived in this form are: a) It creates a link between the Lagrangian and Eulerian descriptions as it uses elements of both to express the conservation of mass, and b) it can serve as the foundation for the implementation of the space conservation law [23] in the MCM SPH code .

The conservation of mass is derived in SPH considering a variable smoothing length and an alternative discretised form of this physical law is supplied. Again, this expression and the methodology presented here can be used as the basis for a fully consistent SPH code that makes use of varying smoothing length when approximating the conservation laws. A 1-D numerical example is also supplied.

Finally, the XSPH method is introduced in the Total Lagrangian SPH code and the implications of smoothing the velocity for the purposes of updating particle positions is considered and the advantages of such a scheme demonstrated by a 1-D example.

7.1 The Conventional SPH Method Based on Eulerian Kernel Functions.

It has been discussed in Chapter 2 that SPH uses a kernel approximation which is based on randomly distributed interpolating points with no fixed connectivity to calculate spatial derivatives through analytical differentiation of a kernel function. In SPH each particle I interacts with all other particles J that are within a given distance (usually assumed to be $2h$) from it. h (the smoothing length) determines the spatial resolution of the calculations and it can be fixed or variable. The interaction between I and J is weighted by the smoothing (or kernel) function $W(|\bar{x}-\bar{x}'|,h)$. Using this principle, the value of a continuous function can be estimated at any location within the domain using known values at surrounding particles J. Likewise, we can construct a differentiable interpolant of a function from its values at the particles J by using a differentiable kernel.

In order to generate SPH equations, the conventional method suggests keeping the position of the kernel support fixed in space ($\bar{\mathbf{x}}$ = constant) while the integration over the support is performed. In other words, the location of the support is determined by the current position of particle *I* and does not change over a given time-step in the integration process. This is represented graphically in Fig. 7.1. The next section is a brief reminder of the procedure followed to obtain SPH equations. Subsequently the general theory for mixed Lagrangian-Eulerian descriptions will be given and the main principles of this theory will be used to derive an alternative form of SPH equations in a moving coordinate system.

7.1.1 The conventional SPH discretisation method revisited.

A vector function *f* can be approximated using the conventional kernel interpolation as [3]:

$$\langle f(\bar{\mathbf{x}})\rangle \approx \int_{\Omega} f(\bar{\mathbf{x}}')\,\mathrm{W}\left(|\bar{\mathbf{x}}-\bar{\mathbf{x}}'|,h\right)d\Omega \tag{7.1}$$

where: W is the kernel function and depends upon distance $|\bar{\mathbf{x}}-\bar{\mathbf{x}}'|$,

$\bar{\mathbf{x}}$ is a parameter,

$\bar{\mathbf{x}}'$ is variable,

h a width control parameter (the smoothing length).

Ω is the kernel support centred at a point $\bar{\mathbf{x}}$

The kernel function must satisfy the following requirements [30, 50, 54, 80]:

- $\mathrm{W}(|\bar{\mathbf{x}}-\bar{\mathbf{x}}'|,h)=0$ when $|\bar{\mathbf{x}}-\bar{\mathbf{x}}'|\geq kh$ (i.e. the kernel should exhibit compact support). k is a scale factor that determines the supporting area of the smoothing function.
- $\mathrm{W}(|\bar{\mathbf{x}}-\bar{\mathbf{x}}'|,h)\geq 0$ in the compact support area where $|\bar{\mathbf{x}}-\bar{\mathbf{x}}'|\leq kh$
- Integration of W over the entire domain is unity

$$\int_{\Omega}\mathrm{W}\left(\bar{\mathbf{x}}-\bar{\mathbf{x}}',h\right)d\bar{\mathbf{x}}'=1$$

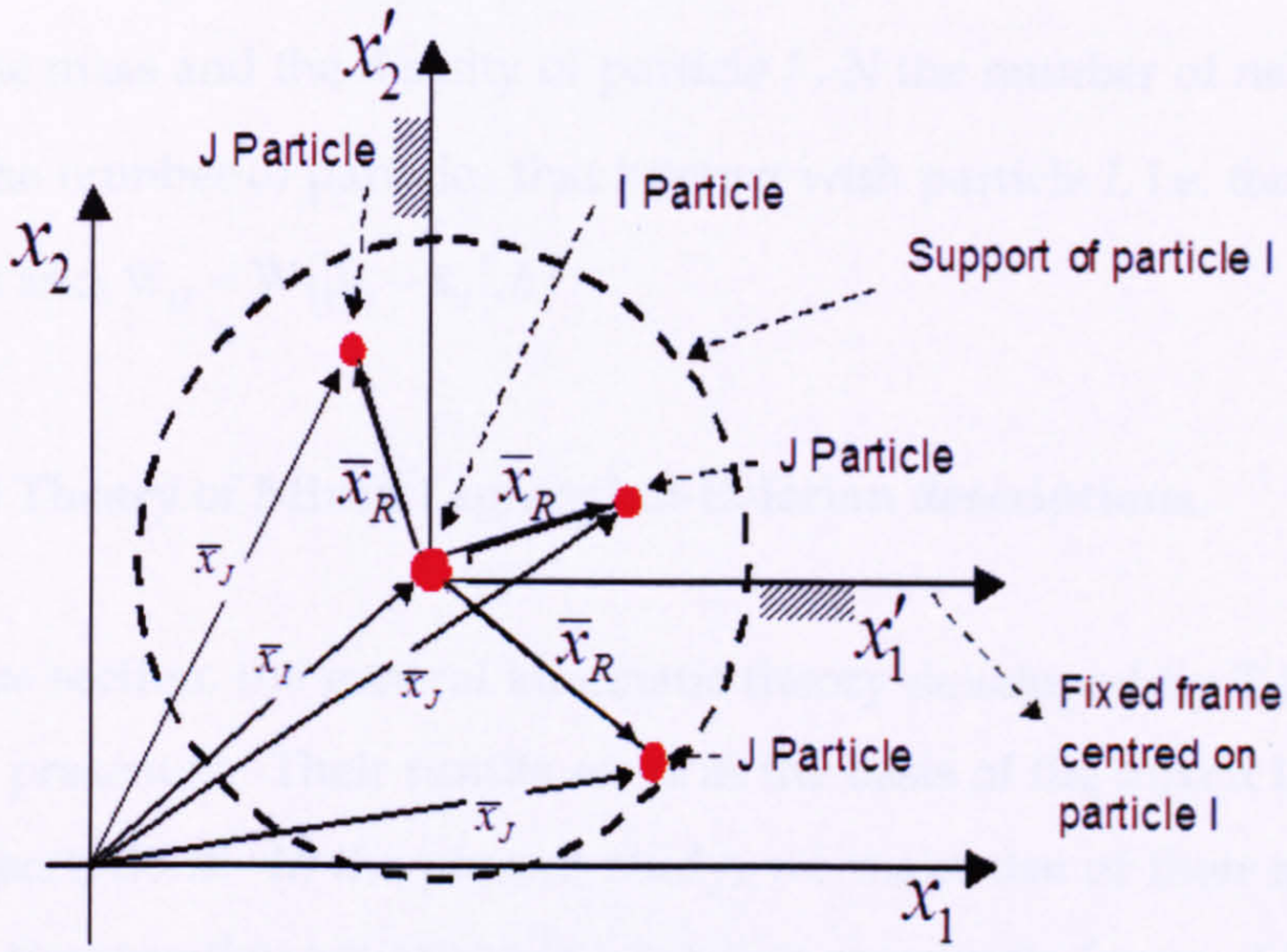

Fig. 7.1 A 2D domain of a kernel function in the conventional SPH method

- Due to the symmetric nature of the kernel function, the following expression should hold:

$$\frac{\partial \mathrm{W}(0,h)}{\partial \bar{\mathbf{x}}'} = 0 \tag{7.2}$$

Note that the kernel has to be differentiable at least once since the kernel approximation allows spatial gradients to be determined from the values of the function and the first spatial derivative of the kernel rather than the derivatives of the function itself. In addition, the derivative should be continuous to prevent large fluctuations in the values of the variables of particle *I*.

- In the limit W equals the Dirac delta function as *h* approaches zero.

$$\lim_{h\to 0} \mathrm{W}\left(\left|\bar{\mathbf{x}} - \bar{\mathbf{x}}'\right|, h\right) = \delta\left(\left|\bar{\mathbf{x}} - \bar{\mathbf{x}}'\right|\right) \tag{7.3}$$

The second step is to convert the kernel integrals into a volume weighted sum. This is known as particle approximation. Thus

$$f_I = f\left(\bar{\mathbf{x}}_I\right) \approx \left\langle f\left(\bar{\mathbf{x}}_I\right)\right\rangle = \sum_{J=1}^{N} f\left(\bar{\mathbf{x}}_J\right) \mathrm{W}_{IJ} \frac{m_J}{\rho_J} \tag{7.4}$$

In the equation above the subscript I and J denote particle number, m_J and ρ_J the mass and the density of particle J, N the number of neighbours of particle I (the number of particles that interact with particle I, i.e. the support of the Kernel) and $W_{IJ} = W\left(\left|\bar{\mathbf{x}}_I - \bar{\mathbf{x}}_J\right|, h\right)$.

7.2 General Theory of Mixed Lagrangian-Eulerian descriptions.

In this section, the general kinematic theory developed by T.J.R. Hughes et al. [41] is presented. Their results serve as the basis of the mixed Lagrangian-Eulerian descriptions. In the present study, we make use of their approach to express the conservation equations in a moving coordinate frame. Likewise, we use their notation to refer to body configurations and co-ordinates systems. The notation used by Hughes et al. is as follows (Refer to Fig 7.2):

r = Referential co-ordinates

Ω_r = Referential domain

x = Spatial/Eulerian co-ordinates

Ω_x = Spatial domain

X = Material/Lagrangian co-ordinates

Ω_X = Initial/Material configuration

$x = \varphi(X,t) =$ mapping of initial into current configuration (7.5)

$x = \hat{\varphi}(r,t) =$ mapping of referential configuration into current configuration (7.6)

$r = \phi(X,t) =$ mapping of initial configuration into referential configuration (7.7)

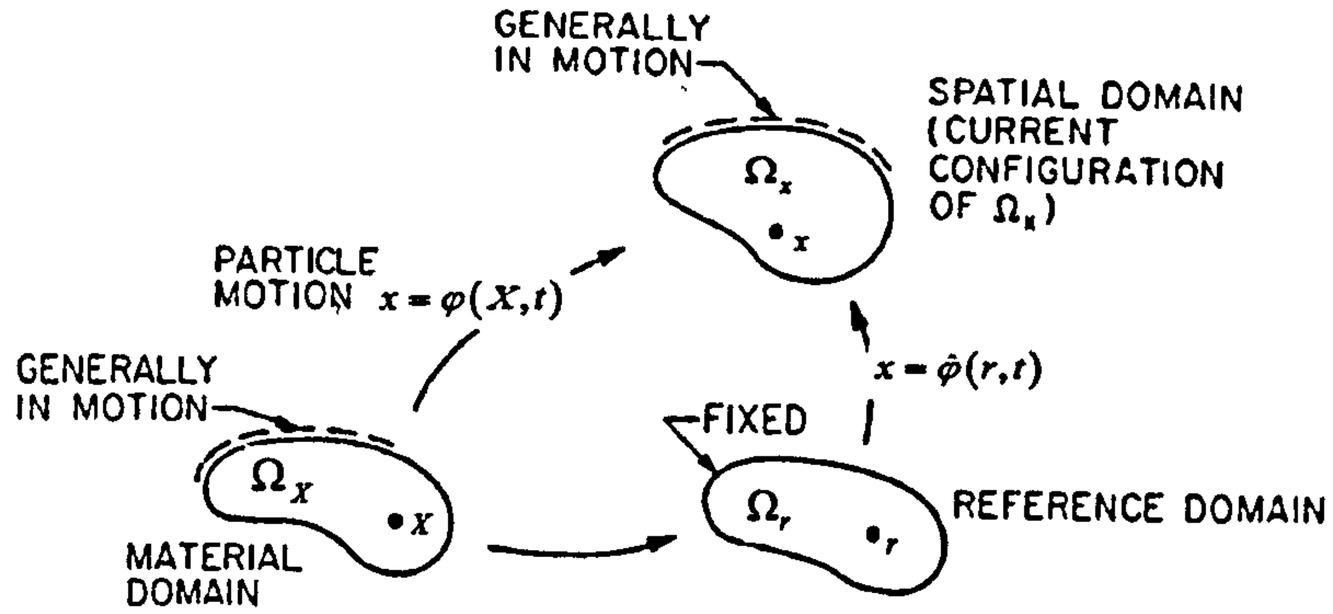

Fig. 7.2 Schematic diagram of domains and mappings for mixed Lagrangian-Eulerian description (from [41]).

$$\text{Time derivatives: } r_i' = \left.\frac{\partial r_i}{\partial t}\right|_r = 0 \ , \ x_{i,t} = \left.\frac{\partial x_i}{\partial t}\right|_x = 0 \ , \ \dot{X}_i = \left.\frac{\partial X_i}{\partial t}\right|_X = 0 \tag{7.8}$$

$$\text{Spatial derivatives: } r_{i,j} = \frac{\partial r_i}{\partial r_j} = \delta_{ij} \ , \ x_{i,j} = \frac{\partial x_i}{\partial x_j} = \delta_{ij} \ , \ X_{i,j} = \frac{\partial X_i}{\partial X_j} = \delta_{ij} \tag{7.9}$$

A convective velocity term is developed as follows:

Using (7.6) and (7.7) we can construct the following composition of functions:

$$x_i = \hat{\varphi}(r,t) = \hat{\varphi}\left(\phi(X,t),t\right) \tag{7.10}$$

Deriving (7.10) with respect to time whilst keeping X constant yields :

$$\left.\frac{\partial x_i}{\partial t}\right|_r = \dot{u}_i = \frac{\partial \hat{\varphi}_i}{\partial r_j}\left.\frac{\partial r_j}{\partial t}\right|_X + \left.\frac{\partial \hat{\varphi}_i}{\partial t}\right|_r \tag{7.11}$$

With $\dfrac{\partial \hat{\varphi}_i}{\partial r_j} = \delta_{ij} + \dfrac{\partial \hat{u}_i}{\partial r_j}$, $\left.\dfrac{\partial r_j}{\partial t}\right|_X = \dfrac{\partial \phi_j}{\partial t} = \dot{w}_j$ and $\left.\dfrac{\partial \hat{\varphi}_i}{\partial t}\right|_r = x_i' = \hat{u}_i'$ as in [41] we can re-write (7.11) as:

$$\dot{u}_i = \left(\delta_{ij} + \frac{\partial \hat{u}_i}{\partial r_j}\right)\frac{\partial \phi_j}{\partial t} + x_i' \tag{7.12}$$

And finally:

$$\dot{u}_i = x_{i,j}\dot{w}_j + \hat{u}_i' \tag{7.13}$$

From (7.13) we can obtain the convective velocity term as follows:

$$\dot{w}_i = \frac{1}{x_{i'j}}\left(\dot{u}_i - \hat{u}_i\right) \tag{7.14}$$

$$\dot{w}_i = r_{i,j}c_i \tag{7.15}$$

where c_i is the convective velocity term $c_i = \left(\dot{u}_i - \hat{u}_i'\right)$ (7.16)

Due to the Eulerian nature of the conventional SPH method, we are interested in mapping Spatial co-ordinates into a Referential domain which remains fixed on a given SPH particle. We define a function g as in [41] such that: $g : \Omega_x \times]0,T[\rightarrow \Re$.

We would like to define the mapping between a function g in Ω_x and a function f in Ω_r. The composition of functions is carried out as follows:

$$g(x,t) = g\left(\hat{\varphi}(r,t),t\right) = f(r,t) \tag{7.17}$$

the derivative of g with respect to time at a referential point r (Using Hughes et al. notation [41] and the derivative of composition of functions rule) yields:

$$\left.\frac{\partial g\left(\hat{\varphi}(r,t),t\right)}{\partial t}\right|_r = f'(r,t)\Big|_r = \left.\frac{\partial g\left(\hat{\varphi}(r,t),t\right)}{\partial x_i}\frac{\partial x_i}{\partial t}\right|_r + \left.\frac{\partial g\left(\hat{\varphi}(r,t),t\right)}{\partial t}\right|_x \tag{7.18}$$

Following Hughes et al. notation [41] we can write:

$$\left.\frac{\partial x_i}{\partial t}\right|_r = \frac{\partial \hat{\varphi}}{\partial t} = \hat{u}_i' \tag{7.19}$$ and $$\frac{\partial f(r,t)}{\partial x_i} = \frac{\partial g\left(\hat{\varphi}(r,t),t\right)}{\partial x_i} \tag{7.20}$$

Using (7.18),(7.19) and (7.20) yields:

$$f'(x,t) = f_{,i}\hat{u}_i' + f_{,t} \tag{7.21}$$

(7.13) in (7.21) yields:

$$f' + f_{,i}x_{i'j}\dot{w}_i = f_{,t} + f_{,i}\dot{u}_i \tag{7.22}$$

which can be re-written as:

$$f' + f_{,i}\dot{w}_i = f_{,t} + f_{,i}\dot{u}_i \tag{7.23}$$

as in [41].

f' represents the time variation of $f(r,t)$ at a constant referential co-ordinate r, *i.e.* the local change.

$f_{,i}$ represents the gradient of $f(r,t)$ with respect to referential co-ordinates r

$\dot{w}_i$ represents the difference between the velocity of a material point X and the velocity of our referential point r multiplied by the Jacobian which transforms spatial into referential co-ordinates.

7.3 SPH discretisation of the Conservation Equations of Continuum Mechanics in a moving reference frame.

In order to express the conservation equations in a referential domain, we make use of the general theory developed by Hughes et al. [41] for the mixed Lagrangian-Eulerian descriptions of motion. To accomplish this task let us introduce a moving Cartesian frame attached to the particle *I*. In doing so the distance $|\bar{\mathbf{x}} - \bar{\mathbf{x}}'|$ that the kernel function W depends on, becomes a function of two variables $\bar{\mathbf{x}}$ and $\bar{\mathbf{x}}'$. The smoothing length h of the interpolation function (centred at particle *I*) defines the kernel support or control volume (CV) over which the smoothing is performed. In general, the continuum occupying the CV moves relative to the CV everywhere apart from the location defined by $\bar{\mathbf{x}}$.

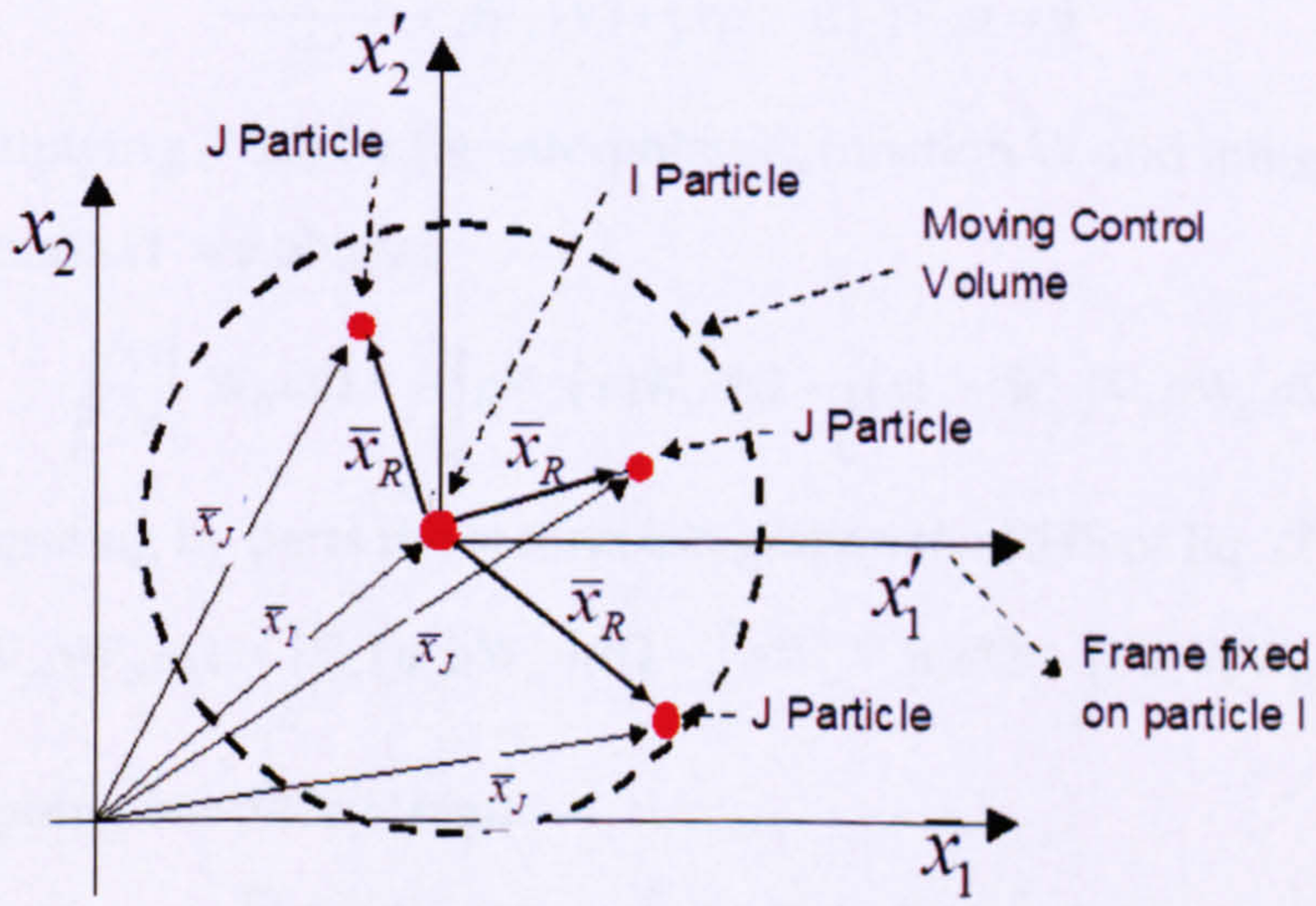

Fig. 7.3 A 2D representation of domain of a kernel function in a moving coordinate system.

In the case of discrete forms, neighbouring particles move relative to the control volume with a velocity $\vec{\mathbf{v}}_R = \vec{\mathbf{v}}'_J - \vec{\mathbf{v}}_I$, where $\vec{\mathbf{v}}'_J$ is the velocity of a material point within the CV and $\vec{\mathbf{v}}_I$ is the velocity of the referential point at $\vec{\mathbf{x}}$. The velocity of the CV is identical to the velocity of particle *I*. This is represented schematically in Fig. 7.3.

In this analysis the SPH derivation uses the strong form of the conservation equations expressed in the moving coordinate system.

7.3.1 Conservation of mass.

Applying the procedure found in [41] the mass conservation equation in spatial coordinates can be rewritten in a referential frame as follows:

$$\left.\frac{\partial \rho}{\partial t}\right|_r + \dot{\mathbf{w}}\nabla_r \rho + \rho \nabla_x \mathbf{v} = 0 \tag{7.24}$$

From the definition of $\dot{\mathbf{w}}$ we obtain:

$$\left.\frac{\partial \rho}{\partial t}\right|_r + \frac{\partial r}{\partial x}\left(\mathbf{v}\big|_X - \hat{\mathbf{u}}'\big|_r\right)\nabla_r \rho + \rho \nabla_x \mathbf{v} = 0 \tag{7.25}$$

The reference and spatial coordinate systems remain parallel, hence (7.6) can be rewritten as:

$$\frac{\partial \rho(r,t)}{\partial t} + \rho \nabla_x(\mathbf{v}) + \left(\mathbf{v}\big|_X - \hat{\mathbf{u}}'\big|_r\right)\nabla_r \rho = 0 \tag{7.26}$$

Multiplying (7.26) by the interpolating function W and integrating over the sub-domain Ω we obtain:

$$\int_\Omega \left.\frac{\partial \rho}{\partial t}\right|_r \mathrm{W}_{IJ} d\Omega = -\int_\Omega \rho \nabla_x(\mathbf{v})\mathrm{W}_{IJ} d\Omega - \int_\Omega \left(\mathbf{v}\big|_X - \hat{\mathbf{u}}'\big|_r\right)\nabla_r \rho \mathrm{W}_{IJ} d\Omega \tag{7.27}$$

Integrating by parts the second integral on the RHS of Eq. (7.27):

$$\int_\Omega \hat{\mathbf{u}}_r \nabla_r \rho \mathrm{W}_{IJ} d\Omega = \int_\Omega \nabla_r(\hat{\mathbf{u}}_r \rho \mathrm{W}_{IJ}) d\Omega - \int_\Omega \rho \mathrm{W}_{IJ} \nabla_r \hat{\mathbf{u}}_r d\Omega - \int_\Omega \rho \hat{\mathbf{u}}_r \nabla_r \mathrm{W}_{IJ} d\Omega \tag{7.28}$$

Dropping boundary terms:

$$\int_\Omega \hat{\mathbf{u}}_r \nabla_r \rho \mathrm{W}_{IJ} d\Omega = -\int_\Omega \rho \mathrm{W}_{IJ} \nabla_r \hat{\mathbf{u}}_r d\Omega - \int_\Omega \rho \hat{\mathbf{u}}_r \nabla_r \mathrm{W}_{IJ} d\Omega \tag{7.29}$$

The first integral on the RHS of Eq.(7.29) yields:

$$-\int_{\Omega}\rho W_{IJ}\nabla_r\hat{\mathbf{u}}_r d\Omega \approx \rho_I\sum_{J\epsilon S}\mathbf{v}_J\frac{\mathrm{m}_J}{\rho_J}\nabla_r W_{IJ} \tag{7.30}$$

And the second integral yields:

$$-\int_{\Omega}\rho\hat{\mathbf{u}}_r\nabla_r W_{IJ}d\Omega \approx -\rho_I\mathbf{v}_I\sum_{J\epsilon S}\frac{\mathrm{m}_J}{\rho_J}\nabla_r W_{IJ} \tag{7.31}$$

Also in the second integral on the RHS of Eq. (7.27):

$$-\int_{\Omega}\mathbf{v}\big|_X\nabla_r\rho W_{IJ}d\Omega \approx \mathbf{v}_I\sum_{J\epsilon S}\mathrm{m}_J\nabla_r W_{IJ} \tag{7.32}$$

The first integral on the RHS of Eq. (7.27) can be discretised as:

$$-\int_{\Omega}\rho\nabla_x(\mathbf{v})W_{IJ}d\Omega \approx \rho_I\sum_{J\epsilon K}\mathbf{v}_J\frac{\mathrm{m}_J}{\rho_J}\nabla_x W_{IJ} \tag{7.33}$$

Finally:

$$\langle\dot{\rho}_I\rangle = \rho_I\sum_{J\epsilon S}(\mathbf{v}_J-\mathbf{v}_I)\frac{\mathrm{m}_J}{\rho_J}\nabla_r W_{IJ}+\mathbf{v}_J\sum_{J\epsilon S}\mathrm{m}_J\nabla_r W_{IJ}+\rho_I\sum_{J\epsilon K}\mathbf{v}_J\frac{\mathrm{m}_J}{\rho_J}\nabla_x W_{IJ} \tag{7.34}$$

7.3.2 Conservation of momentum.

The momentum equation in the absolute co-ordinate frame is stated as:

$$\frac{\partial(\rho\bar{\mathbf{v}})}{\partial t}+\nabla(\rho\bar{\mathbf{v}}\otimes\bar{\mathbf{v}}) = \nabla.\bar{\bar{\sigma}} \tag{7.35}$$

In referential coordinates this is expressed in index notation as:

$$\rho\left[\frac{\partial\left(x_{i,j}\dot{w}_j+\hat{u}_i'\right)}{\partial t}+\dot{w}_j\nabla_j\left(x_{i,k}\dot{w}_k+\hat{u}_i'\right)\right] = \nabla_j\left(\hat{\sigma}_{mn}\frac{\partial r^m}{\partial x^i}\frac{\partial r^n}{\partial x^j}\right) \tag{7.36}$$

$\hat{\sigma}$ is the stress tensor in referential configuration. This expression can be rewritten as:

$$\frac{D\dot{u}(r,t)}{Dt} = \frac{1}{\rho}\nabla_j\left(\hat{\sigma}_{ij}\right) \tag{7.37}$$

kernel approximation of the above leads to:

$$\int_{\Omega}\frac{D\dot{u}}{Dt}W_{IJ}d\Omega = \int_{\Omega}\left(\frac{1}{\rho}\nabla\hat{\sigma}W_{IJ}\right)d\Omega \tag{7.38}$$

7.3.3 *Constitutive equation.*

The velocity gradient in absolute coordinates is written as:

$$L_{ij} = \frac{\partial v_i}{\partial x_j} \tag{7.39}$$

in referential coordinates:

$$\hat{L}_{ij} = \frac{\partial\left(x_{i,l}\dot{w}_l + \hat{u}'_i\right)}{\partial r_j} \tag{7.40}$$

From (7.39) the rate of deformation in referential coordinates can be calculated as the symmetric part of the velocity gradient:

$$\dot{\hat{\varepsilon}} = \frac{1}{2}\left(\frac{\partial\left(x_{i,l}\dot{w}_l + \hat{u}'_i\right)}{\partial r_j} + \frac{\partial\left(x_{j,k}\dot{w}_k + \hat{u}'_j\right)}{\partial r_i}\right) \tag{7.41}$$

for an elastic isotropic material the generalised Hooke's law in referential coordinates is written as:

$$\overset{\nabla}{\hat{\sigma}}_{ij} = C_{ijkl}\dot{\hat{\varepsilon}}_{kl} \tag{7.42}$$

where the stress rate is given by:

$$\overset{\nabla}{\hat{\sigma}}_{ij} = \frac{d\hat{\sigma}_{ij}}{dt} + \hat{\sigma}_{ik}\omega_{kj} + \hat{\sigma}_{kj}\omega_{ki} \tag{7.43}$$

The spin tensor ω can be calculated from (7.40) and (7.41) and $\frac{d\hat{\sigma}_{ij}}{dt}$ is used to update the values of stress.

7.4 Material Form of the Continuity Equation in SPH.

In this section an alternative form of the conservation of mass equation is derived and discretised in an SPH framework. The material form of the continuity equation is provided in [4] without proof. The SPH form of this equation is similar to the standard SPH equation in Eulerian coordinates in that it contains a total derivative and a velocity gradient term. In addition, it also contains a Jacobian term, which is present in the conservation of mass equation expressed in a Lagrangian referential. The resulting SPH equation could be used as a link between Eulerian and Total Lagrangian SPH codes if such a

scheme was required or when mapping from one configuration to another proved advantageous. The continuity equation employed in standard SPH codes adopts the following form in a Cartesian referential:

$$\frac{\partial \rho}{\partial t} + \frac{\partial (\rho v_i)}{\partial x_i} = 0 \tag{7.51}$$

where x is the spatial or Eulerian coordinate, ρ is the density and v is the velocity of material particle i.

If material coordinates are used, the conservation of mass implies:

$$\int_{V_0} \rho_0(X_1, X_2, X_3, t_0) dV_0 = \int_V \rho(x_1, x_2, x_3, t) dV \tag{7.52}$$

where V is the volume occupied at time t by the material which occupied V_0 at time t_0 and X are the material coordinates.

This can be rewritten as:

$$\int_{V_0} \rho_0(X_1, X_2, X_3, t_0) dV_0 = \int_{V_0} \rho(x_1(X_1, X_2, X_3), x_2(X_1, X_2, X_3), x_3(X_1, X_2, X_3), t) |J| dV_0 \tag{7.53}$$

from which we can write:

$$\rho J = \rho_0 \tag{7.54}$$

In Eq. (7.54), the product ρJ and ρ_0 remain constant for each particle.

The equation above bears no resemblance to Eq.(7.51) in spatial coordinates. However, they express the same physical assumption which is the conservation of mass.

By taking the total derivative of the previous expression we obtain:

$$\frac{D(\rho J)}{Dt} = 0 \tag{7.55}$$

where $\frac{D}{Dt} = \frac{\partial}{\partial t} + v\nabla$ (7.56).

the derivative yields:

$$\frac{D(\rho J)}{Dt} = \frac{D\rho}{Dt} J + \frac{DJ}{Dt} \rho = 0 \tag{7.57}$$

The material derivative of the Jacobian is found as follows:

$$\frac{DJ}{Dt} = \frac{D}{Dt}\begin{vmatrix} \frac{\partial x_1}{\partial X_1} & \frac{\partial x_1}{\partial X_2} & \frac{\partial x_1}{\partial X_3} \\ \frac{\partial x_2}{\partial X_1} & \frac{\partial x_2}{\partial X_2} & \frac{\partial x_2}{\partial X_3} \\ \frac{\partial x_3}{\partial X_1} & \frac{\partial x_3}{\partial X_2} & \frac{\partial x_3}{\partial X_3} \end{vmatrix} \tag{7.58}$$

The derivative of a third order determinant is the sum of three terms in each of which only one row is differentiated:

$$\frac{DJ}{Dt} - \begin{vmatrix} \frac{\partial v_1}{\partial X_1} & \frac{\partial v_1}{\partial X_2} & \frac{\partial v_1}{\partial X_3} \\ \frac{\partial x_2}{\partial X_1} & \frac{\partial x_2}{\partial X_2} & \frac{\partial x_2}{\partial X_3} \\ \frac{\partial x_3}{\partial X_1} & \frac{\partial x_3}{\partial X_2} & \frac{\partial x_3}{\partial X_3} \end{vmatrix} - \begin{vmatrix} \frac{\partial x_1}{\partial X_1} & \frac{\partial x_1}{\partial X_2} & \frac{\partial x_1}{\partial X_3} \\ \frac{\partial v_2}{\partial X_1} & \frac{\partial v_2}{\partial X_2} & \frac{\partial v_2}{\partial X_3} \\ \frac{\partial x_3}{\partial X_1} & \frac{\partial x_3}{\partial X_2} & \frac{\partial x_3}{\partial X_3} \end{vmatrix} - \begin{vmatrix} \frac{\partial x_1}{\partial X_1} & \frac{\partial x_1}{\partial X_2} & \frac{\partial x_1}{\partial X_3} \\ \frac{\partial x_2}{\partial X_1} & \frac{\partial x_2}{\partial X_2} & \frac{\partial x_2}{\partial X_3} \\ \frac{\partial v_3}{\partial X_1} & \frac{\partial v_3}{\partial X_2} & \frac{\partial v_3}{\partial X_3} \end{vmatrix} = 0 \tag{7.59}$$

If we regard v_i as a function of x_1, x_2, x_3 then:

$$\frac{\partial v_i}{\partial X_j} = \frac{\partial v_i}{\partial x_k}\frac{\partial x_k}{\partial X_j} \tag{7.60}$$

which implies the first determinant in (7.59) can be rewritten as:

$$\begin{vmatrix} \frac{\partial v_1}{\partial X_1} & \frac{\partial v_1}{\partial X_2} & \frac{\partial v_1}{\partial X_3} \\ \frac{\partial x_2}{\partial X_1} & \frac{\partial x_2}{\partial X_2} & \frac{\partial x_2}{\partial X_3} \\ \frac{\partial x_3}{\partial X_1} & \frac{\partial x_3}{\partial X_2} & \frac{\partial x_3}{\partial X_3} \end{vmatrix} = \begin{vmatrix} \frac{\partial v_1}{\partial x_k}\frac{\partial x_k}{\partial X_1} & \frac{\partial v_1}{\partial x_k}\frac{\partial x_k}{\partial X_2} & \frac{\partial v_1}{\partial x_k}\frac{\partial x_k}{\partial X_3} \\ \frac{\partial x_2}{\partial X_1} & \frac{\partial x_2}{\partial X_2} & \frac{\partial x_2}{\partial X_3} \\ \frac{\partial x_3}{\partial X_1} & \frac{\partial x_3}{\partial X_2} & \frac{\partial x_3}{\partial X_3} \end{vmatrix} \tag{7.61}$$

Now, if each element in any column or row of a determinant is expressed as the sum of two or more quantities (as in the case of the repeated index in the first column of the determinant above), the original determinant can be expressed as the sum of two or more determinants of the same order:

$$\begin{vmatrix} \frac{\partial v_1}{\partial x_k}\frac{\partial x_k}{\partial X_1} & \frac{\partial v_1}{\partial x_k}\frac{\partial x_k}{\partial X_2} & \frac{\partial v_1}{\partial x_k}\frac{\partial x_k}{\partial X_3} \\ \frac{\partial x_2}{\partial X_1} & \frac{\partial x_2}{\partial X_2} & \frac{\partial x_2}{\partial X_3} \\ \frac{\partial x_3}{\partial X_1} & \frac{\partial x_3}{\partial X_2} & \frac{\partial x_3}{\partial X_3} \end{vmatrix} = \begin{vmatrix} \frac{\partial v_1}{\partial x_1}\frac{\partial x_1}{\partial X_1} & \frac{\partial v_1}{\partial x_1}\frac{\partial x_1}{\partial X_2} & \frac{\partial v_1}{\partial x_1}\frac{\partial x_1}{\partial X_3} \\ \frac{\partial x_2}{\partial X_1} & \frac{\partial x_2}{\partial X_2} & \frac{\partial x_2}{\partial X_3} \\ \frac{\partial x_3}{\partial X_1} & \frac{\partial x_3}{\partial X_2} & \frac{\partial x_3}{\partial X_3} \end{vmatrix} + \begin{vmatrix} \frac{\partial v_1}{\partial x_2}\frac{\partial x_2}{\partial X_1} & \frac{\partial v_1}{\partial x_2}\frac{\partial x_2}{\partial X_2} & \frac{\partial v_1}{\partial x_2}\frac{\partial x_2}{\partial X_3} \\ \frac{\partial x_2}{\partial X_1} & \frac{\partial x_2}{\partial X_2} & \frac{\partial x_2}{\partial X_3} \\ \frac{\partial x_3}{\partial X_1} & \frac{\partial x_3}{\partial X_2} & \frac{\partial x_3}{\partial X_3} \end{vmatrix} +$$

$$+ \begin{vmatrix} \frac{\partial v_1}{\partial x_3}\frac{\partial x_3}{\partial X_1} & \frac{\partial v_1}{\partial x_3}\frac{\partial x_3}{\partial X_2} & \frac{\partial v_1}{\partial x_3}\frac{\partial x_3}{\partial X_3} \\ \frac{\partial x_2}{\partial X_1} & \frac{\partial x_2}{\partial X_2} & \frac{\partial x_2}{\partial X_3} \\ \frac{\partial x_3}{\partial X_1} & \frac{\partial x_3}{\partial X_2} & \frac{\partial x_3}{\partial X_3} \end{vmatrix} \tag{7.62}$$

Since all elements in a row are multiplied by a factor, the determinant itself is multiplied by the factor:

$$\begin{vmatrix} \frac{\partial v_1}{\partial x_k}\frac{\partial x_k}{\partial X_1} & \frac{\partial v_1}{\partial x_k}\frac{\partial x_k}{\partial X_2} & \frac{\partial v_1}{\partial x_k}\frac{\partial x_k}{\partial X_3} \\ \frac{\partial x_2}{\partial X_1} & \frac{\partial x_2}{\partial X_2} & \frac{\partial x_2}{\partial X_3} \\ \frac{\partial x_3}{\partial X_1} & \frac{\partial x_3}{\partial X_2} & \frac{\partial x_3}{\partial X_3} \end{vmatrix} = \frac{\partial v_1}{\partial x_1}\begin{vmatrix} \frac{\partial x_1}{\partial X_1} & \frac{\partial x_1}{\partial X_2} & \frac{\partial x_1}{\partial X_3} \\ \frac{\partial x_2}{\partial X_1} & \frac{\partial x_2}{\partial X_2} & \frac{\partial x_2}{\partial X_3} \\ \frac{\partial x_3}{\partial X_1} & \frac{\partial x_3}{\partial X_2} & \frac{\partial x_3}{\partial X_3} \end{vmatrix} + \frac{\partial v_1}{\partial x_2}\begin{vmatrix} \frac{\partial x_2}{\partial X_1} & \frac{\partial x_2}{\partial X_2} & \frac{\partial x_2}{\partial X_3} \\ \frac{\partial x_2}{\partial X_1} & \frac{\partial x_2}{\partial X_2} & \frac{\partial x_2}{\partial X_3} \\ \frac{\partial x_3}{\partial X_1} & \frac{\partial x_3}{\partial X_2} & \frac{\partial x_3}{\partial X_3} \end{vmatrix} +$$

$$+ \frac{\partial v_1}{\partial x_3}\begin{vmatrix} \frac{\partial x_3}{\partial X_1} & \frac{\partial x_3}{\partial X_2} & \frac{\partial x_3}{\partial X_3} \\ \frac{\partial x_2}{\partial X_1} & \frac{\partial x_2}{\partial X_2} & \frac{\partial x_2}{\partial X_3} \\ \frac{\partial x_3}{\partial X_1} & \frac{\partial x_3}{\partial X_2} & \frac{\partial x_3}{\partial X_3} \end{vmatrix} \tag{7.63}$$

where the last two determinants are zero, therefore:

$$\begin{vmatrix} \frac{\partial v_1}{\partial x_k}\frac{\partial x_k}{\partial X_1} & \frac{\partial v_1}{\partial x_k}\frac{\partial x_k}{\partial X_2} & \frac{\partial v_1}{\partial x_k}\frac{\partial x_k}{\partial X_3} \\ \frac{\partial x_2}{\partial X_1} & \frac{\partial x_2}{\partial X_2} & \frac{\partial x_2}{\partial X_3} \\ \frac{\partial x_3}{\partial X_1} & \frac{\partial x_3}{\partial X_2} & \frac{\partial x_3}{\partial X_3} \end{vmatrix} = \frac{\partial v_1}{\partial x_1} J \tag{7.64}$$

Similarly, we can proceed with the rest of the determinants to obtain:

$$\frac{DJ}{Dt} - \frac{\partial v_1}{\partial x_1} J - \frac{\partial v_2}{\partial x_2} J - \frac{\partial v_3}{\partial x_3} J = 0 \tag{7.65}$$

Which is equivalent to

$$\frac{DJ}{Dt} - J\nabla.\vec{\mathbf{v}} = 0 \tag{7.66}$$

This equation is given by Belytschko et al. in [4] without demonstration.

Eq (7.66) in Eq (7.57) yields:

$$\frac{D\rho}{Dt} + \rho\nabla.\vec{\mathbf{v}} = 0 \tag{7.67}$$

i.e. same as Eq. (7.51)

Equation (7.66) was implemented in the SPH code. The results obtained with this equation and Eq (7.67) are identical. In other words, the density update in SPH can be carried out using Eq (7.54) and Eq. (7.66) or alternatively Eq (7.67).

The potential advantage of Eq. (7.66) is that it might prove useful in certain problems that involve a moving integration volume where the conservation of space law has to be solved simultaneously with the mass, momentum and energy conservation equations [23]. The conservation of space law states that:

$$\frac{1}{\sqrt{g}}\left(\frac{\partial\sqrt{g}}{\partial t}\right) - \nabla.\vec{\mathbf{v}} = 0 \tag{7.68}$$

where $\sqrt{g}$ is the determinant of the metric tensor. In a Cartesian coordinate system $\sqrt{g}$ gets calculated through Eq (4.8) provided in Chapter 4.

Note the similarities between (7.68) and (7.66). In the specific case of the Total Lagrangian SPH code the equation that allows us to approximate (7.66) is written as follows:

$$\frac{1}{J^n}\frac{J^{n+1} - J^n}{\Delta t} - trace\,\bar{\bar{\mathbf{D}}} = 0 \tag{7.69}$$

where $J^n = \det\left|\bar{\bar{\mathbf{F}}}^n\right|$

and the gradient of deformation is calculated in SPH as:

$$\left\langle \bar{\bar{\mathbf{F}}}\left(\vec{\mathbf{X}}_I\right)\right\rangle = -\sum_{J\in S}\left(\vec{\mathbf{u}}_J - \vec{\mathbf{u}}_I\right)\otimes\nabla_{\vec{\mathbf{X}}_J}\mathrm{W}\left(\vec{\mathbf{X}}_I - \vec{\mathbf{X}}_J, h_0\right)\mathbf{V}_J^0 + \mathbf{I} \tag{7.70}$$

7.5 Integration of the Conservation of Mass Equation in SPH with Variable Smoothing Length.

In SPH, Eq. (2.51) introduced in Chapter 2 is generally used to update particle densities during the integration process. However, it is Eq. (2.48) that ensures mass is conserved locally at every particle. Note that meeting Eq. (2.51) does not imply Eq. (2.48) is met and vice-versa. Eq. (2.48), $\rho(\vec{\mathbf{x}}_I) = \sum_{J\in S} m_J \mathrm{W}(\vec{\mathbf{x}}_I - \vec{\mathbf{x}}_J, h)$, is rarely used in SPH computations. Most hydrocodes use Eq. (2.51), $\left\langle \frac{D\rho(\vec{\mathbf{x}}_I)}{Dt}\right\rangle = \rho_I \sum_{J\in S}\frac{m_J}{\rho_J}\left(\vec{\mathbf{v}}_I - \vec{\mathbf{v}}_J\right)\cdot\nabla_{\vec{\mathbf{x}}_I}\mathrm{W}\left(\vec{\mathbf{x}}_I - \vec{\mathbf{x}}_J, h\right)$, to perform the density update at every time step.

The purpose of this section is to introduce the concept of variable smoothing length and Eq. (2.48) to ensure conservation of mass as expressed by Eq (2.48) is met which should yield a more accurate density calculation in SPH.

One way in which the particle mass and the smoothing length are related is through the following expression [80]:

$$m = \rho h^{n\mathrm{dim}} \tag{7.71}$$

where $n$dim is the problem dimension, m is the mass and ρ is the particle density.

If the initial mass at a particle level is to be conserved during the deformation process, the following must hold:

$$h = h_0\left(\frac{\rho_0}{\rho}\right)^{1/n\mathrm{dim}} \tag{7.72}$$

In 3-D the previous equation becomes:

$$h = h_0 \left(\frac{\rho_0}{\rho} \right)^{1/3} \tag{7.73}$$

The derivative of the previous equation with respect to time yields the well known Benz relation [7]:

$$\frac{dh}{dt} = -\frac{1}{3} h_0 \frac{\rho_0}{\rho^2} \frac{d\rho}{dt} \left(\frac{\rho_0}{\rho} \right)^{-2/3} \tag{7.74}$$

With the value of h_0 from Eq (7.73) in Eq.(7.74) yields:

$$\frac{dh}{dt} = -\frac{1}{3} \frac{h}{\rho} \frac{d\rho}{dt} \tag{7.75}$$

The main idea is to use Eq. (7.75) to update *h*. With the updated *h*, the smoothing function gets calculated and Eq. (2.48) is then introduced to update the particle density at every particle. Eq (7.72) is then introduced to update the smoothing length independently. If the value of the smoothing length obtained with Eq(7.72) is different from the smoothing length calculated with (7.75), then using the the smoothing length calculated with Eq (7.72), calculate the smoothing function and the new particle density with Eq. (2.48) until the two values of the smoothing length calculated independently converge (refer to the flow chart provided below, Fig. 7.6).

This has been implemented and results obtained for a 1-D case. Refer to figures 7.4 and 7.5 for 1-D stress levels and value of the smoothing length.

The results presented here are for two bars, one stationary and the other one travelling at $100 \frac{\mathrm{m}}{\mathrm{s}}$ towards the stationary bar. The problem was discretised into 2000 particles, 500 of which belonged to the moving bar. The inter-particle spacing was 1E-3 m and the bars were defined as linear elastic. The quadratic bulk viscosity coefficient was set to 1.5 and the linear bulk viscosity coefficient was set to 0.06. The smoothing length was set to 1.2E-3 m and the smoothing function employed was the cubic spline. Kernel type of contact was used to capture the interaction of the two bars. The density of the

bars was set to 1000 $\frac{kg}{m^3}$, the Young modulus was set to 90E 9 Pa and the Poisson ratio was 0.2.

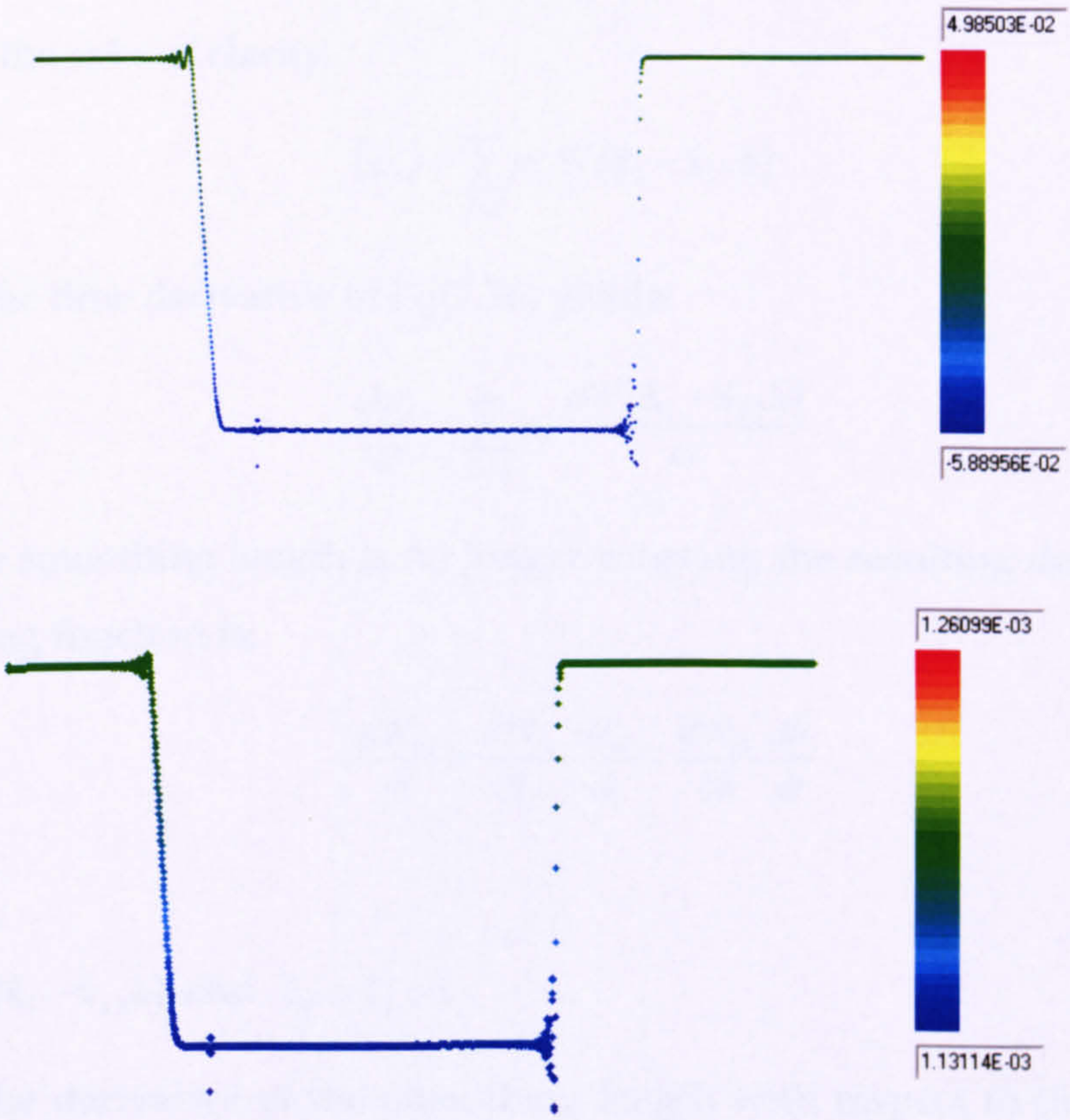

Fig 7.4 Value of smoothing length and value of stress for a variable smoothing length scheme.

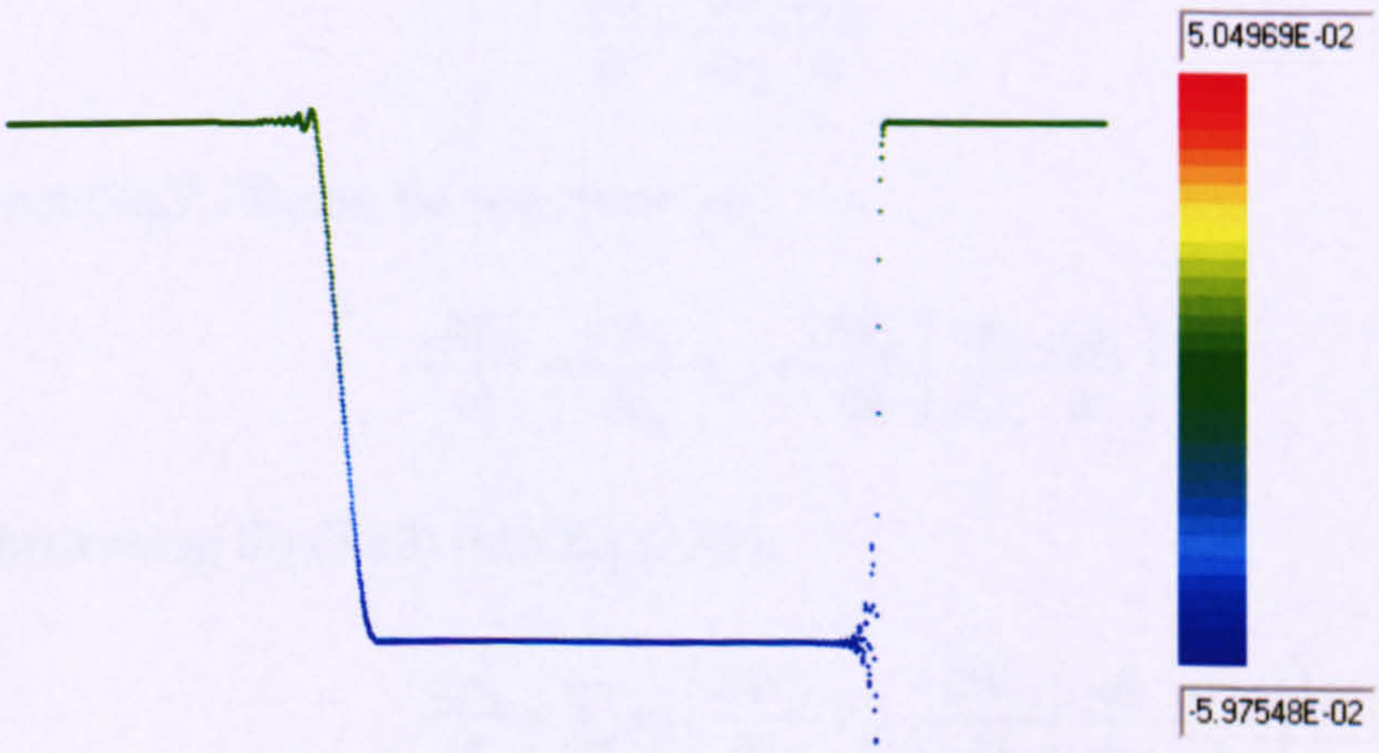

Fig 7.5 Stress wave computed with constant smoothing length scheme.

7.5.1 Derivation of the discretised conservation of mass equation with a variable smoothing length.

In this section an attempt is made to derive a discretised form of the conservation of mass equation which makes use of Eq. (2.48) which is rewritten here for the sake of clarity:

$$\langle \rho_I \rangle = \sum_{J \in S} m_J \mathrm{W}(\vec{\mathbf{x}}_I - \vec{\mathbf{x}}_J, h) \tag{7.76}$$

The time derivative of Eq(7.76) yields:

$$\frac{d\rho_I}{dt} = \sum_{J \in S} m_J \frac{d\mathrm{W}(\vec{\mathbf{x}}_I - \vec{\mathbf{x}}_J, h)}{dt} \tag{7.77}$$

since the smoothing length is no longer constant, the resulting derivative of the smoothing function is:

$$\frac{d\mathrm{W}_{IJ}}{dt} = \frac{\partial \mathrm{W}_{IJ}}{\partial \vec{\mathbf{r}}_{IJ}} \frac{d\vec{\mathbf{r}}_{IJ}}{dt} + \frac{\partial \mathrm{W}_{IJ}}{\partial h} \frac{dh}{dt} \tag{7.78}$$

where:

$\mathrm{W}_{IJ} = \mathrm{W}(\vec{\mathbf{x}}_I - \vec{\mathbf{x}}_J, h)$ and $\vec{\mathbf{r}}_{IJ} = \vec{\mathbf{x}}_I - \vec{\mathbf{x}}_J$

The derivative of the smoothing length with respect to time in Eq(7.78) can be rewritten in the following way:

$$\frac{dh}{dt} = \frac{dh}{d\rho_I} \frac{d\rho_I}{dt} \tag{7.79}$$

Hence Eq(7.78) can be rewritten as

$$\frac{d\mathrm{W}_{IJ}}{dt} = \frac{\partial \mathrm{W}_{IJ}}{\partial \vec{\mathbf{r}}_{IJ}} \vec{\mathbf{v}}_{IJ} + \frac{\partial \mathrm{W}_{IJ}}{\partial h} \left(\frac{dh}{d\rho_I} \frac{d\rho_I}{dt} \right) \tag{7.80}$$

Substituting Eq (7.80) into Eq (7.81):

$$\frac{d\rho_I}{dt} = \sum_{J \in S} m_J \left(\frac{\partial \mathrm{W}_{IJ}}{\partial \vec{\mathbf{r}}_{IJ}} \vec{\mathbf{v}}_{IJ} + \frac{\partial \mathrm{W}_{IJ}}{\partial h} \left(\frac{dh}{d\rho_I} \frac{d\rho_I}{dt} \right) \right) \tag{7.81}$$

which can be rewritten as

$$\frac{d\rho_I}{dt}\left(1-\sum_{K\in S} m_K \frac{\partial W_{IK}}{\partial h}\frac{dh}{d\rho_I}\right)=\sum_{J\in S} m_J \frac{\partial W_{IJ}}{\partial \vec{\mathbf{r}}_{IJ}}\vec{\mathbf{v}}_{IJ} \tag{7.82}$$

From Eq (7.82)

$$\frac{d\rho_I}{dt}=\frac{\sum_{J\in S} m_J \frac{\partial W_{IJ}}{\partial \vec{\mathbf{r}}_{IJ}}\left(\vec{\mathbf{v}}_I-\vec{\mathbf{v}}_J\right)}{\left(1-\sum_{K\in S} m_K \frac{\partial W_{IK}}{\partial h}\frac{dh}{d\rho_I}\right)} \tag{7.83}$$

This procedure can be extended to all conservation laws. The advantage of this procedure over the procedure summarised in Fig. 7.5 is that Eq. (7.83) incorporates a varying smoothing length implicitly. This implies there is no need for an additional equation to be introduced during the simulation process, thus reducing the computational effort during every time step.

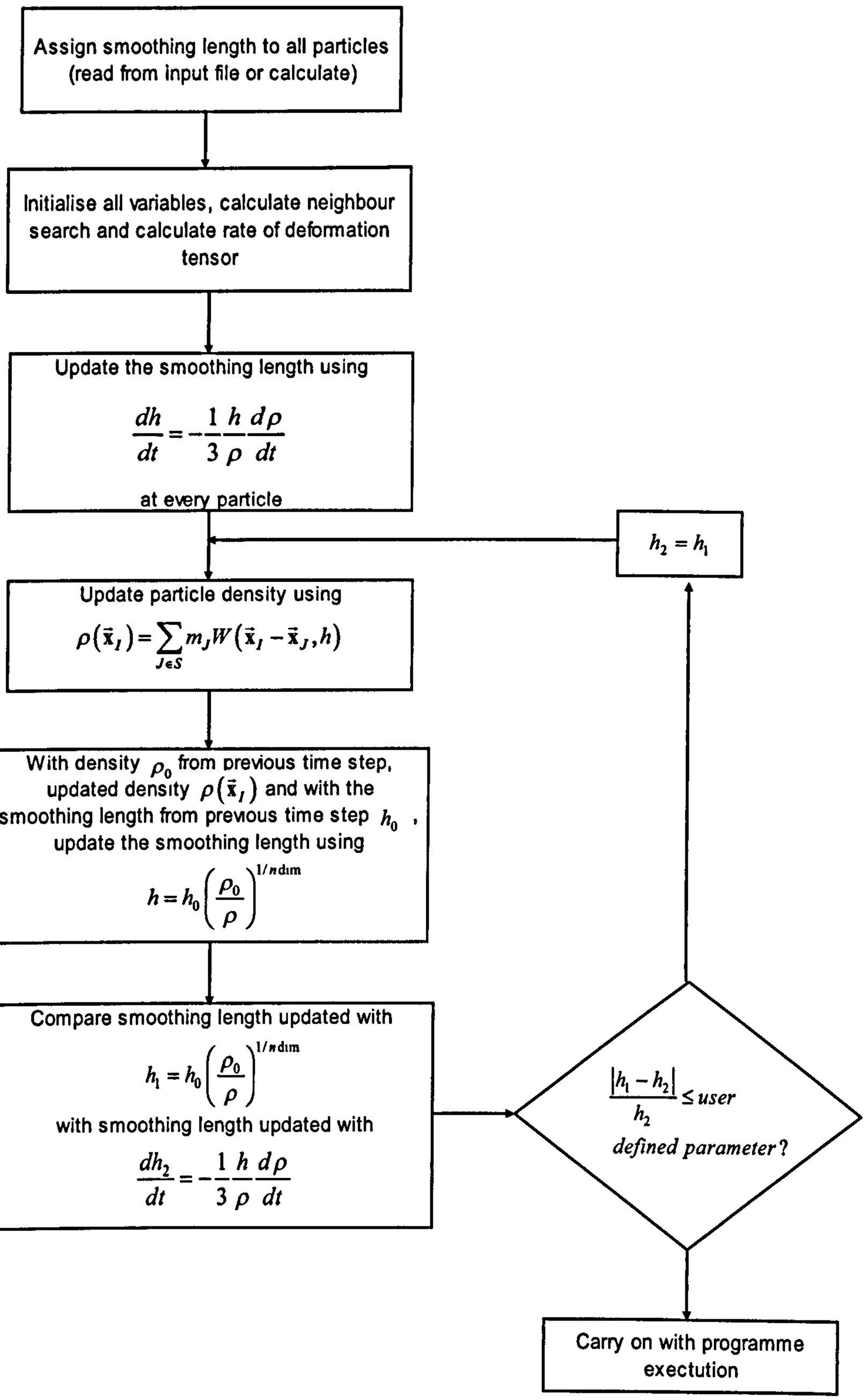

Fig. 7.6 Alternative formulation for conservation of mass equation and variable smoothing length.

7.6 Further Stabilisation of the Code: XSPH.

In conventional SPH the position of the particles is updated using $\frac{du_{I,i}}{dt} = V_{I,i}$. The XSPH variant updates the position of a particle with a velocity that is closer to the average velocity in its neighborhood. The expression for XSPH is given in [62] by:

$$\frac{du_I}{dt} = \hat{V}_I = V_I + \varepsilon \sum_{J \in S} m_J \left(\frac{V_J}{\rho_{JI}} \right) \mathrm{W}(X_I - X_J, h) \tag{7.84}$$

with $\rho_{JI} = \frac{\rho_J + \rho_I}{2}$ and $0 \leq \varepsilon \leq 1$ as a constant.

The XSPH variant has proven useful in the simulation of nearly incompressible fluids such as water, where it keeps the particles orderly in the absence of viscosity.

The results presented here show the effectiveness of SPH to smooth a stress wave profile. XSPH seems to work well for smoothing unphysical oscillations in the wave profile when compared to artificial viscosity. Besides, XSPH is non-dissipative [62] as opposed to the artificial stress component in the momentum equation. This is an extremely important feature of XSPH since it can conserve physical oscillations in the simulations without over-smoothing the stress wave profile. XSPH combined with artificial viscosity (Fig.7.10) results in an over-smoothed profile.

The XSPH subroutine can be used as an alternative to the ordinary update velocity subroutine. Similarly to the ordinary velocity update subroutine, the XSPH subroutine is called at the end of a time step when particle positions need updating.

Figures 7.7 through to 7.10 show the results obtained with no smoothing, with XSPH alone and a combination of XSPH and artificial viscosity.

The test case presented is for two rods travelling at $100\frac{\text{m}}{\text{s}}$ towards each other. Each rod was discretised into 100 particles with an inter-particle distance of 0.02E-2 m, the smoothing function used was the cubic spline and the smoothing length was set to 0.024E-2m. The constitutive model employed for this simulation was the elastic-perfectly plastic model [35]. The material density was set to 7800 $\frac{\text{kg}}{\text{m}^3}$ with a Young's modulus of 2.1 E11 Pa, Poisson ratio of 0.33 and the yield stress was set to 1E9 Pa. Nodal artificial viscosity was employed with a quadratic bulk viscosity coefficient of 2.0 and a linear bulk viscosity coefficient of 0.5. Kernel contact was imposed as the contact type for this simulation.

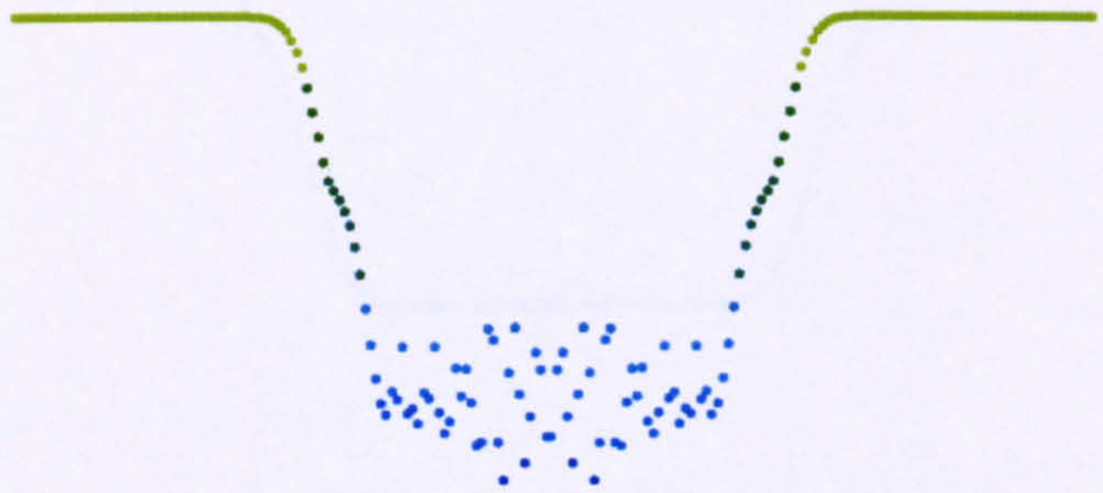

Fig. 7.7 Compressive wave, no artificial viscosity term in momentum equation

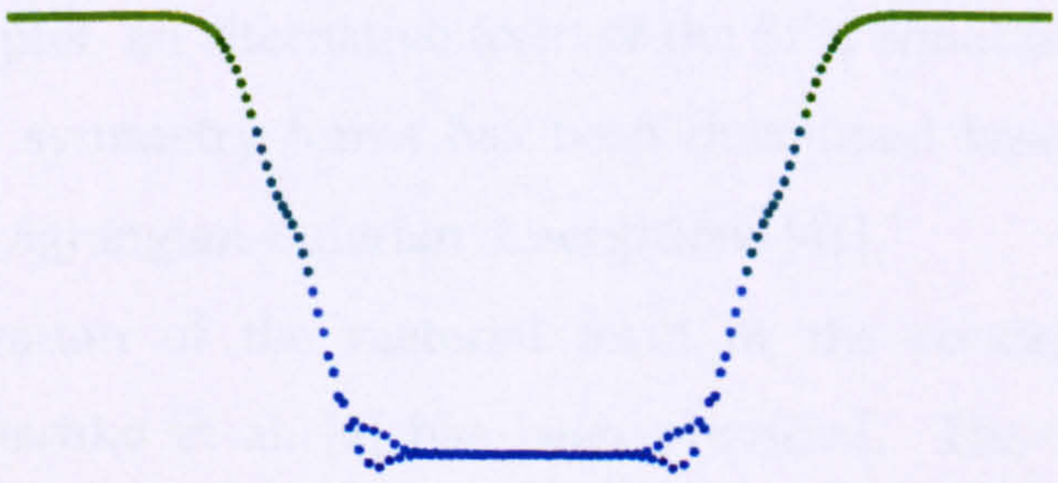

Fig. 7.8 Compressive wave, with artificial viscosity term in momentum equation

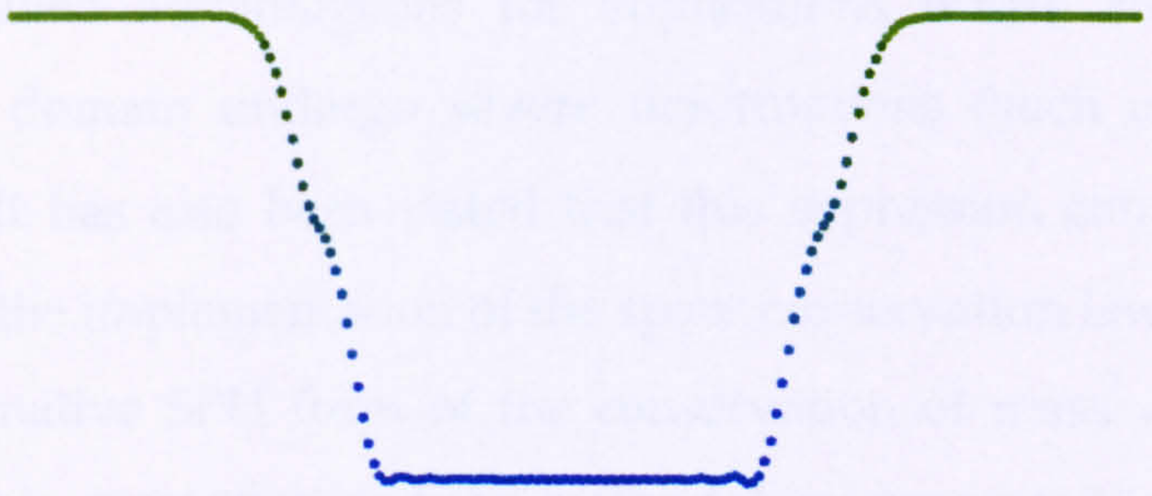

Fig 7.9 Compressive wave, XSPH with no artificial viscosity.

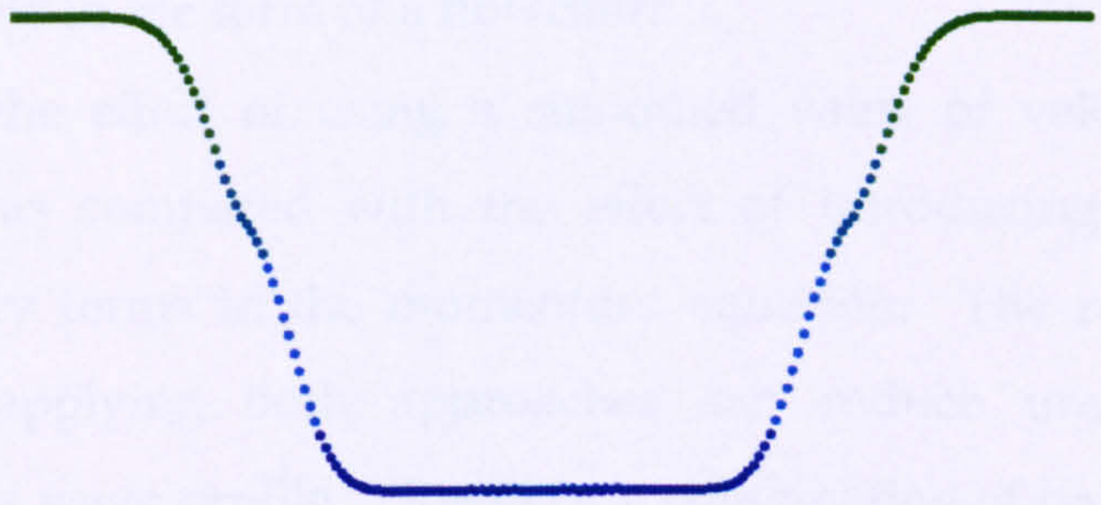

Fig 7.10 Compressive wave, XSPH and artificial viscosity term in momentum equation.

Summary.

In this chapter, an alternative form of the SPH equations which explains the origin of the symmetry terms has been developed based on the general theory of mixed Lagrangian-Eulerian descriptions [41].

The derivation of the material form of the continuity equation as supplied in Belytschko et al. [4] has been provided. The SPH form of this equation is similar to the standard SPH equation in Eulerian coordinates in that it contains a total derivative and a velocity gradient term. In addition, it also contains a Jacobian term, which is present in the conservation of mass equation

expressed in a Total Lagrangian referential. The resulting SPH equation could serve as a link between Eulerian and Total Lagrangian SPH codes if such a scheme is deemed advantageous for applications where zones within the computational domain undergo severe deformations (such as in fluid-solid interactions). It has also been stated that this expression can be used as the foundation for the implementation of the space conservation law in SPH [23].

An alternative SPH form of the conservation of mass was supplied in section 7.6.1. This expression and the methodology presented here can be used as the basis for a fully consistent SPH code that makes use of a varying smoothing length when approximating the conservation laws. The methodology followed for the introduction of this expression into the MCM code was supplied in the form of a flowchart.

Finally, the effect of using a smoothed value of velocity for particle repositioning was compared with the effect of introducing standard nodal artificial viscosity terms in the momentum equation. The results show that independently applying both approaches can reduce unphysical particle oscillations in the wave profile. However, a combination of both could result in an over-smoothed wave profile.

CHAPTER 8

CONCLUSIONS

8.1 Conclusions.

This research work has looked at the use of the Total Lagrangian SPH formulation to characterise dynamic events in solids.

The objectives achieved were:

1.- The SPH code developed at Cranfield University has been enhanced through the introduction of a Total Lagrangian capability. This new feature of the code enables the user to choose from two Total Lagrangian options: a standard version and a normalised corrected version. The code developed in this research work is fully compatible with the material models available in DYNA 3D.

2.- The code has been used in a number of impact scenarios ranging from simple 1-D wave propagation problems to more complex 3-D debris impact and

penetration problems and spall fracture problems. It has thus been demonstrated that dynamic events in solids can be accurately modelled through the use of the SPH code developed for this project.

3.- A stability analysis of the Total Lagrangian SPH equations revealed that when the conservation equations were expressed in a Total Lagrangian form, the particle equations no longer contained the tensile instability term that yields numerical fracture. It was also proved that the Total Lagrangian particle equations contained an instability term which is also present in the equations for continua. This feature, together with the elimination of the tensile instability problem makes the Total Lagrangian SPH code a robust numerical technique for simulating solids under dynamic loading. Problems that address the tensile stability effect were supplied and the results compared with a conventional collocational Eulerian SPH code. The numerical results of Chapter 6 verify the theoretical analysis supplied in Chapter 3.

4.- Further improvements to the code have been highlighted in Chapter 7. Some ideas were fully explored and implemented in the SPH code while other ideas could serve as the basis for future research work in this area.

During the course of this research, the plan to implement adaptivity algorithms was discarded because the instability problem was dealt with successfully through the Total Lagrangian formulation. Furthermore, it was determined that adding an adaptivity algorithm would have made the code extremely complex and computationally expensive; two undesirable effects when computing power is limited. The Total Lagrangian code allows a conventional PC to easily handle problems that involve domains containing tens of thousand of particles without major complications.

Due to the nature of the Total Lagrangian formulation, the extent of deformation that can be modelled with the Total Lagrangian SPH code is limited when relatively simple material models (namely elastic-plastic with hardening models) are used. The limitation is due to the numerical value achieved by the determinant of the deformation gradient tensor during the course of a particular simulation. In spite of this shortcoming, relatively large deformations such as those presented in Chapter 6, could be achieved through the combination of the Total Lagrangian code and complex constitutive models such as the Johnson-Cook model with damage. In this case, the Jacobian is no longer the limiting factor in the simulation: particles that have deformed considerably are removed from the particle equations summations and their mass is no longer updated, which prevents negative (and unphysical) density values.

8.2 Future Work.

The basis for a mixed Lagrangian-Eulerian description has been supplied in Chapter 7. The particle equations resulting from these equations could be further explored through a standard Von Neumann analysis and their advantages and shortcomings identified.

In addition, exploring the implementation of the conservation of space law in SPH could prove advantageous. The basis for such work has been supplied in the form of a "material form" of the continuity equation.

An alternative SPH form of the conservation of mass was supplied in Chapter 7. This expression together with the methodology presented in Chapter 7 can be used as the basis for a fully consistent SPH code that makes use of a varying smoothing length when approximating the conservation laws.

REFERENCES

[1] Attaway SW, Heinstein MW, Swegle JW. *Coupling of smooth particle hydrodynamics with the finite element method,* Nuclear Engineering and Design 1994; vol 150: 199-205.

[2] Balsara, DS. *Von Neumann stability analysis of smoothed particle hydrodynamics –Suggestions for optimal algorithms,* Journal of Computational Physics 1995, 121: 357-372.

[3] Bathe KJ. *Finite element procedures,* Prentice-Hall; 1996: Chapter IX.

[4] Belytschko T, Liu WK, Moran B. *Nonlinear Finite Elements for Continua and Structures,* John Wiley and Sons Ltd; 2000: Chapters I and III.

[5] Belytschko T, Guo Y, Liu WK, Xiao SP. *A unified stability analysis of meshless particle methods*, Int. Journal for Numerical Methods in Engineering 2000; 48: 1359-1400.
http://www.tam.northwestern.edu/xiaosp/stable.html.

[6] Belytschko T, Xiao S P. *Stability analysis of particle methods with corrected derivatives*, Computers and Mathematics with Applications 2002; vol 43 (3-5): 329-350.

[7] Benz W. *Smooth particle hydrodynamics: A review*, in The Numerical Modelling of Nonlinear Stellar Pulsations: Problems and Prospects. edited by Buchler JR, Kluwer Academic Publishers, 1990: 269-288.

[8] Benz W, Asphaugh E. *Simulations of brittle solids using SPH*. Computer Physics Communications 1995; vol 87: 253-265.

[9] Bonet J, Kulasegaram S. *A simplified approach to enhance the performance of smooth particle hydrodynamics methods*. Applied Mathematics and Computation 2002; vol 126, no 2: 133-155.

[10] Bonet J, Kulasegaram S, Rodriguez-Paz MX, Profit M. *Variational formulation for the smooth particle hydrodynamics (SPH) simulation of fluid and solid problems*. Computer Methods in Applied Mechanics and Engineering 2004;vol 193 (12-14): 1245-1256.

[11] Bonet J, Lok TSL, *Variational and momentum preservation aspects of Smooth Particle Hydrodynamics formulation*, Computer Methods and Applied Mechanics and Engineeering 1999; vol 180: 97-115.

[12] Bonet J, Kulasegaram S. *Correction and stabilization of smoothed particle hydrodynamics methods with applications in metal forming simulations*. International Journal for Numerical Methods in Engineering 2000; vol 47: 1189-1214.

[13] Bonet J, Kulasegaram S. *Remarks on tension instability of Eulerian and Lagrangian corrected Smooth particle hydrodynamics (CSPH) Methods*, International Journal of Numerical Methods in Engineering 2001;vol 52: 1203-1220.

[14] Campbell PM. *Some new algorithms for boundary value problems in smoothed particle hydrodynamics*. Technical Report DNA-TR-88-286, Mission Research Corporation, 1989.

[15] Campbell J. *Lagrangian hydrocode modelling of hypervelocity impact on spacecraft*. PhD Thesis, College of Aeronautics, Cranfield University, 1998.

[16] Chaniotis AK, Poulikakos D, Koumoutsakos P. *Remeshed smoothed particle hydrodynamics for the simulation of viscous and heat conducting flows*. Journal of Computational Physics 2002; vol 182: 67-90.

[17] Chen J K, Beraun J E. *A generalized smoothed particle hydrodynamics method for non-linear dynamic problems*, Computer Methods in Applied Mechanics and Engineering 2000; vol 190:225-239

[18] Chevrier P, Klepaczko JR. *Spall fracture: mechanical and microstructural aspects*. Engineering Fracture Mechanics 1999; vol 63, no 3: 273-294.

[19] Chung T. *Continuum Mechanics*. John Wiley and Sons, 1998: Chapters II, III, IV.

[20] Cranfield University internal communication with Dr. N. Bourne.

[21] Crisfield M A, *Non-Linear Finite Element Analysis of Materials and Structures*, John Wiley, England 1995, Volume 1.

[22] Delorme L, Souto Iglesias, *Application of SPH to 2-D shallow water sloshing problem*, 1st SPHERIC workshop conference, Rome 10-12 May 2006.

[23] Demirdzi'c I, Peri'c M. *Space conservation law in finite volume calculations of fluid flow*. International Journal for Numerical Methods in Fluids1988; vol 8; 1037-1050.

[24] De Vuyst T, Vignjevic R, Campbell J. *Coupling between meshless and finite element methods*. International Journal of Impact Engineering 2005; vol 31:1054-1064.

[25] De Vuyst TAI. *Hydrocode modelling of water impact*, PhD Thesis, School of Engineering, Cranfield University, 2003.

[26] Dyka CT, Ingel RP. *An approach for tension instability in smoothed particle hydrodynamics (SPH)*, Computers and Structures 1995, vol. 57, issue 4,17: 573-580.

[27] Elmore W C, Heald M A. *Physics of Waves*, Dover Publications, Inc. New York, first published in 1985, 477 pages. Quoted part of the text is found on page 125.

[28] Fernandez Mendez S, Bonet J, Huerta A. *Continuous blending of SPH with finite elements*. Computers and Structures 2005; vol 83, 1448-1458.

[29] Fraas A P , *Protection of Spacecraft from Meteoroids and Orbital Debris*, Oak Ridge National Laboratory, ORNL/TM ~9904, Published March 1986, 68 Pages.

[30] Gelfand I M and Shilov G E. *Generalized Functions, Properties and Operations*, vol.1 Academic Press, 1964, 423 pages.

[31] Gingold RA, Monaghan JJ. *Smoothed particle hydrodynamics: Theory and application to non-spherical stars*. Mon. Not. Royal Astronomical Society 1977; 181: 375-389.

[32] Gingold R A, Monaghan JJ . *Kernel estimates as a basis for general particle methods in hydrodynamics*. Journal of Computational Physics 1982; 46: 429-453, 1982.

[33] Gomez-Gesteira M, Crespo AJ, Dalrymple R, *Modelling interaction between waves and coastal structures*, SPHERIC Newsletter , 1ST issue, 2005.

[34] Gourma, M. *Smoothed Particle Hydrodynamics Methods, Applications and Analysis*. PhD Thesis, Cranfield University, School of Engineering, 2003.

[35] Hallquist JO. LS-*DYNA Theoretical Manual*, Livermore Software Technology Corporation, May 1998.

[36] Hayashida KB, Robinson JH. *Single wall penetration equations*, NASA Technical Memorandum, NASA TM-103565, December 1991, Marshall SFC.

[37] Hayhurst CJ, Clegg RA. *Cylindrically Symmetric SPH simulations of hypervelocity impacts on thin plates*. Hypervelocity Impact Symposium, Freiburg, Germany. Oct 1996.

[38] Holian K S. *Hydrodynamics code calculations of debris clouds produced by ball-plate impacts,* International Journal of Impact Engineering 1990, vol 10, issues:1-4: 231-239.

[39] Huerta A, Fernandez Mendez S. *Enrichment and coupling of the finite element and meshless methods*. International Journal for Numerical Methods in Engineering 2000; vol48 no 11: 1615-1636.

[40] Huerta A, Fernandez Mendez S, Liu W K. *A comparison of two formulations to blend finite elements and mesh free methods*. Computer Methods in Applied Mechanics and Engineering 2004; vol 193 (issues 12-14): 1105-1117.

[41] Hughes TJR, Liu WK, Zimmermann TK. *Lagrangian-Eulerian Finite Element Formulation for Incompressible Viscous Flows*. Computer Methods in Applied Mechanics and Engineering 1989; vol 29;3: 329-349.

[42] Ikkhurti V R, Chaturvedi S. *Use of different damage models for simulating impact-driven spallation in metal plates*. International Journal of Impact Engineering 2004; vol 30,3: 275-301.

[43] Issa R, Violeau D, Lee ES, *Modelling laminar and turbulent flows*, SPHERIC Newsletter , 1ST issue, 2005.

[44] Jeong JH, Jhon MS, Halow JS, Van Osdol J. *Smoothed particle hydrodynamics: Applications to heat conduction*. Computer Physics Communications 2003; vol. 153, issue 1-1: 71-84.

[45] Johnson G R, Stephen R. Beissel. *Normalized smoothing functions for SPH impact computations*. International Journal for Numerical Methods in Engineering 1996; 39: 2725-2741.

[46] Johnson GR, Stryk RA, Beissel SR. *SPH for high velocity impact computations*. Computer Methods in Applied Mechanics and Engineering 1996;vol 139 (1-4):347-373.

[47] Jones SE, Maudlin PJ, Foster J C Jr. *An engineering analysis of plastic wave propagation in the Taylor test*. International Journal of Impact Engineering 1997; vol 19, no 2: 95-106.

[48] Kiselev, AB, Lukyanov, AA. *Mathematical modeling of dynamic processes of irreversible deforming, micro and macrofracture of solids and structures*. International Journal of Forming Processes 2002; Vol. 5, nos 2-3-4: 351-362.

[49] Li S, Liu W K. *Meshfree Particle Methods*. Springer, ISBN 3-540-22256-1, 2004, chapter 3.

[50] Libersky L D, Petschek A G, Carney T C, Hipp J R and Allahdadi F Z. *High strain Lagrangian hydrodynamics - A three-dimensional SPH code for dynamic material response*. Journal of Computational Physics 1993; vol 109: 67-75.

[51] Libersky L, Petschek A. *Smooth particle hydrodynamics with strength of materials*. 1990. Trease H E, Fritts M J, Crowley W P. Editors. Advances in the free-Lagrange method, Springer-Verlag: 248-257.

[52] Little R W. *Elasticity*. Prentice-Hall ,1973.

[53] Liu G R, Liu M B. *Smoothed particle hydrodynamics: a meshfree particle method*. 2003; World Scientific Publishing Company, Singapore.

[54] Liu M B, Liu G R, Lam K Y. *Constructing smoothing functions in smoothing particle hydrodynamics with applications*. Journal of Computational and Applied Mathematics 2003; vol 155 (2):263-284.

[55] Liu M B, Liu G R, Lam K Y. *Investigation into water mitigation using a meshless particle method*. Shock Waves 2002; 12:181-195.

[56] Liu, W K; Chen, Y. *Wavelet and multiple scale reproducing kernel methods*, International Journal for Numerical Methods in Fluids 1995; vol 21: 901-931.

[57] Liu W K, Jun S, Li S, Adee J, Belytschko. *Reproducing kernel particle methods for structural dynamics*. International Journal of Numerical Methods in Engineering 1995; vol 38:1655-1679.

[58] Lucy L B. *A numerical approach to the testing of the fission hypothesis*. Astronomical Journal 1977; 82: 1013.

[59] Lukyanov A, Reveles JR, Vignjevic R. *Numerical simulation of failure in metals based on irreversible thermodynamics*. Sixth European Conference on Structural Dynamics 2005, Paris, Sept. 2005; vol 3: 1755.

[60] Malvern LE. *Introduction to the Mechanics of a Continuous Medium*. Prentice-Hall, 1969 ; USA.

[61] Meyers M A. *Dynamic Behavior of Materials*. 1994; John Wiley and Sons Inc: Chapters II,VI,XIII.

[62] Monaghan JJ, *Smoothed particle hydrodynamics*, Annual Rev. Astron. Astrophys: 543-574, 1992.

[63] Monaghan JJ. *SPH without a tensile instability*. Journal of Computational Physics 2000; vol 159 no 2: 290-311.

[64] Monaghan JJ, Kocharyan A, *SPH simulation of multi-phase flow*, Computer Physics Commun, 87, 225-235, 1995.

[65] Monaghan JJ, Huppert H, Grae Worster M. *Solidification using smooth particle hydrodynamics*. Journal of Computational Physics 2005; 206: 684-705.

[66] Monaghan JJ. *Simulating free surface flow with SPH*. Journal of Computational Physics 1994; vol 110: 399.

[67] Morris JP. *An overview of the method of smoothed particle hydrodynamics*. November 1995, Universitat Kaiserlautern, Arbeitsgruppe Technomathematik.

[68] Nelson RP, Papaloizou JCB. *Variable smoothing lengths and energy-conservation in smoothed particle hydrodynamics*. Monthly Notice of the Royal Astronomical Society 1994; 270:1-20.

[69] Parishkov AN, Medin S A. *Smoothed particle hydrodynamics using interparticle contact algorithms*. Journal of Computational Physics 2002; vol 180,1: 358-382.

[70] Parishkov A N, Medin S A, Loukashenko I I, Milekhin V A. *Improvements in the SPH method by means of interparticle contact algorithm and analysis of perforation tests at moderate projectile velocities*. International Journal of Impact Engineering 2000; vol 24: 779-796.

[71] Panizzo A, Cuomo C. *Modelling of water waves generated by landslides*. SPHERIC Newsletter , 1ST issue, 2005.

[72] Quinlan N J, Basa M, Lastwika M. *Truncation error in mesh-free particle methods*. International Journal for Numerical Methods in Engineering. John Wiley and sons 2006, 66(13): 2064-2085.

[73] Rabczuk T, Belytschko T, Xiao SP. *Stable particle method based on Lagrangian kernels*. Computer Methods in Applied Mechanics and Engineering 2004; 193:1035-1063.

[74] Randles PW, Libersky LD. *Normalized SPH with stress points*. International Journal for Numerical Methods in Engineering 2000; 48 (10):1445-1462.

[75] Randles P, Libersky L. *Smoothed particle hydrodynamic: Some recent improvements and applications*. Computer Methods in Applied Mechanics and Engineering 1996; vol 139: 375-408.

[76] Reveles J, Lukyanov A, Vignjevic R. *Numerical simulation of debris impact on thin walled metal shields*, European Space Agency /ESTEC. ESA publication 2005; SP vol 581: 823-829

[77] Shao S, *Modelling wave overtopping on a sloping seawall*, SPHERIC Newsletter , 1ST issue, 2005.

[78] Steinberg DJ. *Equation of state and strength properties of selected materials*. Lawrence-Livermore National Laboratory, Feb 1996; UCRL-MA-106439.

[79] Swegle J. *Conservation of momentum and tensile instability in particle methods*. Sandia Report 2000 ;-1223 , May 2000.

[80] Swegle J W, Attaway S W, Heinstein M W, Mello F J, Hicks D L. *An analysis of the smoothed particle hydrodynamics*. Sandia Report 1994; SAND93-2513 UC-705.

[81] Swegle J W, Hicks D L, Attaway S W. *Smoothed particle hydrodynamics stability analysis*. Journal of Computational Physics 1995, vol 116:123-134.

[82] Vignjevic R, Reveles J, Campbell J. *SPH in a total Lagrangian formalism*, Computer Modelling in Engineering and Science 2006; vol 14 no 10: 181-198.

[83] Vignjevic R, Campbell J, Libersky L. *A treatment of zero-energy modes in the smoothed particle hydrodynamics method*. Computer Methods in Applied Mechanics and Engineering 2000; 184: 67-85.

[84] Vignjevic R, De Vuyst T, Campbell JC. *A frictionless contact algorithm for meshless methods*. Computer Modeling in Engineering and Sciences 2006; 13:35-48.

[85] Vignjevic R, Reveles JR, Lukyanov A. *Analysis of compressor blade behaviour under bird impact*. Computational Methods for Coupled Problems in Science and Engineering 2005, Santorini Greek Islands, 25th-27th May 2005. Published in the conference proceedings.

[86] Wingate C A, and Fisher H N. *Strength modeling in SPHC*. Los Alamos National Laboratory, NM. IS-4 Report section, LA-UR-93-3942.

[87] Zukas J A Editor. *High Velocity Impact Dynamics*. 1990; John Wiley, US.

APPENDIX

FORTRAN INPUT FILES.

1.- Hard Debris impact penetration: Steel sphere on Aluminum plate. (Problem 10, Chapter 6)

```
*234567890123456789012345678901234567890123456789012345678901
234567890
3-D hard debris impact penetration problem                    2
* Comment line cm-grms-microsec
* Control card 1: Problem definition
   3   2       2    30912
*
* Control card 2: Time control
*
 2.500E+02 0.800E+00 0.012E+00
*
* Control card 3: Output file control
*
 0.100E+01    3 5.000E-02       0   0       50   0   0
*
* Control card 4: Input and initialization options
*
   1   1   0   0
*
* Control card 5: Analysis options
*
   1   1   1   0
*
* Control card 6: Interpolation options
*
   0   1  40
```

*

* Control card 7: Blank at this time

*

*

1 152.7800E+00 4 0 0.0000E+00 0 0.0000E+00 0.0000E+00 0 0 0

83.400 0.12

Johnson-Cook

2.632E-01 479.0E-05 323.0E-05 0.410E+00 0.101E+00 1.800E+00 8.500E+02 3.000E+02

1.000E-06 875.0E-08 -0.800E-02 1.000E+00 1.000E+00 0.000E+00 0.000E+00 0.000E+00

0.450E+00 0.000E+00 0.000E+00 0.138E-01 0.000E+00 0.000E+00 0.000E+00

0.000E+00

7.000E-01 0.330E+00 0.000E+00 0.000E+00 0.000E+00 0.000E+00 0.000E+00

0.000E+00

0.000E+00 0.000E+00 0.000E+00 0.000E+00 0.000E+00 0.000E+00 0.000E+00

0.000E+00

0.000E+00 0.000E+00 0.000E+00 0.000E+00 0.000E+00 0.000E+00 0.000E+00

0.000E+00

Gruneisen EOS

0.5328E+00 1.338E+00 0.000E+00 0.000E+00 2.000E+00 0.480E+00 0.000E+00

1.000E+00

*

2 37.8700E+00 0 0 0.0000E+00 0 0.0000E+00 0.0000E+00 0 0 0

7.1206 0.12

Elastic-plastic

2.000E+00 0.000E+00 0.000E+00 0.000E+00 0.000E+00 0.000E+00 0.000E+00

0.000E+00

0.300E+00 0.000E+00 0.000E+00 0.000E+00 0.000E+00 0.000E+00 0.000E+00

0.000E+00

0.315E-02 0.000E+00 0.000E+00 0.000E+00 0.000E+00 0.000E+00 0.000E+00

0.000E+00

0.150E+00 0.000E+00 0.000E+00 0.000E+00 0.000E+00 0.000E+00 0.000E+00

0.000E+00

1.000E+00 0.000E+00 0.000E+00 0.000E+00 0.000E+00 0.000E+00 0.000E+00
0.000E+00
0.000E+00 0.000E+00 0.000E+00 0.000E+00 0.000E+00 0.000E+00 0.000E+00
0.000E+00

```
*
* Nodes
*
     1  7    -0.49500E+01   -0.49500E+01   -0.85000E+00   1
     2  7    -0.48500E+01   -0.49500E+01   -0.85000E+00   1
     3  7    -0.47500E+01   -0.49500E+01   -0.85000E+00   1
     4  7    -0.46500E+01   -0.49500E+01   -0.85000E+00   1
 29998  7     0.47500E+01    0.49500E+01   -0.65000E+00   1
 29999  7     0.48500E+01    0.49500E+01   -0.65000E+00   1
 30000  7     0.49500E+01    0.49500E+01   -0.65000E+00   1
 30001  0    -0.15000E+00   -0.15000E+00   -0.55000E+00   2
 30002  0    -0.50000E-01   -0.15000E+00   -0.55000E+00   2
 30910  0    -0.50000E-01    0.15000E+00    0.55000E+00   2
 30911  0     0.50000E-01    0.15000E+00    0.55000E+00   2
 30912  0     0.15000E+00    0.15000E+00    0.55000E+00   2
*
* Time History Nodes
*
*1
*
* Initial Velocities
*
     1  0.000E+00  0.000E+00  0.000e+00
 30000  0.000E+00  0.000E+00  0.000e+00
 30001  0.000E+00  0.000E+00 -5.000e-02
 30912  0.000E+00  0.000E+00 -5.000e-02
*
* Contact
*
```

```
 -1   1
0.02000E+00  4.00000E+00
0.02000E+00  4.00000E+00
```

2.- Impact of a prismatic projectile on an aluminium plate (Problem 8, Chapter 6)

```
*234567890123456789012345678901234567890123456789012345678901234567890123456789
890
Impact problem 819_1 BA, TON/m/miliseconds                    2
* Comment line
* Johnson-Cook Spall type 1, Plynomial EOS, Ref Sra Rate= 1, accurate iterative
solution for plastic strain
* Control card 1: Problem definition
   3  2       2    47730
*
* Control card 2: Time control
*
 1.000E+00 0.800E+00 0.000E+00
*
* Control card 3: Output file control
*
 0.500E-02    3 5.000E-02        0   0       10   0   0
*
* Control card 4: Input and initialization options
*
   1   1   0   0
*
* Control card 5: Analysis options
*
   1   1   0   0
*
* Control card 6: Interpolation options
*
   0   1  50
*
* Control card 7: Blank at this time
*
*
   1  15  2.8E+00   1   00.0000E+00   02.0000E+000.5000E+00   0   0   0
0.002989     0.0034
Johnson-Cook
 2.632E+01 0.479E+00 0.323E+00 0.410E+00 0.101E+00 1.800E+00 8.500E+02 3.000E+02
 99.60E-03 8.750E-04-0.800E+00 1.000E+00 1.000E+00 0.000E+00 0.000E+00 0.000E+00
 0.450E+00 0.000E+00 0.000E+00 0.138E-01 0.000E+00 0.000E+00 0.000E+00 0.000E+00
 7.000E+01 0.330E+00 0.000E+00 0.000E+00 0.000E+00 0.000E+00 0.000E+00 0.000E+00
```

0.000E+00 0.000E+00 0.000E+00 0.000E+00 0.000E+00 0.000E+00 0.000E+00 0.000E+00
0.000E+00 0.000E+00 0.000E+00 0.000E+00 0.000E+00 0.000E+00 0.000E+00 0.000E+00
Polynomial EOS
0.0000E+00 6.863E+01 0.000E+00 0.000E+00 0.000E+00 0.000E+00 0.000E+00 0.000E+00
1.0000e+00
*
2 1 7.82E+00 0 00.0000E+00 02.0000E+000.5000E+00 0 0 0
0.74E-3 0.0034
Elastic
2.100E+02 0.000E+00 0.000E+00 0.000E+00 0.000E+00 0.000E+00 0.000E+00 0.000E+00
0.330E+00 0.000E+00 0.000E+00 0.000E+00 0.000E+00 0.000E+00 0.000E+00 0.000E+00
0.000E+00 0.000E+00 0.000E+00 0.000E+00 0.000E+00 0.000E+00 0.000E+00 0.000E+00
0.000E+00 0.000E+00 0.000E+00 0.000E+00 0.000E+00 0.000E+00 0.000E+00 0.000E+00
0.000E+00 0.000E+00 0.000E+00 0.000E+00 0.000E+00 0.000E+00 0.000E+00 0.000E+00
0.000E+00 0.000E+00 0.000E+00 0.000E+00 0.000E+00 0.000E+00 0.000E+00 0.000E+00
*
* Nodes

1	7	0.14286E-02	0.14286E-02	0.14375E-02	1
2	7	0.42857E-02	0.14286E-02	0.14375E-02	1
3	7	0.71429E-02	0.14286E-02	0.14375E-02	1
4	7	0.10000E-01	0.14286E-02	0.14375E-02	1

47709	0	0.13500E+00	0.16200E+00	0.98533E-01	2
47710	0	0.13800E+00	0.16200E+00	0.98533E-01	2
47711	0	0.14100E+00	0.16200E+00	0.98533E-01	2
47712	0	0.14400E+00	0.16200E+00	0.98533E-01	2
47713	0	0.14700E+00	0.16200E+00	0.98533E-01	2
47714	0	0.15000E+00	0.16200E+00	0.98533E-01	2
47715	0	0.15300E+00	0.16200E+00	0.98533E-01	2
47716	0	0.15600E+00	0.16200E+00	0.98533E-01	2
47717	0	0.15900E+00	0.16200E+00	0.98533E-01	2
47718	0	0.16200E+00	0.16200E+00	0.98533E-01	2
47719	0	0.16500E+00	0.16200E+00	0.98533E-01	2
47720	0	0.13500E+00	0.16500E+00	0.98533E-01	2
47721	0	0.13800E+00	0.16500E+00	0.98533E-01	2
47722	0	0.14100E+00	0.16500E+00	0.98533E-01	2
47723	0	0.14400E+00	0.16500E+00	0.98533E-01	2
47724	0	0.14700E+00	0.16500E+00	0.98533E-01	2
47725	0	0.15000E+00	0.16500E+00	0.98533E-01	2
47726	0	0.15300E+00	0.16500E+00	0.98533E-01	2
47727	0	0.15600E+00	0.16500E+00	0.98533E-01	2
47728	0	0.15900E+00	0.16500E+00	0.98533E-01	2
47729	0	0.16200E+00	0.16500E+00	0.98533E-01	2
47730	0	0.16500E+00	0.16500E+00	0.98533E-01	2

*
* Initial Velocities
*
1 0.000E+00 0.000E+00 0.000E+00

```
  44100 0.000E+00 0.000E+00 0.000E+00
  44101 0.000E+00 0.000E+00-0.1327E+0
  47730 0.000E+00 0.000E+00-0.1327e+0
*
* Contact
*
  -1   1
2.00000E+00 4.00000E+00
2.00000E+00 4.00000E+00
```

3.- Simulation of spall fracture (Problem 9, Chapter 6)

```
*234567890123456789012345678901234567890123456789012345678901234567890123456789
890
Plate impact problem, no spall  elastic plastic with hardening
2
* Comment line
*
* Control card 1: Problem definition
   3   2       2     4675
*
* Control card 2: Time control
*
 4.500E+00 0.700E+00 6.000E-03
*
* Control card 3: Output file control
*
 0.100E+00    3 5.000E-02        0    0      100    0    0
*
* Control card 4: Input and initialization options
*
   1    1    0    0
*
* Control card 5: Analysis options
*
   1    1    0    1
*
* Control card 6: Interpolation options
*
   0    1   40
*
* Control card 7: Blank at this time
*

*
   1    3 8.924E+00    0    00.0000E+00    02.0000E+000.5000E+00    0    0    0
8.92E-4       0.0048
Elastic
 1.100E+00 0.000E+00 0.000E+00 0.000E+00 0.000E+00 0.000E+00 0.000E+00 0.000E+00
```

0.300E+00 0.000E+00 0.000E+00 0.000E+00 0.000E+00 0.000E+00 0.000E+00 0.000E+00
0.015E-01 0.000E+00 0.000E+00 0.000E+00 0.000E+00 0.000E+00 0.000E+00 0.000E+00
0.110E-01 0.000E+00 0.000E+00 0.000E+00 0.000E+00 0.000E+00 0.000E+00 0.000E+00
0.000E+00 0.000E+00 0.000E+00 0.000E+00 0.000E+00 0.000E+00 0.000E+00 0.000E+00
0.000E+00 0.000E+00 0.000E+00 0.000E+00 0.000E+00 0.000E+00 0.000E+00 0.000E+00
*
2 3 7.800E+00 0 00.0000E+00 02.0000E+000.5000E+00 0 0 0
1.56E-3 0.0048
Elastic
1.100E+00 0.000E+00 0.000E+00 0.000E+00 0.000E+00 0.000E+00 0.000E+00 0.000E+00
0.300E+00 0.000E+00 0.000E+00 0.000E+00 0.000E+00 0.000E+00 0.000E+00 0.000E+00
0.015E-01 0.000E+00 0.000E+00 0.000E+00 0.000E+00 0.000E+00 0.000E+00 0.000E+00
0.110E-01 0.000E+00 0.000E+00 0.000E+00 0.000E+00 0.000E+00 0.000E+00 0.000E+00
0.000E+00 0.000E+00 0.000E+00 0.000E+00 0.000E+00 0.000E+00 0.000E+00 0.000E+00
0.000E+00 0.000E+00 0.000E+00 0.000E+00 0.000E+00 0.000E+00 0.000E+00 0.000E+00
*
* Nodes
*

1	0	-0.80000E-02	-0.80000E-02	-0.24799E+00	1
2	0	-0.40000E-02	-0.80000E-02	-0.24799E+00	1
3	0	0.00000E+00	-0.80000E-02	-0.24799E+00	1
4	0	0.40000E-02	-0.80000E-02	-0.24799E+00	1
5	0	0.80000E-02	-0.80000E-02	-0.24799E+00	1
6	0	-0.80000E-02	-0.40000E-02	-0.24799E+00	1

4668	0	0.00000E+00	0.40000E-02	0.49799E+00	2
4669	0	0.40000E-02	0.40000E-02	0.49799E+00	2
4670	0	0.80000E-02	0.40000E-02	0.49799E+00	2
4671	0	-0.80000E-02	0.80000E-02	0.49799E+00	2
4672	0	-0.40000E-02	0.80000E-02	0.49799E+00	2
4673	0	0.00000E+00	0.80000E-02	0.49799E+00	2
4674	0	0.40000E-02	0.80000E-02	0.49799E+00	2
4675	0	0.80000E-02	0.80000E-02	0.49799E+00	2

*
* Time History Nodes
*
*1
*
* Initial Velocities
*

1	0.000E+00	0.000E+00	2.500e-02
1550	0.000E+00	0.000E+00	2.500e-02
1551	0.000E+00	0.000E+00	0.000e+00
4675	0.000E+00	0.000E+00	0.000e+00

*
*Symmetry planes
*

1	1	1	1	0	0

-0.010E+00 0.010e+00-0.010e+00 0.010e+00 0.000e+00 0.000e+00

```
*
* Contact
*
  -1    1
 0.02000E+00 4.00000E+00
 0.02000E+00 4.00000E+00
```

4.- Simulation of spall fracture (Problem 9, Chapter 6)

```
*234567890123456789012345678901234567890123456789012345678901234567890123456789012345678
890
Spall simulation with J-C with damage
2
* Comment line
*
* Control card 1: Problem definition
   3   2        2     9375
*
* Control card 2: Time control
*
 1.500E+01 0.700E+00 5.000E-03
*
* Control card 3: Output file control
*
 0.100E+00    3 5.000E-02         0    0      100    0    0
*
* Control card 4: Input and initialization options
*
   1    1    0    0
*
* Control card 5: Analysis options
*
   1    1    0    1
*
* Control card 6: Interpolation options
*
   0    1   40
*
* Control card 7: Blank at this time
*
*
   1  158.9240E+00    4    00.0000E+00    00.0000E+000.0000E+00    0    0    0
1.78E-3      0.0048
EPHydr
 0.477E-00 90.00E-05 292.0E-05 0.310E+00 0.025E+00 1.090E+00 13.56E+02 3.000E+02
 1.000E-06 383.0E-08 4.900E-02 2.000E+00 1.000E+00 0.000E+00 0.000E+00 0.000E+00
 0.540E+00 4.890E+00-3.030E+00 0.140E-01 0.000E+00 0.000E+00 0.000E+00 0.000E+00
```

0.000E+00 0.000E+00 0.000E+00 0.000E+00 0.000E+00 0.000E+00 0.000E+00 0.000E+00
0.000E+00 0.000E+00 0.000E+00 0.000E+00 0.000E+00 0.000E+00 0.000E+00 0.000E+00
0.000E+00 0.000E+00 0.000E+00 0.000E+00 0.000E+00 0.000E+00 0.000E+00 0.000E+00
Gruneisen EOS
0.394E+00 1.489E+00 0.000E+00 0.000E+00 2.020E+00 0.470E+00 0.000E+00 1.000E+00
*
2 158.9240E+00 4 00.0000E+00 00.0000E+000.0000E+00 0 0 0
3.57E-3 0.0048
ephydr
0.477E-00 90.00E-05 292.0E-05 0.310E+00 0.025E+00 1.090E+00 13.56E+02 3.000E+02
1.000E-06 383.0E-08 4.900E-02 2.000E+00 1.000E+00 0.000E+00 0.000E+00 0.000E+00
0.540E+00 4.890E+00-3.030E+00 0.140E-01 0.000E+00 0.000E+00 0.000E+00 0.000E+00
0.000E+00 0.000E+00 0.000E+00 0.000E+00 0.000E+00 0.000E+00 0.000E+00 0.000E+00
0.000E+00 0.000E+00 0.000E+00 0.000E+00 0.000E+00 0.000E+00 0.000E+00 0.000E+00
0.000E+00 0.000E+00 0.000E+00 0.000E+00 0.000E+00 0.000E+00 0.000E+00 0.000E+00
Gruneisen EOS
0.394E+00 1.489E+00 0.000E+00 0.000E+00 2.020E+00 0.470E+00 0.000E+00 1.000E+00
*
* Nodes
*

1	0	-0.80000E-02	-0.80000E-02	-0.49800E+00	1
2	0	-0.40000E-02	-0.80000E-02	-0.49800E+00	1
3	0	0.00000E+00	-0.80000E-02	-0.49800E+00	1
4	0	0.40000E-02	-0.80000E-02	-0.49800E+00	1
9365	0	0.80000E-02	0.00000E+00	0.99800E+00	2
9366	0	-0.80000E-02	0.40000E-02	0.99800E+00	2
9367	0	-0.40000E-02	0.40000E-02	0.99800E+00	2
9368	0	0.00000E+00	0.40000E-02	0.99800E+00	2
9369	0	0.40000E-02	0.40000E-02	0.99800E+00	2
9370	0	0.80000E-02	0.40000E-02	0.99800E+00	2
9371	0	-0.80000E-02	0.80000E-02	0.99800E+00	2
9372	0	-0.40000E-02	0.80000E-02	0.99800E+00	2
9373	0	0.00000E+00	0.80000E-02	0.99800E+00	2
9374	0	0.40000E-02	0.80000E-02	0.99800E+00	2
9375	0	0.80000E-02	0.80000E-02	0.99800E+00	2

*
* Time History Nodes
*
*1
*
* Initial Velocities
*
1 0.000E+00 0.000E+00 3.050e-02
3125 0.000E+00 0.000E+00 3.050e-02
3126 0.000E+00 0.000E+00 0.000e+00
9375 0.000E+00 0.000E+00 0.000e+00
*
*Symmetry planes

```
*
      1       1       1       1       0       0
-0.010E+00 0.010e+00-0.010e+00 0.010e+00 0.000e+00 0.000e+00
*
* Contact
*
  -1   1
 0.20000E+00 4.00000E+00
 0.20000E+00 4.00000E+00
```

Publications List.

1. Fourth European Conference on Space Debris, *Simulation of Hypervelocity Debris Impact and Spacecraft Shielding Performance,* A. Lukyanov, **J.R.Reveles**, R. Vignjevic, European Space Agency /ESOC, Darmstadt, Germany, 19th-21st April 2005 . ESA publication SP-587.

2. European Conference on Spacecraft Structures, Materials and Mechanical Testing, *Numerical Simulation of Debris Impact on Thin Walled Metal Shields,* **J.R.Reveles**, A. Lukaynov, R. Vignjevic, European Space Agency /ESTEC, Netherlands, 10th-12th May, 2005. ESA publication SP-581.

3. European Conference on Spacecraft Structures, Materials and Mechanical Testing, *Simulation of High-Velocity Impact of Graphite/Epoxy Composite Laminates,* A.Lukyanov, R. Vignjevic, **J.R.Reveles**, ESA/ESTEC, Netherlands,10th-12th May, 2005. ESA publication SP-581.

4. Computational Methods for Coupled Problems in Science and Engineering 2005, *Analysis of Compressor Blade Behaviour Under Bird Impact,* R. Vignjevic, **J.R. Reveles**, A. Lukyanov, Santorini Greek Islands, 25th-27th May 2005.

5. Sixth European Conference on Structural Dynamics 2005, *Numerical Simulation of failure in Metals Based on Irreversible Thermodynamics,* A.Lukyanov, **J.R.Reveles**, R. Vignjevic, Paris France, 4th-7th Sep. 2005, *Vol 3. p 1755.*

6.- SPH in a Total Lagrangian formalism, Computer Modeling in Engineering and Science, CMES, S. Attluri editor, R. Vignjevic, **J. R. Reveles**, J. Campbell, CMES, vol 14 No3, pp 181-198,

7.- Dynamics and control of systems and structures in space, 10-16 July 2006, Old Royal Naval College, Greenwich UK,S Hobbs editor, R. Vignjevic and **J.R.Reveles**, Application of the SPH method in the simulation of solids under impact loading conditions, page 77,ISBN 1 871315 93 X

8.- Corrected Total Lagrangian SPH in the simulation of impact phenomena in solids, **J.R.Reveles**, R. Vignjevic, Int.J. of Impact Eng. (*under review*).

Open Presentations at Cranfield University

1.- Workshop on Computational Modelling, Total Lagrangian formalism for SPH, July 6th 2004, venue: Gold Lecture Theatre, B52.

2.- Development of a Total Lagrangian SPH code for the simulation of solids under dynamic loading conditions, December 9th, 2005, venue: Green Lecture Theatre, B52.

SPH in a Total Lagrangian Framework

Rade Vignjevic[1], Juan R. Reveles[1], James Campbell[1]

Abstract To correct some of the main shortcomings of conventional SPH, a version of this method based on the Total Lagrangian formalism, T. Rabczuk, T. Belytschko and S. Xiao (2004), is developed. The resulting scheme removes the spatial discretisation instability inherent in conventional SPH, J. Monaghan (1992).

The Total Lagrangian framework is combined with the mixed correction which ensures linear completeness and compliance with the patch test, R. Vignjevic, J. Campbell, L. Libersky (2000). The mixed correction utilizes Shepard Functions in combination with a correction to derivative approximations.

Incompleteness of the kernel support combined with the lack of consistency of the kernel interpolation in conventional SPH results in fuzzy boundaries. In corrected SPH, the domain boundaries and field variables at boundaries are approximated with the default accuracy of the method.

Additionally, these corrections are introduced into the Total Lagrangian SPH and compared to the conventional SPH and to a number of selected corrected variants, G. Johnson, R. Stryk, S. Beissel (1996), J. Bonet, S. Kulasegaram (2002), and P. Randles, L. Libersky (1996). The resulting Total Lagrangian SPH scheme not only ensures fist order consistency but also alleviates the particle deficiency (kernel support incompleteness) problem. Furthermore a number of improvements to the kernel derivative approximation are proposed.

To illustrate the performance of the Total Lagrangian SPH and the mixed correction, four numerical examples ranging from simple 1D dynamic elasticity to 3D real engineering problems are also provided.

keyword. Stable particle methods, total Lagrangian SPH, impact, corrected SPH.

1 Introduction

It is well known that the conventional SPH method initially proposed by L. Lucy (1977) and Gingold and Monaghan (1977) has a number of shortcomings including inconsistency (not even zero order consistent for arbitrary distribution of particles), rank deficiency , J. Sweegle, D. Hicks, S. Attaway (1995), and a spatial discretisation related instability, T. Rabczuk, T. Belytschko and S. Xiao (2004) and J. Sweegle, D. Hicks, S. Attaway (1995) often called tensile instability.

The recent improvements of the conventional SPH method which have given the method first order consistency, R. Vignjevic, J. Campbell, L. Libersky (2000) and , J. Bonet, S. Kulasegaram (2002), have been achieved by modifying the properties of the kernel function itself, see W. Liu, Y. Chen (1995) and W. Liu, S. Jun, J. Adee, T. Belytschko (1995) or by applying corrections to the interpolation integral, R. Vignjevic, J. Campbell, L. Libersky (2000), J. Bonet, S. Kulasegaram (2002). The outstanding problems with tensile instability combined with the lack of ngorous treatment of boundary conditions still hamper the full exploitation of the method.

A number of solutions to the tensile instability problem have been proposed, including non-collocational SPH (where stress and velocity fields are discretised at different locations R. Vignjevic, J. Campbell, L. Libersky (2000), C. Dyka, R. Ingel (1995)) and Lagrangian kernel based interpolation T. Rabczuk, T. Belytschko and S. Xiao (2004). In this paper the interest is focused on Lagrangian kernels in a total Lagrangian framework for SPH and the different types of corrections necessary for first order consistency.

A comprehensive overview of current correction techniques with the SPH discretised conservation equations in a total Lagrangian framework is given. Additionally, the effects of the normalisation of the kernel and accuracy of approximations of the derivatives are considered.

[1]Cranfield University, Cranfield, Bedford, MK43 0AL, UK.
:+44 (0)1234 754736, v.rade@cranfield.ac.uk

SIMULATION OF HYPERVELOCITY DEBRIS IMPACT AND SPACECRAFT SHIELDING PERFORMANCE

A. A. Lukyanov, J. R. Reveles, R. Vignjevic, J. Campbell

Crashworthiness, Impact and Structural Mechanics (CISM),
School of Engineering, Cranfield University, Cranfield, Bedford MK43 0AL, UK
Email: a.lukyanov.2003@cranfield.ac.uk
j.r.reveles.2003@cranfield.ac.uk
v.rade@cranfield.ac.uk
j.campbell@cranfield.ac.uk

ABSTRACT

The objective of the work presented in this paper is the simulation of hypervelocity impact on aluminium-carbon/epoxy-aluminium shields; such multi-layered arrangement is being used by the European Columbus module of the International Space Station. In addition, thermodynamically consistent material models are introduced for each component of the multilayered array which yields a more accurate physical representation of the material response to high velocity impact loading.

Thermodynamically consistent models for aluminium and carbon/epoxy are proposed. In order to describe material behavior under high-intensity loadings a 2-D anisotropic elasto-plastic constitutive model coupled with a damage tensor ω_{ij}, an equation of state, and a failure criterion (based on the critical value of a specific entropy function expressed in terms of the dissipation function) have been developed. The model includes the following key aspects of material response to hypervelocity impact: non-linear anisotropic strength, shock effects and associated energy dependence, compaction, compressive and tensile failure and strain rate effects.

The severe deformations occurring in any hypervelocity impact event are best described by meshless methods since they offer clear advantages for modelling large deformations and failure of solids when compared to mesh based methods.

The simulations presented here are the result of the application of the Smoothed Particle Hydrodynamics (SPH) method to the impact and penetration problem and the incorporation of thermodynamically consistent material models into the Cranfield University SPH solver.

1. INTRODUCTION

Novel approaches to designing advanced aerospace systems require evaluation of extreme operating conditions and an assessment of different failure scenarios and their prevention. The hypervelocity impact of space debris and micrometeoroids is a potential threat to spacecraft which requires careful consideration if structural and sub-system integrity is to be maintained throughout the intended spacecraft mission. Current space debris shields can be effective against small particles of up to 1 cm in size. Weight effective debris shields against particles larger than 1cm are not technically feasible. Fragments larger than 10cm are ground-tracked so that the collision probability with the spacecraft is known and avoidance maneuvers can be performed when required.

Passive shielding on space structures has become a key component in structural design as mission duration, and hence the exposure to space debris and micrometeoroids, has been extended over the years. Designing effective protection requires a good understanding of impact phenomena and the development of new techniques for analysing structures and materials. Nowadays multilayered composite structures are commonly used in spacecraft shielding configurations in order to minimise the risk of subsystem failure and potential total loss of the spacecraft.

The use of accurate material models and robust numerical solvers results in a more effective, fast and accurate design process. In the present study thermodynamically consistent material models are introduced for each component of the multi-layered shield array. Additionally, the application of the Smoothed Particle Hydrodynamics (SPH) method to the impact and penetration problem and the incorporation of consistent material models into the Cranfield University SPH solver allows for a more accurate representation of the material response under severe deformations.

This study concentrates on the numerical simulation of debris impact onto a multi-layered shield arrangement. The geometry, materials and dimensions are similar to those typically found in modern spacecraft Hayhurst et al. (1999), Thoma et al. (2004). The overall

NUMERICAL SIMULATION OF DEBRIS IMPACT ON THIN WALLED METAL SHIELDS.

J.R. Reveles, A. A. Lukyanov, R. Vignjevic.

Crashworthiness, Impact and Structural Mechanics (CISM),
School of Engineering, Cranfield University, Cranfield, Bedford MK43 OAL, UK
Email: j.r.reveles.2003@cranfield.ac.uk
a.lukyanov.2003@cranfield.ac.uk
v.rade@cranfield.ac.uk

ABSTRACT

The present study concentrates on the numerical simulation of hypervelocity impact (HVI) and penetration of small metal fragments on thin walled metal shields. The objective of this project is achieved through the combination of a mesh-free particle hydrocode and a thermodynamically consistent constitutive model for metals. Hydrocodes play an important role in the assessment of shielding performance during high energy impact processes. They provide a useful complement to laboratory experiments for estimating impact damage and for investigating the effect of design changes in a cost effective manner. A thermodynamically consistent material model for the aluminium projectile and shield is proposed. In order to describe material behaviour under high-intensity loading a 2-D anisotropic elasto-plastic constitutive model coupled with a damage tensor, an equation of state, and a failure criterion based on the critical value of a specific entropy function have been developed. The simulations presented here are the result of the application of the Smoothed Particle Hydrodynamics (SPH) method to the impact and penetration problem and the incorporation of a consistent material model for metals into the Cranfield University SPH solver. The numerical results obtained are compared to available experimental data and to empirically developed models commonly employed in the study of HVI phenomena.

1. INTRODUCTION

The exposure of spacecraft to space debris and micrometeoroids has been increased as mission duration has been extended over the years. Micrometeoroid impact occurs with a frequency that varies considerably with the type of space mission, it is common practice to specify the risk of impact as a probability figure over the mission duration. Impact of micrometeoroids generally causes a degradation of surface thermal properties although the risk of component failure also exists. The clearest evidence of particle impact on spacecraft comes from the Giotto spacecraft during its approach to Halley's comet in which particle impact led to the failure of some experiments. In addition to natural micrometeoroids, the space environment also presents a threat from man-made space debris. This group of objects consists of aluminium oxide dust particles, nuts and bolts, rocket upper stages etc. which range from 0.001mm to 10m in size, with typical velocities in the range of a few hundred meters per second to 20km/s [5]. The majority of man-made particles originate from satellite and launcher components, hence the average density is assumed to be that of aluminium alloys. System requirements for meteoroid and debris protection dictate that crew safety is ensured in the case of manned spacecraft and that an unmanned spacecraft should remain operational throughout its intended life. Evidently, the hypervelocity impact of space debris and micrometeoroids is a potential threat to spacecraft which requires careful consideration if structural and sub-system integrity is to be maintained throughout the spacecraft mission. Current space debris shields can be effective against small particles of up to 1 cm in size. Weight effective debris shields against particles larger than 1cm are not technically feasible. Fragments larger than 10cm are ground-tracked so that the collision probability with the spacecraft is known and avoidance manoeuvres can be performed when required. Passive shielding on space structures has become a key component in structural design. Designing effective protection requires a good understanding of impact phenomena and the development of new techniques for analysing structures and materials. Nowadays multilayered arrays are commonly used in spacecraft shielding configurations in order to minimise the risk of subsystem failure and potential total loss of the spacecraft.

The use of accurate material models and robust numerical solvers results in a more effective, fast and accurate design process. In the present study thermodynamically consistent material models are introduced for each component of the multi-layered shield array. Additionally, the application of the Smoothed Particle Hydrodynamics (SPH) method to the impact and penetration problem and the incorporation of consistent material models into the Cranfield University SPH solver [3] allows for a more accurate representation of the material response under severe deformations. The first step in the numerical simulation consists of replicating real experiments, namely D2031and D2033 [6], and comparing the resulting

Corrected Total Lagrangian SPH in the simulation of impact phenomena in solids.

Juan R. Reveles*◆, Rade Vignjevic*

*Crashworthiness, Impact and Structural Mechanics Group.

Cranfield University, Bedfordshire, MK43 0AL, United Kingdom.

◆Corresponding author, e-mail.*Jrw@onetel.com* Phone:+44 (0)1234 750111 Ext.5176.

Abstract.

The accuracy and stability of the smoothed particle hydrodynamics (SPH) method can be greatly improved by introducing corrections into the basic algorithms and approximation equations. These corrections are aimed at restoring the consistency and incompleteness of the SPH interpolation and correcting the errors arising from uneven particle distributions. The basic concepts and equations which restore the consistency of the SPH method and enhance its overall accuracy are discussed, conventional and normalised-corrected Total Lagrangian SPH. equations are also provided. Some examples are given to illustrate the suitability of the modified SPH algorithms in the simulation of solids under dynamic loading.

Keywords: Total Lagrangian SPH; impact; tensile instability.

1. Introduction.

The smoothed particle hydrodynamics (SPH) method has been successfully applied to a vast range of problems in solid and fluid mechanics [1,3,6,8,10]. However, some inherent difficulties have hampered the full exploitation of the method. For example, one of the difficulties of conventional SPH algorithms is their inability to correct boundary deficiency problems caused by the truncated integral at the physical boundaries of the domain. Additionally, in its most basic form the resulting interpolating equations are not even zero order consistent and symmetrisation terms have to be introduced to ensure a constant field can be reproduced exactly and ensures the satisfaction of Newton's 3rd law locally [9,18].

SIMULATION OF HIGH-VELOCITY IMPACT OF GRAPHITE/EPOXY COMPOSITE LAMINATES

A. A. Lukyanov, R. Vignjevic, J. R. Reveles

Crashworthiness, Impact and Structural Mechanics (CISM),
School of Engineering, Cranfield University, Cranfield, Bedford MK43 OAL, UK
Email: a.lukyanov.2003@cranfield.ac.uk
v.rade@cranfield.ac.uk
j.r.reveles.2003@cranfield.ac.uk

ABSTRACT

The objective of the work presented in this paper is to generate a thermodynamically consistent coupled macro-homogeneous anisotropic thermo-elastic-plastic damage model for fibre composites. The model is based on the thermodynamics of irreversible processes and the assumption that damage within a continuum can be represented as a damage tensor ϖ_{ij} [12], [13]. In order to describe material behaviour under high-intensity loadings, a 3-D anisotropic elasto-plasticity constitutive model coupled with damage tensor, an equation of state, and a failure criterion for fibre composites have been developed. The model includes the following key aspects of the response of the materials to hypervelocity impact, which occurs in the process of model development: non-linear anisotropic strength, shock effects and associated energy dependence, compaction, compressive and tensile failure, strain rate effects.
The criterion for failure initialisation is the entropy criterion based on a critical value of a specific entropy function expressed through the dissipation function. In order to take into account different modes of composite failure (fracture of fibres, fracture of matrix, de-lamination) several criteria were considered. The smoothed particle hydrodynamics (SPH) technique [4] has been proposed for the numerical simulation of impact damage and penetration of composite structures. The above physics were incorporated into the SPH solver.

1. INTRODUCTION

All spacecraft in orbit are exposed to impacts with meteoroids and debris. Some of these particles are large enough that an impact could cause significant damage to the spacecraft components. Composites materials are commonly employed in spacecraft shielding configurations, and for this reason impact and penetration of composite structures have received considerable attention in the last decade. The physical phenomena occurring in high-velocity impact on composite laminates are complex. Thermomechanical processes which occur in deformable composite under intensive dynamic loading consist of coupled mechanical, thermal and structural stages. Dynamic fracture of composite materials is a complicated multistage process which includes the appearance, evolution and confluence of micro-defects (damage) and cracks.
Novel approaches to designing advanced aerospace systems require evaluation of extreme operating conditions and an assessment of different failure scenarios and their prevention. The hypervelocity impact of space debris and micrometeoroids is a potential threat to spacecraft which requires careful consideration if structural and sub-system integrity is to be maintained throughout the intended spacecraft mission. Current space debris shields can be effective against small particles of up to 1 cm in size. Weight effective debris shields against particles larger than 1cm are not technically feasible. Fragments larger than 10cm are ground-tracked so that the collision probability with the spacecraft is known and avoidance maneuvers can be performed when required.

Designing effective protection requires a good understanding of impact phenomena and the development of new techniques for analysing structures and materials. Nowadays multilayered composite structures are commonly used in spacecraft shielding configurations in order to minimise the risk of subsystem failure and potential total loss of the spacecraft.

The physical phenomena occurring in high-velocity impact on composite laminates are complex. They include bending, local contact, bulging, matrix cracking, fibre breakage, delamination, fragmentation, etc.

In this paper a macromechanics approach for fibre composites is proposed for SPH simulations of impact penetration into Graphite/Epoxy (Gr/Ep) composites. A 3-D elasto-plasticity constitutive model, an EOS, and a failure criterion which account for the anisotropic behaviors of fibre composites were developed. Since materials often undergo large rotation during impact, stress and strain transformations between the principal material axes and the deformed configurations were also considered based on the polar stress rate approach. Numerical simulations were carried out with the Gr/Ep composite laminates impacted by an aluminium sphere projectile. The use of accurate material models and